Metabolic and mitochondrial control of humoral immunity



Yavuz Furkan Yazicioglu

St. Hugh's College, University of Oxford

Kennedy Institute of Rheumatology, NDORMS

Thesis submitted in fulfilment of the requirements for the degree of

Doctor of Philosophy, University of Oxford

September 2024

Abstract

B cells undergo extreme metabolic changes throughout their life cycles. Naive B cells are considered functionally and metabolically quiescent; however, upon differentiating into germinal centre (GC) B cells, they divide at the fastest rate of almost any mammalian cell type. The metabolic mechanisms underlying this process remain poorly understood. How B cells adapt to different tissue environments by switching fuel sources is a growing field of interest. Mitochondria are key players in cellular metabolism, carrying out a wide array of critical functions. Mitochondria actively guide differentiation and activation of lymphocytes by undergoing rapid remodelling. Energy homeostasis and ATP production are typically the primary functions of mitochondria in immune cells; however their influence extends to other molecular processes, such as regulating oxidation/reduction balance, signalling pathways, and biosynthesis, although their involvement in B cell biology remains largely unknown. In this thesis, I demonstrated that the metabolism of asparagine, a non-essential amino acid, is highly upregulated in GC B cells. I found that asparagine is conditionally essential to B cells, and the expression of its synthetic enzyme, asparagine synthetase (ASNS) is robustly induced in GC B cells. When *Asns* is deleted, B cell survival and proliferation in low-asparagine environments is substantially impaired. Furthermore, depleting environmental asparagine using asparaginase or dietary restriction severely compromises the GC reaction, affinity maturation, and humoral response to influenza infection, especially when the capacity to synthesise asparagine was abolished in B cells. I found that B cells adapt to asparagine deprivation through ASNS upregulation, which is critical in supporting oxidative phosphorylation and mitochondrial homeostasis. I also discovered that mitochondria in GC B cells are dynamic and have elevated mitochondrial transcription and translation activity, which is mediated by the activity of the transcription factor mitochondrial A (TFAM). *Tfam* is essential for normal B cell development and controls GC entry. When *Tfam* is deleted, GC formation, organisation, and output are substantially impaired. Loss of *Tfam* also disrupts the actin cytoskeleton and reduces GC B cell mobility in response to chemokines.

Mechanistically, this defect is linked to an imbalance in electron transport chain proteins and the accumulation of mitochondrial reactive oxygen species. Finally, I demonstrated that B cell lymphoma greatly increases mitochondrial translation. Genetic ablation of *Tfam* in B cells provides complete protection against lymphoma development in a *c-Myc* transgenic mouse model, highlighting the potential of targeting mitochondria in B cell malignancies.

Publication list

1. Julia Johnstone*, Yavuz F. Yazicioglu*, Alexander J. Clarke, Fuelling B cells: dynamic regulation of B cell metabolism, *Current Opinions in Immunology*, *Volume 91, 2024, 102484, ISSN 0952-7915, https://doi.org/10.1016/j.coi.2024.102484.*

2. Yavuz F. Yazicioglu*, Eros Marin*, et al. ,Asparagine availability controls germinal center B cell homeostasis. *Sci. Immunol.* 9,eadl4613(2024).DOI:10.1126/sciimmunol.adl4613

3. Yavuz F. Yazicioglu*, Robert J. Mitchell*, Alexander J. Clarke, Mitochondrial control of lymphocyte homeostasis, *Seminars in Cell & Developmental Biology*, Volumes 161–162, 2024, Pages 42-53, https://doi.org/10.1016/j.semcdb.2024.03.002.

4. Mariana Borsa, Ana Victoria Lechuga-Vieco, Amir H. Kayvanjoo, Yavuz Yazicioglu et al., Inheritance of old mitochondria controls early CD8+ T cell fate commitment and is regulated by autophagy, bioRxiv 2024.01.29.577412; doi: https://doi.org/10.1101/2024.01.29.577412

5. Yazicioglu, Y.F., Marin, E., Sandhu, C. et al. Dynamic mitochondrial transcription and translation in B cells control germinal center entry and lymphomagenesis. *Nat Immunol* 24, 991–1006 (2023). https://doi.org/10.1038/s41590-023-01484-3

6. Yazicioglu, Y.F., Clarke, A.J. The kiss a cell can't forget: tracking cell–cell interactions with uLIPSTIC. *Nat Rev Immunol* 23, 477 (2023). https://doi.org/10.1038/s41577-023-00910-9

7. Duygu Sari-Ak, Alvaro Torres-Gomez, Yavuz F. Yazicioglu, et al., Structural, biochemical, and functional properties of the Rap1-Interacting Adaptor Molecule (RIAM), *Biomedical Journal*, Volume 45, Issue 2, 2022, Pages 289-298, https://doi.org/10.1016/j.bj.2021.09.005.

8. Joe N. Frost, Sarah K. Wideman, Alexandra E. Preston, Megan R. Teh, Zhichao Ai, Lihui Wang, Amy Cross, Natasha White, Yavuz Yazicioglu et al., Plasma iron controls neutrophil production and function. Sci.dv.8,eabq5384(2022). DOI:10.1126/sciadv.abq5384

9. Yabas, M., Yazicioglu, Y.F., Hoyne, G.F., Goodnow, C.C. and Enders, A. (2021), Loss of hnRNPLL-dependent splicing of Ptprc has no impact on B-cell development, activation and terminal differentiation into antibody-secreting cells. *Immunol. Cell Biol*., 99: 532-541. https://doi.org/10.1111/imcb.12433

10. Yazicioglu, Y.F., Aksoylar, H.I., Pal, R., Patsoukis, N., Boussiotis, V.A. Unraveling key players of humoral immunity: Advanced and optimized lymphocyte isolation protocol from Peyer's Patches. *Journal of Visual Experiments (JOVE)* e58490, doi:10.3791/58490 (2018)

(*) indicates equal contributions

Statement for re-use of published material

I hereby declare that this thesis is the result of my own work. All experimental data presented were collected and analysed by me unless otherwise specified.

I would like to acknowledge that many textual and graphical elements were previously included in a preprint, a research paper, and two reviews (one published, one *in press*). I am the first author on all these publications. Specific details are provided below.

Chapter 1:

The figures in this chapter were generated by me and have been reused from the following publications:

Yavuz F. Yazicioglu*, Robert J. Mitchell*, Alexander J. Clarke, Mitochondrial control of lymphocyte homeostasis, *Seminars in Cell & Developmental Biology*, Volumes 161–162, 2024, Pages 42-53, https://doi.org/10.1016/j.semcdb.2024.03.002.

Julia Johnstone*, Yavuz F. Yazicioglu*, Alexander J. Clarke, Fuelling B cells: dynamic regulation of B cell metabolism, *Current Opinions in Immunology*, *Volume 91,*

2024, 102484, ISSN 0952-7915, https://doi.org/10.1016/j.coi.2024.102484.

Chapter 2:

The text in this chapter is based on the methods sections of my two research papers. Although the text has been largely rephrased and adapted:

Yavuz F. Yazicioglu*, Eros Marin*, et al. ,Asparagine availability controls germinal center B cell homeostasis. *Sci. Immunol.* 9,eadl4613(2024).DOI:10.1126/sciimmunol.adl4613

Yazicioglu, Y.F., Marin, E., Sandhu, C. et al. Dynamic mitochondrial transcription and translation in B cells control germinal center entry and lymphomagenesis. *Nat Immunol* 24, 991–1006 (2023). https://doi.org/10.1038/s41590-023-01484-3

Chapter 3:

The figures and text in this chapter have been reused from the following preprint. The text has been substantially rephrased and figures have been modified to some extent.

Yavuz F. Yazicioglu*, Eros Marin*, et al. ,Asparagine availability controls germinal center B cell homeostasis. *Sci. Immunol.* 9,eadl4613(2024).DOI:10.1126/sciimmunol.adl4613

Chapter 4:

The data and figures in this chapter have also been reused from the following publication. The text has been substantially rephrased and figures have been modified to some extent.

Yazicioglu, Y.F., Marin, E., Sandhu, C. et al. Dynamic mitochondrial transcription and translation in B cells control germinal center entry and lymphomagenesis. *Nat Immunol* 24, 991–1006 (2023). https://doi.org/10.1038/s41590-023-01484-3

Nuffield Department of Orthopaedics,
Rheumatology and Musculoskeletal Sciences

21st September 2024

To whom it may concern,

Re: DPhil thesis of **Yavuz Yaziciolglu**

I hereby confirm that the DPhil thesis of Yavuz Yazicioglu, whom I have supervised, is all his own work, except where explicitly stated otherwise.

Your faithfully,

Alex Clarke PhD, FRCP
Group Leader, Wellcome Trust Clinical Research Career Development Fellow, and Honorary Consultant Rheumatologist, Oxford University Hospitals

Kennedy Institute of Rheumatology | University of Oxford | Roosevelt Drive | Headington | Oxford | OX3 7FY
Email: alexander.clarke@kennedy.ox.ac.uk | Tel: +44 (0)1865 612644

Acknowledgements

I would like to begin by acknowledging the inspirational scientists who have supported me since my undergraduate days when I was a young, curious medical student fascinated by the immune system. Prof. Colin Anderson, Dr. Anselm Enders, Prof. Vassiliki Boussiotis, Dr. Mehmet Yabas, and many others have been remarkable mentors, for which I am deeply grateful.

A special credit must go to my DPhil supervisor, Dr Alexander Clarke. He provided me with a perfect combination of guidance and intellectual freedom, which nurtured my independent thinking. His trust has been one of the greatest motivators during my DPhil. Being the first DPhil student in a lab can often be daunting, but under his supervision it became one of the best academic experiences I could have hoped for. I will always be grateful for everything he has done for me, and I truly look forward to continuing as a close colleague and collaborator in the future.

I also want to express my heartfelt thanks to all the past and present members of the Clarke Lab; particularly Robert, Julia, Sini, Hana, and Antony. You've been there through experiments, academic challenges (particularly during our epic battles with the infamous Reviewer 2 – twice!), and you've brought so much joy into the work environment in the lab. I will deeply miss our 'mega takedowns', ELISA-Fridays, and our lab meetings that always ran over time – though, of course, that had nothing to do with me (!).

My gratitude extends to several other wonderful people Oxford brought into my life. Fabi, Zhi, Bara, and Lion, who deserve a very special mention. You were always there for me during my DPhil, and when I think back on my cherished memories in Oxford, you were part of so many of them. I will greatly miss our game nights at Thirsty Meeples, dinners at Bennet Crescent, tennis-brunch weekends at Florence Park, and countless other beautiful moments we shared. As we now scatter across the globe and continue our nomadic postdoc lives, I sincerely hope our friendship will endure across time and distance.

And to my dear friends from College, Gultekin and Edie, who were among the first people I met in Oxford—how lucky I was that it grew into a fantastic friendship that I will always treasure.

I would also like to acknowledge all those who helped me overcome the scientific challenges I faced during my DPhil. Special thanks to my co-supervisor Michael Dustin and his lab, as well as the labs of Susie Dunachie, Coles Buckley, Katja Simon, and Irina Udalova. Many others from the Kennedy Institute and the University of Oxford also deserve my thanks.

These DPhil years have come with great sacrifices, and sadly, it's often loved ones who feel the greatest impact. I am forever grateful to my parents, Mebrure and Mustafa, and my little brother, Yusuf Serdar, for always being there for me, even with the distance between us.

Key abbreviations

AAG	Alanine, Aspartate, and Glutamate
AID	Activation induced cytidine deaminase
Asn	Asparagine
ASNase	Asparaginase
ASNS	Asparagine synthetase
Asp	Aspartate
Bcl6	B cell lymphoma 6
BCR	B cell receptor
COX I	Cytochrome c oxidase subunit I
COX IV	Cytochrome c oxidase subunit IV
Cpt2	carnitine palmitoyl transferase 2
Cyt C	Cytochrome C
DLBCL	Diffuse large B cell lymphoma
DZ	Dark zone
ECAR	Extracellular acidification rate
ETC	Electron transport chain
FDC	Follicular dendritic cells
FoB	Follicular B cell
GLUT1	Glucose transporter 1
HIF1α	Hypoxia-inducible factor 1a
KEGG	Kyoto Encyclopedia of Genes and Genomes
LAT1	L-type amino acid transporter 1
LC-MS	Liquid chromatography-mass spectrometry
LDHA	Lactate dehydrogenase A
LZ	Light zone
mtDNA	Mitochondrial DNA
MZB	Marginal zone B cell
NADPH	Nicotinamide adenine dinucleotide phosphate
NP-CGG	4-hydroxy-3-nitrophenylacetyl-chicken gamma globulin
OxPhos	Oxidative phosphorylation
PC	Plasma cell
PHGDH	Phosphoglycerate dehydrogenase
PPP	Pentose phosphate pathway
ROS	Reactive oxygen species
SDHA	Succinate dehydrogenase A
Ser	Serine
SHM	Somatic Hypermutation
SRBC	Sheep red blood cells
SREBP	Sterol regulatory binding protein
TCA	Tricarboxylic acid
TFAM	Mitochondrial transcription factor A
T_{FH}	T follicular helper cell
T_{FR}	T follicular regulatory cell
Treg	Regulatory T cell
UPR^{mt}	Mitochondrial unfolded protein response

Contents (Sections/Figures)

Chapter 1. General Introduction *15*

1.1. Metabolic regulation in lymphocytes 15
1.1.1. Glucose metabolism 18
1.1.2. Amino acid metabolism 19
1.1.3. Lipid metabolism 20
1.1.4. Mitochondrial metabolism 22

1.2. Mitochondrial dynamics in lymphocyte homeostasis 25
1.2.1. Mitochondrial DNA homeostasis 27
1.2.2. Mitochondrial transcription and translation in lymphocytes 30

Chapter 2. Materials and Methods *32*

2.1. Mice 32

2.2. Immunisation 32

2.3. Influenza infection 33

2.4. *In vivo* modification of asparagine levels 33

2.5. Bone marrow chimera generation 34

2.6. Cell isolation 34

2.7. Flow cytometry and imaging flow cytometry 35

2.8. Detection of ETC/UPR^{mt} proteins with spectral flow cytometry 37

2.9. Single-mitochondrion translation assay 37

2.10. *Ex vivo* lymph node slice culture 39

2.11. *Ex vivo* single cell competitive Asn uptake assay 39

2.12. Multiplexed Tissue Imaging using Cell DIVE 40

2.13. Immunohistochemistry and immunofluorescence 41

2.14. Immunocytochemistry 42

2.15. 3D Lattice SIM 43

2.16. STED microscopy 44

2.17. Image analysis 44
2.17.1. CellDIVE 44
2.17.2. GC Identification and area quantification 44
2.17.3. DZ/LZ Analysis 45
2.17.4. Determination of mitochondrial properties 45
2.17.5. PC-PB Quantification 45

2.18. *In vitro* mouse primary B cell culture 45

2.19. iGB culture system 46

2.20. iGB adoptive transfer 47

2.21. Transwell migration assay 47

2.22. Single cell RNA-seq 48

2.23. NP conjugation 49

2.24. ELISA 49

2.25. T_{FH}-B cell co-culture 50

2.26. Cytoplasmic calcium assay....51
2.27. Lymphoma adoptive transfer....51
2.28. Quantification of metabolism by protein translation (SCENITH)....52
2.29. Extracellular flux analysis....52
2.30. Serum and lymph node interstitial fluid (LNIF) collection for LC-MS....53
2.31. Mass spectrometry....54
2.32. Western blotting....56
2.33. Statistical analysis....57
Chapter 3: Asparagine metabolism controls B cell homeostasis....58
3.1. Introduction....58
3.2. Results....61
3.2.1. Protein translation in GCs is highly active....61
3.2.2. Neutral amino acid transporters are upregulated in GC B cells....64
3.2.3. Asparagine uptake is dynamically regulated in GC B and plasma cells....66
3.2.4. Alanine, Aspartate, and Glutamate pathway enzymes are upregulated in GC B cells....69
3.2.5. Specific deletion of Asns in B cells: B-Asns mice....72
3.2.6. ASNS is important for B cell viability when the availability of Asn is limited....74
3.2.7. ASNS is critical for B cell division under conditions of low Asn availability....76
3.2.8. Exogenous Asn is conditionally required for plasmablast development....78
3.2.9. ASNS regulates plasmablast differentiation independently of its role in cell division....80
3.2.10. *Ex vivo* lymph node slice cultures reveal Asn dependency in GC B and plasma cells....82
3.2.11. The GC compartment is sensitive to asparagine depletion....84
3.2.12. Asparagine availability regulates the spatial features of GCs....87
3.2.13. T follicular helper cells remain intact under Asn deprivation....89
3.2.14. Asn deprivation alters GC B cell dynamics....91
3.2.15. Exogenous Asn is required for humoral responses....94
3.2.16. *Asns*-deficient GC B cells are less competitive under Asn restriction....97
3.2.17. Dietary Asn restriction disrupts the function of GC B cells lacking ASNS....100
3.2.18. Asn is required for antibody homeostasis....102
3.2.19. Affinity maturation is influenced by dietary Asn intake....104
3.2.20. Memory B cell responses are dependent on Asn....107
3.2.21. Asn deprivation attenuates boost-induced affinity enrichment....109
3.2.22. Supplementation of Asn does not affect GC B cell dynamics....111
3.2.23. Asn availability regulates the humoral response to influenza infection....113
3.2.24. Affinity maturation in influenza infection depends on Asn....115
3.2.25. Asn deprivation leads to a defective GC response in influenza infected mice....117
3.2.26. Metabolic activity in B cells is regulated by Asn....119
3.2.27. Asn depletion disrupts mitochondrial ETC homeostasis....121
3.3. Discussion....123
Chapter 4: Dynamic mitochondrial transcription and translation control germinal centre entry and lymphomagenesis....129
4.1. Introduction....129
4.2. Results....130
4.2.1. The Mito-QC reporter highlights mitochondria in GCs....130
4.2.2. GC B cells do not perform mitophagy....132

4.2.3. GCs are sites of enhanced mitochondrial density 134
4.2.4. The mitochondrial network in GC B cells is highly dynamic 136
4.2.5. Mitochondrially-encoded proteins are increased in GC B cells 138
4.2.6. GC B cells show distinct mitochondrial transcription and nucleoid organisation 140
4.2.7. B cell-specific deletion of *Tfam* in B cells: B-Tfam mice 142
4.2.8. Loss of *Tfam* leads to defective B cell numbers in the periphery 143
4.2.9. *Tfam* is essential during B cell development 145
4.2.10. Mitochondrial homeostasis in B cells requires TFAM 147
4.2.11. TFAM is critical for the GC reaction 150
4.2.12. Antigen-specific humoral responses are mediated by TFAM 152
4.2.13. Plasma cell development requires *Tfam* 154
4.2.14. TFAM is essential for the emergence of memory B cell responses 156
4.2.15. Rates of apoptosis and cell division remain unaffected in TFAM deficiency 158
4.2.16. TFAM regulates the GC transcriptional program 160
4.2.17. GC B cell somatic hypermutation and clonal evolution depend on TFAM 162
4.2.18. TFAM is essential for GC B cell commitment 164
4.2.19. Deletion of *Tfam* disrupts GC entry 165
4.2.20. Requirement for TFAM in GC B cells is cell intrinsic 168
4.2.21. TFAM regulates mitochondrial translation in activated B cells 170
4.2.22. Mitochondrial translation is dynamically regulated across B cell subsets 172
4.2.23. TFAM is essential for metabolic reprogramming of activated B cells 174
4.2.24. *Tfam* deletion disrupts chemokine-directed GC B cell migration 176
4.2.25. Restoring mitochondrial ROS balance rescues defective mobility 178
4.2.26. B cell lymphoma is critically dependent on TFAM 180

4.3. Discussion 183

Chapter 5: General Discussion 187

Bibliography 191

Appendix 211

Chapter 1. General Introduction

1.1. Metabolic regulation in lymphocytes

The lymphocyte lineage originates from the common lymphoid progenitor in the bone marrow and branches out to T and B cell trajectories[1]. The maturation of B cells primarily occurs in the bone marrow, whilst T cells migrate into the thymus for further development. In the bone marrow, B cell precursors undergo rounds of division and cellular differentiation[1]. Some developmental phases are more energetically demanding than others, creating critical metabolic checkpoints[2].

Prior to activation, both B and T cells enter a phase of metabolic inactivity, after which they may experience significant metabolic changes throughout their life span, going from quiescence to rapid proliferation and, in some instances, returning to quiescence if they differentiate into long-lived subsets[3]. During these processes, metabolic and mitochondrial reprogramming takes place to meet heightened biosynthetic and bioenergetic needs, typically involving upregulation of nutrient uptake, breakdown of glucose—also known as glycolysis—and oxidative phosphorylation (OxPhos)[4].

Immature B cells that functionally assemble a B cell receptor (BCR) in the bone marrow migrate to the spleen, where they further differentiate into transitional B cells before committing to mature subsets of follicular B cells (FoB) or marginal zone B (MZB) cells[5] (outlined in Fig 1.1). B cells play a crucial role in humoral immunity primarily through antibody responses. When activated, they can initiate either the extrafollicular response or the germinal centre (GC) reaction[6]. This critical lineage bifurcation determines B cell fate.

When lymphocytes reach the effector stages, their modes of action and functionality differ. B-cell activation results in antigen presentation, clonal expansion, and chemotaxis. This functional heterogeneity also extends to the T cell lineage. T-cell activation may drive cytokine production, cytotoxicity, and the acquisition of regulatory roles. $CD8^+$ T cells mainly mediate cell killing. $CD4^+$ T cells, on the other hand, differentiate into distinct effector

subsets such as T follicular helper (T_{FH}) cells supporting the GC reaction or regulatory T cells (Tregs) counteracting these effects in GCs and beyond.

Activated B cells seed and form GCs at the interface of the T cell zone and B cell follicle in secondary lymphoid organs. In GCs, B cells move between dark and light zones[7]. The dark zone (DZ) is characterised as a site of rapid proliferation and somatic hypermutation (SHM) driven by the enzyme activation induced cytidine deaminase (AID), which introduces random point mutations in the variable region of immunoglobulin genes that alter BCR specificity[8]. In the light zone (LZ), B cells acquire antigens captured on follicular dendritic cells (FDCs). This is particularly critical for their capacity to present antigens and interact with T_{FH} cells[9]. B cell clones with distinct BCR specificities compete for help from T_{FH} cells to receive signals that boost their metabolism and proliferative capacity, therefore enabling successive rounds of clonal expansion and SHM[8,10] (outlined in Fig 1.1). These GC B cells can then recycle back into the DZ for further rounds of SHM or exit the GC by differentiating into plasma cells (PCs) or memory B cells[9,11]. GC B cell clones that fail to engage with T_{FH} cells are eliminated through apoptosis[12]. SHM is critical in enhancing BCR affinity and maturation, albeit with the risk of introducing BCR-crippling fatal mutations or chromosomal aberrations; the former leads to further waves of apoptosis in the DZ[13], whilst the latter may give rise to malignant clones and subsequent development of B cell lymphomas[14].

Cellular metabolism at each stage is differently programmed and directly tuned to intra- and extracellular signalling and nutrient composition[2,3]. Although B cells have distinct metabolic needs, their metabolic profiles have not been completely defined.

Below, I will discuss the discoveries that identified the key sources of nutrients and the crucial role of the associated metabolic pathways (outlined in Fig. 1.2) involved in B cell homeostasis across different trajectories (outlined in Fig. 1.3).

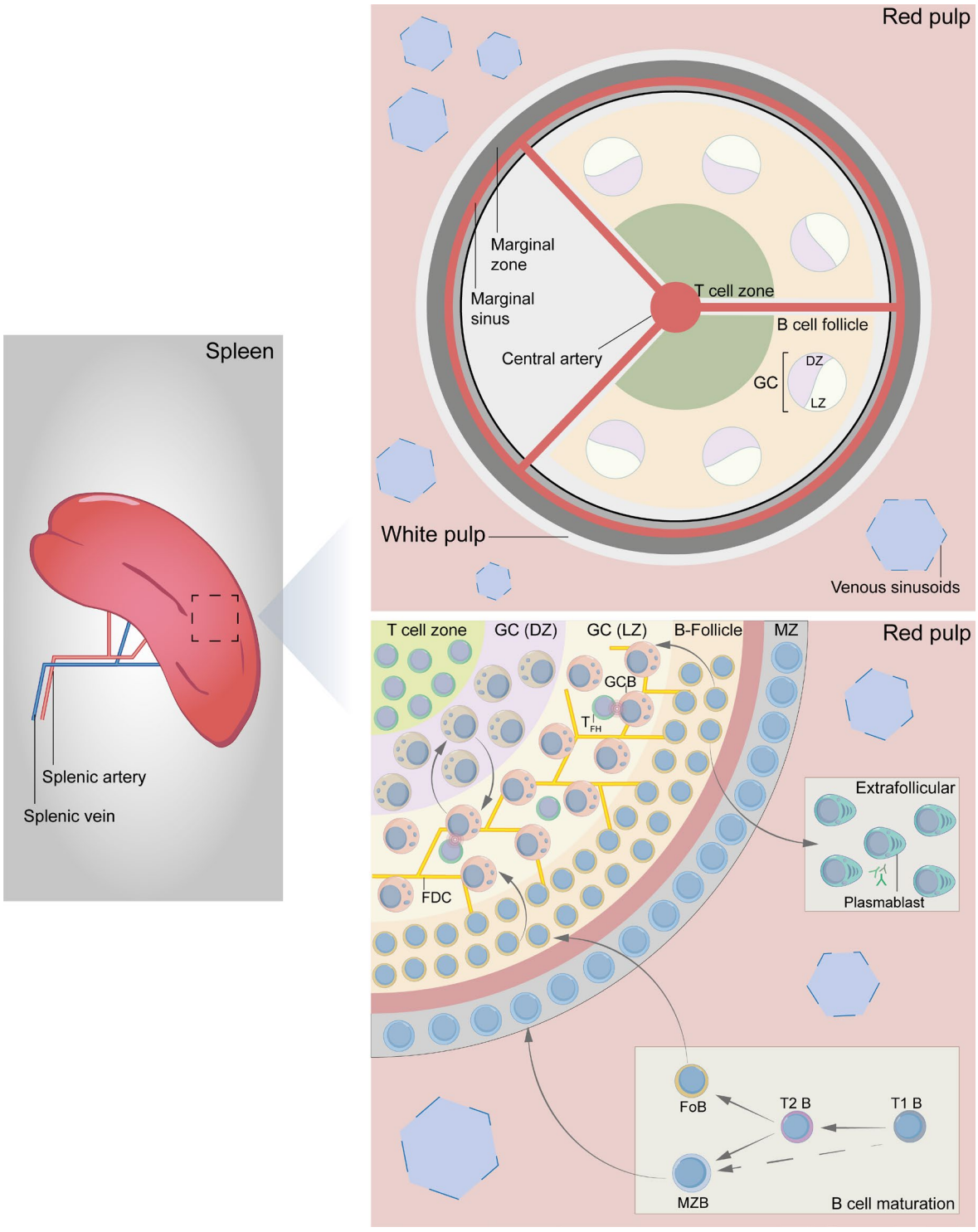


Figure 1.1: Overview of B cell homeostasis in relevant splenic compartments in mouse.

Two functionally distinct compartments of the spleen: the red pulp, rich in venous sinusoids, is critical for filtering blood, and the white pulp, containing major populations of immune cells. Immature B cells migrate from the bone marrow to the spleen, completing their maturation. Transitional B cells develop into FoB or MZB cells following specific developmental cues. The marginal zone and the marginal sinus separate the white pulp from the red pulp. It contains MZB cells, while FoB cells are contained in the B cell follicles. In response to an immunogenic stimulus, some naïve B cells differentiate directly into

plasmablasts to drive extrafollicular responses. In contrast, other activated B cells participate in GCs at the junction of the B cell follicle and the T cell zone. While in the GC LZ, B cells interact with T_{FH} and FDCs. Affinity-enriched selected clones then proliferate rapidly in the GC dark zone. GC processes described here are conserved in other lymphoid organs. I generated this figure and included it in a review article that is currently *in press.*

1.1.1. Glucose metabolism

The development of a B cell throughout its life cycle is marked by strictly regulated glucose uptake and metabolism. The balance between glycolysis and OxPhos is vital and depends on the von Hippel Lindau (vHL)- Hypoxia induced factor (HIF1α) axis in metabolically quiescent naïve B cells[15,16]. The deletion of vHL at early stages in B cell development over-stabilizes HIF1α, inducing an abnormal switch to glycolysis. This leads to severe disturbance of the peripheral B cell compartment. When subjected to physiological stimulation, B cells increase their glucose uptake. However, instead of being metabolized by glycolysis, glucose is shunted towards the pentose phosphate pathway (PPP) and into nucleotide and fatty acid synthesis[17,18]. When glucose is reduced 10-fold in culture media, B cell proliferation and differentiation remain unaltered. However, the ability to switch immunoglobulin class, a process referred to as class-switching that is also driven by AID, is diminished.

However, genetic ablation of lactate dehydrogenase (LDHA), an enzyme critical for aerobic glycolysis, at the naive B cell stage results in a compromised GC response, whereas deletion at the GC B cell stage has very little effect[19]. This therefore indicates distinct metabolic requirements during B cell activation and GC progression. Additional evidence has been provided through *ex vivo* metabolic assays in other studies, showing that activated GC B cell precursors depend on glucose and glycolysis[20,21]. Two recent studies have reported that loss of *Slc2a1*, which encodes glucose transporter 1 (GLUT1), reduces the number of GC B cells, limits the GC reaction, and impairs PC differentiation[22,23]. Although glucose uptake and expression of glycolytic enzymes peaked in LZ GC B cells, DZ GC B cells were more sensitive to *Slc2a1* deletion, likely due to their elevated division rate.

Mechanistically, blocking glucose uptake caused a modest reduction in the extracellular acidification rate (ECAR) but had a much more pronounced effect on the PPP, particularly in GC B cells and PCs. The PPP is critical for providing biosynthetic intermediates for nucleotide synthesis and generating nicotinamide adenine dinucleotide phosphate (NADPH), which is required for redox balance[24]. Indeed, in B cells in which *Slc2a1* was depleted, much higher levels of reactive oxygen species (ROS) were detected compared to wild type controls[22].

1.1.2. Amino acid metabolism

The tricarboxylic acid (TCA) cycle and OxPhos are upregulated in activated B cells *in vitro*. It has been demonstrated that glutamine is needed for B cell differentiation, proliferation, and class-switching, as well as DNA replication and mass accumulation in B cells[17]. Glutamine also plays an important role in the glutathione production, a major cellular redox system[25]. Impaired capacity to synthesise glutathione disrupts the electron transport chain (ETC), leading to ROS accumulation and cellular dysfunction in FoB cells[26]. Antibody production was also hindered in plasmablasts which originated from glutathione-deficient B cells. Glutamate cysteine ligase (*Gclc*), a key enzyme of glutathione synthesis, was also critical during the development of MZB cells[26]. This highlights the interrelationship between redox balance and B cell metabolism. PCs express high levels of glutamine transporters, and it was reported that a burst of plasmablast proliferation during malaria infection decreased the frequency of GC B cells, a defect reversed by glutamine supplementation[27]. This would indicate that plasmablasts are a sink for glutamine, directly competing with GC B cells for this amino acid, and that glutamine is also vital for the GC response.

The reliance of lymphocytes on glutamine metabolism has long been appreciated[28], but the role of other specific amino acids for B cell metabolism is currently under investigation[29]. For example, among them, the essential amino acid L-leucine, was identified to be

regulatory in B cell activation. Notably, inhibition of its transporter, SLC7A5, reduced inflammatory cytokines and antibody production[30].

Genetic ablation of SLC3A2, which, together with SLC7A5, forms the large neutral amino acid transporter (LAT1), revealed defects in B cell proliferation and antibody production, but these were due to its integrin-binding role[31]. One recent study identified a population of B cells with immunosuppressive properties that was expanded in colon tumour polyps, associated with poor prognosis, and had high consumption of leucine[32]. Dietary restriction of leucine reversed this and reduced tumour sizes in a model of colorectal cancer.

Serine (Ser) is also an important nutrient in the development of GCs. Inhibition or deletion of phosphoglycerate dehydrogenase (PHGDH), the rate-limiting enzyme in the pathway of serine synthesis, disrupts the GC reaction and the affinity maturation[33]. Similarly, elevation of enzymes of this pathway has also been documented in B cell lymphoma, rendering it sensitive to PHGDH inhibition.

While the role of other specific amino acids is less well understood, a study reported that dietary tryptophan restriction in mice abrogates the development of B cells more than T cells, although the underlying mechanisms warrant further investigation[34].

1.1.3. Lipid metabolism

Adding to the importance of lipid metabolism in GC B cells, signalling by sterol regulatory binding protein (SREBP) - a transcription factor that initiates expression of genes involved in fatty acid synthesis - is critical for antigen-specific plasma cell and memory responses induced by vaccination in mice[35]. Defects in this pathway caused perturbations in lipid rafts, and the proliferative capacity of B cells was diminished[35]. Glucose feeds the synthesis of monounsaturated fatty acids (MUFAs) in response to B-cell activation by inducing the expression of the gene encoding stearoyl-CoA desaturase (SCD). Blockade of SCD *in vitro* disrupts B-cell proliferation and class-switching, an effect rescued by supplementation of

exogenous MUFAs[36]. *In vivo*, B cell-intrinsic SCD was not required for B cell development or GC formation, suggesting that extrinsic MUFA availability may be able to compensate for a loss of cell-intrinsic production. Short chain fatty acids (SCFAs) have also emerged as important modulators of B cell fate and function. They epigenetically repress the transcription of activation-induced cytidine deaminase (*Aicda)* and *Prdm1*, and subsequently reducing class-switch recombination, somatic hypermutation, and plasma cell differentiation[37].

In contrast with other rapidly proliferating lymphocytes, mainly dependent on aerobic glycolysis, GC B cells upregulate fatty acid oxidation, conducting little glycolysis[21], despite the hypoxic nature of their environment[38]. Knockdown of carnitine palmitoyl transferase 2 (*Cpt2*), which transports fatty acids into mitochondria, also reduced the capacity of B cells to contribute to the GC reaction, highlighting the active role of fatty acid oxidation in GC B cell metabolism[21]. These findings overall highlight the importance of mitochondrial pathways in B cell homeostasis. In the next chapter, I will discuss mitochondrial dynamics and their role in B cell function.

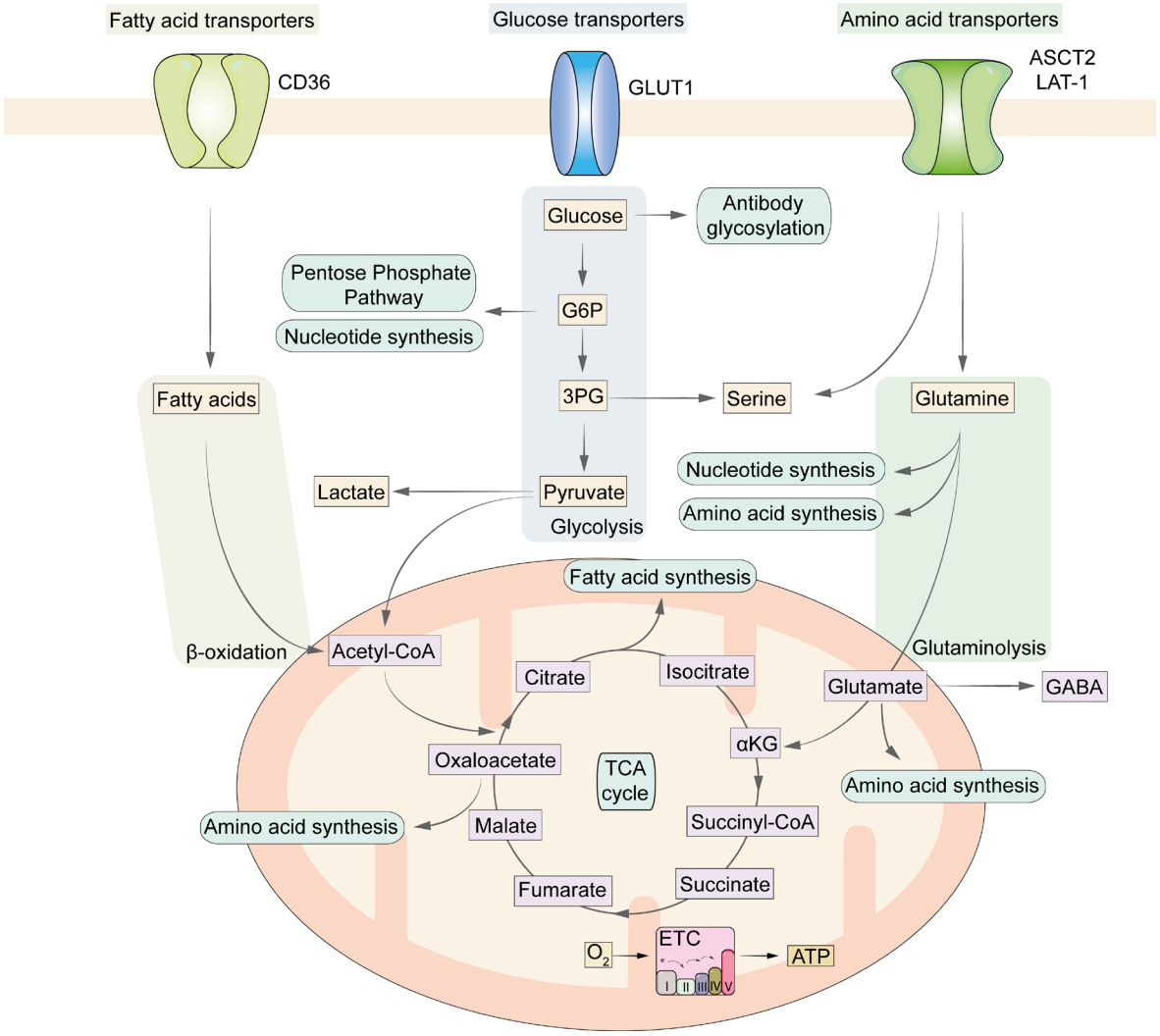


Figure 1.2: Schematic representation of key fuel sources and downstream metabolic pathways.
Specific transporters in B cells import glucose, amino acids, and fatty acids. They undergo catabolic reactions like glycolysis, glutaminolysis, and β-oxidation, while generating intermediate metabolites for anabolic and redox pathways, including nucleotide synthesis, amino acid and fatty acid synthesis, and the pentose phosphate pathway (PPP). These pathways eventually converge upon the mitochondrial TCA cycle. Subsequently, through reactions at the ETC, oxygen is consumed, and ATP is generated. This figure is generated by me and included in a review article that is currently *in press.*

1.1.4. Mitochondrial metabolism

The Warburg effect is a metabolic adaptation in which cells preferentially increase glucose consumption, even in the presence of oxygen. Historically the Warburg effect is seen as a metabolic hallmark of rapidly dividing cells, especially tumour cells[39].

Following B cell activation, downstream signals from CD40, toll-like receptors (TLRs), BAFF-receptor (BAFFR), and the BCR collectively promote glycolysis[40]. As in T cells, this increase in glycolysis is driven by mechanistic target of rapamycin complex 1 (mTORC1) and/or MYC-driven pathways, which simultaneously enhance OxPhos through mitochondrial biogenesis and glutaminolysis[41–45]. There is, however, a growing body of evidence to suggest that B cells favour other modes of metabolism and do not always adhere to classic concepts in immunometabolism, including the Warburg effect[3,46,47]. One such example may be observed in the metabolism of GC B cells.

Germinal centres are hypoxic environments, and B cells in the LZ have been reported to have a hypoxia-associated transcriptional profile[38,44]. However, during transition from pre-GC to GC, OxPhos becomes dominant in B cells and dependence on LDHA decreases[19]. An OxPhos gene signature has also been associated with the development of high-affinity B cell clones within GCs[48]. Deletion of *Cox10*, a subunit of mitochondrial complex IV, disrupted GC B cell division and impaired affinity maturation. In keeping with this, pharmacological activation of OxPhos leads to the generation of higher affinity antibodies[48], while its inhibition with oligomycin disrupts the GC reaction[49].

Work by Kitamura et al. demonstrated that interleukin 4 (IL-4) stimulation reprograms the TCA cycle, leading to accumulation of the metabolite alpha-ketoglutarate (α-KG); this in turn epigenetically increases the accessibility of the *Bcl6* gene locus, driving GC B cell differentiation[49].

During systemic Salmonella infection, B cells undergo a general shift towards glycolysis, but the metabolic fitness of GC B cells is compromised, leading to GC collapse[50].

Beyond its role in lipid raft formation discussed previously, deficiency in the SREBP pathway is also linked to impaired mitochondrial metabolism in B cells[35].

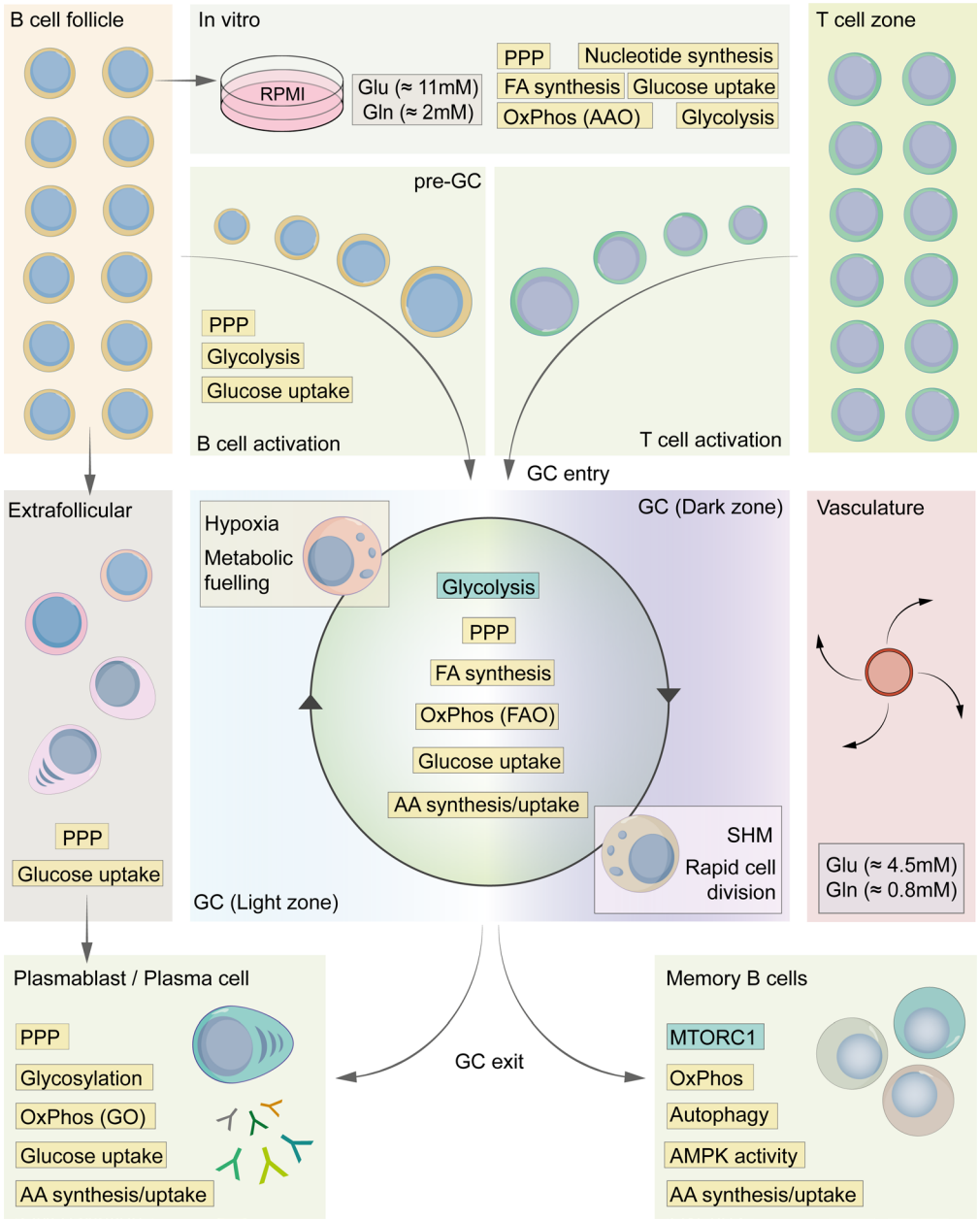


Figure 1.3: Summary of metabolic reprogramming across different B cell compartments.
Throughout the humoral immune response, B cells dynamically adjust their metabolism to meet energetic demands and adapt to the varying metabolic milieus in the distinct microenvironments they encounter. Upregulated metabolic pathways are marked in yellow-orange boxes, while downregulated pathways are shown in blue boxes. This figure is generated by me and included in a review article that is currently *in press.*

1.2. Mitochondrial dynamics in lymphocyte homeostasis

Through the course of evolution, mitochondria have retained a high degree of similarity to their prokaryotic ancestors. Notably, they have their own distinct genome and machinery for transcribing and translating proteins[51]. This endows mitochondria with the capability to synthesise critical protein subunits for their ETC, where OxPhos and respiration occur (outlined in Fig. 1.4). Importantly, 13 protein subunits of the ETC are encoded by mtDNA and synthetised by ribosomes of the mitochondrial matrix [52]. This represents only a tiny fraction of the broader mitochondrial proteome, which relies on substantial input from cytoplasmic protein translation regulated by communication between mitochondria and nucleus[52].

This cooperation between the nucleus and mitochondria is, at least in part, achieved through the transport of select nuclear-encoded proteins from the cytoplasm into mitochondria to support various mitochondrial pathways (outlined in Fig 1.5). For instance, a set of bioenergetic enzymes constituting the TCA cycle, which are intimately linked to ETC, are nuclear encoded and therefore products of cytoplasmic translation[53].

Mitochondria can directly signal to the nucleus via calcium release, production of ROS, or other mechanisms of action, broadly referred to as mitochondrial retrograde signalling. This active mode of communication is important for adaptation and endurance of cells in distinct conditions through mitochondrial remodelling[53].

Mitochondria participate in a range of critical functions, both metabolic and non-metabolic. Therefore, intrinsic or extrinsic defects in mitochondrial function disrupt cellular homeostasis and can cause various disorders. Due to the proximity of mtDNA to ROS production sites, and the limited availability of DNA repair mechanisms, mtDNA is particularly susceptible to mutations that may then give rise to pathological variants. Primary mitochondrial diseases encompass a heterogeneous group of disorders commonly caused by mutations within mtDNA. Patients with mitochondrial diseases are usually immunocompromised, and recent

studies have made important progress in understanding the underlying immune abnormalities associated with these disorders.

It is important to note that mitochondrial biogenesis is one of the hallmarks of lymphocyte activation. This involves not only mitochondrial mass accumulation but also functional changes such as increased mitochondrial respiration and ETC activity[54]. Mitochondrial remodelling may skew the differentiation of activated B and T cells into specific effector trajectories (outlined in Fig. 1.6)[55–57].

In T cells, mtDNA content also varies greatly across naive and memory subsets of both $CD4^+$ and $CD8^+$ T cells[58]. Recent evidence suggests that pathogenic mtDNA variants may be subjected to selection pressure across T cell trajectories[59,60]. The A3243G mutation in mtDNA involves the mitochondrial leucyl-tRNA gene and is the most common pathogenic mtDNA mutation. The mutated version of this gene is responsible for a disease known as mitochondrial encephalomyopathy, lactic acidosis, and stroke-like episodes, abbreviated as MELAS. Interestingly, there was a lower frequency of this mutation in peripheral blood T cells from MELAS patients[61].

Mitochondrial alterations associated with cellular and humoral immune defects have been also reported in children suffering from primary mitochondrial diseases, manifesting as reduced plasma cell counts and antibody diversity[62].

More well characterised, however, is the occurrence of secondary mitochondrial dysfunction in immune cells. Mitochondrial dysfunction has frequently been documented in lymphocytes and play important roles in the pathogenesis of a wide array of diseases[46,63,64].

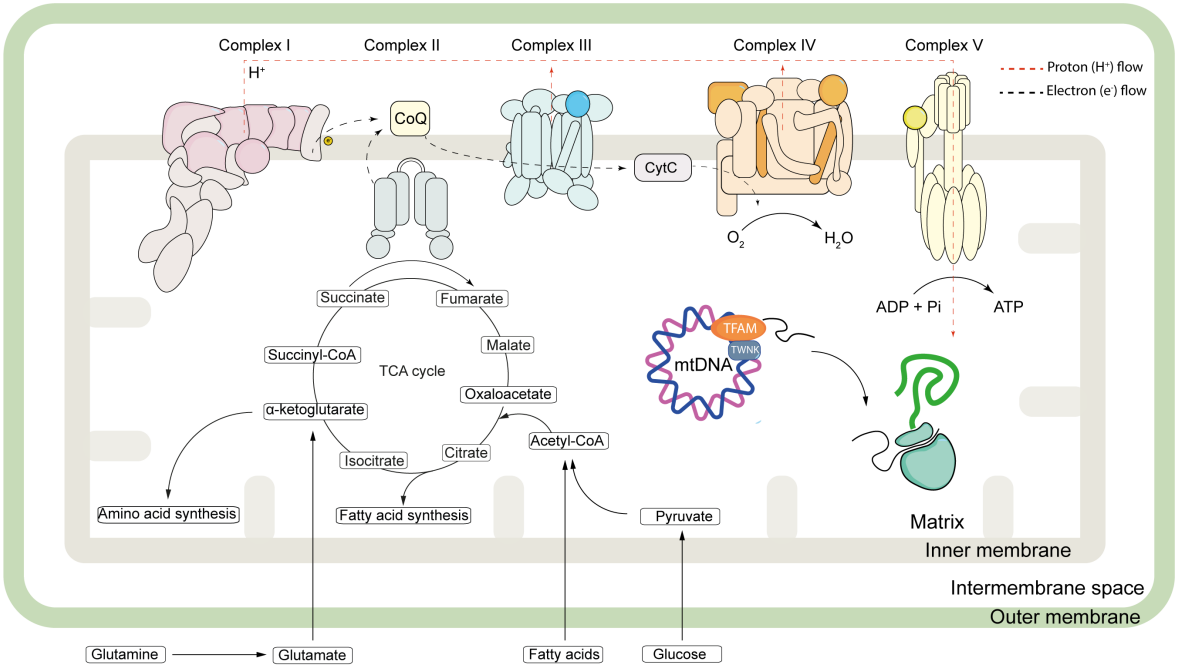


Figure 1.4. An overview of the TCA cycle, ETC, and OxPhos systems.

mtDNA is guarded and compacted by TFAM, which regulates its replication, transcription, and translation, often by cooperating with other associated molecules like Twinkle (TWNK), a mitochondrial helicase. The ETC is made of five complexes, each containing mitochondrially encoded subunits, with the exception of Complex II, also known as succinate dehydrogenase. Complex II participates in a key enzymatic step in the TCA cycle, a cyclic biosynthetic and bioenergetic process that generates electrons and ATP. The TCA cycle incorporates metabolites derived from glucose, amino acids, and lipids, and forms a functional link to the ETC. Electrons reaching the final acceptor O_2 through ETC complexes form a proton gradient in the mitochondrial intermembrane space, which then is used by complex V to catalyse ADP-ATP conversion and generate ATP. The mitochondrially translated ETC units are highlighted in darker shades. This figure is generated by me and included in a review article I published[65]

1.2.1. Mitochondrial DNA homeostasis

mtDNA is a small, circular genome of approximately 17 kilobases in size. It contains genes that encode 13 protein subunits of the ETC, 22 transfer RNAs, and 2 ribosomal RNAs essential for the mitochondrial translation machinery[66]. However, about 1,500 mitochondrial proteins originate from nuclear DNA. These proteins are transcribed inside the nucleus, synthesised by cytoplasmic ribosomes, and then imported into mitochondria. The coordination between the nuclear and mitochondrial genetic systems tightly regulates

mitochondrial and cellular homeostasis[67]. mtDNA typically remains in a compact state, and there may be many replicating copies of it in each cell at any given time. This is quantitatively linked to cellular activity and function[68]. The mtDNA copy number increases dramatically along with mitochondrial biogenesis upon T cell activation. Furthermore, mitochondrial expansion and metabolism depends on the mode of stimulation[41,56,69–71].

One study investigated mtDNA properties in different subsets of human leukocytes, including B and T lymphocytes, by measuring mtDNA copy numbers and respiratory complex activities[58]. The study showed that mitochondrial parameters varied significantly between immune cell types and were further dependent on factors such as sex and age[72]. For instance, B cells had the highest mtDNA copy number; although surprisingly, this was not reflected by their mitochondrial activity, suggesting disparities exist in mitochondrial properties of B cells[58].

mtDNA is assembled into 3D structures termed nucleoids, each containing one or two copies of mtDNA[73,74]. The nuclear DNA-encoded protein mitochondrial transcription factor A (TFAM) plays a key role in mtDNA integrity, replication, and transcription, functionally resembling histones of nuclear DNA[75]. A few studies have suggested that there may be a great heterogeneity among the nucleoids even within a same cell in terms of the ratio of TFAM to mtDNA, which was shown to control the size, structure, and activity of the nucleoid[76]. Urbanczyk et al. described changes in relative mitochondrial DNA content across B cell progenitors and peripheral naïve and activated B cell subsets, including GC B cells[77].

Additionally, oscillations in mtDNA content have been described in human B cell precursors in the bone marrow, mainly driven by a mismatch between the rates of DNA replication in the nucleus and mitochondria during cell division[78,79].

Whilst *Tfam* deletion causes lethality in mice during embryonic development[80], its conditional ablation in immune cells has revealed its role in numerous immune cells by

circumventing embryonic lethality[20,81–83]. For example, *Tfam* deletion in T cells disrupts homeostasis and function, but does not affect their development[84]. Loss of *Tfam* in T cells also triggers a chronic state of inflammation and accelerates aging[85]. Conditional loss of *Tfam* in Tregs also leads to fatal systemic autoimmunity[86] and an aberrant GC B cell reaction occurs owing to defects in GC-resident Tregs, also known as follicular T regulatory cells (T_{FR})[87].

In summary, mtDNA is dynamically regulated in human and murine lymphocytes, exerting numerous distinct functions across T and B cell subsets.

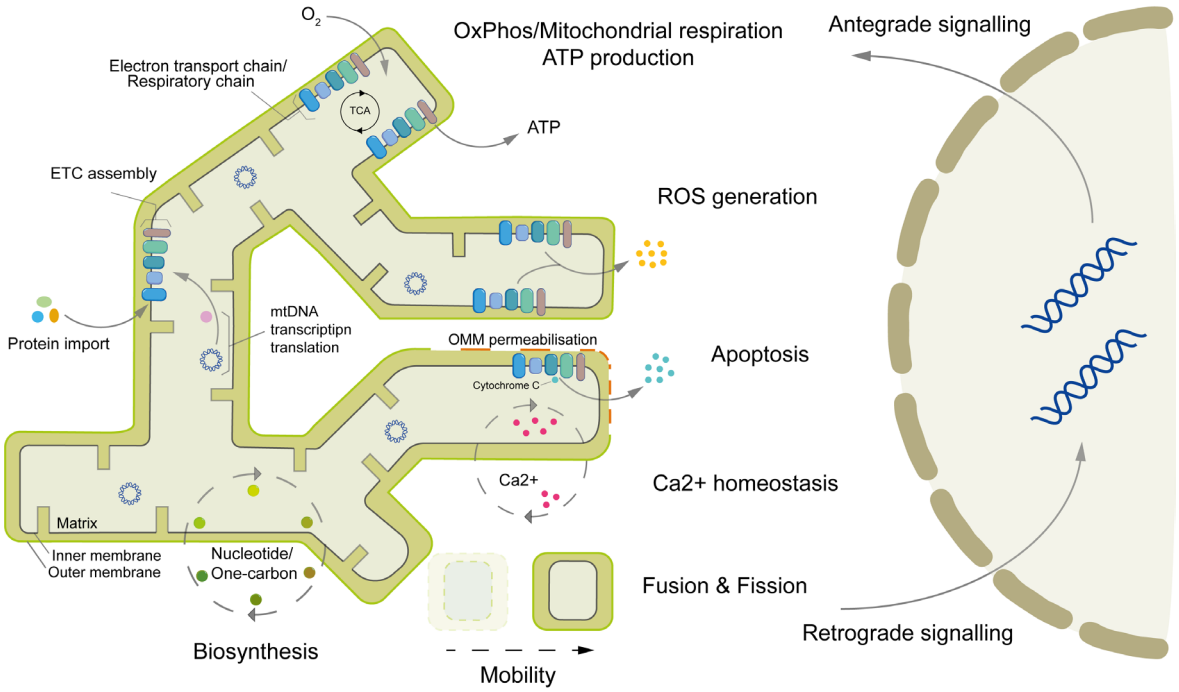


Figure 1.5. Overview of mitochondrial function.

Mitochondria have pleiotropic activities, and among these, the most recognized is generation of energy by OxPhos, which takes place in the ETC, located in the inner mitochondrial membrane. The ETC incorporates protein subunits encoded by mtDNA and translated in the mitochondrial matrix. However, most of the mitochondrial proteome is nuclear-encoded, and imported into mitochondria following cytosolic translation. Complex I and III of the ETC produces ROS, which are part of multiple signalling pathways that regulate cellular responses. Mitochondria also represent an effective Ca^{2+} buffer system that controls cytoplasmic Ca^{2+} concentrations. Mitochondria form a dynamic tubular network that undergoes fusion and fission, with fragments then being transported to different cellular

compartments including lysosomes for degradation, a process known as mitophagy. Mitochondria harbour key biosynthetic enzymes of the TCA cycle, the one-carbon pathway, and nucleotide synthesis and maintain a close communication with the nucleus. Nuclear signals regulate mitochondrial function by activating distinct genetic programs. In turn, mitochondrial products can feedback to the nucleus and alter the program of expression. This creates an integrated antegrade-retrograde signalling loop and is crucial for coexistence of these two organelles. This figure is generated by me and included in a review article I published[65].

1.2.2. Mitochondrial transcription and translation in lymphocytes

Replication, transcription, and translation of mtDNA is vital for the function of the ETC and OxPhos in lymphocytes. It has been recently shown that B cell-intrinsic ablation of the mitochondrial helicase *Twinkle* severely impairs mitochondrial respiration, compromising GC formation, plasma cell output, and antibody production[77]. *Tfam*-deficient B cells similarly were defective at GC recruitment[20,88].

Mitochondrial protein synthesis is also critical for T cell functionality. For instance, fever activates the translation machinery in CD8+ T cell mitochondria therefore boosting their effector function[89]. Conversely, pharmacological inhibition or genetic ablation of the mitochondrial elongation factor G1 disrupts mitochondrial translation in CD4+ T cells and protects mice against development of autoimmune encephalomyelitis[90]. This has been mechanistically associated with reduced capacity to conduct OxPhos. Furthermore, mitochondrial translation contributes to cytotoxic activity in $CD8^+$ T cells, surprisingly in an ATP-independent manner[91].

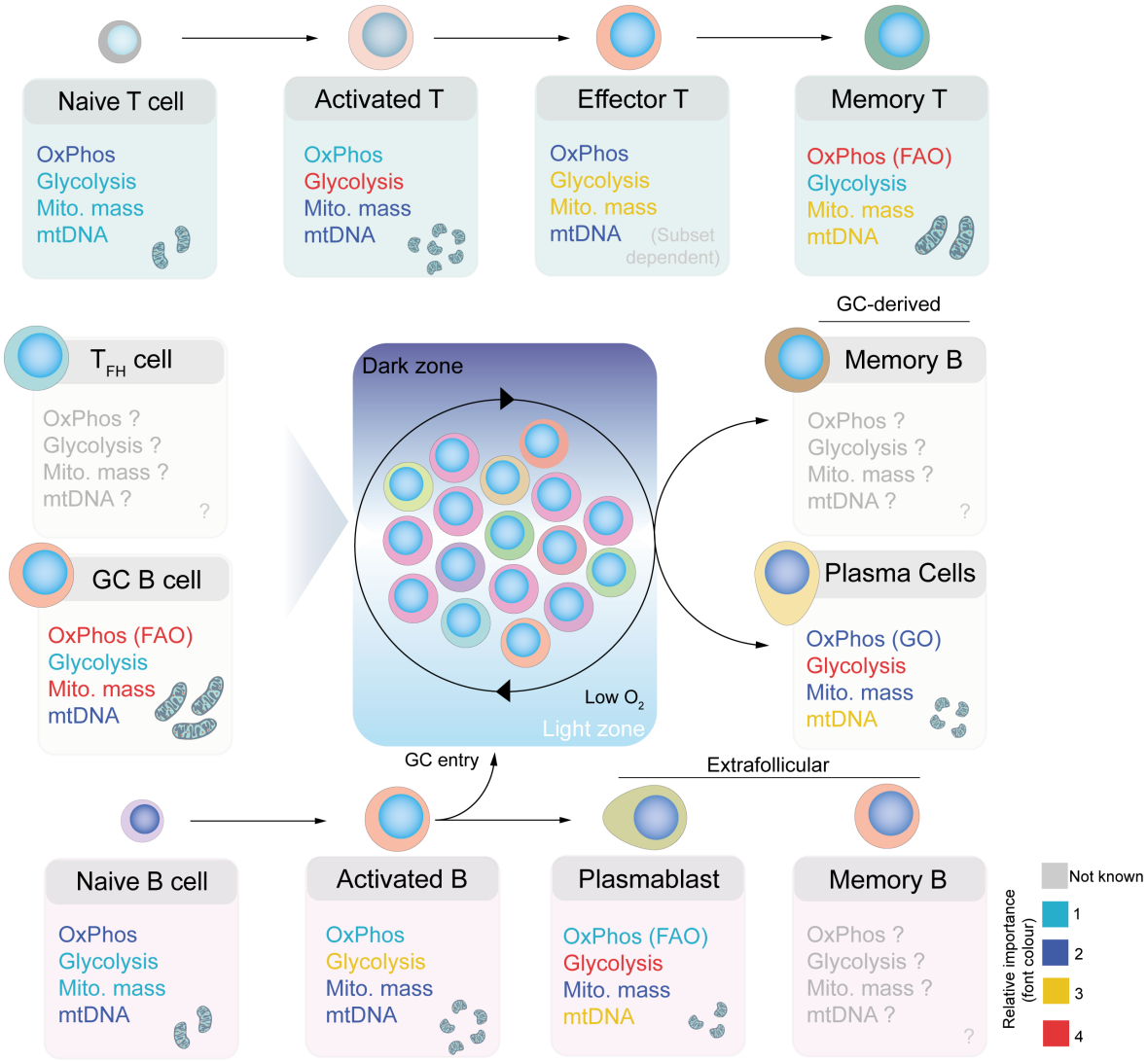


Figure. 1.6. Mitochondrial dynamics across distinct lymphocyte populations.

An overview of mitochondrial properties, including OxPhos capacity, mitochondrial mass, mtDNA content, and the morphological state depicted across various T and B cell trajectories. A representative mitochondrial image is displayed in the lower right corner to illustrate the mitochondrial state within each subset. The font colour is used to indicate the relative significance of each mitochondrial function in the different lymphocyte populations and a relevant scale is added to the right lower corner. This figure is generated by me and included in a review article I published[65].

Chapter 2. Materials and Methods

2.1. Mice

B6.Cg-*Tfam*$^{tm1.1Ncdl/J}$ (JAX:026123), B6.C(Cg)-*Cd79a*$^{tm1(cre)Reth/EhobJ}$ (JAX: 020505), B6.129P2-*Aicda*$^{tm1(cre)Mnz/J}$ (JAX:007770), B6;129S6-*Gt(ROSA)26Sor*$^{tm9(CAG-tdTomato)Hze/J}$ (Ai9, JAX:007905), B6.Cg-Tg(TcraTcrb)425Cbn/J (JAX: 004194), and B6.Cg-Tg(IghMyc)22Bri/J [Eμ-Myc] (JAX: 002728) were purchased from Jackson Laboratories. C57BL/6N-*Asns*^{tm1c}(EUCOMM)Wtsi/H (EM:05307) mice were provided by the Mary Lyon Centre, MRC Harwell, UK. Tg(*Prdm1*-Venus)1^{Sait} [Blimp1-mVenus] (MGI:3805969) mice were a kind gift from Mitinori Saitou (Kyoto University). C57BL/6-Gt(ROSA)26Sor$^{tm1(CAG-mCherry/GFP)Ganl}$ (MitoQC) mice were kindly gifted by Ian Ganley (University of Dundee). B6.SJL.CD45.1 mice were provided by the central breeding facility of the University of Oxford. C57BL/6J mice were obtained from Envigo. Male and female mice aged between 6 and 15 weeks were used. They were bred and maintained in specific pathogen free conditions at the Kennedy Institute of Rheumatology, University of Oxford. Regular microbiological screenings were performed to ensure the absence of pathogens. The mice were housed in individually ventilated cages and supplemented with environmental enrichment. The temperature was maintained between 20-24°C.The humidity range was 45-65%. Mice were kept on a 12-hour light/dark cycle (7 am to 7 pm) with a 30-minute period of dawn and dusk. All procedures and experiments were compliant with UK Scientific Procedures Act (1986) and performed under a project licence authorised by the UK Home Office (PPL number: PP1971784).

2.2. Immunisation

One ml of sterile SRBCs in Alsever's solution (ThermoFisher, EO Labs, or TCS Bioscience) were washed twice with 10ml of ice-cold PBS and reconstituted in 2-3ml of PBS, 0.2ml administered to mice intraperitoneally or intravenously. In some experiments, an enhanced SRBC immunisation method was used to maximise GC B cell yield. This was performed by immunising mice with 0.1ml SRBC on day 0 followed by a second injection of 0.2ml on day

4 or 5[92]. For protein antigen immunisations, 50μg $NP_{(30-39)}$-CGG (Biosearch Tech, cat: N-5055D-5) in PBS was mixed with Imject Alum (ThermoFisher) or Alum Hydrogel (InvivoGen, cat: vac-alu-50) at a 1:1 ratio (vol:vol) and rotated at room temperature for 30 mins (used for Imject Alum) before intraperitoneal injection in 100μl volume, or mixed vigorously with a pipette for 5 mins (used for Alum Hydrogel) followed by injections in the flanks, hock, or intraperitoneal space. As a T-independent immunisation scheme, 50μg NP-AECM-FICOLL (Biosearch Tech) in PBS was mixed with PBS at a 1:1 ratio and intraperitoneally injected.

2.3. Influenza infection

The A/HK-X31 (X31, H3N2) influenza strain was used. Mice were anaesthetised with isoflurane and intranasally inoculated with 5×10^3 PFU of X31 influenza A virus in PBS. Mice were then carefully monitored and regularly weighed for 14 days after infection. Characteristic weight loss was detected in all infected mice.

2.4. *In vivo* modification of asparagine levels

Experimental and control mice were intraperitoneally injected with ≈10U (500U/kg) of asparaginase from *E. coli* (Abcam, ab277068) prepared in PBS. Two main regimes were used for asparaginase (ASNase) experiments: 'standard' and 'post-GC formation'. In the standard schedule, ASNase was administered from one day prior to immunisation, and then every two days over a nine-day period before experimental analysis. In the post-GC schedule, only two doses of ASNase were given, at days six and eight after SRBC-immunisation or at days 6, 9 and 12 after NP-CGG immunisation to target established GCs.

Asparagine-free (Asn-free) diet or control chow (Research Diets, A05080216i and A10021Bi) was administered for 12 days before or 7 days after immunisations and maintained for the duration of the experiment.

Drinking water was supplemented with L-asparagine monohydrate (Merck, cat: A7094-25G) at a concentration of 1.5 g/L and given to the mice starting two weeks before immunisation

and throughout the entire experiment. The drinking water was changed with freshly prepared Asn every 2-3 days.

2.5. Bone marrow chimera generation

B6.SJL.CD45.1 recipient mice received two doses of 5.5Gy irradiation four hours apart. Mice were then intravenously injected with 4×10^6 mixed bone marrow (BM) cells at a 1:1 ratio, isolated from age- and sex-matched CD45.2$^+$ B-WT or B-Asns (Chapter 3) or Aicda-WT and Aicda-Tfam donor mice (Chapter 4), mixed with CD45.1$^+$ WT donor mice. Recipient mice were maintained on antibiotics (Baytril, Bayer corporation) for two weeks. Bone marrow reconstitution was confirmed by flow cytometry in peripheral blood collected at 8 weeks. In chimera experiments combined with diet intervention from Chapter 3, Asn-free diet or control chow (Research Diets, A05080216i and A10021Bi) was administered for 12 days starting from week 8, maintained for additional 9 days (total of 21 days) during immunisation with SRBC until mice were analysed at 11 weeks. In chimera experiments in Chapter 4, mice were given normal standard diet throughout the experimental period.

2.6. Cell isolation

Naïve B cells were isolated using the Pan B cell Isolation II Kit, anti-CD43, and/or anti-CD23 Microbeads (all Miltenyi) according to the manufacturer's instructions. Purity validated was by flow cytometry and it was >90%. Isolation of DZ-LZ-GZ subsets of GC B cells, and T_{FH} cells (CD19$^-$ CD4$^+$ CXCR5$^+$ ICOS$^+$ GITR$^-$) was performed via fluorescence-activated cell sorting (FACS).

For some experiments, untouched GC B cells were isolated using a magnetic bead-based protocol as described[93]. Spleens were collected from SRBC-immunised mice, and single-cell suspensions were prepared in ice-cold MACS isolation buffer (PBS with 0.5% BSA and 2mM EDTA). Red blood cell lysis was performed with ACK RBC lysis buffer (Gibco) for 4 minutes at 20°C, with mixing every 30 seconds. After washing, cells were labelled with anti-

CD43 microbeads (Miltenyi) and biotinylated CD38 and CD11c antibodies (eBioscience, clones 90 and N418). They were then incubated with anti-biotin microbeads and passed through a MACS LS column (Miltenyi). Purity again exceeded 90%.

For *ex vivo* GC B cell mass spectrometry experiments, GC B cells were first enriched using the mouse Germinal Centre B Cell (PNA) MicroBead Kit (Miltenyi), and then further purified by flow sorting (Live/Dead^{-}CD19^{+}IgD^{-}GL-7^{+}CD95^{+}). Total B cells from the same mouse pool were pre-enriched using CD19^{+} Microbeads (Miltenyi), then naïve B cells purified by FACS (Live/Dead^{-}B220^{+}IgD^{+}).

Spleens were crushed using the rough ends of microscope slides to increase cell yield from tissue during preparation for single-cell RNA sequencing. Non-B cells were depleted with the Pan B cell Kit II (Miltenyi). The enriched cells were then stained with a viability dye, anti-CD16/32 (FcBlock), and surface antibodies, including markers for a dump channel (anti-CD3, anti-Gr1, anti-CD11c) to exclude T, dendritic, and myeloid cells. Live Dump^{-}tdTomato^{+} cells were sorted using a BD FACS Aria.

2.7. Flow cytometry and imaging flow cytometry

Flow cytometry experiments were performed as previously described with slight modifications[94]. Briefly, harvested spleens were injected with ice cold PBS and mashed through a 70µm strainer (Falcon) or crushed between the rough ends of ordinary microscope slides. For Peyer's patch dissociation, a 40µm strainer (VWR) was used. Red blood cells were removed by incubating splenocytes with ACK Lysis Buffer (Gibco) for 3-4 mins at 20°C. Single cell suspensions were incubated with Fixable Viability Dye eFluor™ 780 (eBioscience) or Zombie NIR (Biolegend) in PBS, followed by Fc Block (5 mins) and surface antibody cocktail in FACS buffer (PBS supplemented with 0.5% BSA and 2mM EDTA) on ice for 30 mins. For intracellular staining, cells were fixed at 20°C with 4% freshly prepared paraformaldehyde (PFA) (Cell Signaling) for 15 mins and subsequently permeabilised with methanol (90% ice cold for 10 mins on ice with frequent vortexing)

unless specified otherwise. Phalloidin-based F-Actin (Thermofisher, cat no: A30107) staining was performed using BD Perm/Wash reagent (BD, Cat. No. 554723) after 4% PFA fixation. For *in vivo* cell cycle analysis, 5-ethynyl-2'-deoxyuridine (EdU) (1 mg, Thermofisher, cat no: A10044) was administered intraperitoneally and mice were euthanised after 2-2.5 h. Following surface staining, cells were fixed and permeabilised, then labelled using Click chemistry according to the manufacturer's instructions (Click iT Plus EdU Flow cytometry kit, Thermo Fisher). For FoxP3 staining, eBioscience™ Foxp3 / Transcription Factor Staining Buffer Set (ThermoFisher) was used. To measure OPP incorporation *ex vivo*, splenocytes were incubated in RPMI1640 in the presence of 20μM OPP for 30 mins at 37°C. Click labelling was then performed with the Click-iT™ Plus OPP Alexa Fluor 647 Protein Synthesis Assay Kit (ThermoFisher, cat: C10458). The SRBC binding assay was performed as previously reported[95]. Briefly, splenocytes were harvested from mice immunised with SRBC. Following surface staining, cells were mixed with SRBCs labelled with 10μM CellTrace Violet (CTV) (ThermoFisher) on ice for 20 mins and then analysed via flow cytometry.

For mitochondrial superoxide deep red labelling (mtSOX, Dojindo), following viability dye and surface staining, cells were resuspended in warm complete RPMI supplemented with mtSOX (at 10μM) and incubated for 30 mins at 37°C. Cells were washed twice before flow cytometry acquisition on BD Fortessa X-20 or LSR II instruments (both BD), or using a Cytek Aurora (5 laser) spectral flow cytometer. For imaging cytometry, single cell suspensions were prepared from spleens of Mito-QC mice immunised with SRBC, incubated with live-dead dye, stained for surface markers, and then fixed with 4% PFA. After washing, cells were run on an Amnis ImageStream^X Mark II Imaging Flow Cytometer in 50μl FACS Buffer and analysed with IDEAS (EMD Millipore) and FCS Express software (v7.12). Flow cytometry data was analysed using FlowJo (BD).

2.8. Detection of ETC/UPR^{mt} proteins with spectral flow cytometry

Antibodies used listed in an antibody table added to the Appendix. All antibodies targeting intracellular mitochondrial proteins were directly conjugated and of mouse origin, except for the rabbit anti-TFAM monoclonal antibody (Abcam). Goat anti-mouse AF405 Plus secondary antibody (ThermoFisher) was used for detection. Each antibody in the panel was validated for flow cytometry either by the vendor or in the literature or in-house. The mouse anti-mitochondrial complex 1 antibody was conjugated in-house using a PE-Cy7 Lightning-link kit (Novus Bio, cat: 762-0005). Cells were labelled with Zombie NIR viability dye (Biolegend) and Fc Block in PBS for 30 minutes on ice in 96-well V-bottom plates. After washing, surface staining was performed in Brilliant staining buffer (BD, cat: 563794) for 30 minutes. Cells were then fixed in 4% freshly-prepared PFA at 20°C for 15 minutes and permeabilised in freezer-cold methanol for 10 minutes, with occasional vortexing. Anti-TFAM primary staining was done in 50µl FACS buffer with 2% goat serum for 45 minutes at 20°C. After two washes, goat anti-rabbit secondary antibody and the remaining directly conjugated antibodies for ETC/UPR^{mt} proteins were added for 30 minutes at 20°C. The cells were then washed in FACS buffer and acquired on a Cytek Aurora (5 laser) spectral flow cytometer.

Exploratory pilot experiments were conducted to identify the most appropriate single-stained references (beads or cells) for each marker-fluorochrome combination. When cells were used as reference controls, they were obtained from matching organs (spleen or bone marrow) and processed in the same way as fully stained samples. The ‘Autofluorescence (AF) as a fluorescent tag’ option was used to reduce AF interference. Acquired samples were unmixed using SpectroFlo and analysed with FlowJo.

2.9. Single-mitochondrion translation assay

The technique was performed as previously described, with modifications[96]. Total B cells were isolated from spleens of Aicda-WT and Aicda-Tfam mice immunised with NP-CGG through magnetic bead sorting (Pan B Cell Isolation Kit II, Miltenyi). The experiments were

conducted in batches and in each replicate one Aicda-WT and one Aicda-Tfam spleen were processed to reduce bias. Cells were pulsed with OPP (20μM, Jena Bioscience, cat: NU-931-5) in complete RPMI containing the cytoplasmic translation inhibitor harringtonine (1μM, Abcam, cat: ab141941-5mg) for 45 minutes at 37°C. After washing, cells were resuspended in ice-cold Mitochondria Isolation Buffer (320mM sucrose, 2mM EGTA, 10mM Tris-HCl, pH 7.2). Cells were then homogenised using a Dounce homogeniser (Abcam, cat: ab110169), applying 10 strokes with a type B pestle.

The homogenates were subjected to differential centrifugation at 4°C, first pelleting intact cells and nuclei at 1,000×g for 8 minutes. The supernatant, containing mitochondria, was transferred to new tubes and centrifuged at 17,000×g for 15 minutes. The resulting brown mitochondrial pellets were fixed in 1% PFA in 0.5ml PBS on ice for 15 minutes, then washed with PBS. Permeabilisation and antibody staining were performed in BD Perm/Wash buffer at 20°C. Mitochondria were incubated with pre-adsorbed rabbit anti-RFP antibody (1:250, Rockland, cat: 600-401-379) for 30 minutes at 20°C. After washing, the Click reaction was performed by using the Click-iT™ Plus OPP Alexa Fluor 647 Protein Synthesis Assay Kit (ThermoFisher, C10458) for 30 minutes at 20°C. Mitochondria were subsequently stained with AF488-conjugated anti-COX IV (1:100, Proteintech, cat: 66110-1-Ig) and PE-conjugated Donkey anti-rabbit IgG (1:200, Biolegend, cat: 406421). After the final wash, mitochondria were resuspended in 250μl filtered PBS (0.2μm) and acquired using a BD Fortessa X20 flow cytometer, with the SSC-A threshold set to the minimum (20,000) to capture subcellular particles. Submicron Particle Size Reference Beads (ThermoFisher, cat: F13839) were additionally used for accurate mitochondrial identification. Mitochondria were gated based on COX IV and SSC-A properties and RFP^+ (AP-GC-derived) and RFP^- (naïve B cell-derived) mitochondria were distinguished by anti-RFP antibody signal. gMFI for OPP-AF647 fluorescence was then calculated for RFP^+ and RFP^- mitochondrial subsets, and their ratio was used as the translation index after adjusted for batch effects. Mitochondria from reporter-free and OPP-untreated cells served as negative controls.

In validation experiments, chloramphenicol (300µg/ml) or ethanol vehicle was used to block mitochondrial translation, alongside harringtonine to inhibit cytoplasmic translation. Mitochondria were detected using COX IV-AF488 and SDHA-AF594 antibodies (1:250, Abcam, ab170172).

2.10. *Ex vivo* lymph node slice culture

Inguinal lymph nodes (LNs) were collected from B-WT or B-Asns mice immunised subcutaneously on both flanks with NP-CGG (precipitated in Alum hydrogel). LNs were harvested, then cleaned and briefly washed (<1 second) in 0.01% digitonin solution (Thermo Scientific) to remove surrounding fat. Next, they were embedded in 6% w/v low melting point agarose (Lonza) in 1x PBS. Using the Precisionary Compresstome® VF-210-0Z, 300µm thick slices were cut according to the manufacturer's guidelines, with a blade speed of 4 and oscillation of 6. The buffer tank was kept filled with ice-cold PBS containing 1% Pen/Strep to minimise bacterial contamination. Slices were removed from the agarose and placed in 500µl of Asn-replete or Asn-free complete RPMI media in duplicate wells of a 24-well plate. LN slices were allowed to rest and equilibrate in media for 1 hour at 37°C and 5% CO2, before being transferred to fresh media for a 20-hour incubation.

After culture, duplicate slices from the same lymph nodes were pooled. Using an insulin syringe plunger, slices were crushed and cells were liberated into PBS containing 2% FBS and 2mM EDTA to generate a cell suspension in a 96-well U-bottom plate followed by staining with viability dye and surface markers. Cells were then washed and fixed in 4% PFA (Cell Signalling) for 15 minutes at 20°C. They were then permeabilised in methanol for intracellular staining and analysed on an Aurora flow cytometer (Cytek).

2.11. *Ex vivo* single cell competitive Asn uptake assay

The recently published QUAS-R protocol was followed with certain modifications[97]. Spleens were collected 8 days after SRBC immunisation and dissociated through 70µm cell strainers. The resulting single cell suspensions were incubated with Zombie NIR (BioLegend) and Fc block in PBS on ice for 30 minutes, followed by surface staining in

FACS buffer for 30 minutes. Hanks' Balanced Salt Solution (HBSS, ThermoFisher) supplemented with 400μM Click-iT homopropargylglycine (HPG, ThermoFisher) and L-asparagine monohydrate (Merck) at varying concentrations (0, 10, 40, 100, 400, 4000μM), was pre-warmed at 37°C. Cells were resuspended in blank HBSS, and 50μl of the suspension was transferred into 96-well plates and kept at 37°C for 10 minutes. Control cells were correspondingly kept on ice for background detection. HPG-containing media supplemented with each Asn concentration was then applied to the cells and they were incubated for another 3 minutes before undergoing fixation (4% PFA) at room temperature for 25 minutes. The cells were washed and permeabilised with 1× saponin-based buffer (ThermoFisher) for 20 minutes at room temperature followed by the Click chemistry reaction from the Click-iT™ Plus OPP Alexa Fluor™ 647 Protein Synthesis kit, which shares Click Chemistry with HPG due to the conserved alkyne modification[97]. Cells were incubated for 30 minutes at room temperature, washed, and resuspended in FACS buffer for flow cytometry analysis.

2.12. Multiplexed Tissue Imaging using Cell DIVE

Formalin-fixed paraffin-embedded (FFPE) human tonsil sections (5μm) were first deparaffinised and rehydrated, followed by permeabilisation in 0.3% Triton X-100 for 10 minutes and washing in PBS for 5 minutes. Antigen retrieval was performed using a Biocare NxGen decloaker: slides were boiled in a citrate-based antigen unmasking solution (Vector, #H3300) at pH 6, followed by treatment in a Tris-based antigen retrieval solution (1× Tris, EDTA, 0.05% Tween 20, and ddH2O, pH 9) lasting 20 minutes at each step. Slides were blocked overnight in PBS containing 3% BSA (Merck, #A7906) and 10% donkey serum (Bio-Rad, C06SB), next day, incubated with human FcR Blocking Reagent (Miltenyi) at a 1:100 dilution for 1 hour at room temperature. After washing in PBS, the slides were stained with DAPI (ThermoFisher), washed again, and mounted with a mounting solution prepared in-house (50% glycerol, Sigma, and 4% propyl gallate, Sigma, 2370).

Slides were imaged using a GE Cell DIVE imaging platform. A ScanPlan at 10× magnification was performed to select regions of interest (ROIs). Imaging at 20× magnification was then performed to capture the reference background autofluorescence and generate virtual H&E images. This was then used for autofluorescence subtraction during subsequent rounds of staining.

Before staining, slides were decoverslipped in PBS each round, which involved three antibodies applied in staining buffer (3% BSA in PBS). Unconjugated primary antibodies were used in the first round and incubated overnight at 4°C. Following washes with 0.05% PBS-Tween 20 (Sigma, P9416), AlexaFluor 488, 555, or 647 conjugated secondary antibodies were incubated for 1 hour at room temperature. Directly conjugated antibodies were used in subsequent rounds and applied at 4°C overnight. Some antibody conjugation was performed in-house using an antibody labelling kit (Invitrogen).

To inactivate fluorescent dyes, slides were bleached with 0.1 M $NaHCO_3$ (pH 10.9-11.3) (Sigma, S6297) and 3% H_2O_2 (Merck, 216763) for three rounds (each lasting 15 minutes) with a 1-minute wash interval in PBS. Slides were then re-stained with DAPI for 2 minutes. Bleached slides were imaged to determine the new background signal for subsequent staining rounds.

2.13. Immunohistochemistry and immunofluorescence

Spleens were immediately placed in Antigenfix (DiaPath) and fixed overnight at 4°C. The following day, they were washed in PBS and incubated in 30% sucrose (in PBS) overnight at 4°C for cryoprotection. The next day, spleens were snap frozen in 100% methanol on dry ice and stored at -80°C. They were then sectioned at 8-12µm thickness and rehydrated in PBS at 20°C followed by permeabilisation and blocking in PBS containing 0.1% Tween-20, 10% goat serum, and 10% rat serum for two hours. For intracellular staining, Tween-20 was replaced with 0.5% Triton X-100. Primary antibody staining was performed overnight at 4°C in PBS with 2% goat serum and 0.1% Triton X-100 (intracellular) or Tween-20 (surface), followed by secondary staining at 20°C for two hours in PBS with 0.05% Tween-20.

TUNEL imaging was done using the Click-iT Plus TUNEL In Situ Imaging Far Red kit (ThermoFisher, cat: C10619) per the manufacturer's instructions. Slides were mounted with Fluoromount G (Southern Biotech, cat: 0100-01) and imaged on a Zeiss LSM 980 with an Airyscan 2 module.

For visualising germinal centres and B cell follicles, anti-GL-7 AF488 (Biolegend, clone: GL7) and anti-CD21/35 (Biolegend, clone: 7E9) were used at 1:50 and 1:100 dilutions, respectively.

To visualise *in vivo* protein synthesis, mice were immunised with SRBC using an enhanced protocol. On day 14, mice were injected intraperitoneally with 1.5mg L-AHA (ThermoFisher) and four hours later with 1mg OPP (Jena Bioscience) in 100µl PBS or PBS alone as a control. Mice were sacrificed one hour later, and spleens were collected for immunofluorescence analysis. L-AHA and OPP were detected using Click Chemistry with the Click-iT™ Plus L-AHA and OPP Alexa Fluor™ 488 or 647 Protein Synthesis kits (ThermoFisher), following the manufacturer's protocols.

Slides were mounted with Fluoromount G (Southern Biotech, cat: 0100-01) and imaged using a Zeiss LSM 980 with Airyscan 2 or a Zeiss Axioscan 7. Airyscan reconstruction was used with a Medium filter setting for all relevant images.

2.14. Immunocytochemistry

Isolated cells were placed onto 18mm coverslips coated with 0.001% poly-L-lysine (Merck, cat: P4707-50ML, 10× stock) and incubated at 37°C for 10 minutes to ensure firm attachment. Cells were then fixed in pre-warmed 1× PHEM buffer (60mM PIPES, 25mM HEPES, 10mM EGTA, and 4mM $MgSO_4 \cdot 7H20$, pH 6.8) with 4% PFA for 10 minutes at 37°C. After fixation, cells were permeabilised and blocked using 0.2% Triton X-100 with 10% goat serum for 30 minutes. Primary antibody staining was performed overnight at 4°C, followed by secondary staining for 45 minutes at 20°C (see antibody table for details in the Appendix).

For mitochondrial transcription analysis using 5-ethynyl uridine (5-EU) incorporation, untouched naïve and GC B cells were resuspended in complete RPMI with 1mM 5-EU and transferred to poly-L-lysine-coated coverslips. After incubating for 45 minutes, cells were briefly washed and fixed in warm 4% PFA diluted in PHEM buffer. Following permeabilisation and blocking for 30 minutes, the incorporated 5-EU was detected using the Click-iT™ RNA Alexa Fluor 594 Imaging Kit (ThermoFisher, cat: C10330). Intracellular antibody staining was conducted after the Click reaction to avoid interference between Click reagents and fluorochromes.

For *in vivo* RNA synthesis measurement, 2mg of 5-EU (ThermoFisher) was injected intraperitoneally on day 12 following SRBC immunisation. The cells were processed similarly to the *ex vivo* 5-EU assay. DAPI (1µM, Sigma, cat: D8417-1MG) was used to stain nuclei for 5 minutes at 20°C, followed by a brief wash and mounting in Fluoromount G (Southern Biotech). For Mitotracker staining, cells were labelled with 150nM Mitotracker Red CMX ROS (ThermoFisher, cat: M7512). Slides were mounted with Fluoromount G and imaged using a Zeiss LSM 980 equipped with an Airyscan 2 module. Airyscan reconstruction was used with a medium filter setting for all relevant images.

2.15. 3D Lattice SIM

B cells cultured in Asn-modified conditions were transferred to poly-L-lysine-coated coverslips and incubated at 37°C for 10 minutes. Cells were then fixed in 4% PFA for 10 minutes at 37°C before permeabilisation and blocking at 20°C for 30 minutes in PBS containing 0.2% Triton X-100, 10% goat serum, and 10% rat serum. Conjugated antibody staining was carried out overnight at 4°C in PBS with 2% goat serum. For nuclear staining, DAPI (Sigma) was diluted in PBS and applied for 15 minutes at 20°C followed by slide mounting as described before. Imaging was conducted using the Zeiss Elyra 7 lattice SIM with a 63× oil immersion objective and 15 phase SIM. SIM processing was performed in ZEN Black.

2.16. STED microscopy

Stimulated emission depletion microscopy (STED) super-resolution imaging was performed using a Leica TCS SP8 laser scanning STED system with an HC PL APO 100× NA 1.40 oil objective and a 775 nm depletion laser. Isolated naïve and GC B cells, labelled with anti-TFAM (Abcam) and Alexa Fluor 647-conjugated goat anti-rabbit secondary antibody (ThermoFisher Scientific, cat: A55055), were imaged sequentially in confocal and STED modes. COX I, labelled with AF488, was imaged in confocal mode to determine mitochondrial boundaries. STED images were deconvoluted using the Deconvolution Express (Standard settings) in Huygens Essential software (v22.04) and subsequently exported for analysis via ImageJ software.

2.17. Image analysis

Image analysis was performed using ImageJ and Zen Blue (v3.4, ZEISS) software. Specific steps are described below:

2.17.1. CellDIVE

Image analysis was conducted in ImageJ. ROIs of 225μm² were randomly selected from $CD21^-$ IgD^- DZ GC, $CD21^+$ IgD^- LZ GC, surrounding IgD^+ B cell follicles, or $CD3^+$ T cell areas. These ROIs were projected to the ASNS channel, and mean fluorescence was quantified using the Measure function. Seven GCs from each tonsil were pooled for analysis (a total of 21 GCs from 3 tonsils).

2.17.2. GC Identification and area quantification

GCs were identified as $GL\text{-}7^+$ or AID-$tdTomato^+$ clusters and manually counted on splenic sections. For area quantification, GCs were either manually selected or identified using autothresholding (Yen). ROIs were defined and quantified using the Measure or Analyze Particles function with a threshold of 750 μm².

2.17.3. DZ/LZ Analysis

DZ and LZ areas in tissue sections were analysed using the nesting function in Zen Blue. LZ areas were defined by CD21/35 signals, and normalized DZ area was calculated as (GC area – LZ area) / GC area.

2.17.4. Determination of mitochondrial properties

GCs were identified based on AID-tdTomato and/or GL-7 signals, and naïve B cell follicles were marked using IgD. Mitochondria were segmented based on Mito-QC GFP or COX I signals. The Analyze Particles function calculated mitochondrial area and signal intensity. 3D Objects Counter was used for volumetric measurements. Measuring mitochondrial 5-EU incorporation involved removing background noise, defining mitochondrial ROIs, and calculating integrated density. TFAM-mitochondrial nucleoid complexes were enumerated using local maxima and subsequent analysis via 3D Suite[98] plugin. Single cells were defined as ROIs based on COX I signals. 3D mitochondrial morphology and network analysis were performed using an ImageJ plugin[99] with parameters: rolling (1.28 microns) and gamma (0.90).

2.17.5. PC-PB Quantification

Confocal images were split into channels and analysed. Total splenic section area was quantified via the DAPI channel with a size threshold of 20 μm and Gaussian blur applied to CD138, tdTomato, and Blimp1-mVenus channels. Autothresholding and watershed segmentation were used to identify triple positive PC fractions. PB numbers were derived by subtracting triple positive PCs from $CD138^+$ Blimp1-$mVenus^+$ cells. T_{FH} enumeration involved manually counting $CD3^+$ T_{FH} cells within $tdTomato^+$ GC areas.

2.18. *In vitro* mouse primary B cell culture

In chapter 3, total B cells were isolated and cultured at 1-3×10^6 cells/ml in RPMI1640 (custom product from Cell Culture Technologies, lacking glutamate, aspartate, glutamine,

and asparagine), supplemented with 1mM pyruvate, 10mM HEPES, 100 IU/ml penicillin/streptomycin, 50μM 2-mercaptoethanol, and 10% dialysed foetal bovine serum (FBS) (Gibco), with aspartate (150μM), glutamate (140μM), GlutaMAX (2mM), and the indicated concentration of Asn. Cells were stimulated with agonistic anti-CD40 (5μg/ml, FGK45.4, functional grade, Miltenyi), recombinant IL-4 (1, 10, or 50ng/ml, Peprotech), LPS (10μg/ml, Merck), or CpG (100nM, ODN1826, Miltenyi).

For proliferation assays, cells were labelled with CTV (ThermoFisher) according to the manufacturer's instructions before stimulation. The division index was calculated using the Proliferation module of FlowJo (BD).

For Chapter 4, B cells were isolated from the spleens of unimmunised *Tfam*^{loxP} and wild type mice, which carried the *Rosa26-stop-tdTomato* allele but lacked Aicda-Cre, using the Pan B cell Isolation Kit II (Miltenyi). TFAM was deleted by treating the cells with TAT-Cre recombinase (66.6 U/ml, approximately 1.5μM, Merck, cat: SRC508) in serum-free RPMI medium (supplemented with 1× GlutaMAX, 1mM Sodium pyruvate, 10mM HEPES, 50 U/ml Penicillin/Streptomycin, and 50μM 2-Mercaptoethanol, pH 7-7.4) for 45 minutes at 37°C and 5% CO_2. CTV (ThermoFisher Scientific) was added at 10μM at the 30-minute mark during the TAT-Cre incubation, and the cells were further incubated for 15 minutes at 37°C with both CTV and TAT-Cre. Cells were then washed three times with complete RPMI containing 10% FBS, and viable cells were counted manually based on Trypan Blue exclusion. B cells were then cultured in U-bottom 96-well plates at a density of 1×10^6/ml and stimulated with anti-IgM (1μg/ml, Jackson Immuno), agonistic anti-CD40 (1μg/ml, Miltenyi Biotec), and IL-4 (40ng/ml, Peprotech) in complete RPMI for four days at 37°C in a humidified incubator with 5% CO_2.

2.19. iGB culture system

The iGB culture system, as outlined by Nojima et al.[100], involves the use of a 3T3 fibroblast cell line of BALB/c origin, which stably expresses CD40 ligand (CD40L) and B-cell activating factor (BAFF) and is referred to as the 40LB cell line. These cells were maintained in high

glucose DMEM with GlutaMAX (Life Technologies, cat: 31966021) supplemented with 10% FBS and 100 IU/ml penicillin/streptomycin (Life Technologies, cat: 15070063) in T75 tissue culture flasks (Sarstedt, cat: 658175). Upon reaching confluence, the cells were detached with trypsin/EDTA (Gibco, cat: 25200056), washed, and collected in 15 ml tubes containing 5 ml of medium before undergoing irradiation (80 Gy). Cells were then washed, counted, and seeded at 3×10^6 per dish (100 mm, Greiner Bio, G664160) and 0.5×10^6 per well (6-well plate, Falcon, 353046). 40LB cells were allowed to attach and stretch overnight at 37°C and 5% CO_2. The following day, naïve B cells were isolated using anti-CD43 micro-beads and treated with TAT-Cre (~1.5μM) for 45 minutes as previously described. After three washes, cells were counted and cultured on an irradiated 40LB layer at a density of 5×10^5 cells per 100 mm dish or 5×10^4 cells per well in a 6-well plate for 4-6 days.

2.20. iGB adoptive transfer

iGB cells were prepared as described earlier. On day 4, fibroblasts and *in vitro* differentiated plasmablasts (typically less than 10% of the population) were removed using biotinylated anti-H-2Kd (Biolegend, cat: 116604) and anti-CD138 (Biolegend, cat: 142511) antibodies, followed by anti-biotin microbeads (Miltenyi) and negative selection through LS columns. In some experiments, FACS was preferred for the purification of tdTomato$^+$ iGB cells.

For competitive experiments, purified wild type iGB cells (CD45.1/2+) were mixed in a 1:1 ratio (verified by flow cytometry before transfer) with *Tfam*$^{-/-}$ iGB cells and injected intravenously (6×10^6 cells for competitive and 3×10^6 cells for non-competitive settings) into CD45.1+ or CD45.2+ congenic hosts. The hosts were immunised with SRBC using an enhanced protocol to promote the recruitment of transferred iGB cells into the germinal centre (GC). On day 6 post-transfer, spleens were harvested and analysed by flow cytometry and confocal imaging to evaluate GC entry.

2.21. Transwell migration assay

5×10^5 enriched total B cells isolated from SRBC-immunised Aicda-Tfam or Aicda-WT mice were placed in a 6mm transwell chamber with a 5μm pore size (Corning, cat: 3421) and

incubated at 37°C for two hours in the presence of either murine CXCL12 (200 ng/ml, Biolegend) or CXCL13 (1 µg/ml, Biolegend) in complete RPMI. The relative migration index was then calculated as follows: the percentage of GC B cells ($CD38^{-}GL\text{-}7^{+}tdTomato^{+}$) among the total input cells divided by the percentage of GC B cells among the migrated live total cells.

In separate experiments, 2×10^{5} purified total B cells from B-Tfam mice were placed in a similar 6mm transwell chamber and incubated for five hours in the presence or absence of murine CXCL12 (200 ng/ml, Biolegend) with or without mitoTempo (100 µM, Merck) and Ru265 (30 µM, Merck). After incubation, cells were stained with Live/Dead dye and anti-B220 AF488 antibody, resuspended in 100 µl of 96-well V-bottom plates, and analysed on a Cytek Aurora flow cytometer at high flow rate with a stopping volume of 60 µl. Technical duplicates were included. Specific migration (%) was calculated using the formula: 100 × [(Number of B220+ cells migrated in response to CXCL12 – Number of $B220^{+}$ cells migrated in the absence of CXCL12) / Number of input B cells] similar to previously published reports[101].

2.22. Single cell RNA-sequencing

Approximately 17,000 cells per sample were processed using the 10x Genomics Chromium Controller (Chip K). Gene expression and BCR sequencing libraries were prepared with the 10x Genomics Single Cell 5' Reagent Kits v2 (Dual Index) according to the manufacturer's guide (CG000330 Rev B). The final libraries were diluted to ~10 nM for storage, then denatured and further diluted before being loaded onto the NovaSeq6000 sequencing platform (Illumina, v1.5 chemistry, 28 bp/98 bp paired-end) at the Oxford Genomics Centre. Filtered output matrices from Cellranger 6.0.1 were imported into Seurat v4.1.0. Cells with >5% mitochondrial reads and <200 genes were excluded from the analysis. Data were normalised and transformed with SCTransform, adjusting for cell cycle phase and mitochondrial reads, then integrated using FindIntegrationAnchors and IntegrateData. Cells were clustered using RunUMAP, FindNeighbors, and FindClusters functions, with marker

genes identified via FindAllMarkers. Two small contaminant clusters (<1% of cells) expressing non-B cell genes were removed. Clusters were characterised by canonical marker expression, and proportions were computed using DittoSeq. For UMAP visualisation, an equal number of cells from each condition were randomly downsampled. Differential gene expression was assessed with FindMarkers using the 't-test' parameter, and pathway analysis was subsequently performed with the R package SCPA. Pseudobulk differential gene expression between biological replicates was performed with EdgeR after aggregating counts across cells using Scuttle.

Filtered contig outputs from Cellranger 6.0.1 were merged, filtered, and analysed using scRepertoire 1.4. Mutational rate in B cells was quantified with the Immcantation pipeline, germline segment assignment was carried out using Change-O, and SHM counts were computed with SHazaM.

2.23. NP conjugation

NP-APC conjugation was performed as previously reported with certain modifications[102]. Briefly, 1 mg of natural allophycocyanin (APC) protein (Stratech Scientific Ltd) was dialysed using a Slide-A-Lyzer™ MINI Dialysis Device (3.5K MWCO, Thermo Fisher Scientific, cat: 69550) in 1L of 3% NaHCO3 at 4°C for 5 hours, overnight, then for an additional 4 hours. NP-Osu (Biosearch, cat no: N-1010-100) was dissolved in dimethylformamide (Merck) to 10 mg/ml while vortexing. NP-Osu was added to the dialysed APC at a ratio of 20 µg:1 mg (low conjugation) and 80 µg:1 mg (high conjugation) and incubated at 20°C for 2 hours, protected from light. NP-APC conjugates were dialysed overnight in 1L 3% NaHCO3 at 4°C, followed by overnight dialysis in 1L PBS. The final products of NP-APC probes were stored in the dark at 4°C until use. NP-APC conjugates were used at a 1:100 dilution. Directly conjugated NP-PE from Biosearch was used at 1:200.

2.24. ELISA

For enzyme-linked immunosorbent assay (ELISA), 96 well EIA/RIA plates (Corning, cat: 3590) were coated overnight at 4°C with NP-BSA (NP_{1-4} or $NP_{<20}$, cat: N-5050XL-10 and N-

5050H-10) at 5 µg/ml in bicarbonate/carbonate coating buffer. The next day, plates were washed with PBS and blocked with 5% skimmed milk in PBS for 2.5 hours at 37°C. Serially diluted sera from NP-CGG-immunised mice (at various time points) were added to the blocked plates and incubated for 1 hour at 37°C. After washing with PBS containing 0.05% Tween-20, alkaline phosphatase-conjugated goat anti-mouse IgG1 (Southern Biotech, cat: 1071-04) or IgM (Southern Biotech, cat: 1021-04) detection antibodies (1:2000) were added and incubated for 1 hour at 37°C. Following the final wash, plates were developed with alkaline phosphatase substrate (Sigma, cat: P7998-100ML) for 10-30 minutes and read on a FLUOstar Omega plate reader at 5-minute intervals.

For virus-specific antibody detection, plates were coated overnight at 4°C with PFA-inactivated X31 virus in bicarbonate/carbonate coating buffer. After blocking with 1% BSA in PBS-Tween (0.05%) at 20°C for 2 hours, serially diluted sera were added and incubated for 2 hours at 20°C. Following multiple washes, biotinylated goat anti-mouse IgG or IgM detection antibodies (Southern Biotech, 1:1000) were added and incubated for 1 hour at 20°C. After washing, horseradish peroxidase (HRP)-conjugated streptavidin (Jackson ImmunoResearch, 1:1000) was added and incubated for 30 minutes. TMB substrate (ThermoFisher) was subsequently added. The reaction was stopped with 2N H_2SO_4, and absorbance was read at 450 and 570 nm. An additional 15-minute washing step with freshly prepared urea (VWR) in PBS was performed at 1, 2.5, or 5 M concentrations after serum incubation to assess avidity. Detection and development were conducted as described above.

2.25. T_{FH}-B cell co-culture

The method was adopted from Sage et al[103]. Briefly, $CD19^{-}CD4^{+}CXCR5^{hi}ICOS^{+}GITR^{-}$ T_{FH} cells were purified from SRBC-immunised (enhanced protocol) wild type mice at day 14. Naïve B cells were isolated from *Tfam*^{loxP} and wild type mice, both carrying the *Rosa26-stop-tdTomato* allele, using anti-CD43 microbeads (Miltenyi Biotec) as described above. After treatment with TAT-Cre (~1.5µM, 45 min), 5×10^4 wild type or *Tfam*$^{-/-}$ B cells were co-

cultured with 3×10^4 T_{FH} cells in a U-bottom 96-well plate with anti-CD3 (2μg/ml, 145-2C11, Thermo Fisher Scientific) and anti-IgM (5μg/ml, Jackson Immuno) for 6 days. At the end of the culture period, the percentages of $CD19^+$ $GL\text{-}7^+$ $IgG1^+$ $tdTomato^+$ *in vitro* generated GC B cells (iGCs) were determined by flow cytometry.

2.26. Cytoplasmic calcium assay

Experiments were conducted in four separate batches, each including one wild-type and one B-Tfam mouse spleen owing to the time and temperature sensitivity of calcium measurements. Single cell suspensions were prepared from spleens, with 2×10^6 cells transferred to V-bottom 96-well plates. Cells were first labelled with a fixable viability dye and anti-B220 antibody, then labelled with the cytoplasmic calcium indicator dye Fluo-4 AM (ThermoFisher Scientific, cat: F14201) at 10μg/ml in Iscove's Modified Dulbecco's Media (IMDM) with 1% FBS at 37°C for 15 minutes. After a wash, cells were resuspended in 400μl of warm IMDM with 1% FBS. To maintain physiological activity, samples were kept in warm (~37°C) throughout flow cytometry acquisition. Baseline fluorescence intensity was recorded for 30 seconds before rapidly stimulating with CXCL12 (200ng/ml) or anti-IgM (10μg/ml). Flow acquisition was performed at a low-speed setting for an additional 5 minutes. To minimise bias, the acquisition ordered alternated between wild type and experimental samples within each replicate. Data analysis was conducted using the Kinetics module in FlowJo software.

2.27. Lymphoma adoptive transfer

Upon the appearance of clinical lymphoma symptoms, spleens were collected from Eμ-Myc mice. Non-B cells were removed using the Pan B cell Isolation Kit II (Miltenyi Biotec) to isolate lymphoma cells. Subsequently, 2×10^6 lymphoma cells were intravenously injected into congenic B6.SJL.CD45.1 recipient mice in 200μL PBS. The recipient mice were sacrificed three weeks after the adoptive transfer, and inguinal lymph nodes were collected for further characterisation.

2.28. Quantification of metabolism by protein translation (SCENITH)

This method was adapted from previous protocols[104]. Briefly, splenocytes were divided into four groups and incubated at 37°C for 30 minutes with or without metabolic inhibitors (1µM oligomycin and/or 100mM 2DG, both from Merck) in a 96-well plate. The alkynylated puromycin analogue OPP (20µM final concentration, ThermoFisher Scientific) was then added for an additional 30 minutes. After washing, cells were labelled with Live/Dead viability dye and surface antibodies, then fixed with 4% PFA. Click Chemistry labelling was performed using the Click-iT™ Plus OPP Alexa Fluor 647 Protein Synthesis Assay Kit (Thermo Fisher Scientific, cat: C10458) following permeabilisation. The percentages of mitochondrial dependence, glycolytic capacity, glucose dependence, and FAO/AAO (fatty acid oxidation and amino acid oxidation) were calculated using gMFI values of OPP-AF647 obtained from B cells treated with 2-deoxyglucose (2-DG), oligomycin, or both. Used calculations are below:

$$\text{Glucose dependence (\%)} = 100 \times [(OPP_{\text{No inhib}} - OPP_{2DG}) / (OPP_{\text{No inhib}} - OPP_{(2DG \,\&\, \text{oligomycin})})]$$

$$\text{FAO/AAO capacity (\%)} = 100 - (\text{Glucose Dependence})$$

$$\text{Mitochondrial dependence (\%)} = 100 \times [(OPP_{\text{No inhib}} - OPP_{\text{oligomycin}}) / (OPP_{\text{No inhib}} - OPP_{(2DG \,\&\, \text{oligomycin})})]$$

$$\text{Glycolytic capacity (\%)} = 100 - (\text{Mitochondrial Dependence})$$

2.29. Extracellular flux analysis

Real-time oxygen consumption rates (OCR) and extracellular acidification rates (ECAR) were assessed by a Seahorse XFe96 Extracellular Flux Analyzer (Agilent). Naïve or stimulated B cells (3×10^5 cells) were plated on a poly-D lysine (PDL)-coated XF96 cell culture microplate and incubated at 37°C for at least 30 minutes in a CO_2-free incubator with assay medium (XF RPMI medium pH 7.40, supplemented with 2 mM L-glutamine, 1 mM pyruvate, and 10 mM glucose). For iGB cells, cells were detached from a fibroblast

feeder layer and rested in IL-4 overnight. Subsequently, 2×10^5 cells per well were plated on the PDL-coated XF96 plate with 5-6 technical replicates. Basal OCR and ECAR were recorded, followed by the addition of MitoStress Test inhibitors: oligomycin (1 μM), FCCP (2 μM), and rotenone + antimycin A (both at 0.5 μM) (Agilent).

For Asn-modified experiments of Chapter 3, B cells from B-WT and B-Asns mice were stimulated overnight (anti-CD40 at 5μg/ml and IL-4 at 10ng/ml) in the presence of varying concentrations of Asn, and then plated at 2×10^5 cells per well on a PDL-coated XF96 plate and the assay was performed as described above. However, assay medium was switched to XF DMEM medium pH 7.40 in these experiments to achieve measurements under Asn-free conditions. MitoStress Test settings remained the same. Data analysis was performed using Wave software (Agilent).

2.30. Serum and lymph node interstitial fluid (LNIF) collection for LC-MS

To collect serum, mice were either bled from the tail vein or subjected to terminal bleeding via cardiac puncture following CO_2 asphyxiation. Collected blood samples were then centrifuged at 1000 × g for 10 minutes at 4°C, and the serum was stored at -20°C until use.

For lymph node interstitial fluid (LNIF) collection, mice were first euthanised using CO_2 asphyxiation. The inguinal, brachial, axial, cervical, mediastinal, and mesenteric lymph nodes were harvested and transferred to 1.5ml tubes containing PBS kept on ice. After collecting lymph nodes from 9-14 mice into two to three tubes, the elution phase was proceeded. Lymph nodes from four mice were pooled in each tube, treated as a single batch for subsequent LNIF elution. Lymph nodes pooled from four mice were placed on two 10μm strainers (pluriSelect) in 1.5ml tubes and centrifuged at 400 × g for 10 minutes at 4°C. The strainers were then reversed and centrifuged again at 400 × g for an additional 10 minutes at 4°C to maximise fluid extraction.

The LNIF collected at the bottom of the tubes was pipetted into new collection tubes, avoiding any contaminating cell pellets. The LNIF from all batches was pooled together,

with a final pooled volume from 9-14 mice treated as one biological replicate. This procedure was repeated to obtain three biological replicates, using a total of 35 mice, excluding those used for serum isolation. Approximately 1-1.5µl of LNIF was possible to collect from each mouse on average.

2.31. Mass spectrometry

To extract molecules, cells were pelleted and washed twice with cold PBS and once with ice cold ammonium acetate (150mM, pH 7.3). The pellet was then resuspended in 1ml 80% LC-MS grade methanol/ultrapure water chilled on dry ice. The samples were vortexed three times on dry ice, and then centrifuged at 15,000×g for 5 mins. The initial supernatant was then transferred into a 1.8ml glass vial, and the pellet resuspended in 200µl 80% methanol as above, then centrifuged again at 15,000×g for 5 mins. The second supernatant was then combined with the first, dried at 4°C using a Centrivap (Conco), then stored at -80°C until analysis.

Dried metabolites were resuspended in 50% ACN:water and 1/10th was loaded onto a Luna 3µm NH_2 100A (150 × 2.0 mm) column (Phenomenex). The chromatographic separation was performed on a Vanquish Flex (Thermo Scientific) with mobile phases A (5mM NH_4AcO pH 9.9) and B (ACN) and a flow rate of 200µl/min. A linear gradient from 15% A to 95% A over 18 min was followed by 7 min isocratic flow at 95% A and reequilibration to 15% A. Metabolites were detected with a Thermo Scientific Q Exactive mass spectrometer run with polarity switching (+3.5 kV/− 3.5 kV) in full scan mode with an m/z range of 70-975 and 140.000 resolution. Maven (v8.1.27.11) was used to quantify the targeted metabolites by area under the curve using expected retention time (as determined with pure standards) and accurate mass measurements (< 5 ppm). Values were normalized to cell number.

Relative amounts of metabolites were calculated by summing up the values for all measured isotopologues of the targeted metabolites. Metabolite Isotopologue Distributions were corrected for natural ^{15}N abundance. Integrated pathway analysis was performed using MetaboAnalyst[105] (https://www.metaboanalyst.ca/) with default parameters. This function

uses over-representation analysis (ORA) based on the hypergeometric distribution, to generate *P* values for the over representation of genes or metabolites within KEGG pathways. The *P* values are then merged, and network topology analysis used to determine an impact score for the pathway. The input metabolite and gene sets were those differentially expressed/abundant in GC B cells compared with follicular B cells (using multiple testing correction).

For amino acid detection in serum and lymph node interstitial fluid following LC-MS protocol was used. Data acquisition was performed using an adaptation of a method previously described[106]. Samples were injected onto a Dionex UltiMate 3000 LC system (Thermo Scientific) with a Fortis C18 column (100 x 2.1 mm, 3 µm; Fortis Technology Ltd). Mobile phases: Solvent A was 0.1 % acetic acid in water (both Optima HPLC grade, Sigma Aldrich); solvent B was Acetonitrile (Optima HPLC grade, Sigma Aldrich). The column temperature, flow rate, and injection volume were 50 °C, 0.2 mL min^{-1}, and 5 µL, respectively. Gradient elution was as follows: 0% B, 0-3 minutes; 0 – 60% B, 3-5 minutes; hold for 2 minutes; 0% B, 7.01, hold for 4 minutes (re-equilibration). MS was performed in positive and negative polarities using a TQS Quantiva Triple Quadrupole Mass Spectrometer (Thermo Scientific) with an electrospray ionization (ESI) source. Qualitative and quantitative analyses were performed using Xcalibur Qual Browser and Tracefinder 5.1 software (Thermo Scientific) according to the manufacturer's workflows. Analyses were performed using selected reaction monitoring (SRM). Results were processed using GraphPad Prism 10 software.

Samples were prepared as follows: (a) 20 µL serum were mixed with 60 µL MeOH containing internal standard (IS, 100 µmol L^{-1} $^{13}C_5$-glutamine and 50 µmol L^{-1} of $^{13}C_4$-asparagine), vortexed briefly and centrifuged (10 minutes, 4 °C, 12,700 rpm). 60 µL supernatant was collected and dried under a N_2 stream. Samples were resuspended in 60 µL water, vortexed briefly, and analysed by LC-MS (see above). (b) 15 µL mouse lymph node interstitial fluid (LNIF) and mixed with 45 µL methanol containing IS (same

concentration as above). Sample preparation and analysis continued as above, but with a final resuspension volume of 45 µL water. For both a and b relative abundances of metabolites were measured by comparison of their peak areas compared to those of their labelled equivalents (i.e. IS). For serum, calibration curves (300, 150, 75, 37.5, 18.8, 9.3, and 4.6 µmol L^{-1}) for labelled IS were generated using a matrix of human serum, prepared as above.

Reagents used were as follows: Optima water (Optima HPLC grade, Sigma Aldrich), Acetonitrile (Optima HPLC grade, Sigma Aldrich), Acetic acid (Fisher Chemical), Methanol (Optima HPLC grade, Sigma Aldrich), $^{13}C_4$-asparagine (Cambridge Isotope Laboratories, Item number CLM-8699-H-PK), $^{13}C_5$-glutamine (Cambridge Isotope Laboratories, C.N 184161-19-1).

2.32. Western blotting

Cells were lysed on ice in RIPA buffer (Merck) with added protease and phosphatase inhibitors (complete™ ULTRA Tablets and PhosSTOP™, Roche) for 30 minutes under frequent vortexing. The lysates were then centrifuged at 15,000 × g for 15 minutes at 4°C, and the supernatant was collected. Protein concentration was quantified by performing BCA assay (Pierce, Thermo). Samples were denatured in Laemmli buffer (Bio-Rad) with 10% β-mercaptoethanol at 90°C for 5 minutes, then cooled on ice. The proteins were separated on a 4-15% gel (Mini-PROTEAN TGX Precast Gels, Bio-Rad), and transferred onto PVDF membranes (Bio-Rad). The membranes were blocked with 2.5% skimmed milk for 1 hour. This was followed by an incubation with primary antibody diluted in 2.5% BSA / 0.05% TBS-Tween 20 at 4°C overnight. Following washing steps, membranes were incubated with HRP-conjugated goat anti-rabbit secondary antibody in 2.5% milk / 0.05% TBS-Tween 20 at room temperature for 1 hour. Anti-rabbit IgG, HRP-linked Antibody (#7074, Thermo Fisher) and SuperSignal™ West Pico PLUS Chemiluminescent Substrate (Thermo Fisher) were used for Chemiluminescence detection. Antibodies used were ASNS (14681-1-AP, Proteintech) and (β-actin 4970, Cell Signalling used)

2.33. Statistical analysis

Statistical analyses and tests are described in the respective figure legends. All error bars represent mean ± S.E.M. Significance was defined as *P* values ≤ 0.05. Analyses were conducted using GraphPad Prism v9 & 10 or R 4.1. No statistical methods were used to pre-determine sample sizes, they are comparable to those in previous studies[107]. Data distribution was examined with normality tests to select appropriate statistical methods; otherwise, assumed to be normally distributed. *In vivo* experiments were conducted with experimental mice matched by sex and age within experimental batches, but other randomisation methods were not employed. Data collection and analysis were generally not performed blindly. Mice that showed no germinal centres or Alum spots after immunisation were excluded from analysis as they were considered to have failed intraperitoneal immunisation. For some experiments, batch correction was performed using the R package *Batchma*.

Chapter 3: Asparagine metabolism controls B cell homeostasis

3.1. Introduction

Amino acid metabolism is a crucial regulator of T cell homeostasis and function, as shown by changes in environmental abundance, synthesis, or following interference with cellular uptake via solute transporters[108–115]. Fundamentally critical for protein homeostasis, amino acids also regulate other metabolic processes[116]. It is demonstrated in T cells that the availability of certain amino acids can profoundly alter their homeostasis and function[114].

Although B cell-derived lymphomas are sensitive to amino acid depletion[117–120] and loss of serine synthesis or deletion of CD98, a component of large neutral amino acid transporters, disrupts GC formation[31], the significance of amino acid availability in B cell metabolism and humoral immunity is unclear.

GCs have distinct characteristics. Their poorly vascularised hypoxic milieu with an unknown availability of nutrients, diverse cellular composition and interactions in their distinct zones coupled with extreme rates of cell death pose great challenges in studying their immunometabolism. To this end, metabolomics approaches are highly valuable as they can be quickly performed with minimal impact on cellular metabolic programs after isolation[121]. The results in this chapter originate from observations obtained by targeted metabolomic profiling in *ex vivo*-isolated GC B cells, in comparison to their naïve B cell counterparts (Fig. 3.1A). This analysis revealed a broad increase in the levels of metabolites in GC B cells with overrepresentation of amino acids, including asparagine (Asn), serine (Ser), alanine, lysine, and glycine (Fig. 3.1B). The combined integrated pathway analysis with an RNAseq dataset[122] illustrated notable enrichment of the Kyoto Encyclopedia of Genes and Genomes (KEGG) Alanine, Aspartate (Asp), and Glutamate (AAG) metabolism pathway in GC B cells, which includes the amino acid Asn (Fig. 3.1C). Although primarily considered a non-essential amino acid, Asn can act in a conditionally essential manner[123]. Asn has been shown to be critical for maintaining metabolic balance, specifically in the TCA cycle and nucleotide biosynthesis pathways. It has also regulatory roles in important cellular

processes such as cell proliferation, viability and signalling in cancer and T cells[112–114,124,125]. Its exogenous abundance is vital especially for cells that lack the capacity to synthesise Asn, an ATP-dependent reaction catalysed by the enzyme asparagine synthetase (ASNS)[126]. However, no studies on asparagine metabolism exist in B cells to date. Although there is mechanistic work on Asn in cancer cells, it is entirely unclear whether they are relevant to normal immune cell physiology. Therefore, in this chapter I have aimed to answer the following questions:

- Which adaptive changes occur in Asn metabolism during B cell activation and differentiation?
- What is the functional importance of exogenous or endogenously produced Asn for the GC reaction and distinct B cell subsets?
- What are the effects of depleting exogenous or endogenous Asn on humoral responses in both infectious and non-infectious settings?

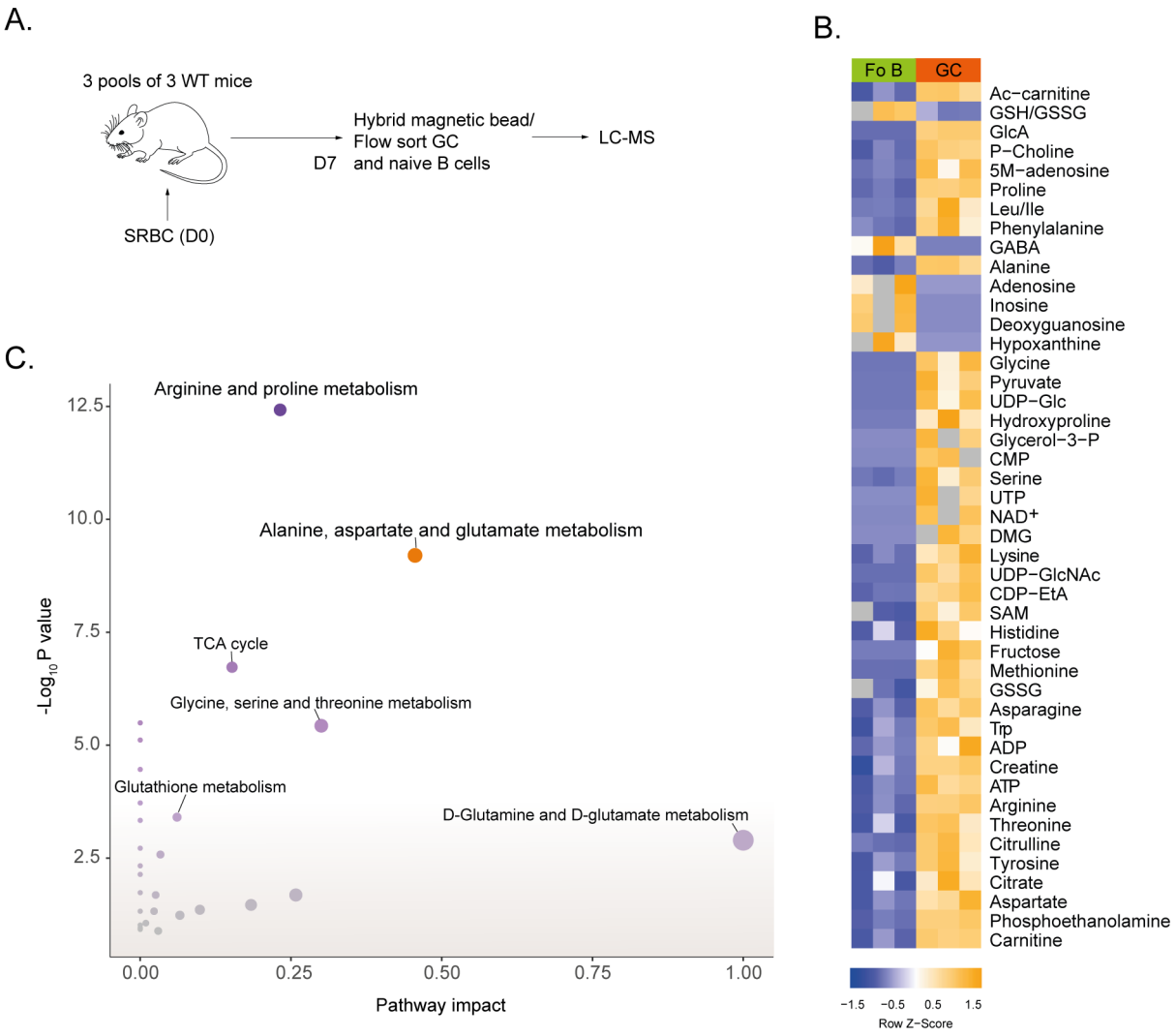


Figure 3.1. Asparagine metabolism is upregulated in GC B cells.
(A) Diagram illustrating the layout and structure of the experimental design. Three groups of three wild type mice were immunised with sheep red blood cells (SRBC). On day 7, GC and naïve B cells (FoB) were separated using a combination of magnetic beads and flow sorting. The isolated cells were then examined for polar metabolites using LC-mass spectrometry (LC-MS). (B) Heatmap displaying metabolites that are significantly differentially abundant (with an adjusted *P* value (Padj) value of less than 0.05) in naïve and GC B cells at day 7 from wild type mice that were immunised with SRBC. The metabolites were evaluated using LC-MS, with a sample size of 3 pools, each including 3 mice per pool. Representative of two independent experiments. (C) An integrated pathway analysis reflecting the differences in metabolites and gene expression between GC and naïve B cells. The metabolites were identified as differentially abundant. The gene expression profiles were obtained from ImmGen (GSE15907[122]). Statistical significance was determined by two-way ANOVA with Tukey's multiple testing correction (B), or hypergeometric test (C). (The data were generated by Dr. Alexander Clarke and are included in a preprint in which I am first author[127].)

3.2. Results

3.2.1. Protein translation in GCs is highly active

To directly measure protein synthesis rates in GC B cells *in vivo* in their splenic microenvironment, I developed an *in vivo* bio-orthogonal non-canonical amino acid tagging (BONCAT) protocol with the amino acid analogues L-azidohomoalanine (L-AHA) and O-propargyl-puromycin (OPP), which allows *in situ* detection of their incorporation using Click chemistry[128]. L-AHA is an amino acid analogue that does not lead to ribosomal stalling once included in peptides. OPP is a puromycin analogue that enters the acceptor site of ribosomes and is incorporated into nascent proteins and terminates elongation[129].

To better measure dynamic and kinetic activity, I performed dual BONCAT. Because of the distinct chemistry of L-AHA and OPP, with the former carrying an azide and the latter alkyne residues, it was possible to co-label these analogues[130]. Although there have been reports of *in vivo* BONCAT protocols for immune and non-immune compartments[128,130], this technique has not been previously applied to GCs *in vivo* using this dual labelling strategy.

To label GC B cells, I employed mice expressing *Rosa26*^{STOP}*tdTomato* under the control of *Aicda-Cre*[14], the gene encoding AID, and immunised them with sheep red blood cells (SRBC), a T cell-dependent immunogen. When *Aicda-Cre* drives its expression, tdTomato, chemically resistant to the Click reaction, provides selective and efficient detection of GCs[20]. On day 14 post-immunisation, an intraperitoneal pulse of L-AHA was given, and four hours later, an OPP pulse. An hour later, the spleens were collected for analysis (Fig. 3.2A). This sequential pulse regimen was essential for preserving physiological translation activity up until the injection of OPP, which causes translation termination. Subsequently, OPP and L-AHA were fluorescently co-labelled in splenic sections using different Click chemistry reactions. I observed that the incorporation of L-AHA and OPP by GCs was significantly higher than that of the nearby naïve B cell follicle, suggesting highly active translation (Fig. 3.2B). PBS injected spleens did not show signal enhancement in GCs at significant levels (Fig. 3.2C).

Subsequently, I labelled GC B cells with OPP *ex vivo*, and after 30 minutes, I measured its incorporation using flow cytometry (Fig. 3.2D). After doublet, dead cell, and $CD4^+$ T cell exclusion, naïve and GC B cells were gated as $CD19^+$ IgD^+ $GL\text{-}7^-$ and $CD19^+$ $CD38^-$ $GL\text{-}7^+$, respectively (Fig. 3.2E and F). The DZ ($CXCR4^{hi}$ $CD86^{low}$) and LZ ($CXCR4^{low}$ $CD86^{hi}$) fractions of GC B cells were further distinguished by flow cytometry (Fig. 3.2G). When GC B cells were compared to IgD^+ naïve B cells, flow cytometry analysis demonstrated a significant increase in OPP incorporation, especially in the DZ subset (Fig. 3.2H).

Therefore, the DZ compartment, where GC B cells are undergoing SHM and active division, is the site of highly active protein synthesis.

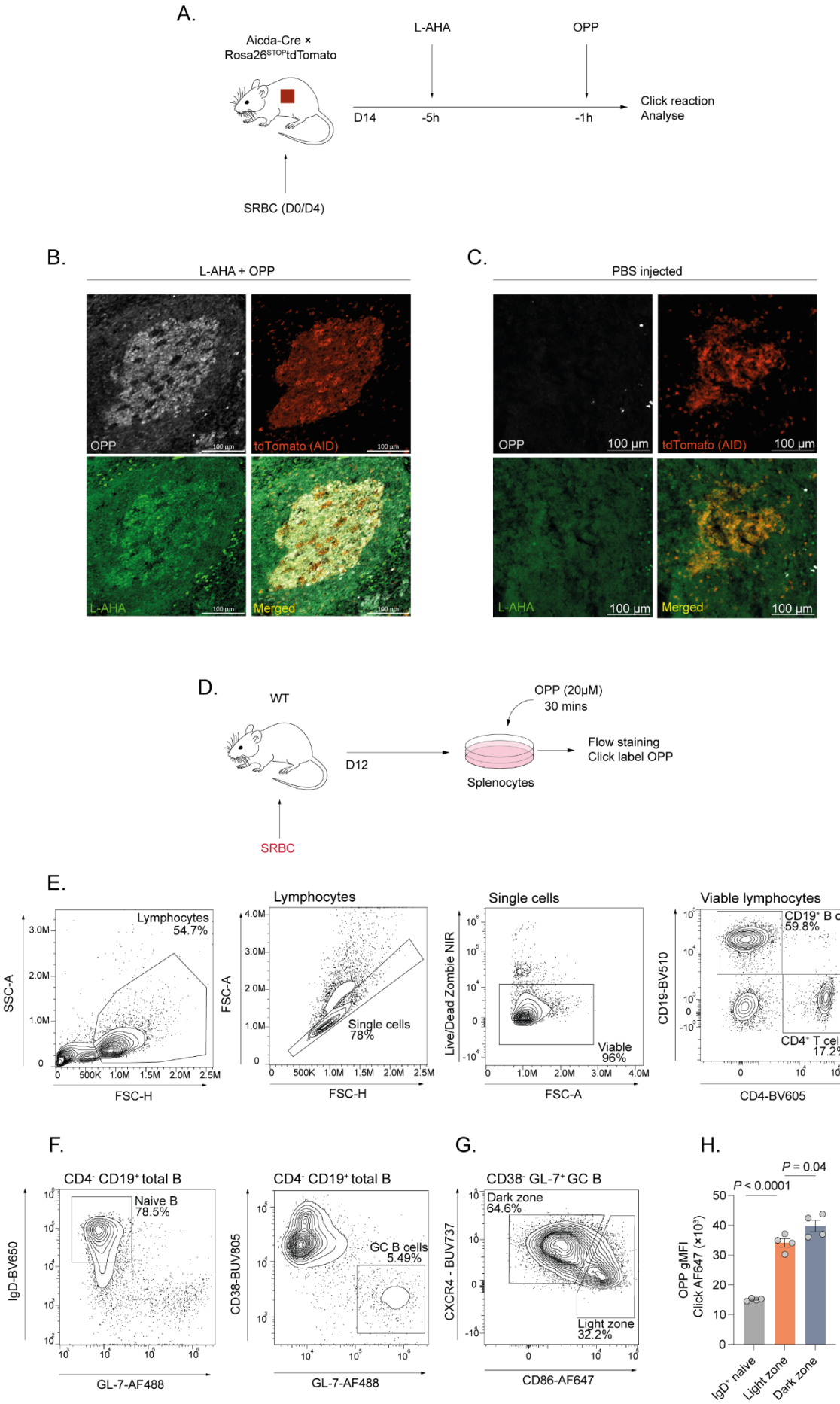

A.
Aicda-Cre ×
Rosa26STOPtdTomato
L-AHA
OPP
D14
-5h
-1h
Click reaction
Analyse
SRBC (D0/D4)
B.
L-AHA + OPP
OPP
tdTomato (AID)
L-AHA
Merged
C.
PBS injected
OPP
100 µm
tdTomato (AID)
100 µm
L-AHA
100 µm
Merged
100 µm
D.
WT
OPP (20µM)
30 mins
D12
Flow staining
Click label OPP
Splenocytes
SRBC
E.
Lymphocytes
54.7%
SSC-A
FSC-H
Lymphocytes
Single cells
78%
FSC-A
FSC-H
Single cells
Live/Dead Zombie NIR
Viable
96%
FSC-A
Viable lymphocytes
CD19+ B cell
59.8%
CD4+ T cells
17.2%
CD19-BV510
CD4-BV605
F.
CD4- CD19+ total B
Naive B
78.5%
IgD-BV650
GL-7-AF488
CD4- CD19+ total B
GC B cells
5.49%
CD38-BUV805
GL-7-AF488
G.
CD38- GL-7+ GC B
Dark zone
64.6%
Light zone
32.2%
CXCR4 - BUV737
CD86-AF647
H.
P = 0.04
P < 0.0001
OPP gMFI
Click AF647 (×10³)
IgD+ naive
Light zone
Dark zone

Figure 3.2. Protein translation in germinal centres (GCs) is highly active.
(A) Diagram of bio-orthogonal non-canonical amino acid tagging *in vivo*. Aicda-Cre × Rosa26^{STOP}tdTomato mice were immunised with SRBC and then boosted at day four. On day 14, they received an L-AHA injection, followed by an OPP pulse four hours later. An hour afterward, they were euthanised and Click chemistry was performed. (B) Representative splenic GC immunofluorescence images labelled with L-AHA, tdTomato (AID), and OPP, reflecting the results of two separate experiments. Scale bar 100μm. (C) Representative immunofluorescence images of splenic GCs labelled with PBS as a negative control for the panels in **B.** Data represent two independent experiments. (D) Diagram illustrating the process of *ex vivo* OPP labelling in splenocytes 12 days after SRBC immunisation. (E) Gating strategy for splenic CD19^{+} B cells as live (Live dead^{-}) CD4^{-} lymphocytes. (F) Further gating strategies of IgD^{+} GL-7^{-} Naïve B and CD38^{-} GL-7^{+} GC B cells. (G) Representative gating for DZ (CXCR4^{hi} CD86^{low}) and LZ (CXCR4^{low} CD86^{hi}) GC B cells. (H) OPP-AF647 signal quantification and comparison in Naïve B, LZ and DZ GC B cells. Representative of two independent experiments. Statistical significance was determined by one-way ANOVA with Tukey's multiple testing correction (**H**).

3.2.2. Neutral amino acid transporters are upregulated in GC B cells

I hypothesised that enhanced protein translation and incorporation of amino acid analogues in GC B cells might be associated with elevated capacity for amino acid uptake. Therefore, I analysed a publicly available RNAseq dataset (GSE133971)[131] and compared the transcriptional levels of anionic, cationic, and neutral amino acid transporters in murine naïve and GC B cells. While anionic and cationic transporters did not show much change, a subset of neutral amino acid transporters were upregulated in GC B cells, including *Slc7a5* (Fig. 3.3A). L-type amino acid transporter 1 (LAT1) is made up of the proteins encoded by *Slc7a5* and *Slc3a2* (CD98). CD98 is also an essential component of the sodium-independent cystine-glutamate antiporter SLC7A11, also known as the xCT transporter[132]. Despite the lack of transcriptional upregulation of *Slc3a2* in the dataset (Fig. 3.3A), immunohistochemistry staining revealed that protein levels of CD98 were highly abundant in splenic GCs following SRBC immunisation at day 12 (Fig. 3.3B-C). Flow cytometry analysis confirmed the increase in CD98 at the protein level and showed a more robust upregulation. This occurred more markedly in the DZ (Fig. 3.3B-C), in line with their higher translation capacity demonstrated in Fig. 3.2H. Additionally, I observed robust upregulation of SLC3A2 in human GCs by performing IHC staining on human tonsils using CellDIVE, a multiplexed tissue imaging platform[133] (Fig. 3.3E). Therefore, both mouse and human GC

B cells have higher amounts of a specific set of neutral amino acid transporters, which is consistent with their greater capacity to synthesise proteins.

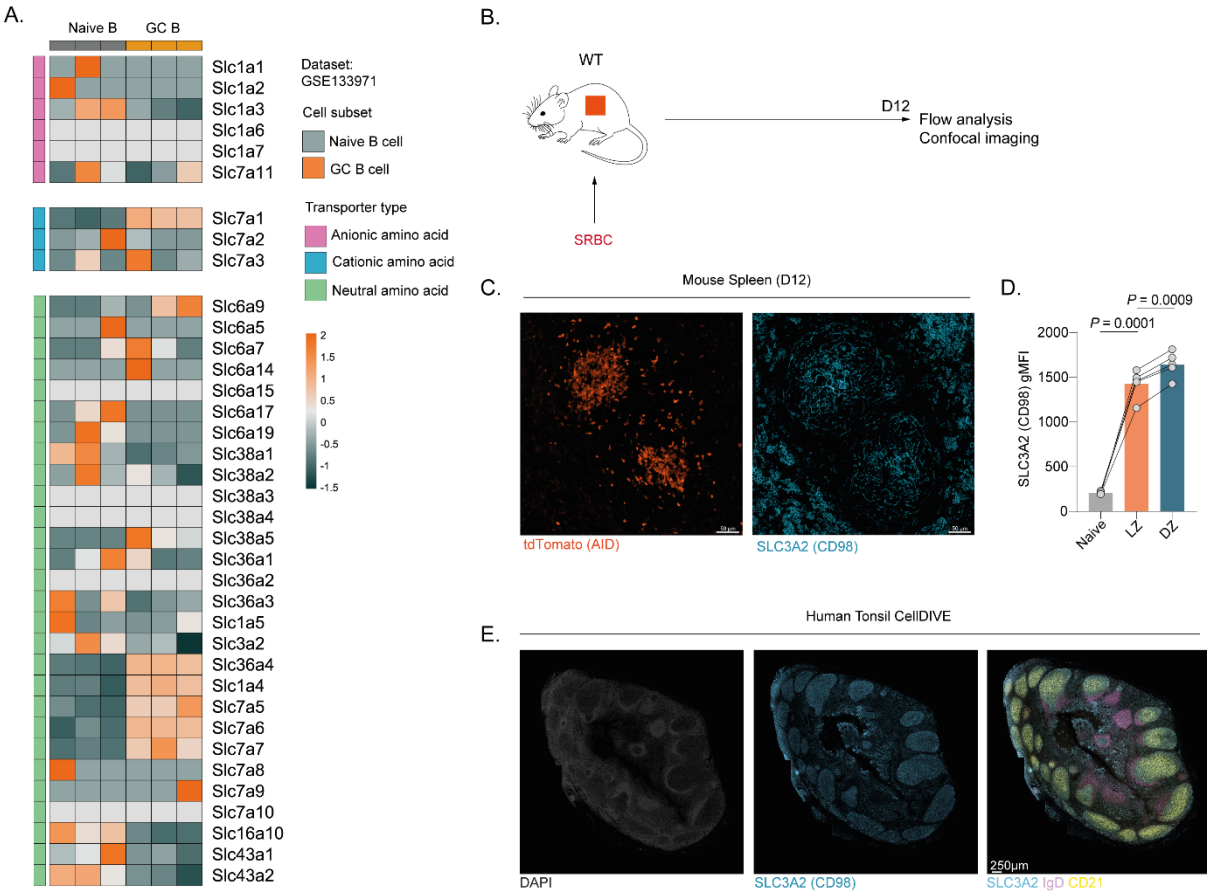


Figure 3.3. Neutral amino acid transporters are upregulated in GC B cells.

(A) Heatmap of row z-scores for the normalised RNA count of the indicated amino acid transporters in GC vs naïve B cells. GC B cells were from NP-CGG immunised mice (n=3) at day 10 and naïve follicular B cells were isolated from unimmunised mice. Data from GSE133971. (B) Schematic of SRBC immunisation in Aicda-Cre × Rosa26^{STOP}tdTomato mice. At day 12, spleens were harvested and analysed by confocal imaging and flow cytometry. (C) Representative immunofluorescence images of splenic GCs labelled with tdTomato (AID) and CD98. Representative of two independent experiments. Scale bar 100µm. (D) Flow cytometry quantification of CD98 in Naïve B, LZ and DZ GC B cells (as described and gated in Fig 3.2H. (E) Multiplexed CellDIVE images of normal human tonsil section with immunofluorescence staining for SLC3A2 (CD98), CD21, and IgD. Representative of 3 separate tonsils. DAPI as counter staining. Scale bar 250µm. Statistical significance was determined by one-way ANOVA with Tukey's multiple testing correction (**D**).

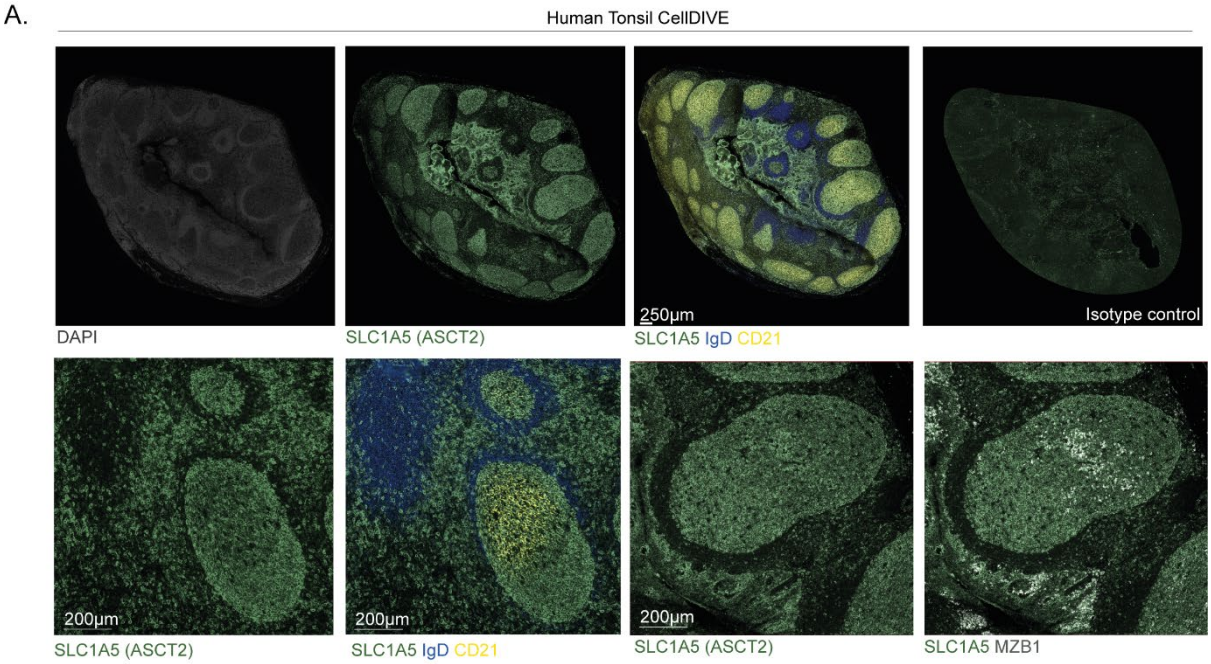
3.2.3. Asparagine uptake is dynamically regulated in GC B and plasma cells

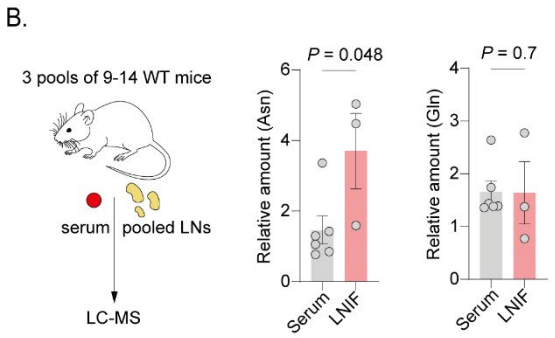
The *in vivo* translation assay I performed showed elevated uptake and incorporation of L-AHA in GCs (Fig 3.2B). A recent study demonstrated that L-AHA uptake is mediated by the neutral amino acid transporter Alanine-Serine-Cysteine Transporter (ASCT2), also known as SLC1A5[130]. Therefore, I examined SLC1A5 levels in human tonsils and found its robust upregulation in GCs (Fig 3.4A). $CD21^{low}$ DZ areas showed higher expression compared to the $CD21^{hi}$ LZ. Plasma cells marked by MZB1 also showed elevated levels of SLC1A5 (Fig 3.4A). SLC1A5 has been shown to be important for the uptake of Asn[112]. Substantial increase in the intracellular amounts of Asn was observed in GC B cells (Figure 3.1A-B). To determine tissue Asn levels, I quantified Asn and Gln levels in interstitial fluid obtained from lymph nodes (LNIF). By pooling all harvestable lymph nodes (axial, brachial, inguinal, cervical, mediastinal, and mesenteric), I was able to collect approximately 1-1.5µL of LNIF from a single mouse. By combining lymph nodes from 35 wild type mice into three experimental pools, I obtained sufficient LNIF and corresponding serum samples to perform relative quantification of Asn and Gln via LC-MS. The analysis showed that Asn levels in LNIF were substantially higher than those in serum, which is estimated to be around 40µM[134,135], while Gln levels were comparable between the two compartments (Fig. 3.4B). This points to the possibility that lymphocytes have adapted to the elevated concentration of Asn in their specific environments, compared to the levels found systemically.

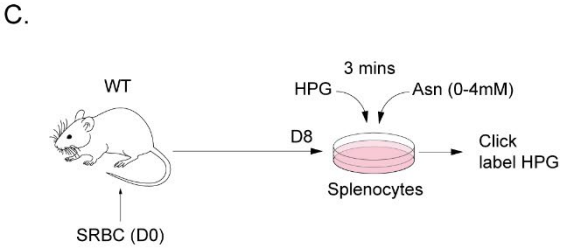
I then functionally evaluated the Asn uptake capacity of SLC1A5 by performing a competitive amino acid uptake assay in which the bio-orthogonal amino acid analogue homopropargylglycine (HPG) competes with Asn for transport through ASCT2 (Fig 3.4C). I designed this uptake assay by modifying a similar assay proposed for Glutamine uptake through SLC1A5 in T cells[130]. The HPG signal was substantially higher in *ex vivo* GC B cells kept at 37°C compared to those maintained at 4°C. This indicates biologically active uptake (Fig 3.4D). Addition of Asn induced a robust fall in HPG uptake signal, indicating its competitive transport through SLC1A5 (Fig. 3.4E). After validating the assay, I screened B

cell subsets isolated *ex vivo* following SRBC immunisation and found that there was clear dose-dependent competition between HPG and Asn in GC B cells and plasmablasts unlike naive B cells (Fig 3.4E). This was most evident in DZ GC B cells, in keeping with their high levels of OPP incorporation and SLC1A5 expression (Fig 3.4E).

Asn uptake is therefore markedly upregulated in GC B cells and plasma cells, associated with elevated levels and activity of SLC1A5.


A.
Human Tonsil CellDIVE
DAPI
SLC1A5 (ASCT2)
SLC1A5 IgD CD21
250μm
Isotype control
200μm
SLC1A5 (ASCT2)
200μm
SLC1A5 IgD CD21
200μm
SLC1A5 (ASCT2)
SLC1A5 MZB1


B.
3 pools of 9-14 WT mice
serum
pooled LNs
LC-MS
P = 0.048
Relative amount (Asn)
Serum
LNIF
P = 0.7
Relative amount (Gln)
Serum
LNIF


C.
WT
SRBC (D0)
D8
3 mins
HPG
Asn (0-4mM)
Splenocytes
Click
label HPG

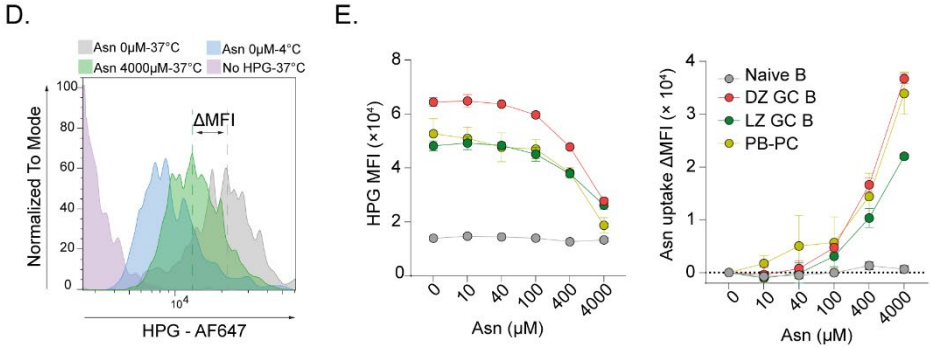

D.
Asn 0μM-37°C
Asn 0μM-4°C
Asn 4000μM-37°C
No HPG-37°C
Normalized To Mode
ΔMFI
HPG - AF647
E.
HPG MFI (×10⁴)
Asn (μM)
Naive B
DZ GC B
LZ GC B
PB-PC
Asn uptake ΔMFI (× 10⁴)
Asn (μM)

Figure 3.4. Asparagine uptake is dynamically regulated in GC B and plasma cells. (A) Multiplexed CellDIVE images of normal human tonsil section with immunofluorescence staining for SLC1A5 (ASCT2), CD21, IgD and MZB1 (in close-up images). Representative of 3 separate tonsils. DAPI was used for counter staining and an isotype control for negative staining. Scale bar = 250μm. (B) Diagram illustrating the process of collecting serum and pooled lymph nodes (axial, brachial, inguinal, cervical, mediastinal, and mesenteric) and using LC-MS to quantify the relative quantities of Asn and glutamine (Gln) in serum and lymph node interstitial fluid. The LC-MS analysis was performed on three pools of 9-14 unimmunised WT mice for lymph node interstitial fluid (LNIF) and 2-3 unimmunised WT mice for serum. The data are collectively derived from three independent experiments. (C) Schematic of *ex vivo* SLC1A5-mediated competitive Asn uptake assay on *ex vivo* B cell subsets isolated at day 8 post-SRBC immunisation. (D) Representative flow cytometry histogram of HPG-AF647 signal at the competing Asn concentrations in $IgD^{-}GL\text{-}7^{+}$ GC B cells at 4°C or 37°C. (E) **Left panel:** Quantification of HPG (400μM) uptake at increasing concentration of Asn (0-4000μM) in IgD^{+} $GL\text{-}7^{-}$ naive B, IgD^{-} $CD138^{+}$ plasmablasts/plasma cells (PB-PC), $CXCR4^{low}$ $CD86^{hi}$ LZ and $CXCR4^{hi}$ $CD86^{low}$ DZ GC B cells harvested from n=4 mice at day 8 following SRBC immunisation. Background signal subtraction was performed based on 4°C and no-HPG controls. **Right panel:** Quantification of the shift in the HPG signal intensity (ΔMFI) as in left panel reflecting Asn uptake calculated as following: Asn uptake at x concentration = HPG $MFI_{[Asn0]}$ – HPG $MFI_{[Asn\ x\ ]}$. Representative of two independent experiments. Statistical significance was determined by a two-tailed Mann–Whitney U-test (**B**).

3.2.4. Alanine, Aspartate, and Glutamate pathway enzymes are upregulated in GC B cells

Asparagine can be acquired exogenously or produced endogenously by synthetic enzymes. An enrichment of amino acid metabolic pathways was previously observed in GC B cells, particularly the AAG metabolism pathway as described in the KEGG (Fig. 3.1C). In an independent transcriptional dataset (GSE133971)[131], I found that the leading-edge genes of the AAG pathway showed a generalised upregulation in synthetic enzymes. There was an approximately 40-fold increase in *Asns* expression in GC B cells relative to naive counterparts (Fig. 3.5A). ASNS catalyses the synthesis of Asn from aspartate (Asp) in an ATP-dependent reaction (Fig. 3.5B). By immunoblotting, I verified the increased protein abundance of ASNS in GC B cells isolated from immunised mouse spleens (Fig. 3.5C). To examine the spatial distribution of ASNS expression, I again used the CellDIVE platform and performed multiplex imaging of human tonsils. The expression of ASNS was markedly upregulated in GCs and $MZB1^{+}$ plasmablasts (Figure 3.5D). In the IgD^{+} B cell follicle or the

$CD3^+$ T cell zone however there was only minimal expression. Differential abundance of ASNS was observed in the GC, with increased expression in the DZ (Fig. 3.5E). Notably, this spatial distribution of ASNS largely mirrors SLC1A5 as depicted in Fig. 3.4A.

In summary, these findings suggest that the AAG pathway is markedly upregulated in GC B cells and the synthetic enzyme of Asn, ASNS, may have an important role in GCs.

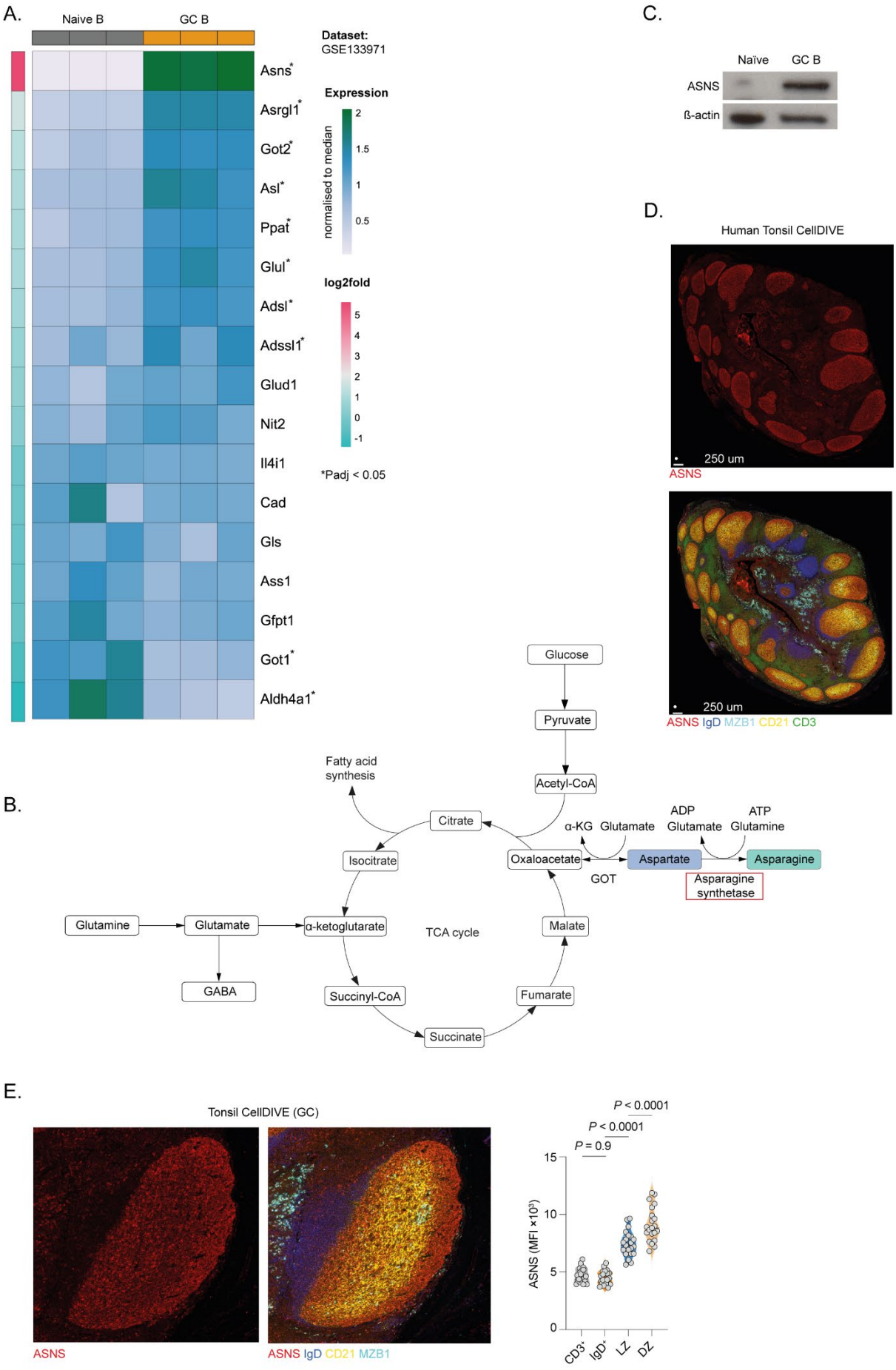

A.
Naive B
GC B
Dataset:
GSE133971
Asns*
Asrgl1*
Got2*
Asl*
Ppat*
Glul*
Adsl*
Adssl1*
Glud1
Nit2
Il4i1
Cad
Gls
Ass1
Gfpt1
Got1*
Aldh4a1*
Expression
normalised to median
2
1.5
1
0.5
log2fold
5
4
3
2
1
0
-1
*Padj < 0.05
C.
Naïve
GC B
ASNS
ß-actin
D.
Human Tonsil CellDIVE
250 um
ASNS
250 um
ASNS IgD MZB1 CD21 CD3
B.
Glucose
Pyruvate
Acetyl-CoA
Fatty acid synthesis
Citrate
Isocitrate
α-KG
Glutamate
ADP
Glutamate
ATP
Glutamine
Oxaloacetate
Aspartate
Asparagine
GOT
Asparagine synthetase
Glutamine
Glutamate
α-ketoglutarate
TCA cycle
Malate
GABA
Succinyl-CoA
Fumarate
Succinate
E.
Tonsil CellDIVE (GC)
ASNS
ASNS IgD CD21 MZB1
P < 0.0001
P < 0.0001
P = 0.9
ASNS (MFI ×10³)
15
10
5
0
CD3+
IgD+
LZ
DZ

Figure 3.5. Alanine Aspartate Glutamate pathway enzymes are upregulated in GC B cells.
(A) Heatmap of the normalised RNA count normalised to median of the row for indicated AAG pathway genes in GC vs naive B cells. Data are from GSE133971[131]. Genes with Padj< 0.05 highlighted with an asterisk* according to analysis performed by DESeq2 R package. (B) Diagram illustrating asparagine synthesis and its link with the TCA cycle. (C) ASNS immunoblot in magnetic bead-sorted GC B cells and naive B cells from wild type mice immunised with SRBC on day 0 and day 4, with analysis performed on day 12. Representative of two independent experiments. Beta-actin serves as a loading control. (D) Images of a normal human tonsil section using multiplexed CellDIVE imaging, immunofluorescence staining for ASNS, CD21, IgD, MZB1, and CD3. Illustrative of three distinct tonsils. Scale bar 250μm. (E) $CD21^+$ LZ, $CD21^-$ DZ, IgD^+ naïve, and $MZB1^+$ plasma cell niches are highlighted in CellDIVE immunofluorescence images of a GC from a tonsil. The mean fluorescence intensity (MFI) / mean grey value of ASNS in these areas is quantified. Twenty-one GCs in total were analysed, pooled from three tonsils, each dot representing a randomly selected GC with a representative DZ, LZ, and surrounding IgD^+ naïve B cell follicle. Statistical significance was determined by one-way ANOVA with Tukey's multiple testing correction (E).

3.2.5. Specific deletion of *Asns* in B cells: B-Asns mice

Previously, our laboratory generated *Cd79a-Cre* × $Asns^{LoxP}$ mice (B-Asns hereafter) to investigate the function of Asn synthesis in B cell biology. *Cd79a* encodes a component of the B cell receptor[136]. In *Cd79a-Cre* mice, Cre recombinase is expressed during the early phases of B cell development[137]. The efficient deletion of *Asns* was verified by quantitative PCR (qPCR) analysis in activated B cells after *in vitro* stimulation with IL-4 and agonistic anti-CD40 (Fig. 3.6A), which mimics the activating signals typically provided by T cells via CD40 ligand (CD40L). Similar to earlier immunoblot and CellDIVE-based immunostaining of ASNS, naïve B cells that were not stimulated at day 0 displayed minimal expression of *Asns* (Fig. 3.6B). B-Asns mice were viable and fertile without any sign of overt immune deficiency. There was no numerical or proportional abnormality in the development of B cells in B-Asns mice according to the Hardy Classification[1] (Fig. 3.6B-C). Therefore, the B-Asns mouse model allows for targeted deletion of *Asns* in B cells, which is not required for B cell development at the steady state.

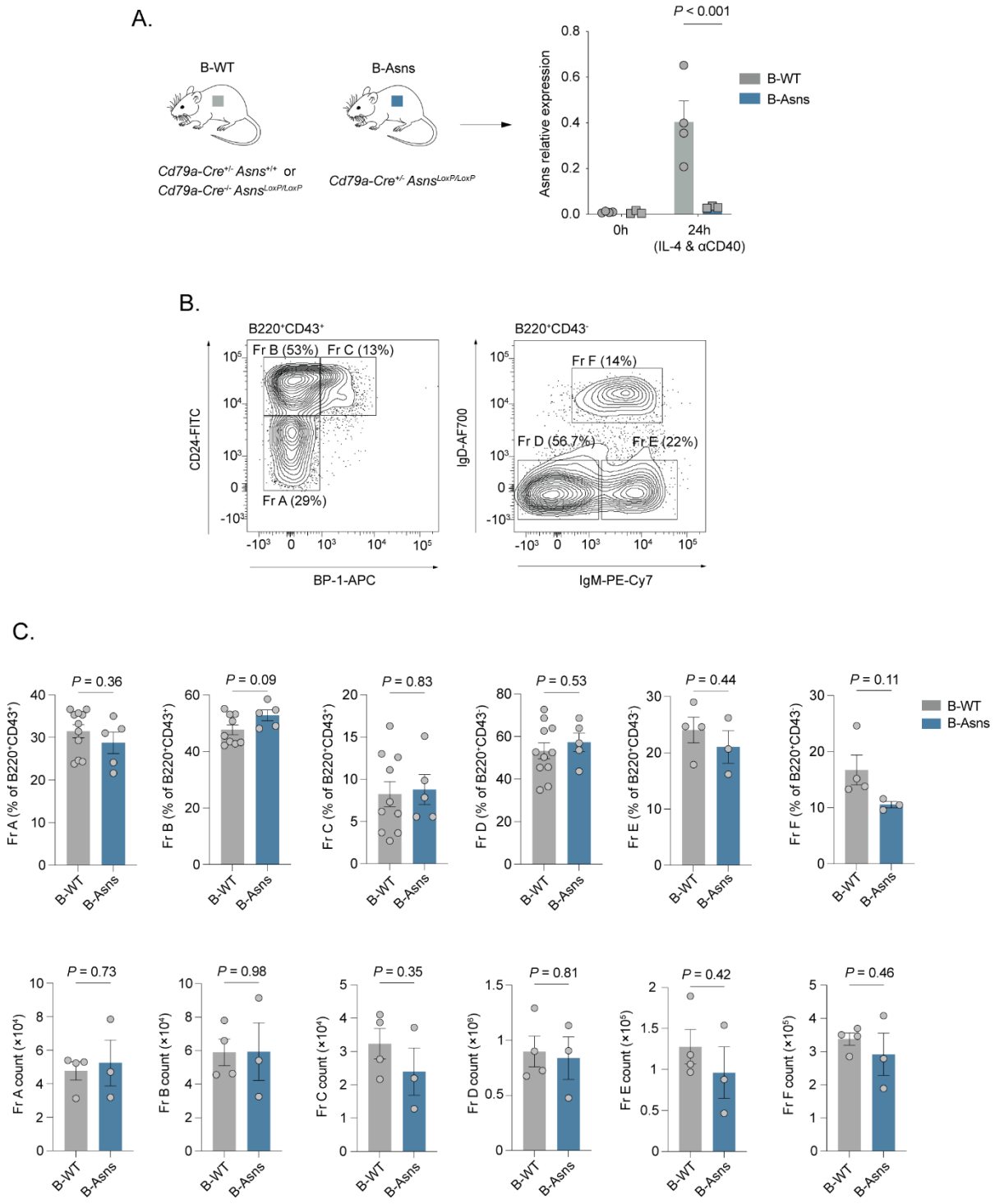


Figure 3.6. Specific deletion of Asns in B cells: B-Asns mice.
(A) Schematic of B-WT and B-Asns mouse genotypes and qPCR quantification of relative Asns expression in B-WT and B-Asns B cells at naïve or activated states following agonistic anti-CD40 + IL-4 stimulation. (B) Representative gating approach for the specified Hardy stages of B cell maturation in bone marrow. (C) Quantification of the specified Hardy stages of B cell maturation in the bone marrow. Each data point corresponds to a mouse. Cumulative data from two separate experiments. Statistical significance was determined by a two-way ANOVA with Šidák's multiple testing correction (**A**) or unpaired two-tailed t test (**C**).

3.2.6. ASNS is important for B cell viability when the availability of Asn is limited

Lymphocyte homeostasis *in vitro* is critically dependent on the availability of amino acids. The concentration of Asn in standard RPMI-1640 (378μM) is in excess of the physiological levels reported in serum (40μM)[134,135]. By using a custom-formulated Asn-free RPMI-1640 base medium, I adjusted the levels of Asn in the medium to test its impact on B cell biology.

To examine the dependencies of B cells on exogenous Asn during activation, I stimulated B cells isolated from B-WT and B-Asns mice with agonistic anti-CD40 and IL-4 in RPMI-1640 media supplemented with varying concentrations of Asn for 72h (Fig. 3.7A).

When B cells were completely deprived of Asn (0μM) or supplemented with a low concentration of Asn (10μM), there was a reduction in cell viability compared with supplementation of Asn at 40μM or 400μM concentrations (Fig. 3.7B-C).

Survival of B-Asns B cells was much more severely compromised when Asn was limited in the culture medium, but normal when Asn was supplemented at 40μM or higher (Fig. 3.7B-C), which is likely to reflect the physiological range of Asn found in lymphoid tissues as measured in Fig. 3.4B.

These findings indicate that ASNS critically supports B cell survival when Asn availability is low.

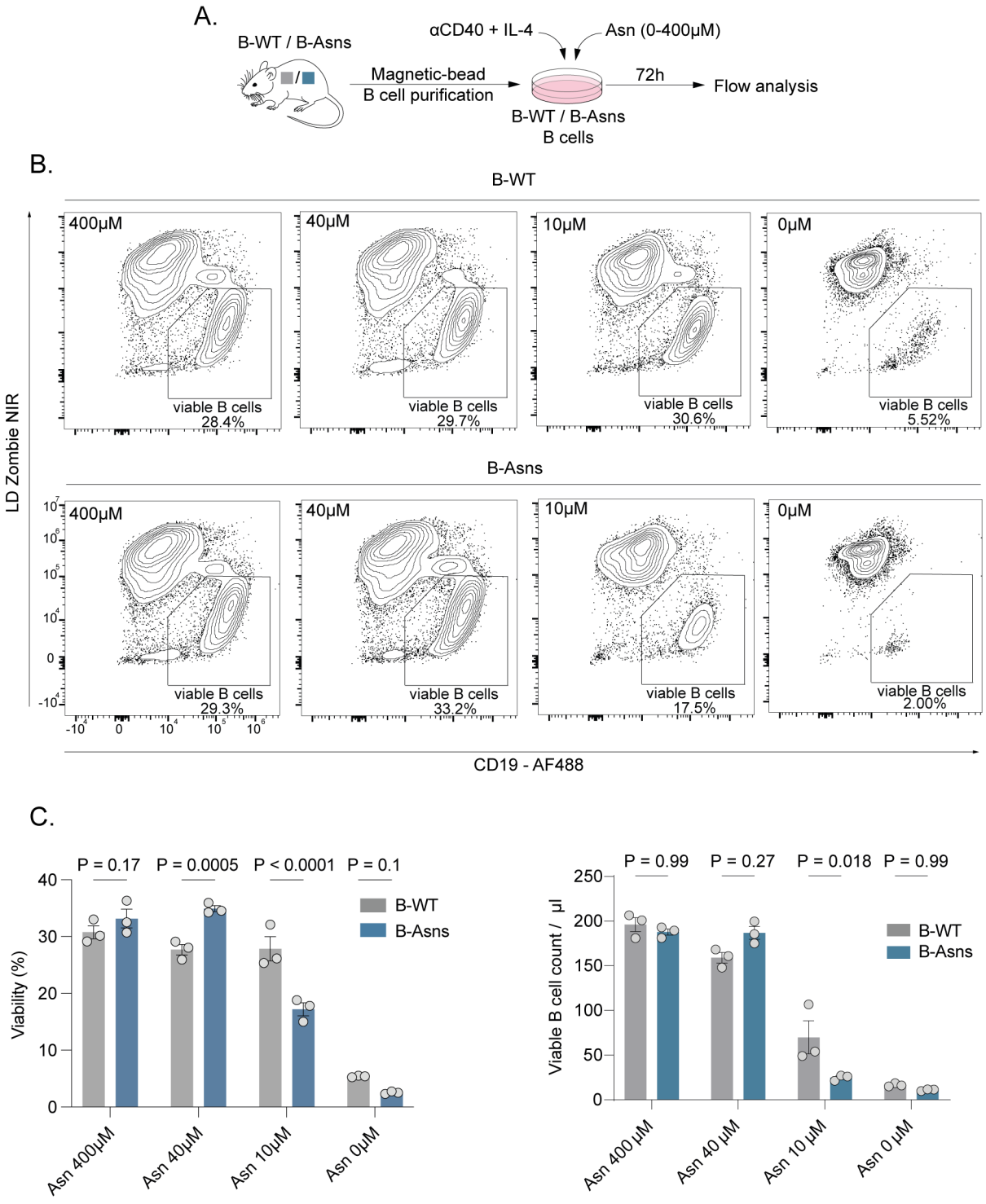


Figure 3.7. ASNS is important for B cell viability when the availability of Asn is limited.

(A) Illustration depicting the *in vitro* B cell activation culture system for B-WT and B-Asns mice. Viable B cells (10^5 cells) were isolated using magnetic beads and stimulated with IL-4 (10ng/ml) and agonistic anti-CD40 (5μg/ml) for 72 hours while being exposed to different concentrations of Asn (0-400μM). (B) Representative flow cytometry gating for LiveDead Zombie$^-$ CD19$^+$ viable B cells at 72h. (C) Proportional and numerical quantification of **B.** Results are pooled from two independent experiments. Statistical significance was determined by a two-way ANOVA with Šidák's multiple testing correction (**C**).

3.2.7. ASNS is critical for B cell division under conditions of low Asn availability

Next, I investigated the proliferative capacity of B cells following a similar experimental approach *in vitro*. I labelled purified B cells from B-WT and B-Asns mice with CellTrace Violet (CTV), a reactive dye which reflects proliferation dynamics, then cultured these cells for 72h in the presence of IL-4 and anti-CD40 at varying concentrations of Asn (Fig. 3.8A). In Asn-replete conditions (40μM and 400μM) there was robust division in B-WT and B-Asns B cells (Fig. 3.8B-C). At 10μM Asn, B-WT B cells showed mild proliferative defects, whilst B cells from B-Asns mice remained even more defective in this condition. In the complete absence of Asn however, both B-WT and B-Asns B cells showed almost completely abrogated proliferation (Fig. 3.8B-C). B cells form large cellular clusters *in vitro* when proliferating. I imaged B-WT and B-Asns B cells following 72h of cell culture, and observed that, in keeping with their reduced CTV dilutions, B-WT B cells formed markedly smaller cell clusters, which were nearly absent in B-Asns B cells in the absence of Asn. In the presence of Asn (400μM), clusters in B-WT and B-Asns B cells were comparably larger, suggesting intact proliferation (Fig. 3.8D).

Therefore, exogenous Asn levels control proliferative capacity of B cells and the requirement for ASNS during cell division.

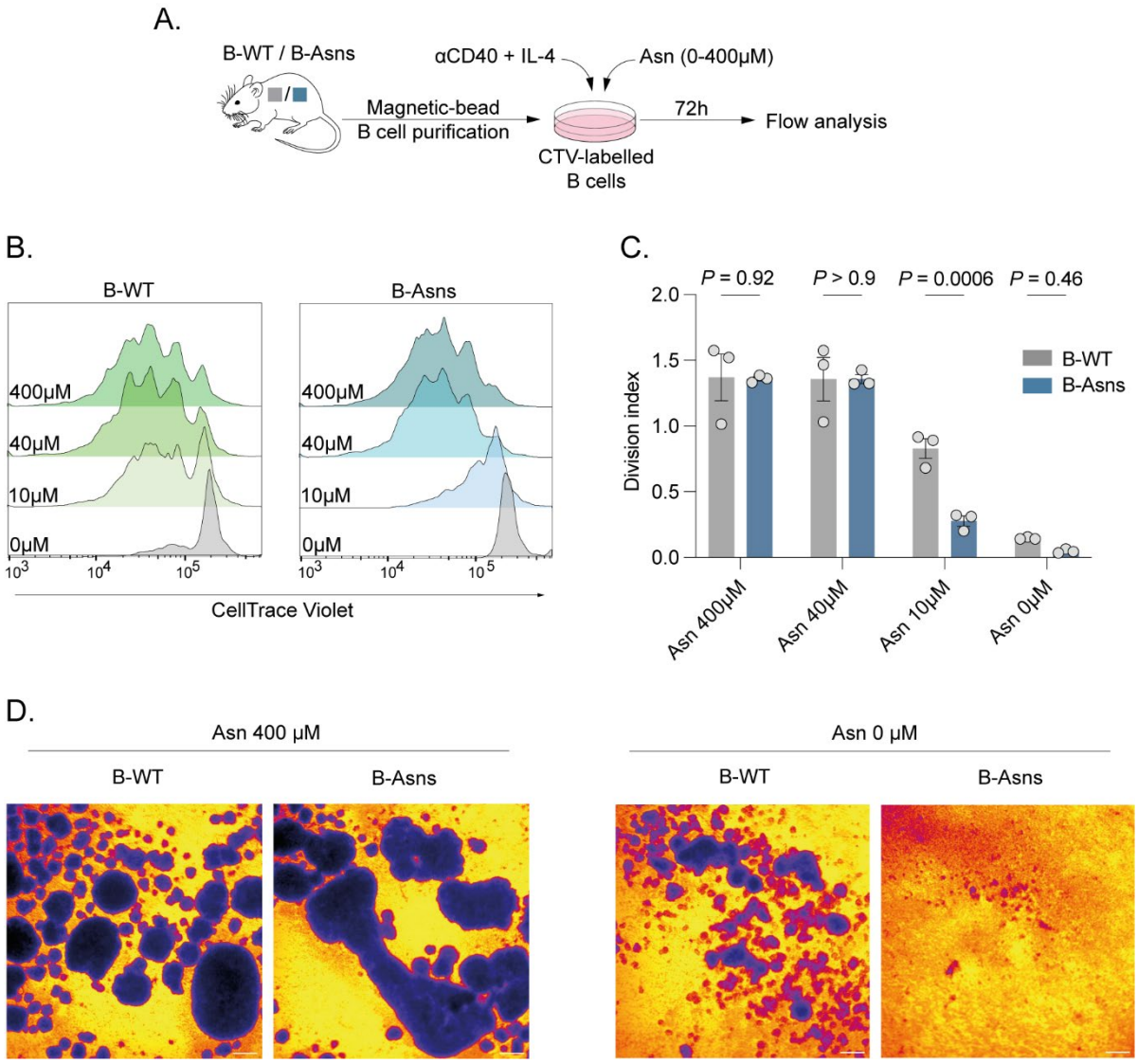


Figure 3.8: ASNS is critical for B cell division under conditions of low Asn availability.
(A) Schematic of *in vitro* B cell activation culture system. Magnetic-bead purified B cells (10^5 cells) were labelled with CellTrace Violet (CTV) (20μM) and stimulated with IL-4 (10ng/ml) and anti-CD40 (5μg/ml) for 72h in the presence of varying Asn concentrations (0-400μM). (B) Representative flow cytometry histograms of CTV dilutions of LiveDead Zombie$^-$ CD19$^+$ viable B cells at 72h. (C) Quantification of division index of **B**, which reflects average number of cell divisions cells underwent. Each datapoint represents a biological replicate from single mouse cultured as technical duplicates then averaged. (D) Phase contrast microscopy images of B cell clusters following 72h culture. Scale bar in arbitrary pixel units and consistently the same size across experimental conditions. Statistical significance was determined by a two-way ANOVA with Šidák's multiple testing correction (**C**).

3.2.8. Exogenous Asn is conditionally required for plasmablast development

B cell activation can initiate a differentiation program in a subset of B cells, leading to the formation of plasmablasts. They play an indispensable role in the early stages of humoral immune response[138]. Established stimulatory conditions exist for generating plasmablasts *in vitro*, and it has been shown that lipopolysaccharide (LPS) in combination with high doses of IL-4 induces strong plasmablast differentiation, which is only weakly achieved with anti-CD40 and IL-4 stimulation[139]. I therefore substituted anti-CD40 for LPS and carried out B cell stimulation as described (Fig. 3.9A).

Plasmablasts were identified by IgD downregulation and CD138 expression (Fig. 3.9B). After 72 hours, plasmablast differentiation induced by LPS and IL-4 was almost completely blocked in B-Asns B cells when Asn was absent or limited (10μM), while in B-WT cells, differentiation remained proportionally unchanged despite a significant reduction in cell numbers (Fig. 3.9B-C). In keeping with viability and proliferation results, plasmablast differentiation remained normal in B cells of both genotypes when Asn was sufficiently provided (Fig. 3.9B-C).

Overall, the synthesis and uptake of Asn are necessary for the differentiation of plasmablasts, and the absence of synthetic capacity impairs their development when exogenous Asn is defective.

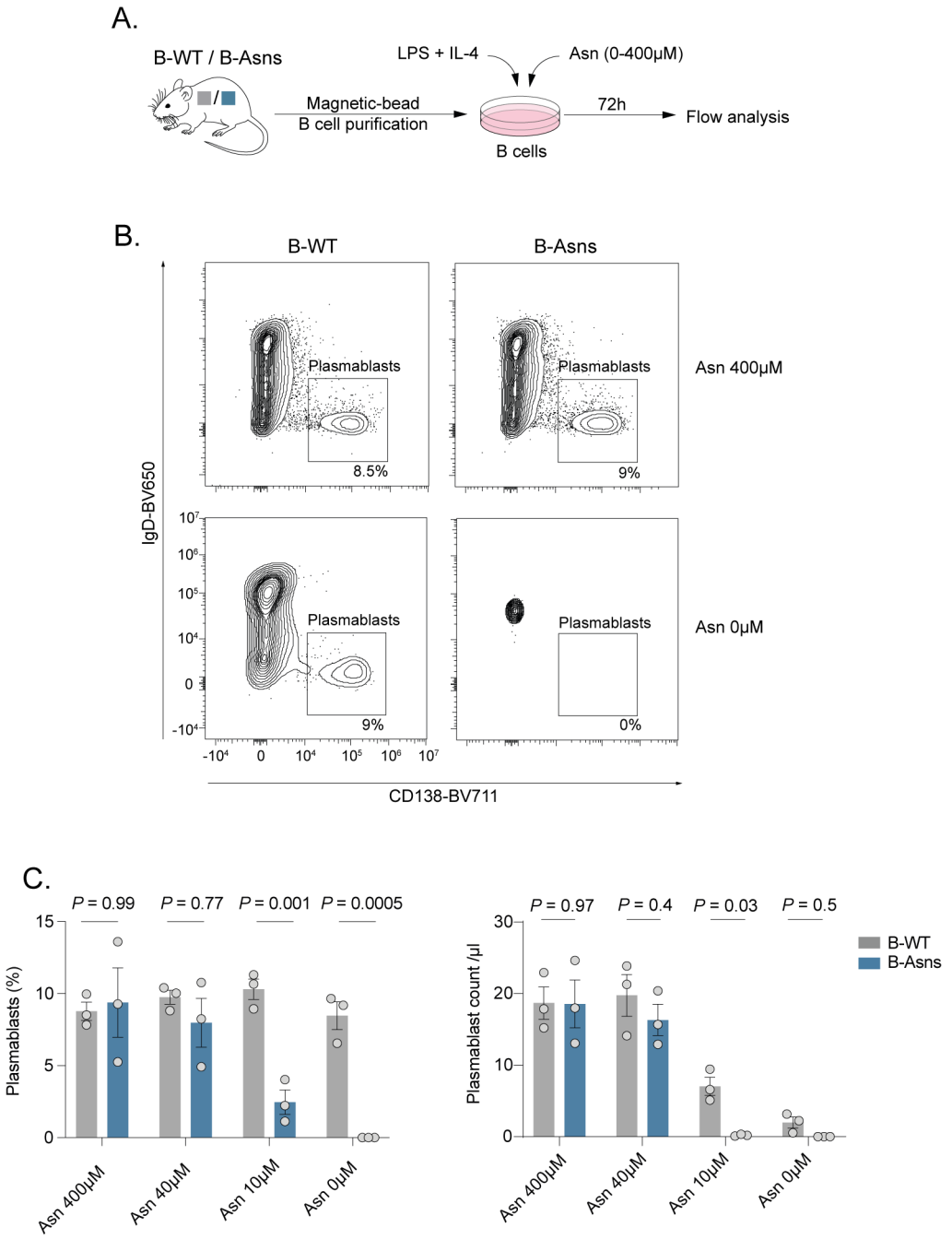


Figure 3.9. Exogenous Asn is conditionally required for *in vitro* plasmablast development.
(A) Illustration depicting the *in vitro* B cell activation culture system used. Viable B cells (10^5 cells) were isolated using magnetic beads and stimulated with IL-4 (50ng/ml) and LPS (10μg/ml) for 72 hours while being exposed to different concentrations of Asn (0-400μM). (B) Representative flow cytometry plots of IgD^-CD138^+ plasmablasts generated as in **A**. (C) Quantification of plasmablast counts and proportions as in **B.** Statistical significance was determined by a two-way ANOVA with Šidák's multiple testing correction (**C**).

3.2.9. ASNS regulates plasmablast differentiation independently of its role in cell division

Plasmablast differentiation is intimately coupled to cell division[140]. Given the diminished proliferative capacity observed with low Asn availability, I asked whether this alone was responsible for the defective plasmablast development.

I examined the transition to a plasmablast phenotype in B cell fractions with comparable proliferative history following *in vitro* stimulation with LPS and IL-4, as in Fig. 3.9A. As B cells divided, they downregulated IgD (Fig. 3.10A), and IgD downregulation positively correlated with CTV, therefore I used IgD as a proxy for cell division to retrospectively analyse cell division. Only IgD^- B cells with the lowest level of IgD expression developed a $CD138^+$ plasmablast phenotype (Fig. 3.10B-C). B-Asns B cells cultured with 10μM Asn downregulated IgD to a lesser extent than B-WT B cells (Fig. 3.10B). However, within the IgD^- compartment, they remained defective in differentiating into plasmablasts compared to their B-WT counterparts, despite showing potentially similar proliferative activity (Fig. 3.10D). In addition to the proportional reduction, the expression level of CD138 was severely decreased, further supporting an impaired differentiation program in B-Asns plasmablasts deprived of Asn (Fig. 3.10E). This suggests that Asn metabolism plays a key role in plasmablast differentiation beyond cell division.

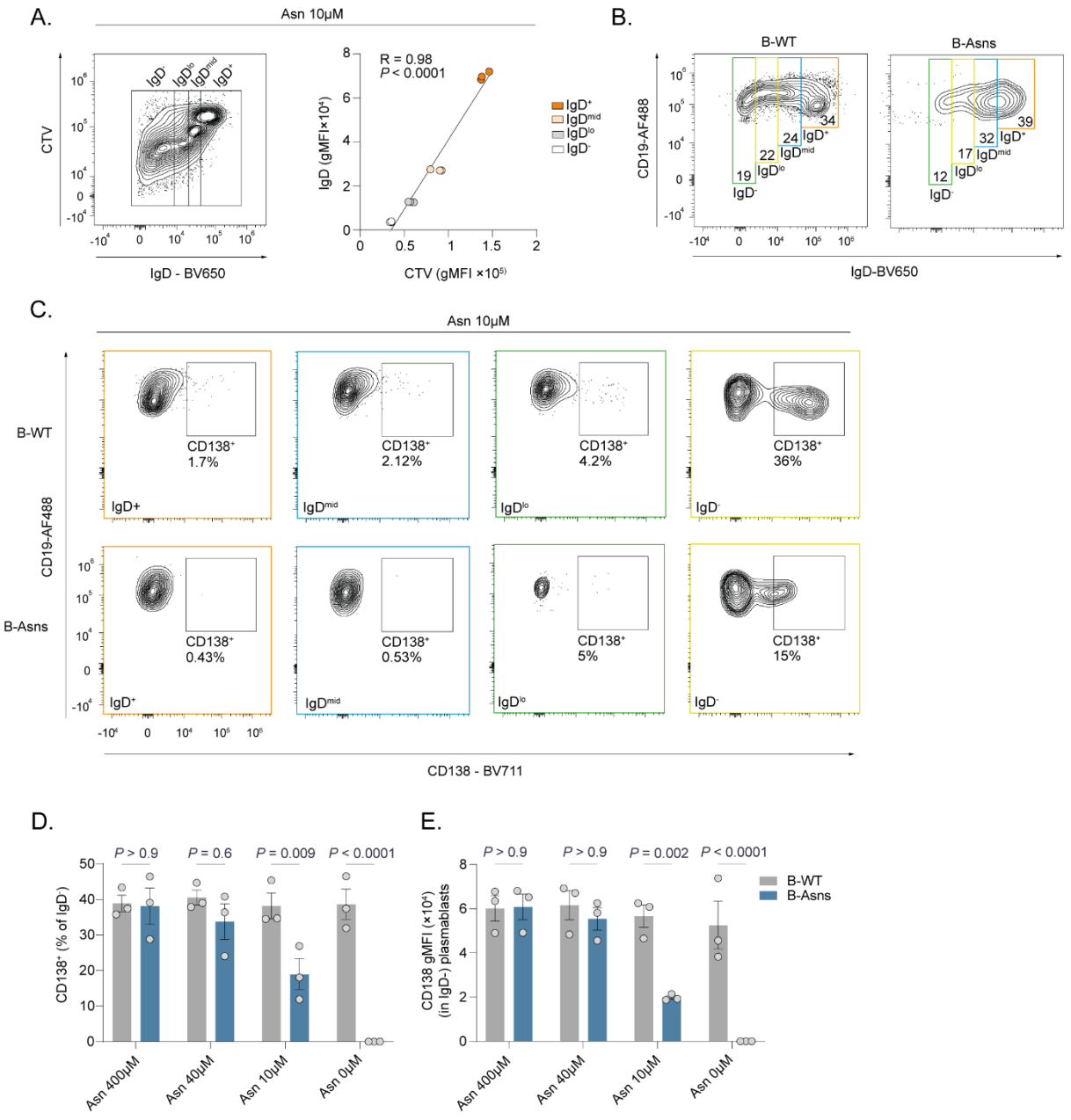


Figure 3.10. ASNS regulates plasmablast differentiation independently of its role in cell division.

(A) Flow cytometry plot and X-Y correlation plot illustrating the interrelation of IgD and CTV in B cells stimulated in the presence of 10μM Asn. (B) Representative flow cytometry comparison of IgD downregulation in B-WT and B-Asns B cells stimulated with LPS and IL-4 for 72h at 10μm Asn. (C) Representative flow cytometry comparison of IgD^{-} $CD138^{+}$ plasmablasts in fractions with varying IgD downregulation from B-WT and B-Asns B cells stimulated and cultured at varying Asn concentrations (0-400μM). (D) Quantification of **C.** (E) Quantification of CD138 geometric MFI in IgD^{-} $CD138^{+}$ B cells gated in **C.** Statistical significance was determined by a Pearson correlation (**A**) or two-way ANOVA with Šidák's multiple testing correction (**D-E**).

3.2.10. *Ex vivo* lymph node slice cultures reveal Asn dependency in GC B and plasma cells

Unlike plasmablasts, *in vitro* culture systems for the generation of bona-fide GC B cells do not exist[49]. Moreover, *in vitro* culture systems lack the spatial complexity and cellular heterogeneity of lymphoid tissue and may therefore not reproduce normal immune cell dynamics. To this end, I designed a live lymph node slice *ex vivo* culture system to investigate how exogenous or synthesised Asn controlled effector B cells in a more physiological setting. Sliced lymph node culture systems have been used previously, and well-preserved cellular complexity and integrity have been noted over short culture periods[141].

I collected inguinal lymph nodes at day 14 from B-WT or B-Asns mice that were subcutaneously immunised with 4-hydroxy-3-nitrophenylacetyl-chicken gamma globulin (NP-CGG) in alum. Lymph node slices cut at 300µm were then cultured in the presence (400µM) or absence of Asn (0µM) for 20h (as illustrated in Fig. 3.11A). The next day, lymph node slices were homogenised, stained, and analysed by flow cytometry. Whilst total B and T cell proportions remained largely unaltered, GC B cells and plasma cells from B-Asns lymph nodes were significantly reduced after 20h of culture without Asn compared with the serially sectioned neighbour slice cultured with Asn (Fig. 3.11 B-C).

Based on the observation that GC B cells express ASNS and that B cells increase ASNS expression after stimulation, I hypothesised that ASNS may be protective against Asn limitation. I stimulated B-Asns or B-WT B cells in the presence of Asn, which was then withdrawn for a duration of 24 hours (Fig. 3.11D). Interestingly, unlike with the absence of Asn at the culture start, the subsequent removal had only minimal impact on B-WT B cells. In B-Asns B cells, however, this protective effect was significantly diminished (Fig. 3.11E). These results confirmed that the capacity to synthesise Asn through ASNS is required for GC B and plasma cells to adapt to Asn-restricted conditions *ex vivo*.

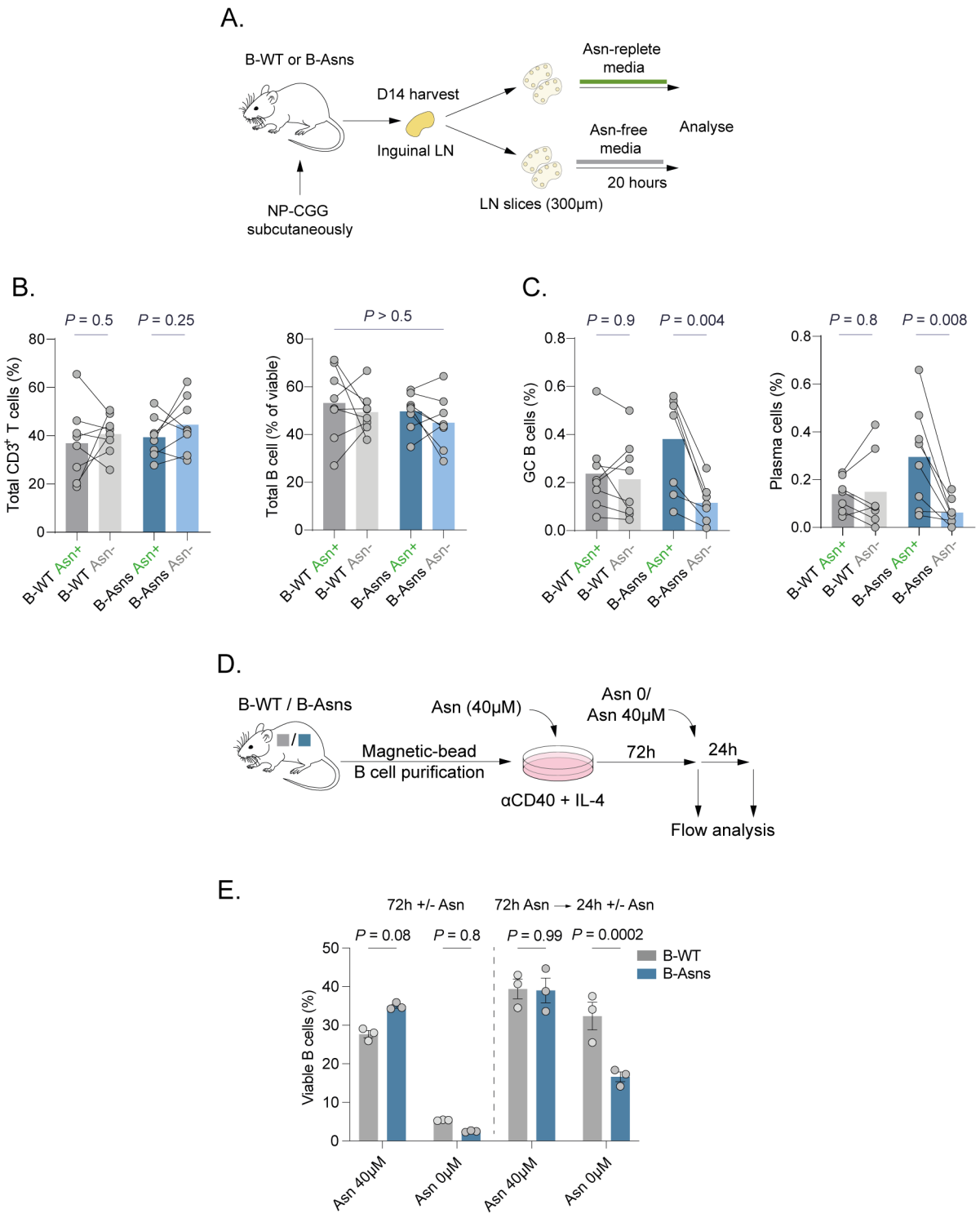


Figure 3.11. An ex vivo lymph node slicing culture platform reveals the physiological dependency of GC B and plasma cells on ASNS.
(A) Diagram illustrating the lymph node slice culture system. Immunisation of B-WT and B-Asns mice with NP-CGG in alum subcutaneously was performed, and inguinal lymph nodes were collected on day 14. Slices measuring 300µm in thickness were cultured for 20 hours in duplicate with or without Asn and then examined using flow cytometry. (B) Quantification of $CD19^+$ B cell and $CD3^+$ T cell proportions by flow cytometry in lymph node slices (300µm thick sections) cultured for 20h in the presence or absence of Asn (400µM) obtained from inguinal lymph nodes of B-WT and B-Asns mice immunised with NP-CGG (day 14). Each

dot represents a single lymph node. Data pooled from two independent experiments. (C) Quantification of $CD38^{-}$ $GL\text{-}7^{+}$ GC B cell and IgD^{-} $CD138^{+}$ plasma cell proportions by flow cytometry in lymph node slices cultured for 20h in the presence or absence of Asn (400μM). Each dot represents a single lymph node (n=8 lymph nodes from n=4 mice). Pooled from two independent experiments. (D) Illustration depicting the *in vitro* B cell activation culture system used for B cells. Viable B cells (10^5 cells) were isolated using magnetic beads and stimulated with IL-4 (10ng/ml) and anti-CD40 (5μg/ml) for 72 hours, with some cultured for an additional 24h while being exposed to different concentrations of Asn (0-40μM). (E) **Left panel:** viability of B cells from B-Asns and B-WT mice stimulated for 72h with IL-4 and anti-CD40 at the indicated concentration of Asn (40μM), data from **Fig 3.7C**. **Right panel:** viability of B cells stimulated with IL-4 and anti-CD40 with 40μM Asn for 72h, then restimulated for an additional 24h in the presence (40μM) or absence of Asn (n=3 mice). Data pooled from two independent experiments. Statistical significance was determined by a paired two-tailed t test (**B-C**) or two-way ANOVA with Šidák's multiple testing correction (**E**) (I would like to acknowledge the assistance of Dr. Joannah Ferguson with experiments in A-C)

3.2.11. The GC compartment is sensitive to asparagine depletion

Although *in vitro* and *ex vivo* experimental systems can closely approximate certain cellular features, the metabolic microenvironment and cellular physiology *in vivo* are distinctively complex. To examine the impact of Asn deprivation on B cell responses *in vivo*, I administered asparaginase (ASNase), a bacterial enzyme that rapidly degrades plasma Asn into Asp and is widely employed in clinical settings and murine models for leukaemia treatment[120]. I designed two treatment schedules (Fig. 3.12A). The 'standard' protocol entailed administering ASNase at a dose of 500 units per kg (approximately 10 units per mouse), starting one day before immunisation with SRBC. This was followed by four additional doses delivered every two days until analysis on day 9. The 'standard' regimen allowed for GC exposure to asparagine depletion throughout their development, establishment, and expansion. In contrast, the 'post-formation' schedule involved administering only two doses, on days six and eight after immunisation, specifically targeting already established GCs (Fig. 3.12A).

Treatment with ASNase was well-tolerated by the mice, with no noticeable adverse reactions, and it significantly reduced serum Asn levels without affecting glutamine (Fig. 3.12B).

I found that ASNase administration significantly impaired the GC response in B-Asns mice under both treatment regimens, leading to reduced proportions and numbers of GC B cells. In contrast, B-WT mice were unaffected by the post-formation regimen but remained susceptible to the ‘standard’ regimen (Fig. 3.12C-D). Additionally, the impact on naïve B cells was minimal. There was no apparent genotype effect, in keeping with the lack of ASNS expression in the naïve state (Fig. 3.12E).

Taken together, these findings indicate that GC B cells are highly vulnerable to environmental Asn deprivation, particularly when their capacity to produce Asn is targeted.

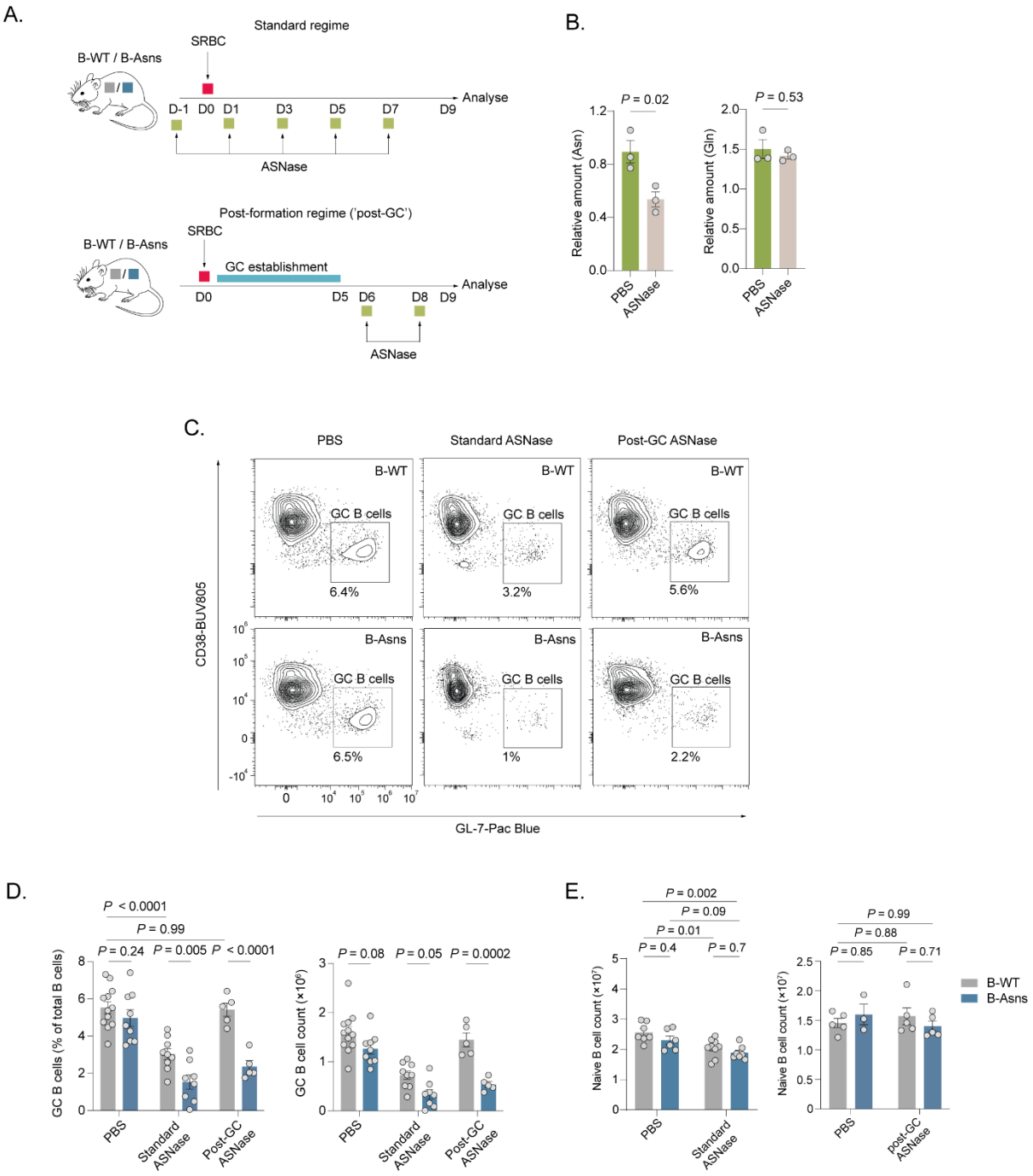


Figure 3.12. The GC compartment is sensitive to Asn depletion.
(A) Illustration depicting the *in vivo* administration regimes of ASNase. Under the standard regime, B-WT or B-Asns mice received intraperitoneal injections of ASNase (500U/kg: ≈10U/mouse) or PBS vehicle one day before being immunised with SRBC (day 0). These mice were then given repeated ASNase injections every two days until day 7. Spleens were collected on the ninth day and examined using immunohistochemistry and flow cytometry. Post-formation 'post-GC' regime: B-WT or B-Asns mice received intraperitoneal injections of SRBC on day 0 and were administered two injections of ASNase (500U/kg: ≈10U/mouse) or PBS on days 6 and 8. Analysis took place on day 9. (B) Quantification of serum Asn and Gln using LC-MS. Wild type mice were injected intraperitoneally with ASNase (500U/kg:

≈10U/mouse) or vehicle PBS. After 48 hours, the mice were bled and their sera were collected for LC-MS analysis of Asn and Gln. There were 3 pools of 1-2 wild type mice, with control samples. Representative of two independent experiments. (C) Day 9 post-immunization with SRBC, representative flow cytometry plot of GC B cells ($CD19^+CD38^-GL\text{-}7^+$) from B-WT and B-Asns mice treated with PBS, standard ASNase, or post-GC ASNase. (D) Quantification of splenic GC B cell proportions (% of $CD4^-CD19^+$ B cells) and counts as gated in **C**. Each data point represents a single mouse. Data pooled from four independent experiments. (E) Quantification of splenic naïve B cell ($CD19^+IgD^+GL\text{-}7^-$) counts from B-WT or B-Asns mice treated with ASNase (standard or post-GC) or PBS. Each point represents a single mouse. Data pooled from four independent experiments. Statistical significance was determined by a two-tailed unpaired t test (B) or two-way ANOVA with Šidák's (D) or Tukey's (E) multiple testing correction.

3.2.12. Asparagine availability regulates the spatial features of GCs.

After profiling the GC compartment via flow cytometry, I assessed GCs by IHC. This analysis was important for determining the precise role of Asn in key GC properties such as formation and expansion. Although B cell follicles identified by CD21/35 displayed mostly normal characteristics across all conditions, GC numbers significantly decreased in B-WT mice, with an even greater reduction observed in B-Asns mice, following standard ASNase treatment (Fig. 3.13A-B). This reduction was reversed in the post-GC schedule for B-WT mice and only partially for B-Asns mice, suggesting that early exposure to ASNase may impair GC formation or lead to premature GC termination. However, the remaining GCs in B-WT mice had a normal size distribution regardless of the treatment regimen, whether standard or post-GC formation (Fig. 3.13A-B). In contrast, the GC area in B-Asns mice was substantially reduced, indicating that, beyond its potential role in GC formation, ASNS is necessary for GC expansion in the face of asparagine deprivation.

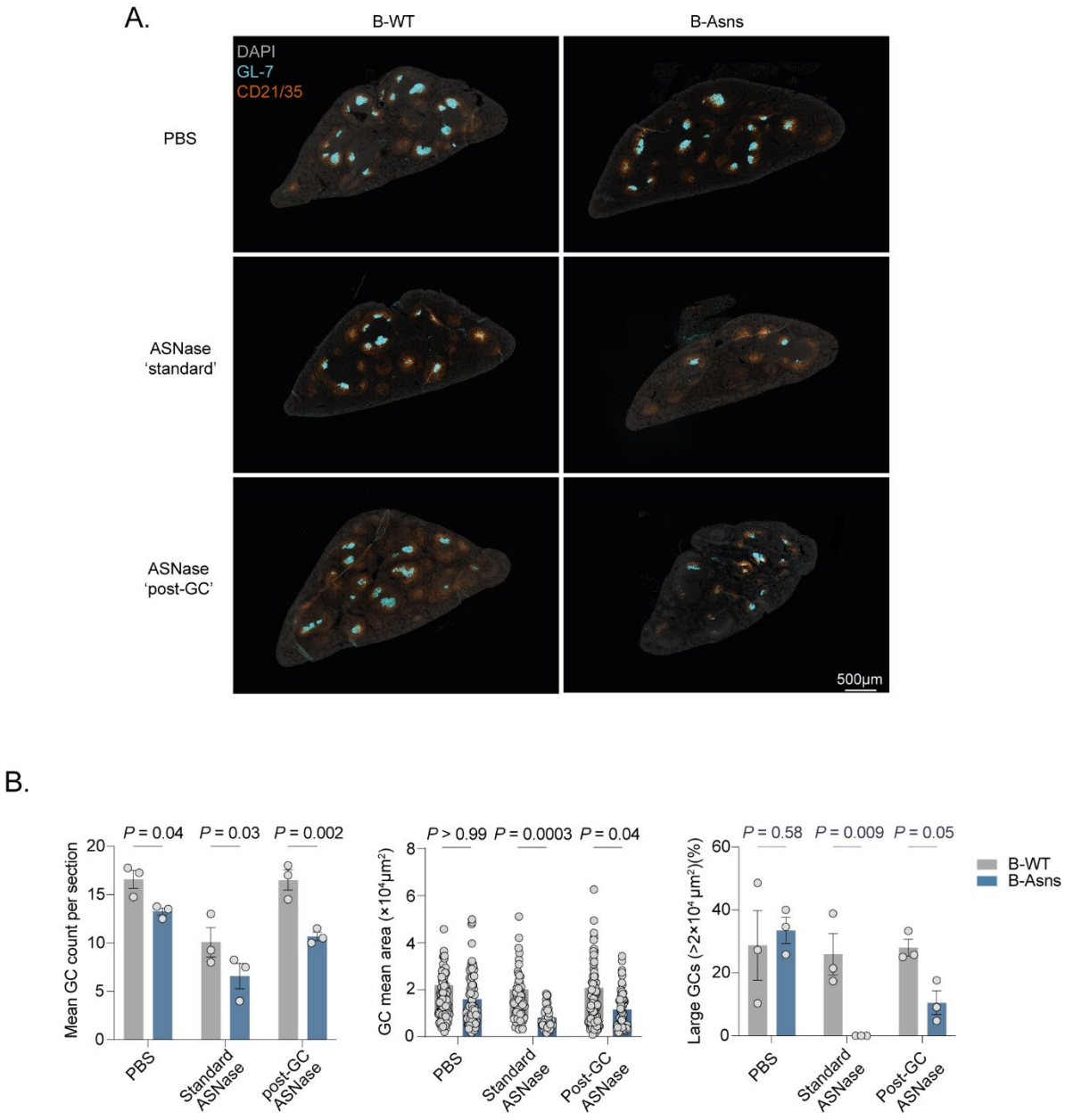


Figure 3.13. Asparagine availability regulates the spatial features of GCs.
(A) Immunohistochemistry of representative spleen sections (8µm) at day 9 post SRBC immunisation. GL-7 and CD21/35 highlights GCs and B cell follicles, respectively. DAPI is used as background staining. Scale bar 500µm. Data pooled from three independent experiments. (B) Image quantification of splenic GCs from **A**. **Left panel:** quantification of GC numbers per spleen sections (average of at least two non-serially cut sections). Each point represents a mouse. **Middle panel**: mean area of individual GCs (µm^2). Each data point represent a GC pooled from n=3 mice per condition. **Right panel:** frequency of GCs larger than 20,000µm^2 (0.02mm^2). Each data point indicates a mouse. n=3 from each condition. Data pooled from three independent experiments**.** Statistical significance was determined by two-way ANOVA with Šidák's multiple testing correction.

3.2.13. T follicular helper cells remain intact under Asn deprivation

The GCs contain $CD4^+$ T cell subsets that have regulatory functions. T_{FH} cells express high levels of the chemokine receptor CXCR5, which promotes T_{FH} participation in the GC LZ. A distinct subset of T_{FH} cells, called T_{FR} cells, suppress GC B cells and T_{FH} cells, thus limiting the GC reaction[142,143].

As T_{FH} and T_{FR} cells reside in GCs and share a microenvironment with GC B cells, their characterisation may address whether the dependence on Asn arises from the GC metabolic microenvironment or if GC B cells intrinsically require more Asn. Therefore, I quantified T_{FH} and T_{FR} cells in B-WT and B-Asns mice treated with ASNase as previously described (Fig. 3.12A) and found no proportional or numerical change in $Foxp3^-$ $CXCR5^+$ $PD\text{-}1^{hi}$ T_{FH} or $Foxp3^+$ $CXCR5^+$ $PD\text{-}1^{hi}$ T_{FR} cells across all experimental groups. This suggests a shared Asn-dependent metabolic program is less likely in GC-associated T cells (Fig. 3.14A-D). Additionally, in B-Asns mice treated with the post-GC formation regime, there was a significant reduction in GC B cells relative to T_{FH} numbers, indicating a targeted effect on the GC B cell compartment (Fig. 3.14E). Additionally, I have quantified the expression of key T_{FH} and T_{FR} functional molecules, including programmed cell death protein 1 (PD-1), Cytotoxic T-lymphocyte associated protein 4 (CTLA4), inducible costimulator (ICOS), B-cell lymphoma 6 (BCL6), and T-cell receptor beta (TCRβ) by flow cytometry[144]. These were not affected by ASNase or genotype (Fig. 3.14F). Collectively, these findings make a substantial T cell-mediated effect unlikely in GCs and highlight a more selective impairment of GC B cells following Asn depletion.

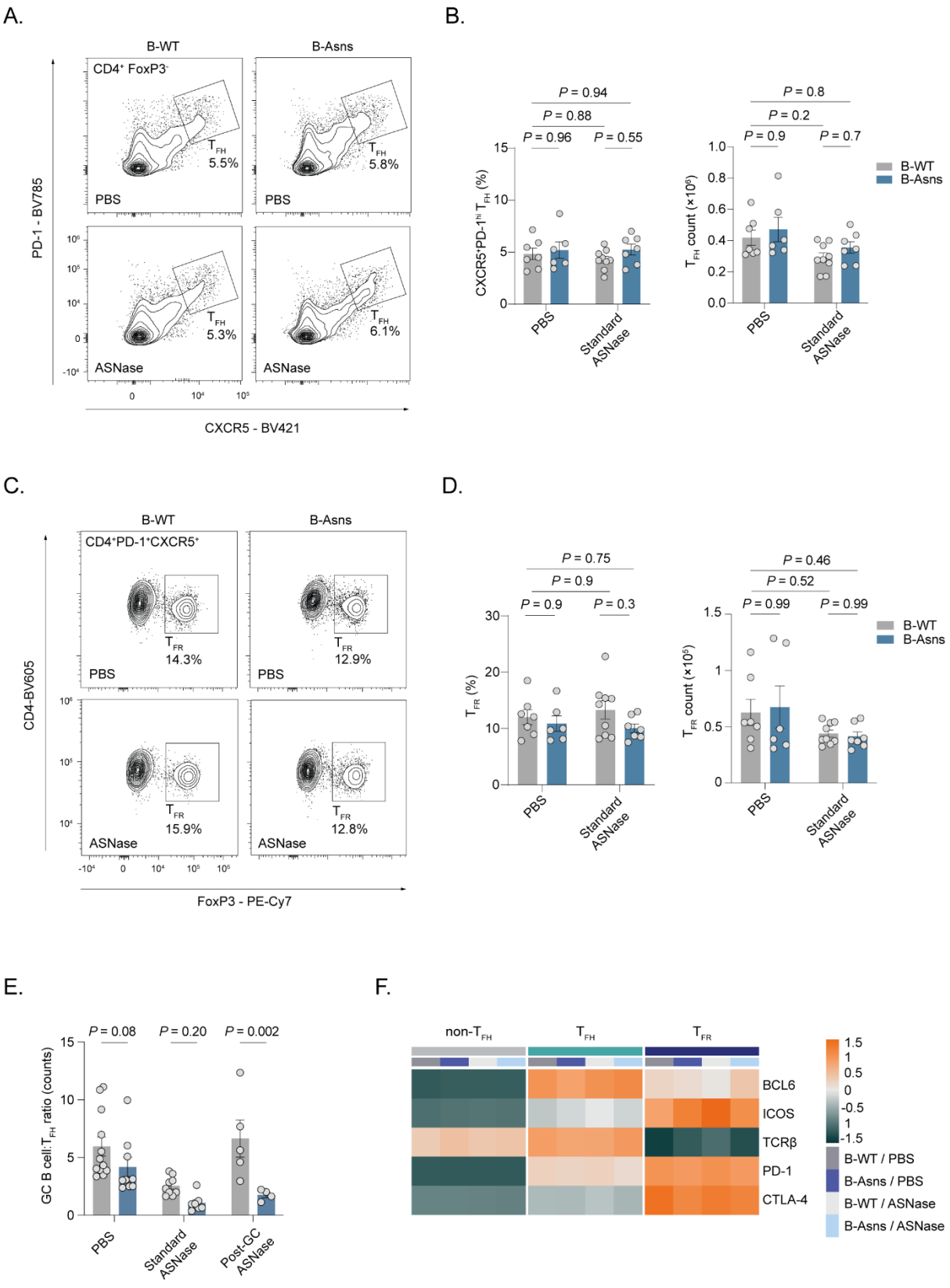


Figure 3.14. T follicular helper cells remain intact under Asn deprivation.
(A) Representative gating strategy for CD19$^-$CD4$^+$ Foxp3$^-$ CXCR5^{hi} PD-1$^+$ T_{FH} cells. (B) Quantification of T_{FH} cell numbers and frequency (% of CD19$^-$ CD4$^+$ Foxp3$^-$) at day 9 post

SRBC immunisation following standard ASNase or PBS treatment regime. Each point represents a single mouse. Data pooled from three experiments. (C) Representative gating strategy for $CD19^{-}CD4^{+}CXCR5^{+}PD\text{-}1^{+}Foxp3^{+}$ T_{FR} cells. (D) Quantification of T_{FR} ratio (% of $CD19^{-}CD4^{+}CXCR5^{+}PD\text{-}1^{+}$) and counts at day 9 post SRBC immunisation following standard ASNase or PBS treatment regime. Each point represents a single mouse. Data pooled from three experiments. (E) Quantification of the GC B cell numbers relative to T_{FH} numbers gated as $CXCR5^{hi}$ $PD\text{-}1^{+}$ within $CD19^{-}$ $CD4^{+}$ $FoxP3^{-}$ T cells. Each data point represents a single mouse. Data pooled from >3 independent experiments. (F) Heatmap of row z-scores for the gMFI values of indicated functional T_{FH}-T_{FR} proteins (BCL6 and CTLA4 measured intracellularly) in non-TFH ($CD19^{-}$ $CD4^{+}$ $PD\text{-}1^{-}$ $CXCR5^{-}$), T_{FH} ($CD19^{-}$ $CD4^{+}$ $FoxP3^{-}$ $CXCR5^{+}$ $PD\text{-}1^{+}$), T_{FR} ($CD19^{-}$ $CD4^{+}$ $FoxP3^{+}$ $CXCR5^{+}$ $PD\text{-}1^{+}$), measured by flow cytometry at day 9 SRBC immunisation following post-GC ASNase regime (mean of n = 4-5 mice each condition). Data are pooled from two independent experiments. Statistical significance was determined by two-way ANOVA with Tukey's multiple testing correction (B,D) or Šidák's multiple testing correction (E)

3.2.14. Asn deprivation alters GC B cell dynamics

Having ruled out potential T cell defects under Asn deprivation, I proceeded to assess GC B cell function. GC B cells undergo dynamic proliferative phases throughout the GC reaction, and their cyclic distribution between the DZ and LZ is an important indicator of normal GC homeostasis[145]. Next, I profiled GC subcompartments using flow cytometry (as described in Fig. 3.2G) and found that ASNase-treated B-Asns mice showed a substantial fall in DZ GC B cells, but an increase in cells with a 'grey zone' (GZ) phenotype ($CXCR4^{hi}$ $CD86^{hi}$) (Fig. 3.15A-D). The GZ is the compartment of peak cell proliferation in the GC[146], characterised by elevated levels of the cell cycle protein cyclin B1, which was correspondingly elevated in B-Asns GC B cells (Fig. 3.15E). Flow cytometric analysis of GC B cells did not reveal any abnormality at the S phase as determined by the incorporation of the thymidine analogue 5-Ethynyl-2′-deoxyuridine (EdU) within 2 h following *in vivo* administration. Conversely, EdU^{+} GC B cells were proportionally elevated in B-Asns mice in conditions of Asn-deprivation (Fig. 3.15F-G). Within EdU^{+} GZ GC B cells, there were significantly fewer mitotic cells in B-Asns mice given ASNase, identified by phosphorylation of histone 3 (H3) protein on Ser10, an event which specifically occurs upon mitotic entry[147]. Mitotic cells were largely absent in the LZ, further confirming the specificity of the flow strategy (Fig. 3.15H).

These findings therefore suggest that Asn availability affects GC B cell dynamics and mitotic progression.

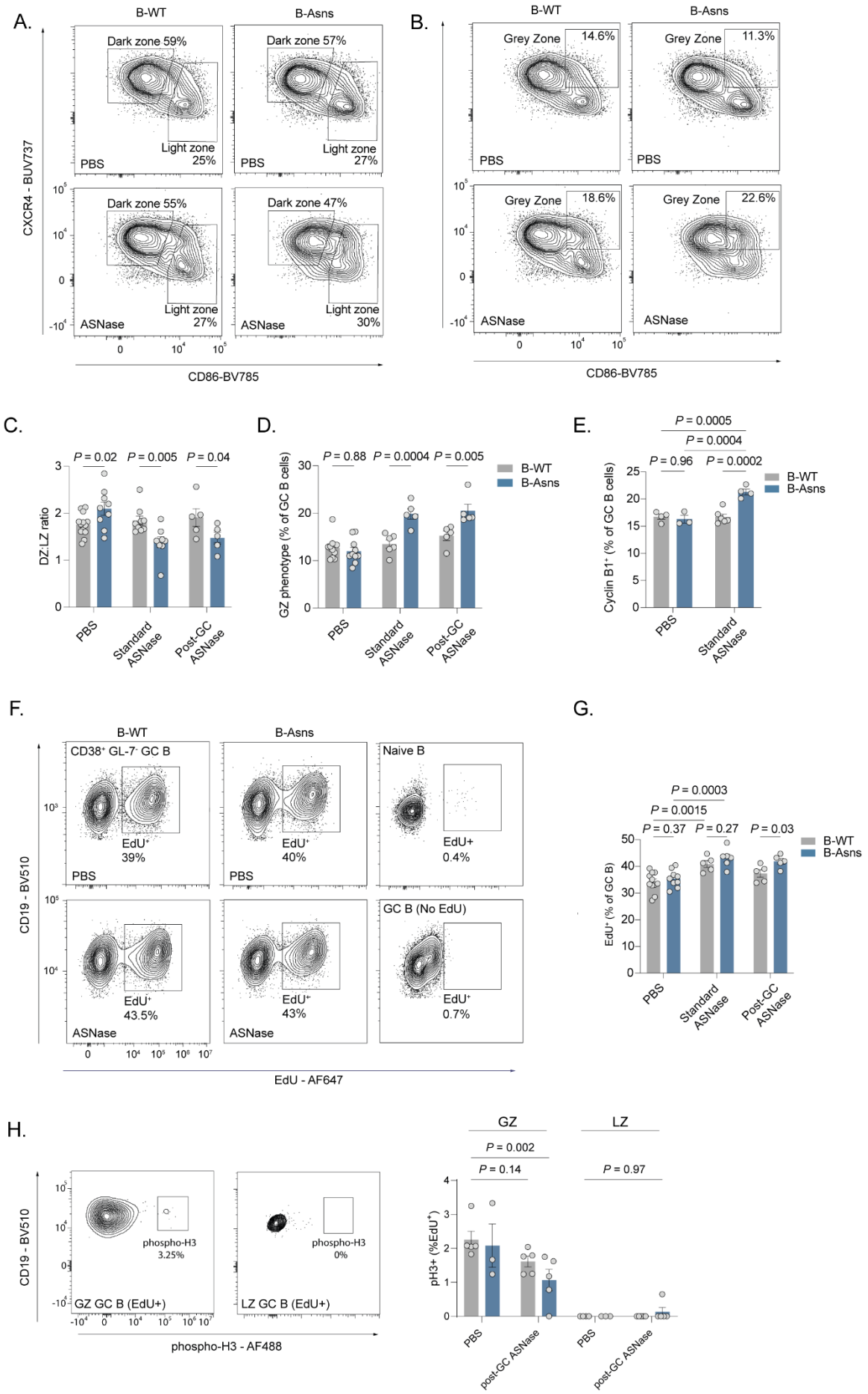

A.
B-WT
B-Asns
Dark zone 59%
Light zone 25%
Dark zone 57%
Light zone 27%
PBS
Dark zone 55%
Light zone 27%
Dark zone 47%
Light zone 30%
ASNase
CXCR4 - BUV737
CD86-BV785
B.
Grey Zone 14.6%
Grey Zone 11.3%
Grey Zone 18.6%
Grey Zone 22.6%
C.
P = 0.02
P = 0.005
P = 0.04
DZ:LZ ratio
PBS
Standard ASNase
Post-GC ASNase
D.
P = 0.88
P = 0.0004
P = 0.005
GZ phenotype (% of GC B cells)
B-WT
B-Asns
E.
P = 0.0005
P = 0.0004
P = 0.96
P = 0.0002
Cyclin B1+ (% of GC B cells)
F.
CD38+ GL-7+ GC B
Naive B
GC B (No EdU)
EdU+ 39%
EdU+ 40%
EdU+ 0.4%
EdU+ 43.5%
EdU+ 43%
EdU+ 0.7%
CD19 - BV510
EdU - AF647
G.
P = 0.0003
P = 0.0015
P = 0.37
P = 0.27
P = 0.03
EdU+ (% of GC B)
H.
phospho-H3 3.25%
phospho-H3 0%
GZ GC B (EdU+)
LZ GC B (EdU+)
phospho-H3 - AF488
GZ
LZ
P = 0.002
P = 0.14
P = 0.97
pH3+ (%EdU+)
post-GC ASNase

Figure 3.15. Asn deprivation alters GC B cell dynamics.

(A) Representative flow cytometry plots of light zone ($CD86^{hi}CXCR4^{lo}$) and dark zone ($CD86^{lo}CXCR4^{hi}$) GC B cells. (B) Representative flow cytometry plots of grey zone ($CD86^{hi}CXCR4^{hi}$) GC B cells. (C) Quantification of DZ:LZ ratio. Data pooled from >3 independent experiments. (D) Quantification of the proportion of the grey zone (GZ) ($CD86^{hi}CXCR4^{hi}$) GC B cells (as % of GC B cells). Data pooled from >3 independent experiments. (E) Quantification of cyclin $B1^{+}$ GC B cells following standard ASNase regime or PBS control. Data representative of two independent experiments. (F) B-WT or B-Asns mice were treated with standard or post-GC ASNase regimes as described in **A**. On day 9 post-SRBC immunisation, mice were pulsed with 1mg EdU intraperitoneally and two hours later EdU incorporation in splenic GC B cells was analysed by flow cytometry. Representative gating strategy for the EdU^{+} GC B cell fraction with negative controls. (G) Quantification of **G.** Data pooled from four independent experiments. (H) Representative flow cytometry plots and quantification of phosphor-Histone 3 (Ser10) mitotic GC B cells in EdU^{+} GZ and LZ as gated in **A**, **B** and **F.** Statistical significance was determined by two-way ANOVA with Šidák's multiple testing correction.

3.2.15. Exogenous Asn is required for humoral responses

Immunogenic challenges induce two types of antibody-secreting cell output. The extrafollicular component of this response occurs a few days after immunisation and rapidly produces plasmablasts, which are responsible for the IgM peak typically observed within the first week. The more delayed antibody wave is mediated by plasma cell clones originating from the GC reaction[138].

Using flow cytometry, I characterised the plasmablast compartment formed after SRBC immunisation. With the standard ASNase regime, B-WT and B-Asns mice showed substantially impaired plasmablast differentiation with no effect of genotype. Surprisingly, a genotype difference only occurred following the post-GC ASNase treatment (Fig. 3.16 A-B).

To examine antibody dynamics, I immunised B-WT or B-Asns mice with the model protein antigen NP-CGG. Following NP-CGG immunisation, serum was collected on day 14 from B-WT and B-Asns mice that were given ASNase at days 6, 9, and 12 (post-GC regime) (Fig. 3.16C). NP-CGG induces a long-lasting GC response allowing affinity maturation, a process that predominantly occurs after the first week following T-dependent immunisation.

Detection of affinity maturation involves measuring the relative binding capacity of class-switched IgG antibodies to low-conjugation NP-BSA (NP_2) versus high conjugation (NP_{20}) via ELISA[148]. While predominantly high-affinity antibodies resulting from affinity maturation, hence GC-derived, can bind to the former, both low and high-affinity antibodies can bind to the latter (Fig. 3.16D). Notably, IgM antibodies, generated by plasmablasts of extrafollicular origin, do not undergo affinity maturation.

I then evaluated affinity maturation through anti-NP antibody production after NP-CGG immunisation in mice given post-GC formation ASNase. NP-specific IgM levels were slightly lower in B-Asns mice given ASNase although lack of statistical significance was noted (Fig. 3.16E). Anti NP_{20} IgG1 showed a similar but significant trend with an evident compensatory effect of ASNS against ASNase in B-WT sera (Fig. 3.16F). Surprisingly however, GC-derived high-affinity anti-NP_2 IgG1 and the corresponding affinity maturation index (NP_2:NP_{20}) were substantially reduced even in B-WT mice, in which we had not observed a decrease in GC B cell numbers (Fig. 3.16G-H). This suggests that the compensatory capacity of ASNS has limits in affinity maturation.

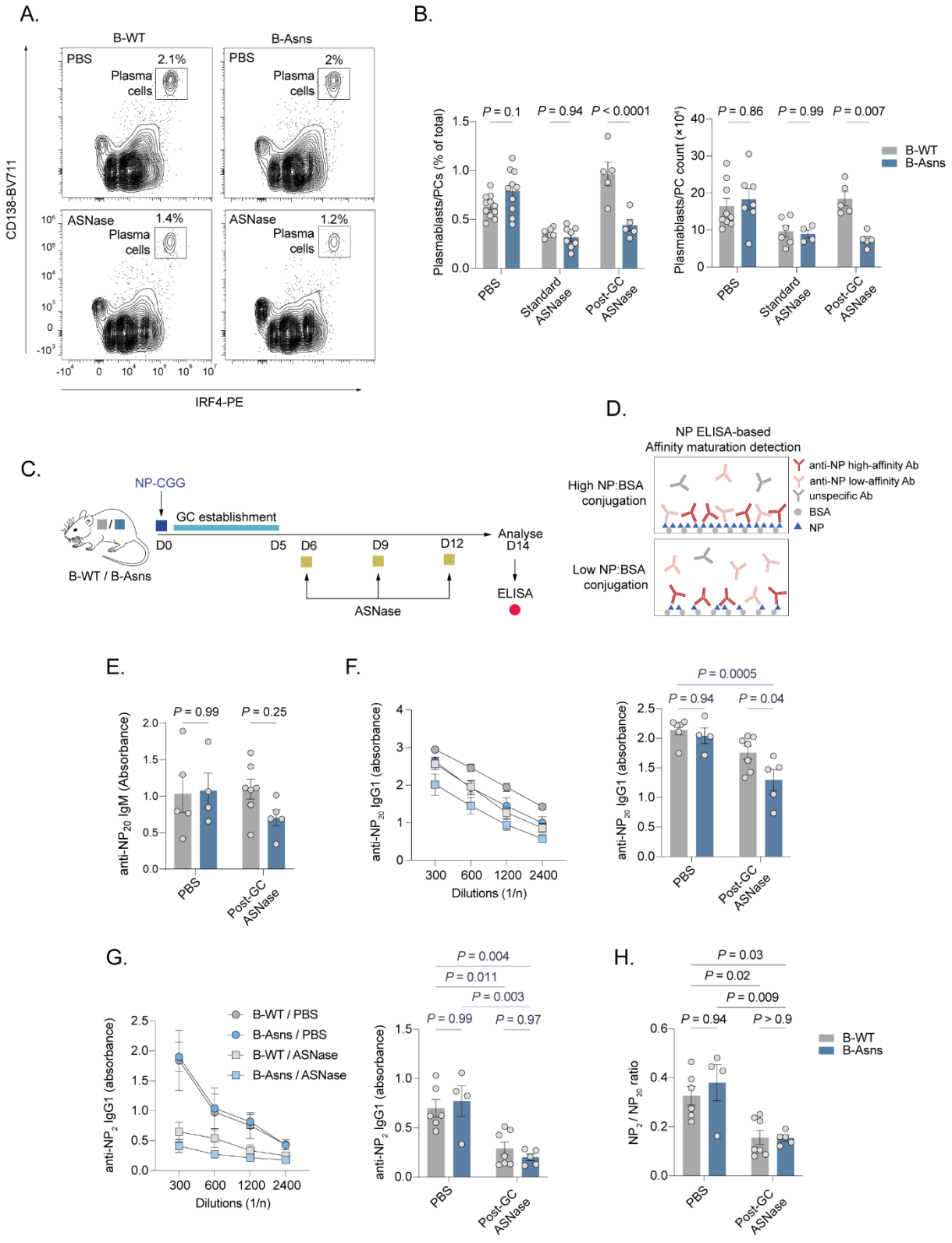

A.
B-WT
B-Asns
PBS
2.1%
Plasma cells
2%
ASNase
1.4%
1.2%
CD138-BV711
IRF4-PE
B.
Plasmablasts/PCs (% of total)
P = 0.1
P = 0.94
P < 0.0001
Plasmablasts/PC count (×10⁴)
P = 0.86
P = 0.99
P = 0.007
PBS
Standard ASNase
Post-GC ASNase
B-WT
B-Asns
C.
NP-CGG
GC establishment
B-WT / B-Asns
D0
D5
D6
D9
D12
Analyse D14
ELISA
ASNase
D.
NP ELISA-based Affinity maturation detection
High NP:BSA conjugation
Low NP:BSA conjugation
anti-NP high-affinity Ab
anti-NP low-affinity Ab
unspecific Ab
BSA
NP
E.
anti-NP20 IgM (Absorbance)
P = 0.99
P = 0.25
F.
anti-NP20 IgG1 (absorbance)
Dilutions (1/n)
P = 0.0005
P = 0.94
P = 0.04
G.
anti-NP2 IgG1 (absorbance)
B-WT / PBS
B-Asns / PBS
B-WT / ASNase
B-Asns / ASNase
P = 0.004
P = 0.011
P = 0.003
P = 0.99
P = 0.97
H.
NP2 / NP20 ratio
P = 0.03
P = 0.02
P = 0.009
P = 0.94
P > 0.9

Figure 3.16. Exogenous Asn is required for humoral responses.

(A) Representative gating strategy for plasma cells as IgD^- $IRF4^+$ $CD138^+$. (B) Quantification of $IgD^-IRF4^+CD138^+$ splenic plasmablast/plasma cell proportions (% of total) and absolute counts. Each data point represents a single mouse. Data pooled from >3 independent experiments. (C) Schematic of *in vivo* ASNase administration regime for affinity maturation detection. B-WT or B-Asns mice were subcutaneously injected with 50µg NP-CGG precipitated in Alum hydrogel (1:1) subcutaneously on both flanks and given three ASNase (500U/kg: ≈10U/mouse) or PBS injections at day 6, 9, and 12 followed by serum collection at day 14 for ELISA. (D) Diagram illustrating NP-based affinity maturation detection by ELISA. (E) ELISA quantification of IgM anti-NP antibodies ($NP_{>20}$-BSA) at day 14, n=4-7 mice for each condition. Data pooled from two independent experiments. (F) Dilution curve and ELISA quantification of IgG1 anti-NP antibodies ($NP_{>20}$-BSA) at day 14, n=4-7 mice each condition. Data pooled from three independent experiments. (G) Dilution curve and ELISA quantification of IgG1 anti-NP antibodies ($NP_{>2}$-BSA) at day 14, n=4-7 mice each condition. Data pooled from three independent experiments. (H) ELISA quantification of NP_2:NP_{20} ratio at day 14, n=4-7 mice for each condition. Data pooled from two independent experiments. Statistical significance was determined by two-way ANOVA with Šidák's multiple testing correction.

3.2.16. *Asns*-deficient GC B cells are less competitive under Asn restriction

Studies in the literature have reported that an isocaloric diet, which is specifically devoid of asparagine (Asn-free diet), can significantly decrease serum asparagine levels[125,149]. To investigate the requirement for Asn in a more physiologically relevant regimen and over an extended period, I restricted environmental asparagine *in vivo* through dietary means. I established mixed bone marrow chimeras using congenic CD45.1 wild type and either CD45.2 B-Asns or B-WT bone marrow to further refine the experimental system as potential cage effects or differences in food consumption could be confounding. This experimental setup was designed to allow competition between wild type and *Asns*-deficient B cells in a shared microenvironment *in vivo*, where they were exposed to identical Asn levels. Following an 8-week period of bone marrow reconstitution, mice were assigned to either an Asn-free or standard diet group and fed with the assigned diet for 12 days. Subsequently, they were immunised with SRBC, and then examined after an additional 9 days of dietary modification (Fig. 3.17A).

Notably, the relative proportion of GC B cells within CD45.2 B-Asns cells markedly decreased in mice on an asparagine-free diet, in keeping with my observations from ASNase intervention experiments (Fig. 3.17B-C). The IHC analysis of splenic GCs confirmed the diminished contribution of CD45.2 B-Asns cells to the GL-7^{+} GC compartment compared with CD45.2 B-WT cells in recipients of Asn-free diet (Fig. 3.17D). Overall, these findings suggest that B-Asns GC B cells are at a competitive disadvantage following dietary asparagine restriction, largely mirroring the effects of ASNase treatment.

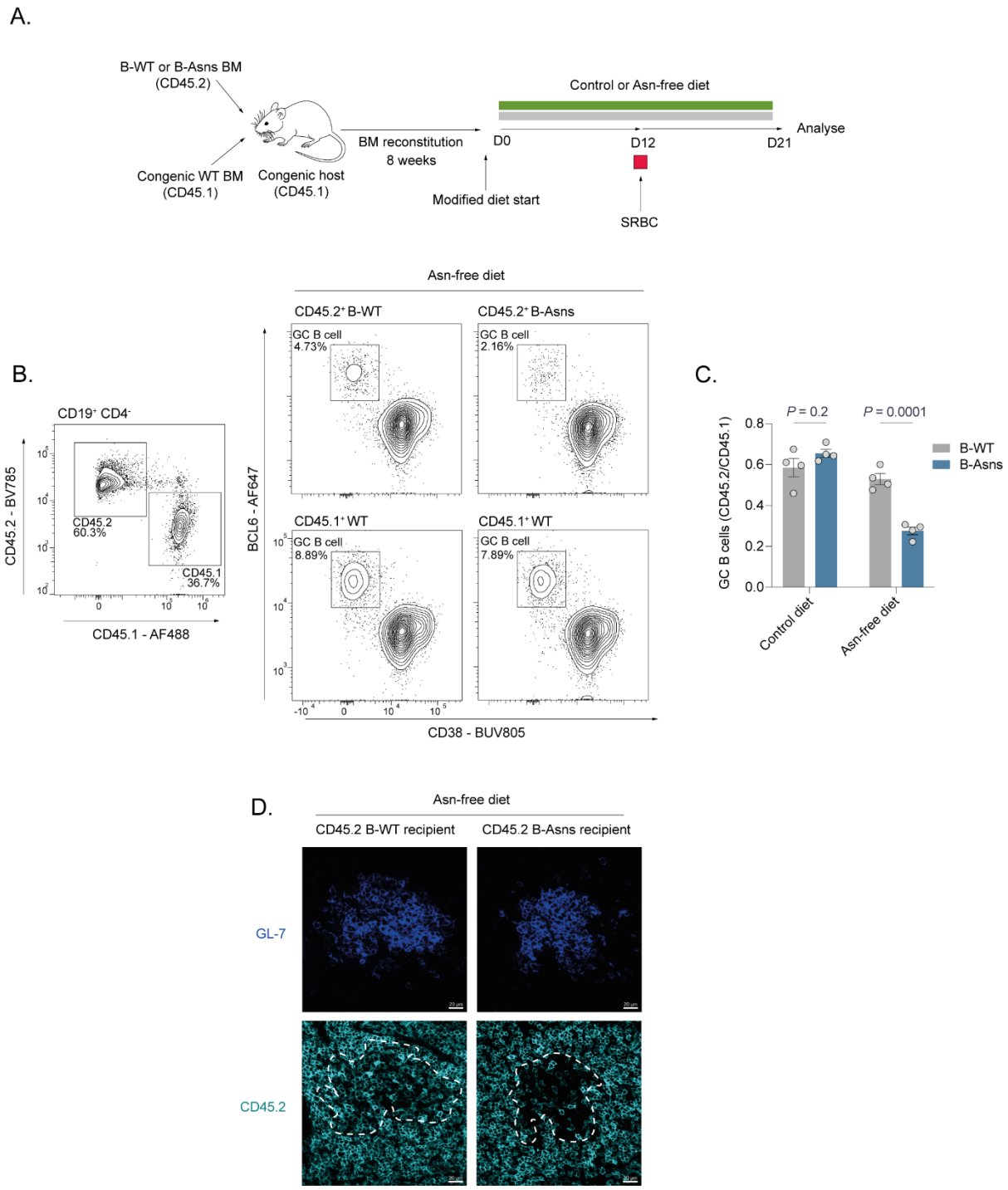


Figure 3.17. *Asns*-deficient GC B cells are less competitive under Asn restriction

(A) Schematic of bone marrow (BM) chimera/dietary modification experiment. Mixed BM chimeras were generated with B-WT (CD45.2) or B-Asns (CD45.2) and CD45.1 wild type BM, with n=4 congenic CD45.1 recipient mice for each condition. After an 8-week reconstitution period, mice were transferred to a control (Asn-replete) or Asn-deficient diet for 12 days, before immunisation with SRBC. Spleens were analysed 9 days after immunisation. (B) Representative flow cytometry plots of splenic GCs ($CD38^{-}BCL\text{-}6^{+}$) from recipients of CD45.1 WT and CD45.2 B-WT or CD45.2 B-Asns cells, given an Asn-free diet

as described in **A**. (C) Ratio of splenic GC B cells in CD45.2$^+$ B cells normalised to CD45.1$^+$ WT counterparts from bone marrow chimeric mice as described in **A**. Each data point represents a single mouse. Data pooled from two independent experiments. (D) Representative IHC images of splenic GCs (GL-7$^+$) from recipients of CD45.1 WT and CD45.2 B-WT or B-Asns cells subjected to Asn-free diet as described in **A**. Scale bar 20μm. Statistical significance was determined by two-way ANOVA with Šidák's multiple testing correction.

3.2.17. Dietary Asn restriction disrupts the function of GC B cells lacking ASNS

The GC reaction promotes the development and persistence of GC B cell clones that are specific to antigens, leading to their gradual accumulation over time[8]. Thus, the antigen specificity within GC B cells is an important measure of normal GC B cell function. A study previously reported the binding of GC B cells to fluorescently labelled SRBCs as a measure of antigen specificity following SRBC immunisation[150]. Using a similar approach with my bone marrow chimera cohort, I found a marked reduction in GC B cells of CD45.2 B-Asns origin that have a high binding capacity for SRBC in recipient mice given an Asn-free diet (Fig. 3.18A-C). However, SRBC-binding remained unchanged in control CD45.1 WT GC B cells across all conditions. Binding was negligible in naïve B cells. This further supports a selective and specific SRBC-binding defect in Asn-deprived B-Asns GC B cells (Fig. 3.18D-E) and highlights a disruption in the development of antigen-specific clones under the combined deficiency of ASNS and environmental asparagine.

The ratio of DZ to LZ B cells was compromised in B-Asns GC B cells following treatment with an Asn-free diet (Fig. 3.18F). Splenic plasma cells originating from B-Asns donors were also significantly reduced when Asn was limited through a defective diet (Fig. 3.18G). Overall, these results replicate the findings observed with ASNase treatment and underpin the requirement for ASNS in regulating the dynamic homeostasis of GC B cells when dietary Asn intake is limited.

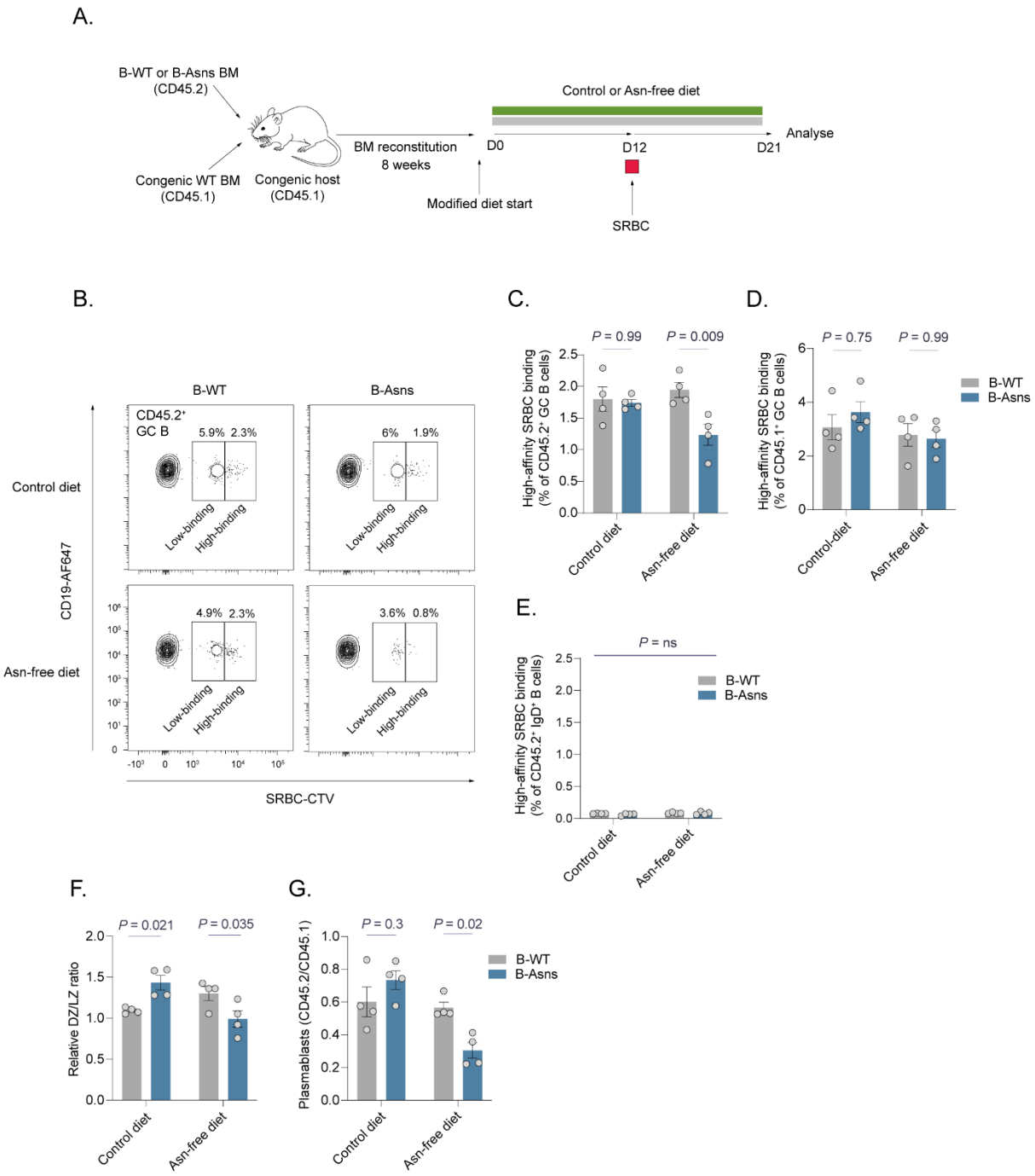


Figure 3.18. Dietary Asn restriction disrupts the function of GC B cells lacking ASNS

(A) Diagram of BM chimera system and the following dietary modification setup as described in Fig. 3.16A. (B) Representative high and low binding fractions of CD45.2 GC B cells from bone marrow (BM) chimeric recipient mice to SRBCs labelled with CTV. (C) Ratio of splenic CD45.2$^+$ SRBC-binding (high-binding as described in **B**) GC B cells from bone marrow chimeric mice as described in A. Data pooled from two independent experiments. (D) Ratio of splenic CD45.2$^+$ SRBC-binding (high-binding as described in B) naïve B cells (IgD$^+$ GL-7$^-$). Data pooled from two independent experiments. (E) Ratio of splenic CD45.1$^+$ SRBC-binding (high-binding as described in B) WT GC B cells. Data pooled from two

independent experiments. (F) Ratio of DZ:LZ in CD45.2$^+$ GC B cells normalised to CD45.1$^+$ WT counterparts from bone marrow chimeric mice as described in A. Data pooled from two independent experiments. (G) Ratio of splenic plasma cells (CD138$^+$IRF4$^+$) in CD45.2$^+$ cells normalised to CD45.1$^+$ WT counterparts from bone marrow chimeric mice as described in A. Data pooled from two independent experiments. Statistical significance was determined by two-way ANOVA with Šidák's multiple testing correction.

3.2.18. Asn is required for antibody homeostasis

Given the observed plasma cell defect in bone marrow chimeras, I investigated the effect of dietary asparagine (Asn) restriction on antibody responses. For 12 days, I placed non-chimeric B-WT or B-Asn mice on either an Asn-free or control diet (Fig. 3.19A). First, serum samples were collected to assess baseline antibody levels by ELISA without any immunogenic challenge (Fig. 3.19A). The changes in the total circulating immunoglobulin profile were apparent following 12 days of dietary modification (Fig. 3.19B). A significant reduction in total IgG levels was noted in B-Asns mice fed an Asn-free diet compared to B-WT controls. A similar declining trend in IgG1 was also present, but total IgM did not significantly change (Fig. 3.19B).

I next evaluated antigen-specific antibody responses. The hapten–high molecular weight polysaccharide conjugate 4-hydroxy-3-nitrophenyl-Ficoll (NP-Ficoll) is a widely used immunogen known to typically induce extrafollicular antibody responses with minimal interference from GCs, which also lack T_{FH} cells[151,152]. I assigned B-WT and B-Asns mice to either a control or Asn-free diet for 12 days, which was followed by immunisation with NP-Ficoll. On day 7 post-immunisation, serum was collected to measure antibodies specific to NP (Fig. 3.19C). There was a strong and significant reduction in anti-NP IgM levels specifically in B-Asns mice under Asn deprivation (Fig. 3.19D). However, the primary isotype-switched class, IgG3 antibodies, did not show a significant change, although a downward trend was observed in B-Asns mice on an Asn-free diet (Fig. 3.19D).

These results collectively suggest that both global and antigen-specific immunoglobulin compartments are sensitive to Asn.

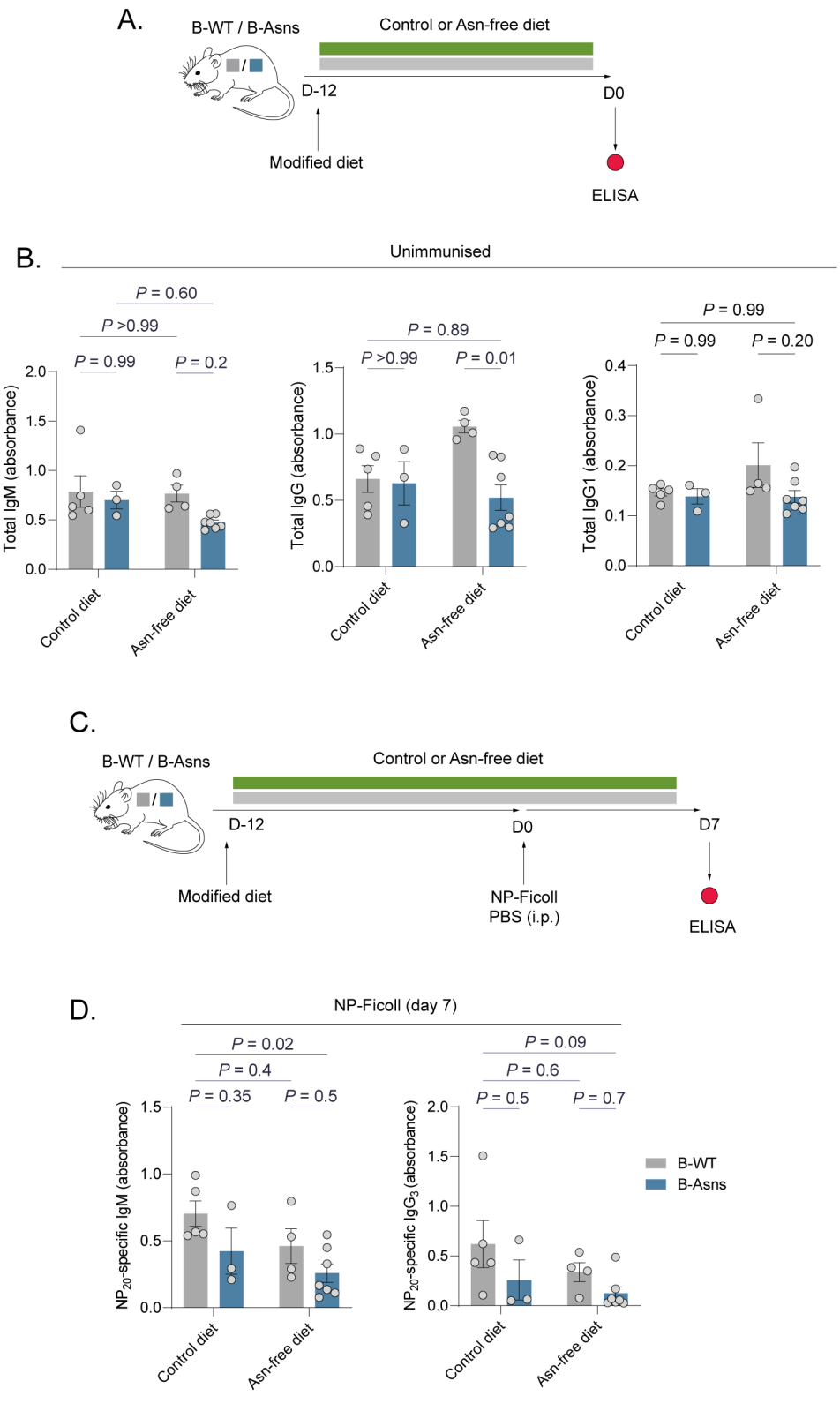

A.
B-WT / B-Asns
Control or Asn-free diet
D-12
D0
Modified diet
ELISA
B.
Unimmunised
P = 0.60
P >0.99
P = 0.99
P = 0.2
Total IgM (absorbance)
Control diet
Asn-free diet
P = 0.89
P >0.99
P = 0.01
Total IgG (absorbance)
P = 0.99
P = 0.99
P = 0.20
Total IgG1 (absorbance)
C.
B-WT / B-Asns
Control or Asn-free diet
D-12
D0
D7
Modified diet
NP-Ficoll
PBS (i.p.)
ELISA
D.
NP-Ficoll (day 7)
P = 0.02
P = 0.4
P = 0.35
P = 0.5
NP20-specific IgM (absorbance)
P = 0.09
P = 0.6
P = 0.5
P = 0.7
NP20-specific IgG3 (absorbance)
B-WT
B-Asns

Figure 3.19. Asn is required for antibody homeostasis.

(A) Diagram of diet modification. Unimmunised B-WT or B-Asns mice were given an Asn-free or control diet for 12 days, and serum was collected for ELISA quantification. (B) ELISA quantification of total steady-state IgM, IgG, and IgG1 levels. (C) Schematic of NP-Ficoll/dietary modification experiment. B-WT or B-Asns mice were assigned to either an Asn-free or control diet (Asn-replete) for 12 days, before immunisation with 50µg NP-Ficoll in PBS (1:1) intraperitoneally. Mice were bled on day 7 for ELISA detection. (D) ELISA quantification of anti-NP_{20} IgM and IgG3 antibodies at day 7 post-NP-Ficoll immunisation. Each point represents a single mouse. Data pooled from two independent experiments. Statistical significance was determined by two-way ANOVA with Šidák's multiple testing correction.

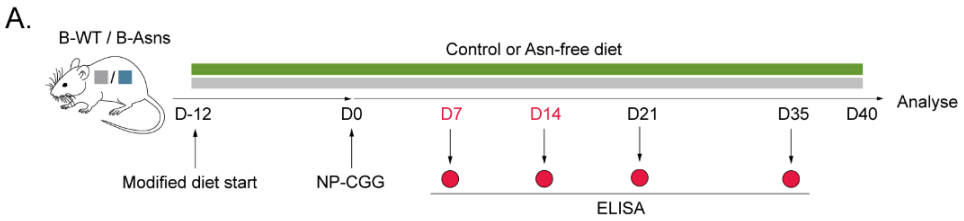
3.2.19. Affinity maturation is influenced by dietary Asn intake

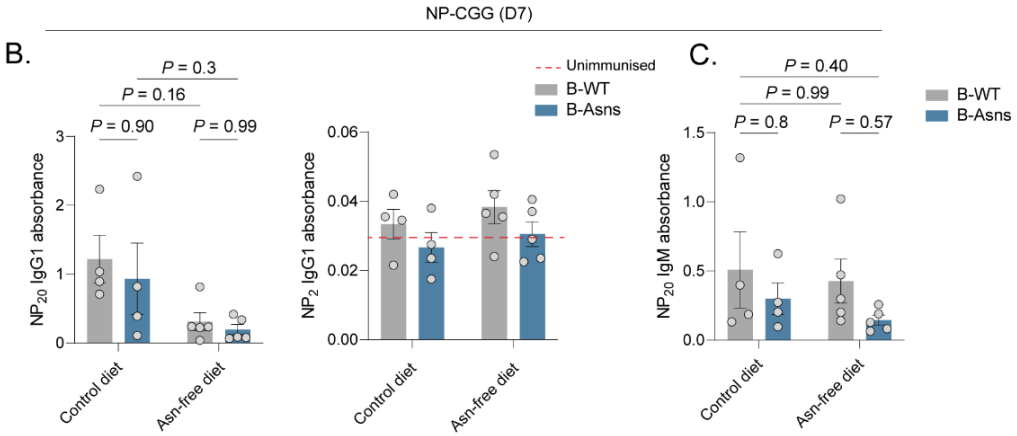
SHM introduces random mutations into the heavy chain variable region of BCR (*Ighv*) leading to enhanced affinity in selected clones, which is then reflected in the antibody binding[148]. To examine affinity maturation, I immunised B-WT or B-Asns mice subjected to dietary modification with a model protein antigen NP-CGG. Following immunisation, serum was collected at weekly intervals for ELISA analyses (Fig. 3.20A).

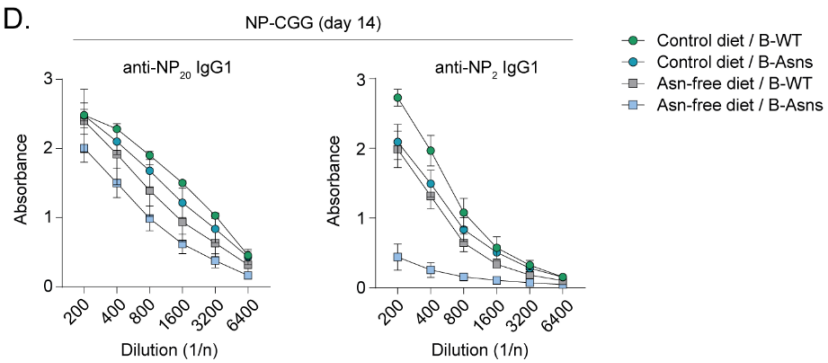
Unlike NP-Ficoll, NP-CGG induces long-lasting GCs containing T_{FH}, thus, allowing for affinity maturation, which typically takes place after the initial week following T-dependent immunisation[153].

At day 7, although not statistically significant, there was a trend towards lower levels of IgG1 antibodies binding to high-conjugation NP-BSA (NP_{20}) in mice fed an Asn-free diet, independent of genotype (Fig. 3.20B). As expected, the levels of high-affinity IgG1 anti-NP antibodies, binding to low-conjugation NP-BSA (NP_2), did not show a substantial increase in any of the groups over the unimmunised serum control. This indicates that GCs are too premature at day 7 to support high SHM rates (Fig. 3.20B). The levels of anti-NP IgM antibodies showed a similar trend with some genotype effect, resembling the NP-Ficoll-induced antibody responses. However, it did not pass the threshold of statistical significance (Fig. 3.20C).

At day 14, I observed a more settled antibody profile. High-affinity NP_2-binding antibodies were notably detectable unlike day 7. Dilution curves generated from serially diluted sera revealed lower levels of IgG1 anti-NP antibodies binding to the high conjugated version of NP-BSA (NP_{20}) in B-Asns mice deprived of Asn (Fig. 3.20D). There was a much more significantly reduced binding to low-conjugation NP_2, reflecting defective affinity maturation, a phenotype also observed to some extent in B-WT mice on an Asn-free diet (Fig. 3.20E). The relative quantification of NP_2 to NP_{20} binding suggested significantly impaired affinity maturation in B-WT mice following Asn restriction, in keeping with the much stronger defect seen with ASNase, and to a much greater degree in B-Asns mice that were given an Asn-free diet (Fig. 3.20F). NP-specific IgM levels indicative of the extrafollicular response remained minimally changed across all conditions, likely owing to adaptations developed after the peak period of extrafollicular response (Fig. 3.20G). Overall, these results suggest that Asn is required for effective affinity maturation not only in B-Asns but also in wild type mice. When B cells have a defective capacity to synthesise asparagine, asparagine limitation substantially disrupts the emergence of high-affinity antibodies during the peak GC response.


A.
B-WT / B-Asns
Control or Asn-free diet
D-12
D0
D7
D14
D21
D35
D40
Analyse
Modified diet start
NP-CGG
ELISA


NP-CGG (D7)
B.
C.
P = 0.3
P = 0.16
P = 0.90
P = 0.99
Unimmunised
B-WT
B-Asns
NP20 IgG1 absorbance
NP2 IgG1 absorbance
Control diet
Asn-free diet
P = 0.40
P = 0.99
P = 0.8
P = 0.57
NP20 IgM absorbance


D.
NP-CGG (day 14)
anti-NP20 IgG1
anti-NP2 IgG1
Absorbance
Dilution (1/n)
Control diet / B-WT
Control diet / B-Asns
Asn-free diet / B-WT
Asn-free diet / B-Asns

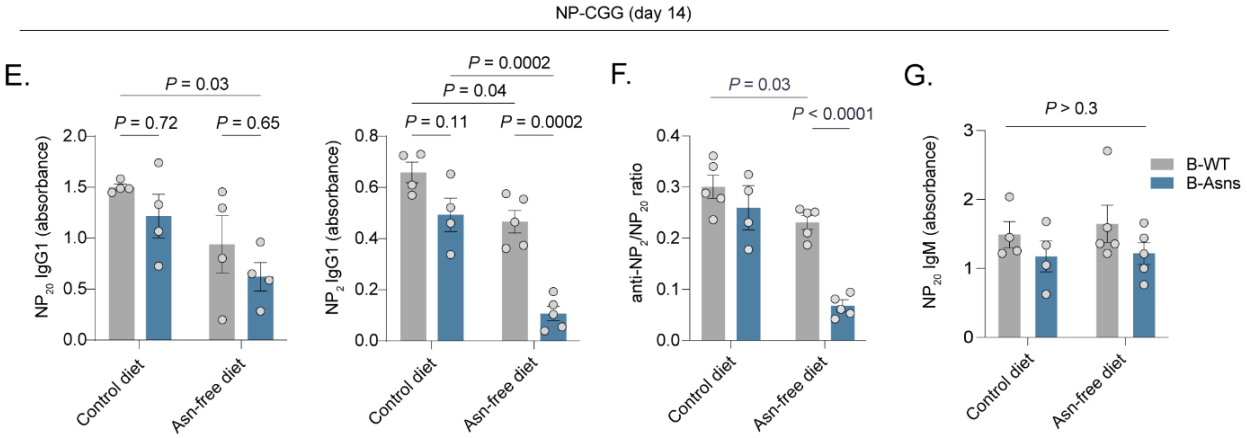

NP-CGG (day 14)
E.
F.
G.
P = 0.03
P = 0.72
P = 0.65
P = 0.0002
P = 0.04
P = 0.11
P = 0.0002
P < 0.0001
P > 0.3
NP20 IgG1 (absorbance)
NP2 IgG1 (absorbance)
anti-NP2/NP20 ratio
NP20 IgM (absorbance)
B-WT
B-Asns
Control diet
Asn-free diet

Figure 3.20. Affinity maturation is influenced by dietary Asn intake.

(A) Schematic of non-chimeric NP-CGG/dietary modification experiment. B-WT or B-Asns mice were assigned to either an Asn-free or control diet (Asn-replete) for 12 days, before immunisation with 50µg NP-CGG precipitated in Alum hydrogel (1:1) subcutaneously on both flanks. Mice were bled on day 7, 14, 21, and 35 post-immunisation and spleens were analysed following sacrifice at day 40. (B) Quantification of IgG1 anti-NP antibodies ($NP_{>20}$-BSA and NP_2-BSA dilution respectively) at day 7, n=4-5 mice each condition. Data pooled from two independent experiments. (C) Quantification of IgM anti-NP antibodies ($NP_{>20}$-BSA and NP_2-BSA dilution respectively) at day 7, n=4-5 mice each condition. Data pooled from two independent experiments. (D) Dilution curves of IgG1 anti-NP antibodies ($NP_{>20}$-BSA and NP_2-BSA respectively) at day 14, n=4-5 mice each condition. Data pooled from three independent experiments. (E) Quantification of IgG1 anti-NP antibodies ($NP_{>20}$-BSA at 1:1600 and NP_2-BSA at 1:200 dilution respectively) at day 14, n=4-5 mice each condition. Data pooled from two independent experiments. (F) Quantification of NP_2:NP_{20} ratio (at 1:200 dilution) of IgG1 anti-NP antibodies at day 14, n=4-5 mice each condition. Data pooled from two independent experiments. (G) Quantification of IgM anti-NP_{20} antibodies (at 1:1000) at day 14, n=4-5 mice each condition. Data pooled from two independent experiments. Statistical significance was determined by two-way ANOVA with Tukey's multiple testing correction.

3.2.20. Memory B cell responses are dependent on Asn

The GC reaction persists for several weeks beyond its peak[154]. Therefore, I continued to monitor affinity maturation capacity (NP_2/NP_{20}) beyond day 14 (Fig. 3.21A). Due to the relative nature of the NP_2/NP_{20} ratio, which served as an internally controlled parameter, I was able to perform comparative longitudinal analyses over three additional weeks. From day 14, in B-Asns mice fed an Asn-free diet, the affinity index remained substantially lower than B-WT controls until day 35 post-immunisation (Fig. 3.21B).

The establishment of the memory B cell compartment is an important outcome of immunisation or vaccination, representing a long-lived immune response following the GC reaction[11,155].

At day 40 post immunisation, I examined splenic NP-specific memory B cells. Following Asn limitation, B-Asns mice showed both proportional and numerical reductions in NP-binding memory B cells (Fig. 3.21C), which were identified as $CD19^+$ IgD^- $GL\text{-}7^-$ $CD138^-$ $CD73^+$ $CD38^+$ NP^+ in splenocytes excluded from naïve B, GC B, and plasma cells (Fig. 3.21D). These findings collectively highlight the regulatory role of Asn availability in the dynamics

and temporal kinetics of both affinity maturation and memory B cell responses, particularly evident in the absence of ASNS.

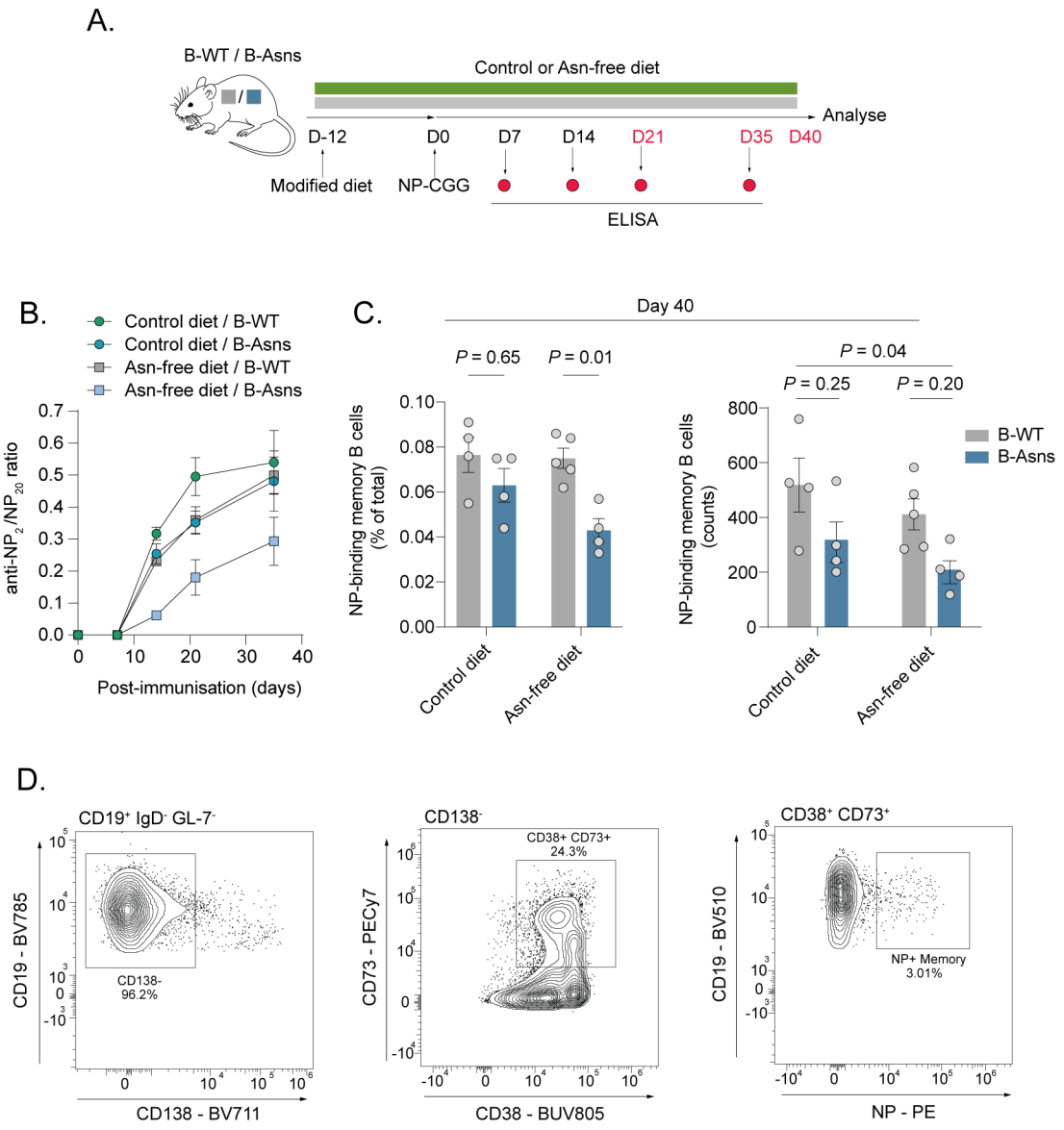


Figure 3.21. Memory B cell responses are dependent on Asn.

(A) Experimental diagram as previously described in Fig. 3.19A. (B) Comparison of the ratio of IgG1 NP-specific high-affinity antibodies to low-affinity antibodies detected by binding to NP_2 and $NP_{>20}$ antigens, respectively, from B-WT/control diet (n=4), B-Asns/control diet (n=4), B-WT/Asn-free diet (n = 5), B-Asns/Asn-free diet (n=5) across different time points. Data pooled from two independent experiments. (C) Comparison of the proportions and absolute counts of splenic NP-binding memory B cells gated as $CD19^+$ $B220^+$ IgD^- $GL\text{-}7^-$ $CD138^-$ $CD38^+$ within total cells at day 40. Data pooled from two independent experiments. (D) Representative gating strategy of memory B cells. Statistical significance was determined by two-way ANOVA with Šidák's multiple testing correction.

3.2.21. Asn deprivation attenuates boost-induced affinity enrichment

Antigenic boost is an essential immunological phenomenon that drives further enhancement of high-affinity therefore commonly employed in vaccination strategies[6]. I performed experiments in which mice were immunised with NP-CCG a week prior to dietary modification, and then at day 36 boosted with NP-CGG (Fig. 3.22A). This experimental setup also enabled the assessment of how diet intervention affects affinity maturation in established GCs during the pre-boost period. Following 28 days of dietary Asn restriction, at day 35 post-NP-CGG primary immunisation, there was an impairment in affinity maturation measured by NP_2/NP_{20} ELISA index (Fig. 3.22B). This indicates that affinity maturation remains sensitive to dietary limitation of Asn particularly in B-Asns mice after GC establishment. Following the NP-CGG boost, at day 49, there was a robust elevation in anti-NP IgG1 antibodies, resulting in further increase in NP_2/NP_{20} affinity index (Fig. 3.22C-D). I found attenuation of the boost-associated increase in affinity maturation in B-WT and to a greater extent B-Asns mice fed an Asn-free diet (Fig. 3.22E). This illustrates the importance of Asn on boost-induced humoral responses and confirms its important role in long-lived memory.

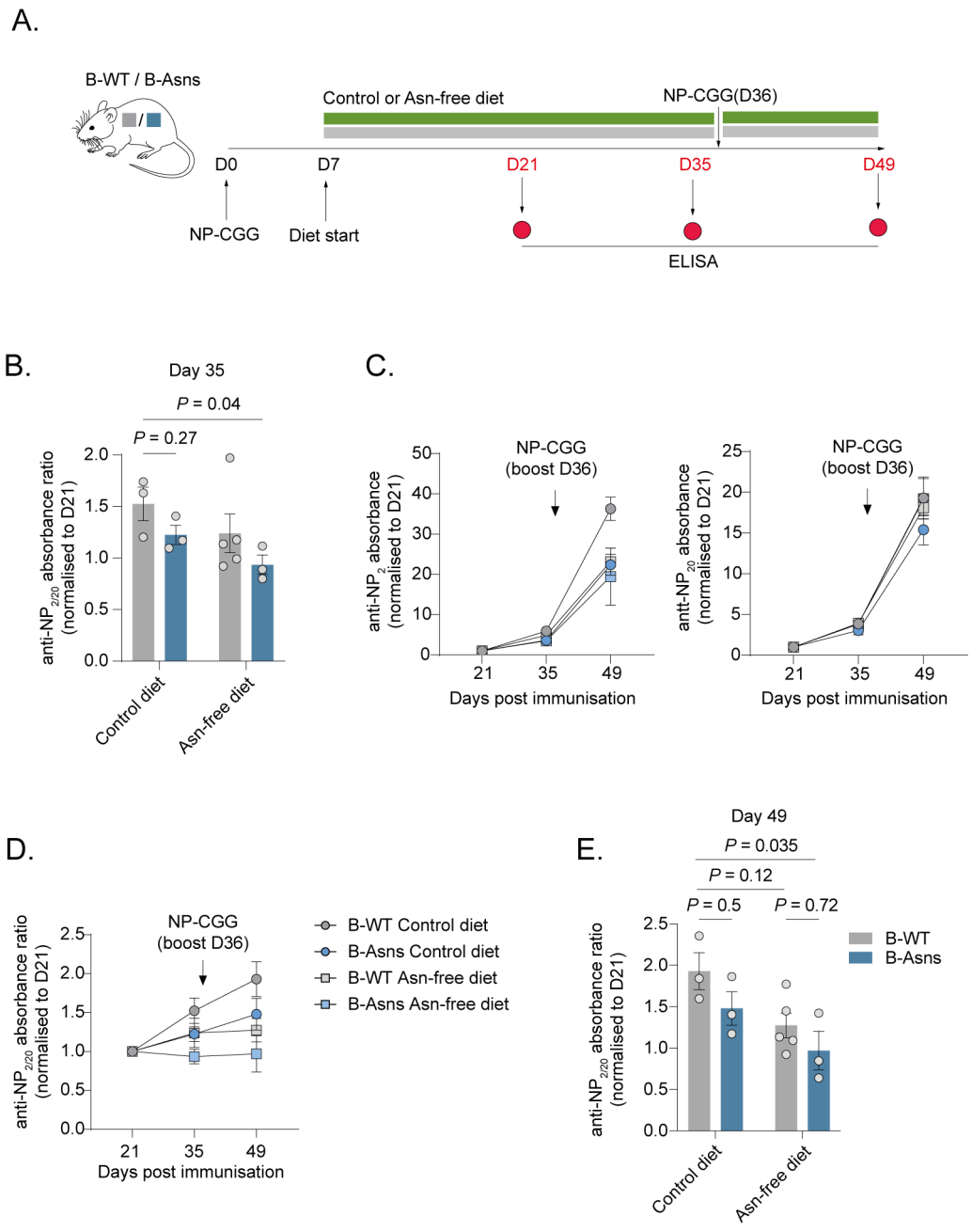


Figure 3.22. Asn deprivation attenuates boost-induced affinity enrichment.

(A) Schematic of NP-CGG/dietary modification experiment. B-WT or B-Asns mice immunisation with 50μg NP-CGG precipitated in Alum hydrogel (1:1) subcutaneously on both flanks, one week later, they were assigned to either an Asn-free or control diet (post-GC diet treatment) and maintained on the assigned diet for the rest of the experiment. Sera were collected on D21 and D35 before boost immunisation was given with 50μg NP-CGG precipitated in Alum hydrogel (1:1) subcutaneously on only right flank at D36. Two weeks later, mice were bled at day 49 timepoint and experiment was terminated. (B) Anti-NP_2/NP_{20} ratio quantification at day 35 after primary NP-CGG immunisation (normalised to day 21). Each point represents a serum sample from single mouse. Data pooled from two independent experiments. (C) ELISA quantification of anti-NP_2 IgG1, anti-NP_{20} IgG1 antibodies at day 21, 35 and 49 after primary NP-CGG immunisation (normalised to day 21). Each point represents a serum sample from single mouse. Data pooled from two independent experiments. (D) Anti-NP_2/NP_{20} ratio quantification at day 21, 35 and 49 after

primary NP-CGG immunisation (normalised to day 21). Each point represents a serum sample from single mouse. Data pooled from two independent experiments. (E) Comparison of normalised NP_2/NP_{20} ratio between conditions at day 49 based on **D**. Statistical significance was determined by two-way ANOVA with Šidák's multiple testing correction.

3.2.22. Supplementation of Asn does not affect GC B cell dynamics

Asn can also be supplemented to increase its systemic and local availability[112,156].

After demonstrating that Asn deprivation reduces GC outputs, I investigated whether supplementation with Asn could enhance them. I administered Asn through drinking water to wild type mice on a standard diet for 14 days prior to subcutaneous immunisation with NP-CGG. Subsequently, I evaluated the antigen-specific GC response using flow cytometry at day 14 post-immunisation (Fig. 3.23A). The GC B cell compartment showed no significant changes between mice given Asn-supplemented water and the control group (Fig. 3.23B). Furthermore, the NP-binding capacity of GC B cells remained correspondingly unchanged (Fig. 3.23C).

Next, I assessed serum IgG1 anti-NP antibodies and the NP_2/NP_{20}-based affinity index, which is a sensitive measurement of GC affinity maturation (Fig. 3.23D). Additionally, I included another experimental group where wild type mice received two ASNase injections, which served as a negative control due to its adverse effects on the GC function (Fig. 3.23D). ASNase treatment significantly reduced the concentration of high-affinity NP_2-specific IgG1 antibodies as well as affinity maturation (NP_2/NP_{20}), in keeping with findings in Fig. 3.16. However, no alteration was seen in sera from Asn-supplemented mice (Fig. 3.23E).

Consistent with high Asn abundance detected in LN interstitial fluid, this result indicates that amount of Asn provided by a standard diet is sufficient to sustain the GC reaction and affinity maturation.

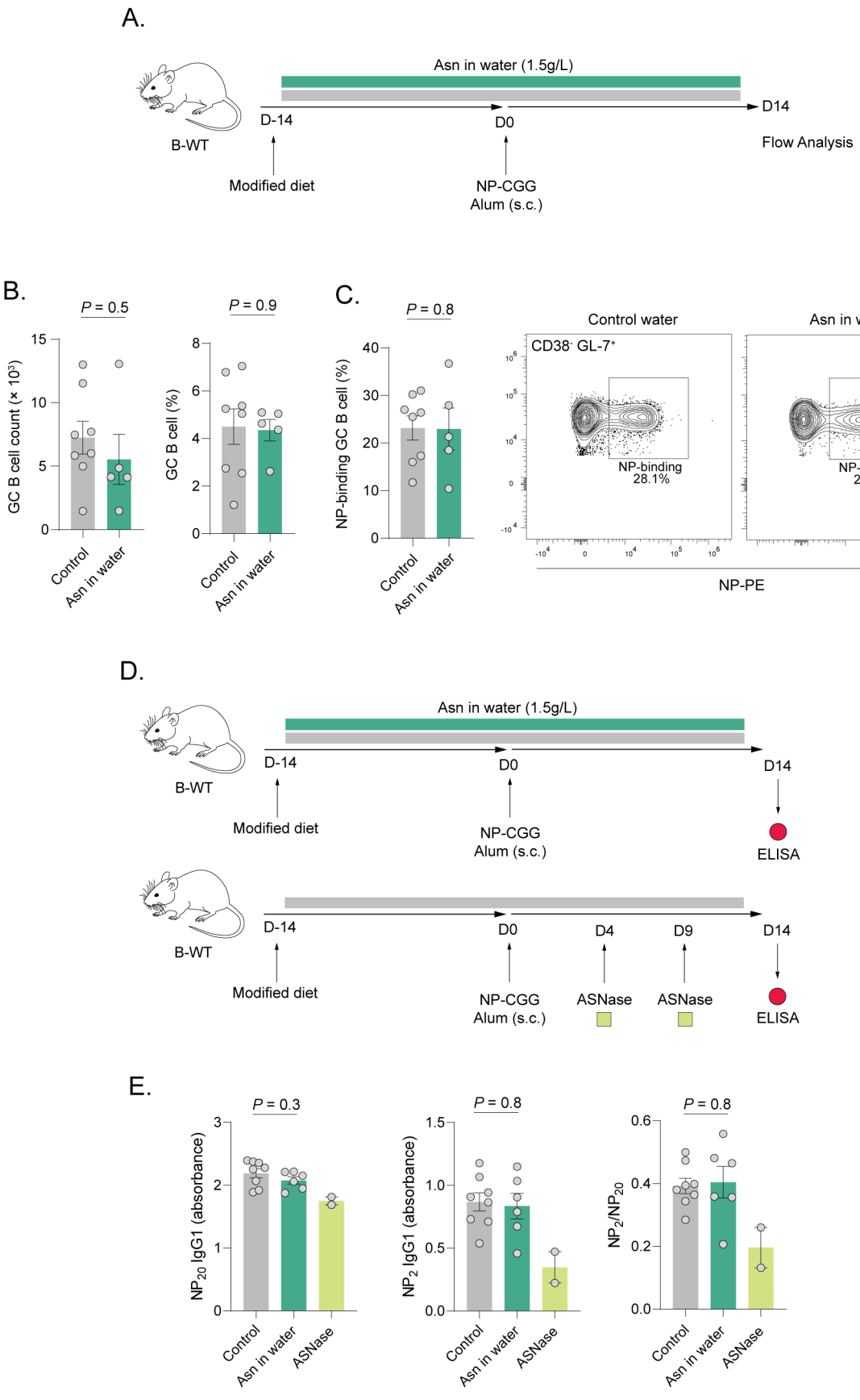

A.
Asn in water (1.5g/L)
B-WT
D-14
D0
D14
Flow Analysis
Modified diet
NP-CGG
Alum (s.c.)
B.
P = 0.5
GC B cell count (× 10³)
Control
Asn in water
P = 0.9
GC B cell (%)
C.
P = 0.8
NP-binding GC B cell (%)
Control water
Asn in water
CD38⁻ GL-7⁺
NP-binding
28.1%
NP-binding
26.4%
NP-PE
D.
Asn in water (1.5g/L)
B-WT
D-14
D0
D14
Modified diet
NP-CGG
Alum (s.c.)
ELISA
D4
D9
ASNase
E.
P = 0.3
NP20 IgG1 (absorbance)
P = 0.8
NP2 IgG1 (absorbance)
NP2/NP20
ASNase

Figure 3.23. Supplementation of Asn does not affect GC B cell dynamics.

(A) Schematic of NP-CGG/Asn supplementation in water experiment. B-WT mice were administered normal or Asn supplemented-water (1.5g/L) for 14 days before subcutaneous immunisation with NP-CGG. Lymph nodes were analysed by flow cytometry. (B) Quantification of GC B cell numbers and proportions ($CD38^-$ $GL\text{-}7^+$). (C) Quantification and representative flow plot of NP-binding GC B cells. (D) Experimental design, similar to **A** with the additional negative control group administered ASNase (50U per mouse) on days 4 and 9. Sera were collected at day 14 post-immunisation for the detection of NP-specific antibodies by ELISA. (E) ELISA quantification of anti-NP_2 and anti-NP_{20} IgG1 antibodies along with the NP_2/NP_{20} ratio (affinity maturation index) at day 14 post-NP-CGG immunisation**.** Each point represents a single mouse. Data pooled from two independent experiments. Statistical significance was determined by a two-tailed unpaired t test.

3.2.23. Asn availability regulates the humoral response to influenza infection

The GC reaction is essential to humoral immune responses following influenza infection[6]. Therefore, I examined whether Asn availability could control influenza-induced GC and antibody responses. Mice were assigned to either an Asn-free or a normal control diet for 12 days, as previously described, and then intranasally infected with the X31 H3N2 influenza A strain (Fig. 3.24A). From day 3 after infection, noticeable weight loss began, reaching its highest point around day 7 (Fig. 3.24B). Elimination of viral load during primary influenza infection is largely driven by the activity of T cells and other non-B cell subsets, which coincides with the initiation of weight recovery in mice[157]. I observed that the rate of weight recovery under all conditions remained comparable. This suggests that perturbation of the non-B cell compartment is unlikely (Fig. 3.24B).

The antibody response to X31 influenza strain was initially assessed in mouse sera at day 14 post-infection. Levels of anti-X31 IgG antibodies were substantially reduced in B-Asns mice given an Asn-free diet (Fig. 3.24C-D). However, I did not detect a significant change in anti-X31 IgM levels (Fig. 3.24C-D). Furthermore, at day 21 post-infection, levels of anti-X31 IgG antibodies remained substantially lower in B-Asns mice on an Asn-free diet, in keeping with the findings at day 14 (Fig. 3.24E).

Therefore, Asn metabolism controls the humoral immune responses derived from the GC during influenza infection. When environmental Asn is limited, *Asns* plays an important role in this process.

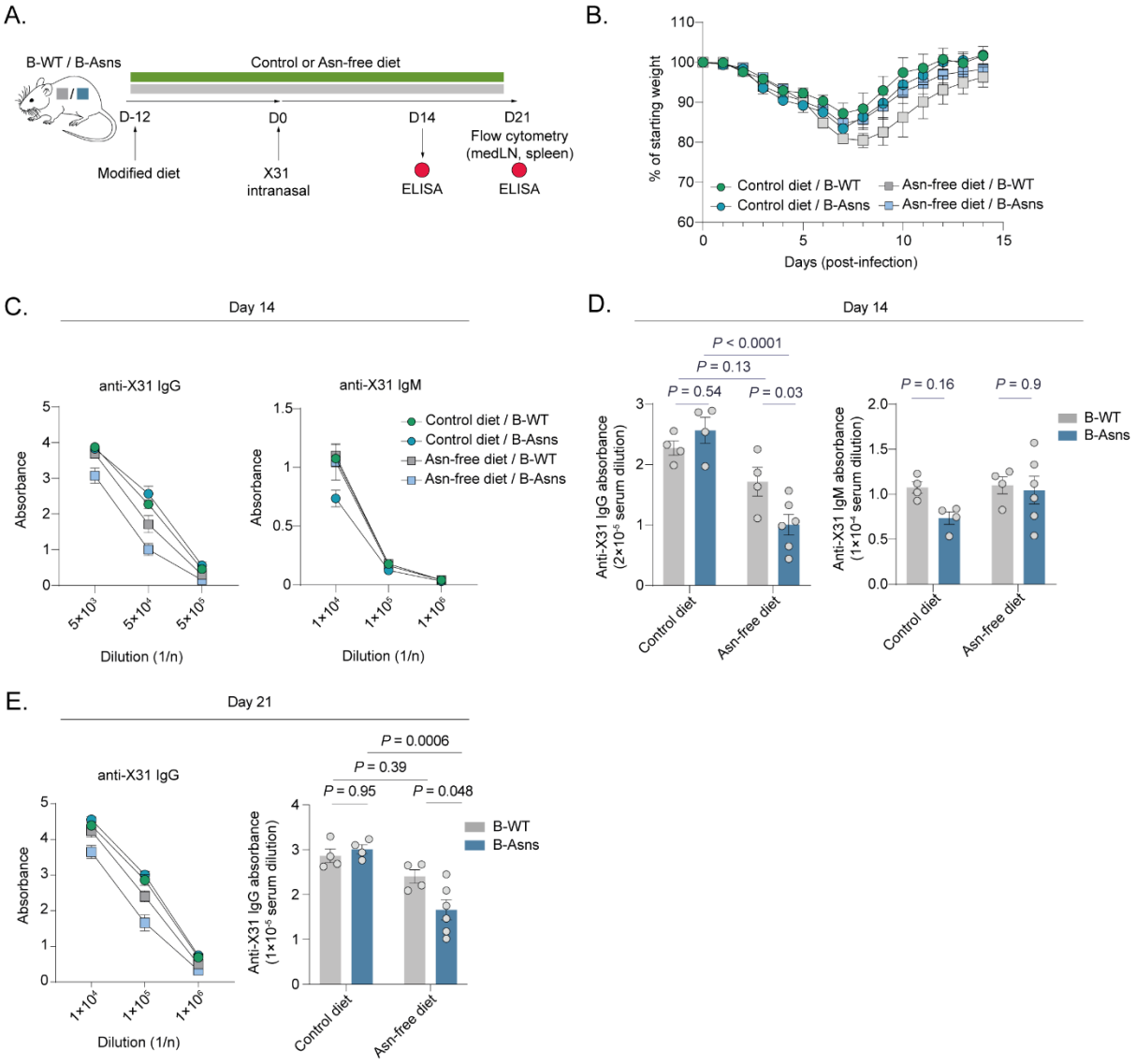


Figure 3.24. Asn availability regulates the humoral response to influenza infection.

(A) Schematic of influenza/dietary modification experiment. B-WT and B-Asns mice were transferred to a control (Asn-replete) or Asn-deficient diet for 12 days, before intranasal infection with X31 influenza A strain. Mice were weighed daily for 14 days and bled at days 14 and 21. Mediastinal lymph node and spleen were harvested for flow cytometry and immunohistochemistry analyses following sacrifice at day 21. (B) Quantification of weight loss as % of initial weight over 14 days. Control diet/ B-WT (n = 4), control diet/B-Asns (n = 4), Asn-free diet/B-WT (n = 4), Asn-free diet/B-Asns (n=6). Data pooled from two

independent experiments. (C) Dilution curves of X31-specific IgG and IgM antibodies at day 14. n=4-6 mice each condition. Data pooled from two independent experiments. (D) Comparison of X31-specific IgG (at $1/5\times10^4$ dilution) and IgM (at $1/10^4$ dilution) at day 14. n=4-6 mice each condition. Data pooled from two independent experiments. (E) Dilution curves and quantification of X31-specific IgG antibodies at day 21. n=4-6 mice each condition as in **B**. Data pooled from two independent experiments. Statistical significance was determined by two-way ANOVA with Tukey's multiple testing correction (D,E).

3.2.24. Affinity maturation in influenza infection depends on Asn

Affinity maturation in GCs is integral to the development of influenza-specific high-affinity antibodies[158]. I previously demonstrated that reduced Asn availability substantially impairs affinity maturation of NP-specific IgG antibodies. However, it was untested whether this occurs in an infectious context. To address this, I examined the functional affinity (avidity) of X31-specific antibodies by using urea at increasing concentrations as a chaotropic agent to elute weakly binding antibodies (Fig. 3.25A). The addition of a washing step with urea disrupts antibody-antigen complexes that are weakly bound[158]. The decrease in ELISA absorbance values after urea treatment then provides an internally controlled avidity/affinity index, reflecting the binding capacity of captured antibodies (as illustrated in Fig. 3.25A). Consistent with previous reports, urea treatment led to a dose-dependent decrease in antibody binding, confirming the validity of the experimental approach (Fig. 3.25B).

At day 14, I found that anti-X31 IgG antibodies from B-Asns mice were significantly more sensitive to urea treatment when they were maintained on Asn-limited diet (Fig. 3.25C). This reflects impaired affinity in this experimental group. As anticipated, the sensitivity of anti-X31 IgM antibodies to urea was higher across all experimental groups likely due to their inherently lower avidity than that of IgG antibodies (Fig. 3.25D). By combining the avidity index information from the urea assay and total anti-X31 antibody ELISA quantification from Fig 3.24D, I performed estimated quantification of X31-specific high affinity antibody levels. This demonstrated that an Asn-free diet diminished IgG affinity maturation in B-WT and had a more pronounced effect in B-Asns mice, with no similar impact observed in IgM class antibodies, as anticipated (Fig. 3.25E).

Overall, these findings indicate that the affinity maturation of GC-derived antibodies following influenza infection is highly sensitive to Asn availability, similar to what is observed in immunisation.

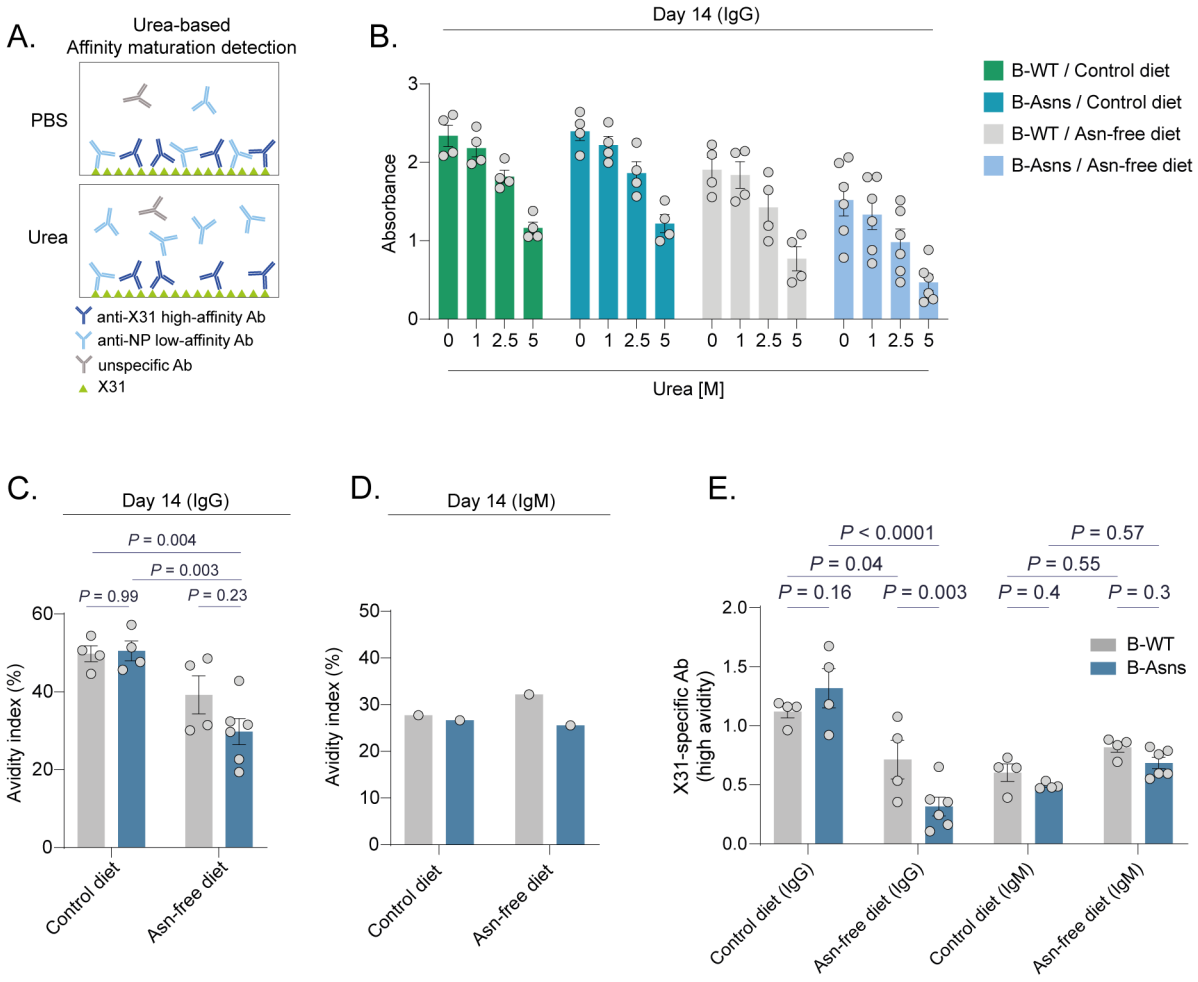


Figure 3.25. Affinity maturation in influenza depends on Asn.

(A) Schematic describing urea-based affinity maturation detection strategy. (B) ELISA quantification at day 14 for anti-X31 IgG absorbance at $1/5\times10^4$ dilution following increasing concentration of urea treatment (at 0, 1, 2.5 or 5M). Each point represents a single mouse. Data pooled from two independent experiments. (C) Comparison of avidity (functional affinity) of X31-specific IgG at day 14 which was calculated as following: Absorbance [5M urea] / Absorbance [0M urea] × 100 also indicated in **C**. Data pooled from two independent experiments. (D) Avidity index quantification for anti-X31 IgM based on 5M Urea treatment calculated as in **D**. Each point represents a pooled sera from n=4-6 mice per condition. Data representative of two independent experiments. (E) Comparison of high-avidity X31-specific IgG and IgM (at $1/5\times10^4$ dilution) quantified by values in **Fig 3.24D** with matching avidity values in **D and E** at day 14. n=4-6 mice each condition. Data pooled from two independent

experiments. Statistical significance was determined by two-way ANOVA with Tukey's multiple testing correction (D,E).

3.2.25. Asn deprivation leads to a defective GC response in influenza infected mice

In mice, intranasal influenza infection drives the formation of GCs in the mediastinal lymph nodes and spleen[159]. These GCs are highly critical for the development of affinity-matured antibodies, which confer humoral protection against influenza.

After assessing antibody responses, I collected spleen and lymph node samples on day 21 post-influenza and analysed the GC reaction by flow cytometry (Fig 3.26A). I found a significant reduction both in the number and proportion of GC B cells from the mediastinal lymph nodes of B-Asns mice that were given an Asn-free diet, in keeping with their defective IgG antibody levels (Fig. 3.26B).

There was also a notable reduction in the ratio of GC B cells to T_{FH} cells. Also decreased was the ratio of DZ to LZ GC B cells, resembling the phenotype seen with ASNase treatment (Fig. 3.26C). Slightly milder but consistent GC-related defects were observed among the splenic GC B cells of B-Asns mice on an Asn-free diet (Fig. 3.26D). Spatial characterisation of influenza-induced GCs identified a size restriction on GCs specifically present in B-Asns mice under Asn limitation. However, numbers of GC clusters did not significantly change (Fig. 3.26E-F).

These findings suggest that Asn metabolism plays a crucial role in regulating GC homeostasis during influenza infection.

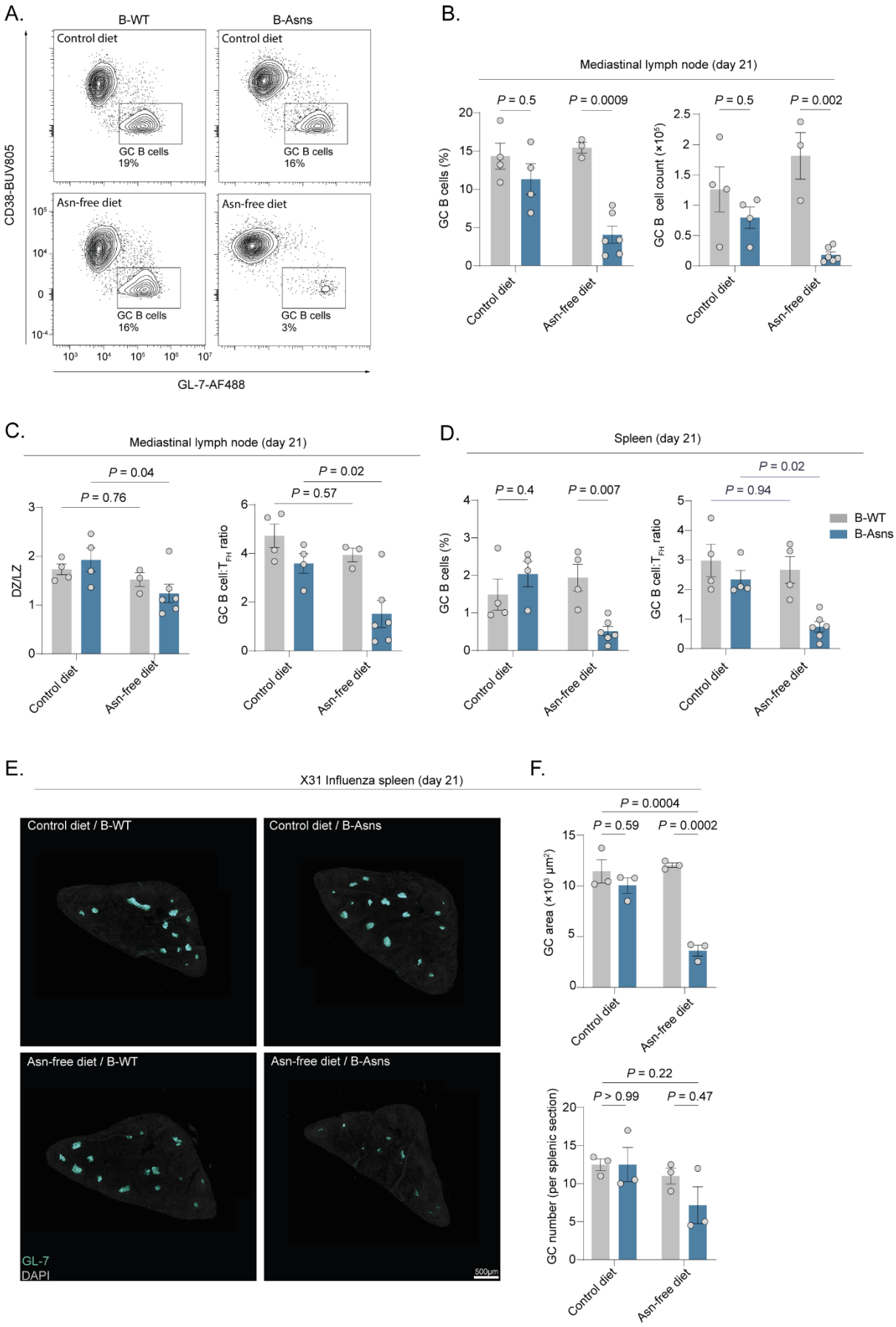

A.
B-WT
B-Asns
Control diet
GC B cells
19%
Control diet
GC B cells
16%
Asn-free diet
GC B cells
16%
Asn-free diet
GC B cells
3%
CD38-BUV805
GL-7-AF488
B.
Mediastinal lymph node (day 21)
P = 0.5
P = 0.0009
P = 0.5
P = 0.002
GC B cells (%)
GC B cell count (×10⁵)
Control diet
Asn-free diet
C.
Mediastinal lymph node (day 21)
P = 0.04
P = 0.76
P = 0.02
P = 0.57
DZ/LZ
GC B cell:T_FH ratio
D.
Spleen (day 21)
P = 0.4
P = 0.007
P = 0.02
P = 0.94
GC B cells (%)
GC B cell:T_FH ratio
B-WT
B-Asns
E.
X31 Influenza spleen (day 21)
Control diet / B-WT
Control diet / B-Asns
Asn-free diet / B-WT
Asn-free diet / B-Asns
GL-7
DAPI
500µm
F.
P = 0.0004
P = 0.59
P = 0.0002
GC area (×10³ µm²)
P = 0.22
P > 0.99
P = 0.47
GC number (per splenic section)

Figure 3.26. Asn deprivation leads to a defective GC response in influenza infected mice.

(A) Representative flow cytometry plots of GC B cells in mediastinal lymph nodes at day 21. (B) Quantification of GC B cell ratio and counts in mediastinal lymph nodes at day 21. n=3-6 mice each condition. Data pooled from two independent experiments. (C) Quantification of DZ/LZ ratio in $CD38^-$ $GL\text{-}7^+$ GC B cells and GC B:T_{FH} ratio in mediastinal lymph node at day 21 post-influenza infection. Each point represents a single mouse (n=3-6 mice each condition). Data pooled from two independent experiments. (D) Flow cytometric quantification of splenic GC B cell (as gated in **A**) proportions and GC B:TFH ratio at day 21. n=4-6 mice each condition Data pooled from two independent experiments. (E) Immunohistochemistry of representative spleen sections (8μm) at day 21 post X31 influenza infection. GL-7 highlights GCs. DAPI is used as background staining. Scale bar 500μm. Data pooled from two independent experiments. (F) Image quantification of X31-induced splenic GCs from **E**. Mean GC area (μm^2) per mouse and GC count per splenic section (average of two non-serially sliced) per mouse. Each data point indicates a mouse. n=3 from each condition. Data pooled from two independent experiments. Statistical significance was determined by two-way ANOVA with Tukey's multiple testing correction (B,C,F) or Šidák's multiple testing correction (D).

3.2.26. Metabolic activity in B cells is regulated by Asn

Asn has been reported to play a vital role in mitochondrial activity and the metabolic reprogramming of eukaryotic cells[113,114]. Metabolic reprogramming of B cells is particularly important for their activation and subsequent participation in GC reactions[160,161]. I asked whether cellular metabolism is impacted by Asn deprivation.

To this end, I performed extracellular flux assays and assessed OxPhos and glycolysis in B cells subjected to Asn limitation. I isolated naïve B cells and stimulated them with agonistic anti-CD40 and IL-4 in the presence of varying concentrations of Asn, as previously defined (Fig. 3.27A). 24 hours later, cells were harvested and subjected to the MitoStress test, which is designed to test OxPhos reserve and mitochondrial capacities using select mitochondrial inhibitors[44,162] (Fig. 3.27A). Intriguingly, I found that the Asn concentration provided to wild type B cells during stimulation strongly correlated with the oxygen consumption rate (OCR) and extracellular acidification rate (ECAR), reflecting OxPhos and glycolytic activity, respectively (Fig. 3.27B-C).

I observed no significant difference in ECAR capacity between B-WT and B-Asns B cells across all tested conditions (Fig. 3.27D). However, the detrimental effect of low Asn

concentrations (<40 μM) on basal OCR was more pronounced in B-Asns B cells, which displayed intact OxPhos activity when Asn was supplemented (≥40 μM) (Fig. 3.27E-F).

Surprisingly, the maximal respiration induced by the mitochondrial uncoupler carbonyl cyanide-p-trifluoromethoxyphenylhydrazone (FCCP) did not differ between B-WT and B-Asns B cells across all Asn concentrations (Fig. 3.27G). In the light of defective basal OCR values, this resulted in a significantly elevated maximal-to-basal respiration ratio, also known as the spare respiratory capacity (SRC), in B-Asns B cells when Asn was absent (Fig. 3.27H).

Overall, these findings indicate that Asn availability is critical for the metabolic reprogramming of activated B cells, and ASNS regulates mitochondrial respiration under low Asn conditions.

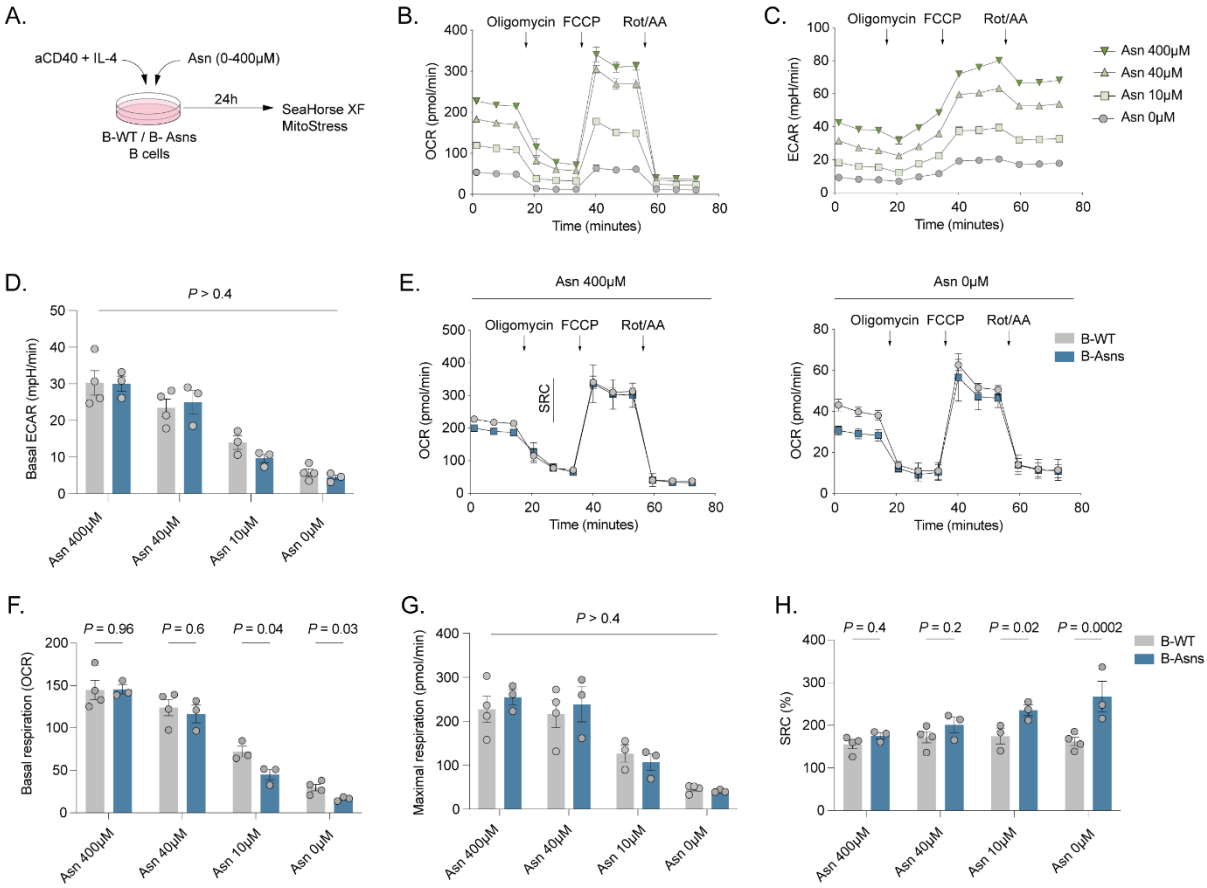


Figure 3.27. Metabolic activity in B cells is regulated by Asn.
(A) Schematic illustrating the experimental design for the SeaHorse XF MitoStress assay. (B) Seahorse extracellular flux analysis of B cells stimulated for 24h with IL-4 and agonistic anti-CD40 at the indicated concentrations of Asn. Oxygen consumption rate (OCR) was measured during the MitoStress test (n=3-4 mice). Data pooled from three independent experiments with 5-6 technical replicates averaged per mouse. FCCP, carbonyl cyanide-p-trifluoromethoxyphenylhydrazone; Rot/AA, rotenone/antimycin A. (C) Seahorse extracellular flux analysis of B cells as in **A** (n=3-4 mice). Extracellular acidification rate (ECAR) was measured during the MitoStress test. Data pooled from three independent experiments with 5-6 technical replicates averaged per mouse. (D) Quantification of basal ECAR. (E) Seahorse OCR quantification in B-WT (n=3-4 mice) and B-Asns (n=3 mice) B cells stimulated for 24h with IL-4 and agonistic anti-CD40 at the indicated concentrations of Asn. Spare respiratory capacity (SRC) is illustrated. Data pooled from three independent experiments. (F) Quantification of basal OCR in B-WT and B-Asns B cells stimulated for 24h with IL-4 and agonistic anti-CD40 at the indicated concentrations of Asn. Each data point represents a mouse. Data pooled from three independent experiments. (G) Quantification of maximal respiration. (H) Quantification of SRC (%) based on quantifications in **F and G** (Maximal/Basal OCR * 100). Statistical significance was determined by two-way ANOVA with Tukey's multiple testing correction.

3.2.27. Asn depletion disrupts mitochondrial ETC homeostasis

The ETC is crucial for OxPhos. Upon activation, B cells undergo robust mitochondrial remodelling, which is associated with changes in ETC protein expression[20].

Using a flow cytometry panel designed for mitochondrial proteins, herein referred to as Mitoflow, I profiled the abundance of ETC proteins in stimulated B cells (Fig. 3.28A). I found that Asn deprivation caused a notable decrease in the expression of ETC proteins in both B-WT and B-Asns B cells. Reduced were cytochrome c oxidase subunit I (COX I), cytochrome c oxidase subunit IV (COX IV), succinate dehydrogenase A (SDHA), and cytochrome C (Cyt C) (Fig. 3.28B). This effect was more pronounced in B-Asns B cells, in keeping with their defective mitochondrial respiration.

Next, I used 3D lattice structured illumination microscopy (SIM), a super-resolution imaging technique, to directly visualise mitochondria in B-WT and B-Asns B cells. While mitochondrial volume and count appeared normal when Asn was supplemented, they were substantially reduced in its absence. Once again, this reduction was more severe in B-Asns B cells (Fig. 3.28C-E).

Using the same Mitoflow panel, I examined ETC homeostasis in GC B cells under Asn limitation by ASNase treatment (Fig. 3.28F). I found a modest increase in SDHA and COX I expression specifically in B-Asns GC B cells treated with ASNase (Fig. 3.28G). In contrast, COX IV and CytC were substantially reduced by ASNase without genotype effect (Fig. 3.28G).

Overall, these results suggest that Asn availability controls ETC homeostasis and mitochondrial remodelling both *in vitro* and *in vivo*.

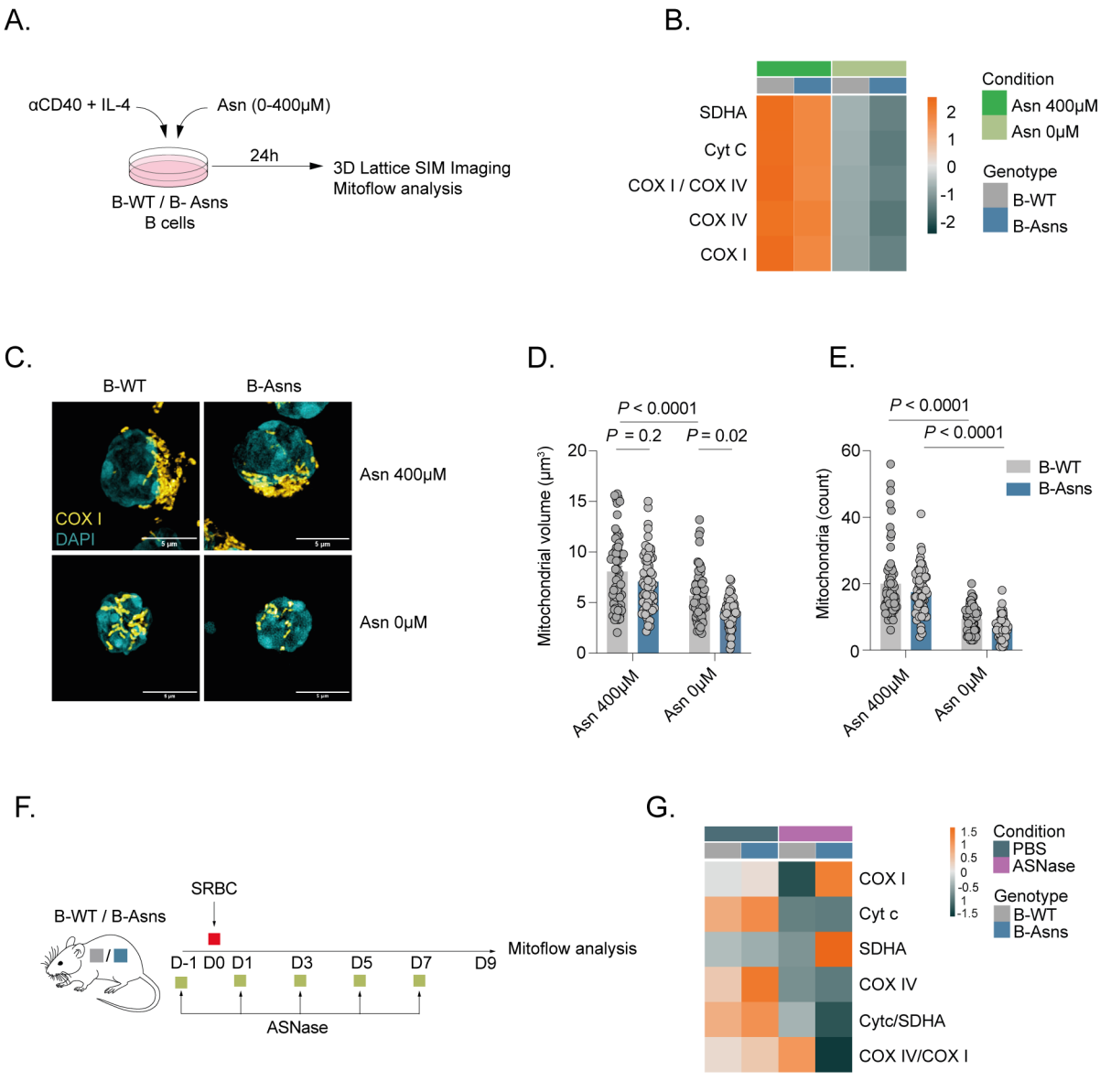


Figure 2.28. Asn depletion disrupts mitochondrial ETC homeostasis.

(A) Schematic illustrating the experimental design for 3D SIM and Mitoflow experiments. (B) Heatmap of row z-scores for the gMFI of indicated ETC proteins, measured by flow cytometry in B-WT or B-Asns B cells stimulated for 24h with IL-4 and agonistic anti-CD40 in the presence or absence of Asn (400μM) (mean of n = 2), Results are representative of two independent experiments with n = 3 mice per group in total. (C) 3D lattice SIM images of COX I and DAPI in B-WT and B-Asns B cells stimulated for 24h with IL-4 and agonistic anti-CD40 in the presence or absence of Asn (400μM). Scale bar 5μm. (D) Quantification of mitochondrial volume as in **F**. Each data point represents a cell (n=57 B-WT/Asn400, n=66 B-Asns/Asn400, n=65 B-WT/Asn0, n=53 B-Asns/Asn0) pooled from n=3 mice B-WT or B-Asns mice. Representative of two independent experiments. (E) Quantification of mitochondrial count as in C. Each data point represents a cell pooled from n=3 B-WT or B-Asns mice. Representative of two independent experiments. (F) *Ex vivo* Mitoflow workflow following ASNase treatment (G) Heatmap of row z-scores for the gMFI of indicated ETC proteins and ratios, measured by flow cytometry in $CD38^{-}$ $GL\text{-}7^{+}$ GC B cells from B-WT or B-Asns (mean of n = 3-4) mice treated with ASNase (standard regime). Data representative of two independent experiments. Statistical significance was determined by two-way ANOVA with Tukey's multiple testing correction (D-E).

3.3. Discussion

Here, I demonstrated that the non-essential amino acid asparagine is highly critical in B cells. This was reflected in the increased uptake via the transporter SLC1A5 (ASCT2) and the elevated levels of its synthetic enzyme, ASNS. I found that asparagine depletion severely impaired the GC reaction and subsequent antibody responses to protein and infectious antigens. The synthetic enzyme of Asn, ASNS, was critical for B cell homeostasis to counteract the effects of Asn restriction. Mechanistically, limited asparagine availability disrupted cellular metabolism and destabilised ETC homeostasis.

One of the key findings was that GC B cells exhibited high levels of protein synthesis *in vivo*. Translational activity is closely linked to the metabolic capacity of cells[163]. While increased translation might suggest a globally elevated metabolism in GC B cells, detailed proteomic analyses are needed to uncover the unique protein landscape of these cells[146]. Ribosome profiling techniques combined with BONCAT methods could be useful to unravel the translational dynamics and proteome composition of GC B cells[164]. In this context, the *in vivo* BONCAT protocol with dual amino acid incorporation that I developed and applied to GCs may serve as a valuable reference point for future research.

I observed that SLC1A5, a key neutral amino acid transporter, was significantly upregulated in GCs and mirrored the spatial distribution of ASNS. By modifying and repurposing a recently published glutamine uptake assay[130], I found highly active Asn uptake capacity in both GC B and plasma cells. These findings suggest that the dual sources of Asn-uptake and synthesis-may enable metabolic compensation and adaptation, particularly in cells with high uptake and synthetic capacity, such as GC B cells. Indeed, it was shown that genetic ablation of *Slc1a5* resulted in minimal changes to GC B cell dynamics in mice. This to a certain extent resembles B-Asns mice under conditions of unrestricted Asn availability[165] and raises the question of whether the synthetic activity of ASNS or other enzymes compensates for defective SLC1A5.

Using LC-MS, our laboratory demonstrated that metabolic pathways involving Asn were significantly upregulated in GC B cells[127]. Following this up, I observed elevated RNA and protein levels of ASNS in these cells, in keeping with the metabolite measurements. Under physiological conditions, it remains unclear whether ASNS contributes to the cellular Asn pool in GC B cells or acts as a fail-safe mechanism in anticipation of reduced Asn levels. Despite the clear abundance of ASNS in GC B cells, one challenge I encountered was demonstrating its catalytic activity directly *in vivo*. Addressing this would require an *in vivo* isotope tracing approach, which remains technically challenging for cell types like GC B cells. However, promising advancements have been reported in the field of T cell immunometabolism[166].

The absence of phenotypic changes in B-Asns B cells without Asn restriction supports the idea that the GC niche has sufficient Asn to sustain GC B cells despite their high metabolic demands. In fact, it has recently been shown that although ASNS was highly expressed in B-cell lymphoma, it was not catalytically active, rendering lymphoma cells dependent on exogenous Asn, which kept them vulnerable to ASNase[120].

Another piece of evidence I presented was the lack of phenotypic impact of Asn supplementation on GC B cell outcomes. However, Asn supplementation has been shown

to enhance antigen-specific T cell responses[112]. Potential differences in metabolite availability between T and B cell zones (e.g., the GC microenvironment) might explain the divergence between these findings. Recent studies have highlighted that the genetic ablation of enzyme phosphoglycerate dehydrogenase (PHGDH) in B cells, which primarily produces Ser, or its pharmacological inhibition is detrimental to the GC B reaction. This surprisingly occurs even without any nutritional modification on *in vivo* Ser levels[119]. This could be attributed to the differential abundance of Ser and Asn in lymphoid compartments especially in GCs.

Whilst the concept of tissue-specific nutrition availability has received attention in the context of the tumour microenvironment, very little is known about normal tissues and particularly in complex structures like GCs. GCs are hypoxic and poorly vascularised, but local concentrations of Asn remain unclear. I found a much higher concentration of Asn in eluted LNIF compared to serum, which was not the case for Gln. This is in keeping with a previous study[149], which demonstrated that tissue Asn levels in the lung and mammary gland are higher than serum levels. The high abundance of Asn found in lymph nodes may underlie the lack of phenotypic changes in B-Asns mice under physiological conditions without Asn restriction, as well as the unchanged affinity maturation in WT mice following supraphysiologic Asn supplementation in drinking water. Given the metabolic heterogeneity in SLOs and the distinct metabolite composition identified in the GC microenvironment, as shown by MALDI Imaging Mass Spectrometry[167], it remains uncertain how accurately LNIF actually represents amino acid availability within B cell follicles or GCs. Advances in mass spectrometry imaging may allow more precise quantification of metabolites in their spatial context in the future[167].

In addition to the synthetic role of ASNS, which may be minimal when Asn is abundant, it remains unknown whether ASNS might have other, non-synthetic functions, as has been recently demonstrated for PHGDH, whose main function is to produce Ser[168]. Interestingly, a study has shown that ASNS is recruited to mitotic spindles in human cells thus might have

moonlighting roles[169]. The potential non-synthetic activities of ASNS, therefore, warrants further investigation.

An important consideration in all studies of metabolism *in vitro* is how to approximate the concentrations of metabolites found within tissue. Most importantly I have now measured the Asn concentration of lymph node interstitial fluid, and this provides a reference point for *in vitro* experiments. I observed impaired B cell homeostasis at Asn concentrations below 40μM *in vitro*, which reflects the serum levels. While 10μM Asn was largely tolerated by WT B cells, B-Asns B cells exhibited significant physiological defects at this concentration. However, complete absence of Asn from the onset of culture was detrimental to both genotypes, unlike the later removal of Asn, which only caused defects in *Asns*-deficient B cells. This finding is in keeping with previous observations in $CD8^+$ T cells[113]. Kinetic changes in exogenous Asn dependency were also noted in my *in vivo* experiments. When ASNase was administered early, namely before GC establishment, WT mice exhibited GC defects, although physical expansion of GCs remained intact. This suggests that WT mice were only susceptible to ASNase during the phase of GC establishment, which coincides with ASNS induction and upregulation. But once GCs were established, they became resistant to deleterious effects of ASNase likely owing to compensatory activity of ASNS.

I further substantiated this by administering ASNase only after day 5 post-immunisation, therefore minimising impact on GC formation. B-Asns mice continued to exhibit GC defects with both ASNase treatment schemes and maintained a smaller GC characteristics. The impact of amino acid availability on the physical expansion of an immunological niche has not been extensively documented in previous studies. Although *in vivo* EdU incorporation did not reveal defects in the S phase, I observed alterations in GC B cell distributions in B-Asns mice treated with ASNase, particularly centred on the DZ-GZ intersection. This suggests that cell cycle stages beyond S phase may remain sensitive to Asn availability; indeed, a defect in mitotic progression was observed with Asn deprivation. Since SHM occurs specifically in post-mitotic GC B cell fractions in the DZ, this aligns with the severe

impairment in affinity maturation observed in B-Asns mice under Asn deprivation. Interestingly, the compensatory role of ASNS in affinity maturation was limited. A significant mismatch was evident between GC B cell numbers and antibody quality in B-WT mice treated with ASNase. This is a phenomenon also observed with dietary Asn limitation, albeit to a lesser extent. Why this occurs is currently unclear. One possible explanation is that it represents an onco-protective mechanism. Coupling a highly mutagenic and potentially oncogenic process like SHM with the activity of a synthetic enzyme might otherwise promote malignant transformation into lymphoma[120].

Another intriguing finding was the absence of a genotype effect on the plasmablast compartment when ASNase was administered early, unlike with the post-GC formation regimen. This suggests that extrafollicular plasmablast differentiation may be sensitive to Asn deprivation. Since this differentiation occurs within a few days after immunisation, ASNS levels might not be sufficient to compensate at this stage. This observation is further consistent with the effects of Asn on *in vitro* plasmablast differentiation and the defective antibody response to NP-Ficoll following dietary Asn restriction.

Reliance on exogenous amino acids particularly glutamine has been reported in plasmablasts, and shown to be highly important for the metabolic activity[27]. Additionally, OxPhos was reported to be critical for the plasmablast compartment[170]. Here, I demonstrated that Asn restriction severely impacted cellular metabolism in B cells. This was in stark contrast to reports in $CD8^+$ T cells, where Asn deprivation is known to activate OxPhos and increase nucleotide synthesis, leading to enhanced proliferative capacity and an increase in mitochondrial mass[114]. However, other studies have noted reduced cell division in this cell type, as well as in cancer cells in the absence of Asn[113,124]. In our study, Asn deprivation caused a significant fall in mitochondrial volume in B cells, and we observed a mismatch in the expression of ETC proteins. Balanced OxPhos and ETC are critical regulator for GC B cell homeostasis[20,65,88,160] and therefore might underlie the parts the of the defective GC B cell phenotype following Asn depletion. Indeed, mitochondrial

characterisation of *ex vivo* GC B cells showed alterations in ETC proteins following Asn depletion. It is unclear why B cells are more vulnerable to Asn deprivation compared to $CD8^+$ T cells, but this may arise from more profound cellular remodelling following activation or other differences in core metabolism. Despite their shared microenvironment with GC B cells, no defects were observed in T_{FH} cells under Asn depletion, which underscores their distinct metabolic profiles.

For decades, ASNase has been a key therapeutic in the treatment of leukaemia[171]. Whether ASNS could also represent a novel therapeutic target for non-malignant autoimmune diseases driven by the GC reaction warrants further investigation. Another important aspect of ASNase is its role in bacterial infections due to its bacterial origin. It is tempting to speculate that its ability to deplete environmental Asn might impair protective humoral responses, further potentiating its virulence. A recent study reported evidence that infections of *Salmonella Typhi,* which is a bacterial pathogen with high ASNase activity, lead to GC collapse[50]. It remains to be elucidated whether ASNS could have evolved as a protective mechanism to counteract such effects. An evolutionary interrogation might also provide insights into the functional role of ASNS in humoral immunity.

Another important implication of this mechanism is related to malnutrition. Although an Asn-free diet likely does not exist in nature, protein-deficient diets or malnutrition have been shown to significantly lower Asn levels[172]. Despite this, the effect of malnutrition on vaccine-induced antibody responses has been minimal[173,174]. Thus, it would be interesting to study the role of ASNS in compensating for low Asn levels in a clinical setting in patients suffering protein malnutrition.

Chapter 4: Dynamic mitochondrial transcription and translation control germinal centre entry and lymphomagenesis

4.1. Introduction

Double-stranded breaks introduced by AID into immunoglobulin gene loci can lead to oncogenic mutations, such as *MYC* translocations with *IGH* or *IGL* loci during SHM[175]. GC B cells are the origin of most diffuse large B cell lymphomas (DLBCL), the most common type of non-Hodgkin lymphoma. Their metabolic phenotype is carried over into a significant proportion of DLBCL, which also displays OxPhos dependence[176].

As the GC reaction progresses, the capacity for OxPhos increases, and B cell clones with high SHM rates show the strongest OxPhos gene signatures[48]. Whilst the bioenergetic functions of mitochondria in B cells are relatively well established, their broader regulatory roles remain largely understudied. Mitochondria mediate calcium flux and apoptotic processes in B cells[177,178]. Furthermore, these organelles generate ROS through ETC activity, which has been shown to regulate B cell signalling via redox mechanisms *in vitro*. However, whether these findings are applicable to the GC *in vivo* remains unknown[179–181]. Mitochondrial DNA contributes to the ETC through its transcription and translation inside the mitochondria[65]. These must be coordinated with nuclear-encoded ETC subunits to maintain ETC balance; failure to do so triggers the mitochondrial unfolded protein response (UPR^{mt}), leading to adaptive changes in the cell[182].

Regulation of mitochondrial transcription and translation is important in other immune cells, such as $CD8^+$ T cells and $CD4^+$ T cells, where it controls cytotoxicity and cytokine production, respectively[183–185]. A key regulator of mitochondrial transcription and translation is TFAM, a DNA-binding high mobility group box (HMBG) protein that helps package the mitochondrial genome into nucleoids, resembling histones. In addition, it is the master regulator of mitochondrial biogenesis[186,187]. Global deletion of *Tfam* leads to embryonic lethality in mice[80], and mutations in *Tfam* cause mtDNA depletion syndrome in humans[188]. In T cells, TFAM restrains immunosenescence by limiting inflammatory cytokine

production[189]. In fibroblasts and myeloid cells, it modulates the antiviral immune response[190]. Recent studies have shown that the mitochondrial DNA helicase TWINKLE, an interaction partner of TFAM, is essential for GC formation and plasma cell differentiation but is dispensable for B cell development[160]. However, the dynamics, function, and regulation of mitochondria in GC B cell homeostasis remain largely unexplored.

In this chapter, therefore, I will address the following questions:

- What are the dynamic changes in mitochondria during B cell activation and GC B cell differentiation?
- How does impaired transcription or translation in mitochondria impact humoral immunity and B cell lymphoma?
- What molecular mechanisms underlie mitochondrial dysfunction and its impact on B cells?

4.2. Results

4.2.1. The Mito-QC reporter highlights mitochondria in GCs

To study mitochondrial distribution and turnover dynamics *in vivo*, I employed the mitochondrial reporter mouse strain (Mito-QC), which has been previously described[191]. In Mito-QC mice, ubiquitously expressed green fluorescent protein (GFP) and red fluorescent protein (RFP) derivative mCherry reporter constructs were tagged onto the outer mitochondrial membrane protein, Mitochondrial Fission 1 Protein (FIS1)[191]. This dual reporter strategy enables the detection of mitochondria in compartments with low pH, such as autolysosomes, because unlike GFP, mCherry is resistant to low pH environments (Fig. 4.1A).

I first immunised Mito-QC mice with SRBCs, examining splenic GCs and chronic GCs resident in Peyer's patches (PPs) by confocal microscopy (Fig. 4.1B). There was a strong GFP signal in GCs, along with multiple large GFP^- $mCherry^+$ puncta distributed across the $GL\text{-}7^+$ GC areas in both the spleen and PPs, suggesting that GCs contained an abundant mitochondrial network and active mitochondrial degradation (Fig. 4.1C-D).

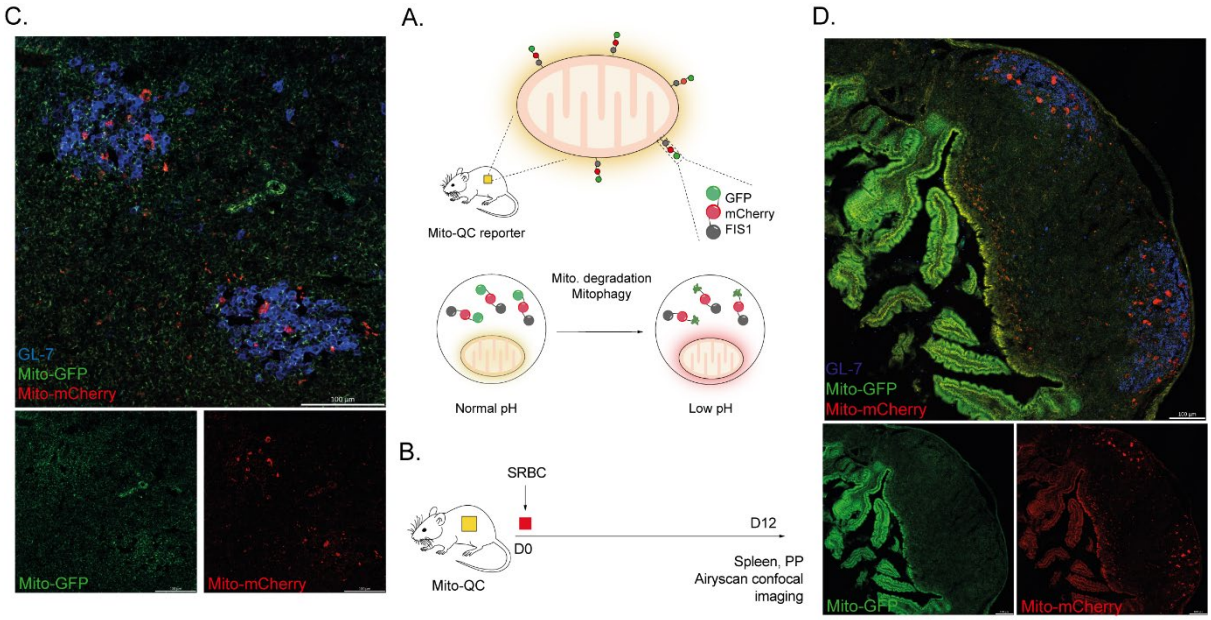


Figure 4.1. Mito-QC reporter highlights mitochondria in GCs.

(A) Schematic depicting Mito-QC construct and dual reporter strategy allowing the visualisation of lysosomal mitochondrial degradation. (B) Immunisation strategy of Mito-QC mice with SRBCs for the generation of GC response. (C) Spleen sections from Mito-QC mice immunised with SRBC and analysed on day 12 showing two $GL\text{-}7^+$ established GCs and GFP^- $mCherry^+$ mitochondrial degradation signal. Scale bar 100μm. (D) Peyer's patch sections from Mito-QC mice depicting two chronically established GCs GFP^- $mCherry^+$ mitochondrial degradation signal. Scale bar 100μm. All experiments are representative of two or more independent experiments

4.2.2. GC B cells do not perform mitophagy

Mitophagy is a key mitochondrial degradation process that involves engulfment of mitochondria and their subsequent digestion in autophagic lysosomes[191]. Mitophagy has been shown to be a regulator in critical cellular processes in lymphocytes[192]. Autophagic activity has been reported in GC B cells[193], however, mitophagy has not been specifically interrogated in GC B cells to this date, therefore whether mitophagy occurs in GC B cells is unclear. To answer this, I used multispectral imaging flow cytometry, a camera-based imaging platform with flow cytometry capabilities also known as ImageStream. It is also important to highlight that Mito-QC signal detection has not been attempted via imaging flow cytometry before. I immunised Mito-QC mice with SRBC and screened GC B cells for the presence of characteristic mitophagy GFP^- $mCherry^+$ puncta (Fig. 4.2A). I found that mitophagic foci were readily detectable by ImageStream across various immune subsets (Fig. 4.2B-C). Importantly, mitophagic loci colocalised with lysosomal-associated membrane protein 1 (LAMP1) and therefore confirmed the specificity of the Mito-QC detection (Fig. 4.2C). While both $CD38^+$ B cells and $CD19^-$ non-B cells showed mitophagy to a certain level, this was completely absent in GC B cell compartment (Fig. 4.2D). Additionally, I noted a highly dense and enhanced mitochondrial network in GC B cells, illustrated by robust Mito-GFP and Mito-mCherry signals (Fig. 4.2C).

Overall, despite the active mitophagy in other immune cells, mitochondria are not degraded through the autophagic route in GC B cells.

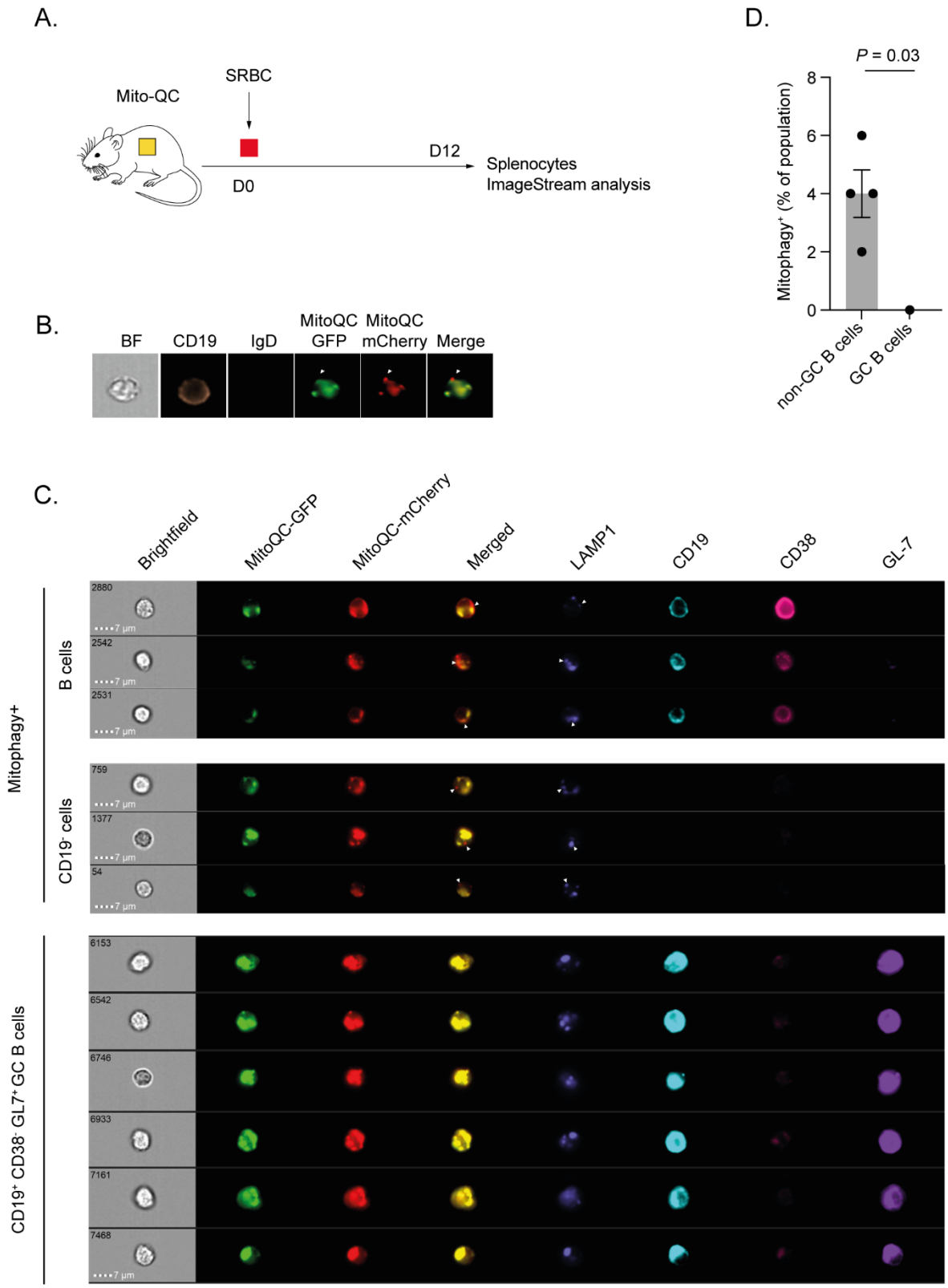


Figure 4.2. GC B cells do not perform mitophagy.
(A) Immunisation strategy of Mito-QC mice with SRBC for the characterisation of GC B cells at day 12 by imaging flow cytometry (ImageStream). (B) Representative images of a CD19+ B cell acquired by ImageStream. Arrow indicates Mito-GFP^{-} Mito-mCherry+ mitophagic

event. (C) Representative ImageStream image galleries of splenic $CD19^-$ non-B cells, $CD19^+$ B cells defined as undergoing mitophagy along with splenic GC B cells ($CD19^+CD38^-$ $GL\text{-}7^+$). Arrows indicate foci of Mito-mCherry without Mito-GFP co-localisation. (D) Proportions of GC B cells within total $mitophagy^+$ population. Mitophagy was defined as the presence of foci of MQC-mCherry signal with LAMP1 positivity in the absence of Mito-GFP co-localisation (as in **C**). Representative of two independent experiments with n=4 total. Statistical significance was determined by a two-tailed Mann Whitney U test (**D**).

4.2.3. GCs are sites of enhanced mitochondrial density

My ImageStream analysis revealed a lack of mitophagy in GC B cells whilst revealing a high mitochondrial signal. Next, I examined mitochondrial content in splenic GCs from Mito-QC mice immunised with SRBC via confocal microscopy and flow cytometry at day 12 (Fig. 4.3A). I observed a strong Mito-GFP signal centred on $GL\text{-}7^+$ GCs (Fig. 4.3B), covering a much larger area and having a higher intensity than the nearby IgD^+ B cell follicle (Fig. 4.3C).

The newly identified GZ, which was explored in Chapter 3, constitutes an intermediate state linked to the G2-M phase of the cell cycle[194]. Flow cytometric characterisation revealed that the Mito-GFP signal was highest in the GZ, followed by the LZ, and lowest in the DZ, this was highly conserved in the spleen and Peyer's patches (Fig. 4.3D-E). Due to their sharing a hypoxic microenvironment in GCs, I additionally analysed mitochondrial content in T_{FH} cells. Interestingly, mitochondrial abundance was similarly increased in T cells as they differentiated into mature T_{FH}. Again, that was conserved across lymphoid tissues (Fig. 4.3F-G). Collectively, these results suggest that B and T cells undergo extensive mitochondrial biogenesis and elevate their mitochondrial content during the GC reaction.

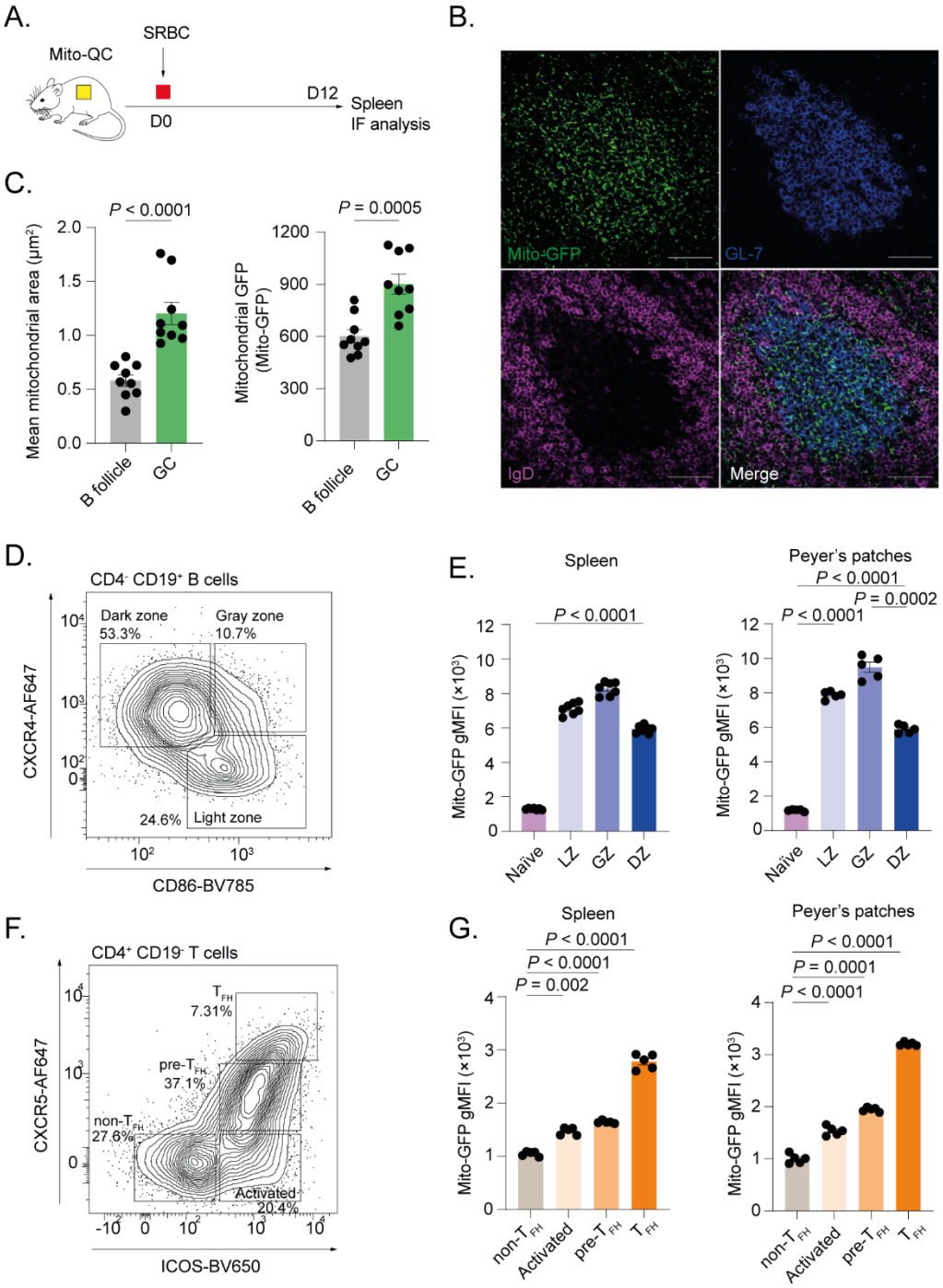


Figure 4.3. GCs are sites of enhanced mitochondrial density.
(A) Illustration depicting immunisation strategy of Mito-QC mice with SRBC for immunofluorescence at day 12. (B) Spleen sections from Mito-QC mice immunised with SRBC and analysed at day 12. Scale bar 50µm. Representative of two independent experiments. (C) Quantification of mitochondrial GFP signal intensity and area (µm^2) in GCs. Each point represents an individual GC, pooled from three individual Mito-QC mice immunised as in A. Representative of two independent experiments. (D) Gating strategy for GC B cells and their subsets in the spleen. GC and naïve B cells were gated as CD19$^+$CD38$^-$ GL-7$^+$ and CD19$^+$IgD$^+$GL-7$^-$ respectively. GC B cells from the DZ, GZ, and LZ were identified based on CXCR4 and CD86 expression signatures as depicted. (E) Comparison of gMFI of mitochondrial GFP in subsets from D in spleen and Peyer's patches, (n=5-7 mice). Data pooled from two independent experiments. (F) Gating strategy for T_{FH}, pre-T_{FH}, and non-T_{FH} cells in CD4$^+$ CD19$^-$ cells. (G) Comparison of gMFI of mitochondrial GFP in subsets from

F in spleen and Peyer's patches, (n=5 mice). Data pooled from two independent experiments. Statistical significance was calculated by unpaired two-tailed t-test (B) or ordinary one-way ANOVA with Tukey's multiple comparisons test (E,G).

4.2.4. The mitochondrial network in GC B cells is highly dynamic

To directly image the mitochondrial network and assess the differences in mitochondrial morphology and volume across B cell subsets, I isolated naive, GZ, DZ, and LZ GC B cells from Mito-QC mice immunised with SRBC (Fig. 4.4A-B). Subsequently, I resolved the mitochondrial network in 3D with an Airyscan confocal setting, which enables confocal imaging at near super-resolution. 3D mitochondrial imaging revealed that mitochondrial mass and volume were greatly elevated in the GZ subset, and GC B cells from the DZ had the lowest mitochondrial volume, in keeping with the flow cytometry profiling (Fig. 4.4C-D). Moreover, mitochondria within GC B cells were morphologically distinct, with highly polarised and fused architecture compared to those found in naïve B cells which were small and had a fragmented morphology. This was again most prominent in the GZ GC B cells (Fig. 4.4C).

These findings therefore suggest mitochondria display dynamic remodelling within GC B cells, and this peaks at the GZ stage.

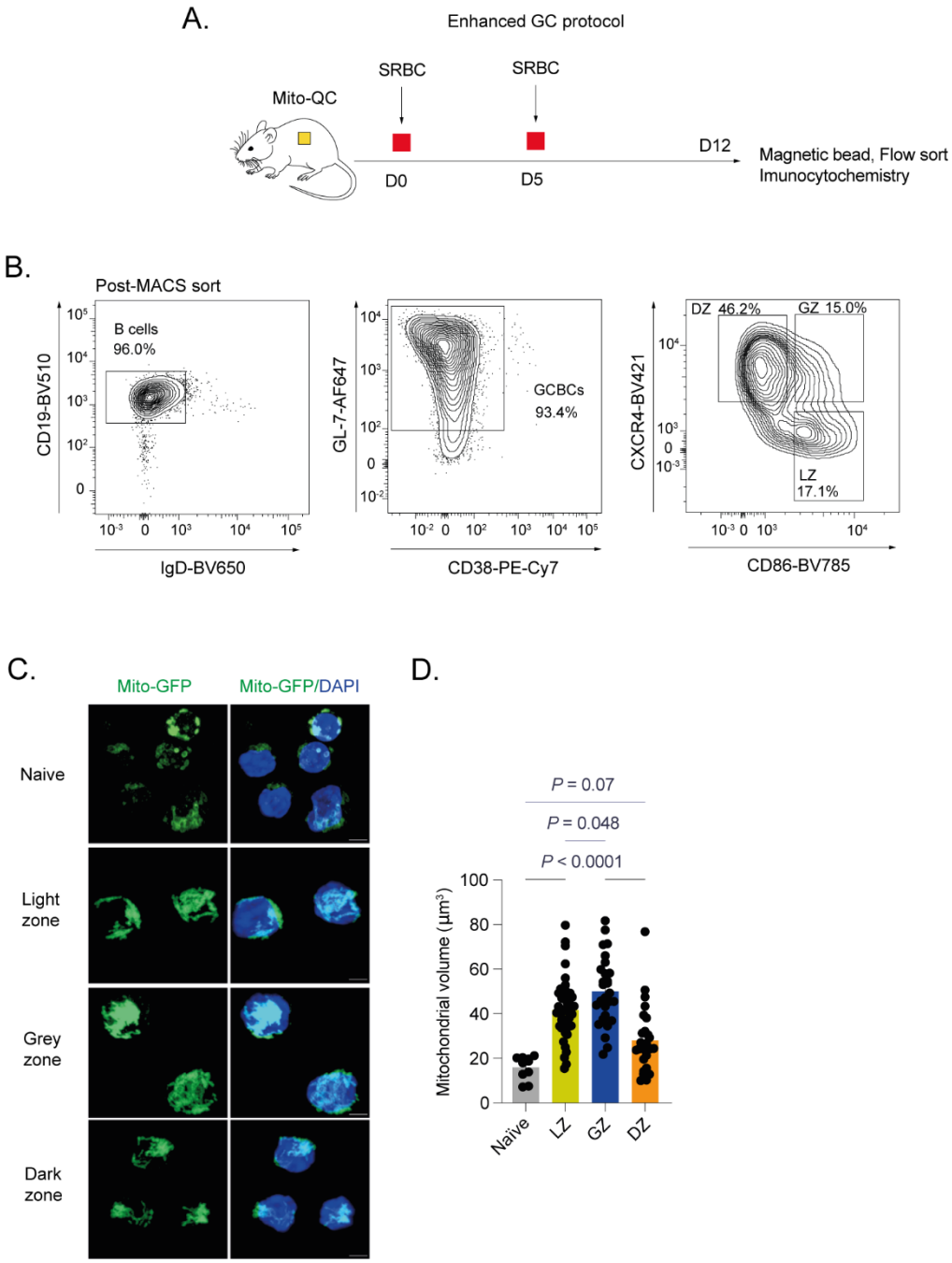


Figure 4.4. The mitochondrial network in GC B cells is highly dynamic.
(A) Schematic of the experimental design depicting enhanced SRBC immunisation. (B) Flow sorting strategy for LZ, GZ, and DZ GC B cells. (C) 3D Airyscan immunocytochemistry (ICC) images depicting the mitochondrial network (GFP) in Magnetic bead-enriched and flow sorted GC B cells (LZ, GZ, and DZ) and magnetic bead sorted naïve B cells harvested from immunised (enhanced SRBC immunisation protocol at D12) and unimmunised Mito-QC spleens, scale bar 3µm. (D) 3D mitochondrial volume (µm^3) quantification in naïve, LZ, GZ, and DZ compartments, isolated as in B. Each symbol represents one cell. Statistical significance was calculated by ordinary one-way ANOVA with Tukey's multiple comparisons test (**D**).

4.2.5. Mitochondrially-encoded proteins are increased in GC B cells

Whilst Mito-QC is a highly sensitive tool for detecting mitochondria and their degradation, the mitochondrial protein FIS1, which carries the reporter construct, is not directly associated with the bioenergetic state[191]. Thirteen protein subunits involved in the ETC are encoded by mtDNA and synthesised by the mitochondria's own translational machinery[65]. I hypothesised that the elevated rates of mitochondrial biogenesis observed in GC B cells is driven by active mitochondrial transcription and translation.

I profiled GCs from immunised Aicda-cre × Rosa26-stop-tdTomato reporter mice (Aicda-tdTomato), which have endogenously labelled GCs, by IHC (Fig. 4.5A), and found a substantial rise in levels of COX I, a mitochondrially encoded component of ETC complex IV, colocalised with translocase of outer mitochondrial membrane 20 (TOMM20) in GCs (Fig. 4.5B). Upregulation of COX I was further confirmed via 3D confocal imaging of isolated naïve and GC B cells, which also identified changes in mitochondrial density and morphology consistent with my previous analysis of Mito-QC mice (Fig. 4.5C). Intracellular flow cytometry further confirmed the significantly higher COX I levels in GC B cells compared to $IgD^{+}GL\text{-}7^{-}$ naïve B cells (Fig. 4.5D).

The mitochondrial protein composition in GC B cells, therefore, is distinctly balanced, with a substantial contribution from mitochondrially translated subunits.

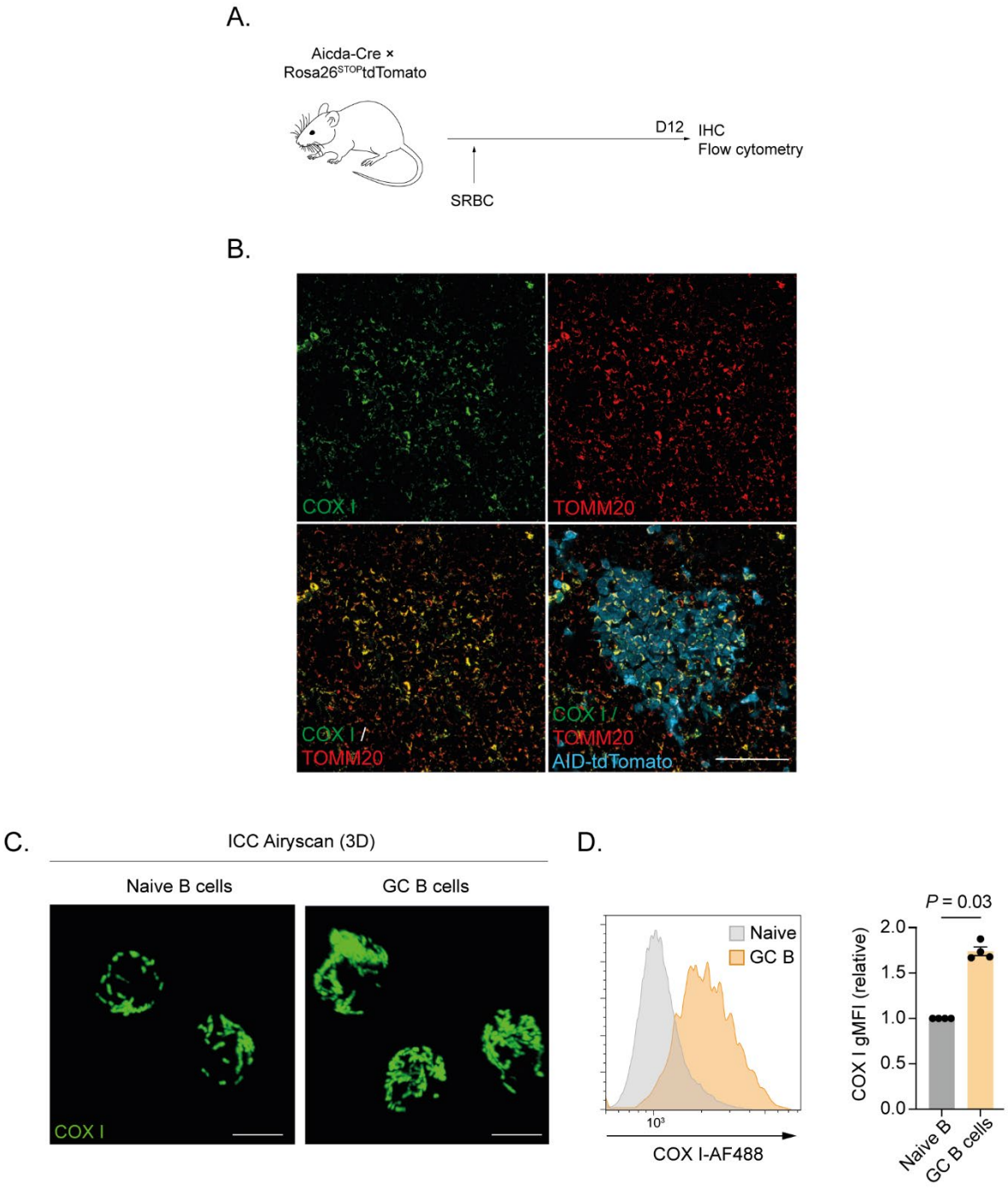


Figure 4.5. Mitochondrially-encoded proteins are increased in GC B cells. (A) Illustration depicting immunisation strategy in Aicda-tdTomato mice. (B) Spleen sections from wild type Aicda-tdTomato mice immunised with SRBC and analysed at day 12, with IHC for COX1 and TOMM20. Scale bar 50μm. Representative of two independent experiments. (C) Representative 3D Airyscan ICC images of mitochondrial network stained with COX I in isolated naïve B and GC B cells. Representative of two independent experiments. (D) Flow cytometry histogram plots and quantification of COX I protein levels in GC B cells, normalised to IgD^{+} naïve B cells (n=4). Representative of three independent experiments. Statistical significance was calculated by two-tailed Mann Whitney U test (D).

4.2.6. GC B cells show distinct mitochondrial transcription and nucleoid organisation

To directly assess mitochondrial transcription, I administered 5-ethynyl uridine (5-EU) to mice, which incorporates into newly synthesised nascent RNA, and then analysed its intracellular distribution (Fig. 4.6A). I observed a higher degree of co-localisation between 5-EU and COX I in GC B cells (Fig. 4.6B). Mitochondrial 5-EU incorporation was globally upregulated in GC B cells compared to naïve B cell counterparts (Fig. 4.6C).

Next, I determined the expression and localisation of TFAM, which governs the transcription and translation of mtDNA and plays a key role in mitochondrial biogenesis[186]. I found that TFAM was arranged in punctate structures representing mitochondrial nucleoids, which co-localised with 5-EU (Fig. 4.6B,D). These nucleoids were more abundant and larger in GC B cells (Fig. 4.6D-F), with an elliptical shape associated with active transcription (Fig. 4.6G-H)[195]. Additionally, the increased nucleoid number was confirmed by stimulated emission depletion (STED) microscopy at super-resolution (Fig. 4.6I).

Together, these findings underscore the highly active mitochondrial transcription in GC B cells, which is closely linked to the mitochondrial master regulator TFAM.

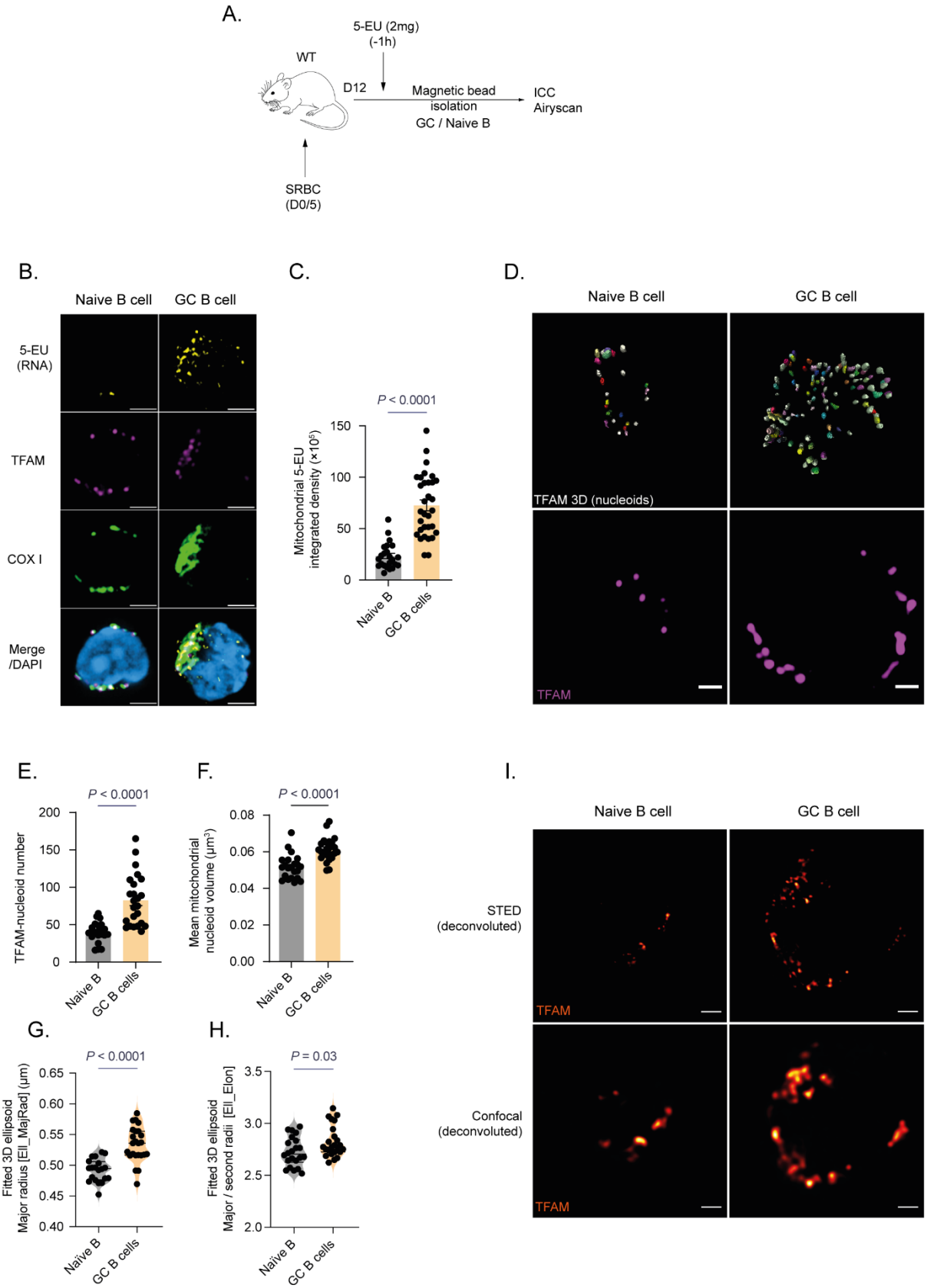

A.
5-EU (2mg)
(-1h)
WT
D12
Magnetic bead
isolation
GC / Naive B
ICC
Airyscan
SRBC
(D0/5)
B.
Naive B cell
GC B cell
5-EU
(RNA)
TFAM
COX I
Merge
/DAPI
C.
P < 0.0001
Mitochondrial 5-EU
integrated density (×10⁶)
150
100
50
0
Naive B
GC B cells
D.
Naive B cell
GC B cell
TFAM 3D (nucleoids)
TFAM
E.
P < 0.0001
TFAM-nucleoid number
200
150
100
50
0
Naive B
GC B cells
F.
P < 0.0001
Mean mitochondrial
nucleoid volume (µm³)
0.08
0.06
0.04
0.02
0.00
Naive B
GC B cells
G.
P < 0.0001
Fitted 3D ellipsoid
Major radius [Ell_MajRad] (µm)
0.65
0.60
0.55
0.50
0.45
0.40
Naive B
GC B cells
H.
P = 0.03
Fitted 3D ellipsoid
Major / second radii [Ell_Elon]
3.5
3.0
2.5
2.0
Naive B
GC B cells
I.
Naive B cell
GC B cell
STED
(deconvoluted)
Confocal
(deconvoluted)
TFAM
TFAM

Figure 4.6. GC B cells show distinct mitochondrial transcription and nucleoid organisation.
(A) Schematic depicting in vivo 5-EU administration to mice immunised with SRBC (enhanced protocol). (B) Airyscan images of in vivo 5-EU incorporation (indicating RNA synthesis), with COX I and TFAM ICC in naïve and GC B cells. Scale bar 3μm. (C) Quantification of mitochondrial 5-EU integrated signal density in naïve and GC B cells following *ex vivo* incorporation. (D) 2D Airyscan ICC images of TFAM in naïve and GC B cells, with 3D reconstruction indicating individual mitochondrial nucleoids. (E) Quantification of nucleoid number. Each symbol represents one cell. Scale bar 1μm. (F) Quantification of volume. Each symbol represents one cell. Scale bar 1μm. (G) Quantification of average major radius of mitochondrial nucleoids based on 3D fitted ellipsoid volume model. (H) Quantification of aspect ratio (major radius/second radius) of mitochondrial nucleoids based on 3D fitted ellipsoid volume model. (I) Deconvoluted confocal and STED super-resolution ICC images of TFAM in naïve and GC B cells. Scale bar 1μm. Statistical significance was calculated by unpaired two-tailed t-test.

4.2.7. B cell-specific deletion of *Tfam* in B cells: B-Tfam mice

Deletion of *Tfam* has been shown to induce mitochondrial dysfunction in nearly all cell types studied to date[81,83,84]. Whilst TFAM plays a role in preventing long-term inflammatory immunosenescence in T cells, it is not essential for their development[189]. However, its role in B cell development and function remains unknown, as is the regulation of ETC components in B cell development. To investigate this, I first conditionally deleted *Tfam* in B cells by crossing $Tfam^{LoxP}$ mice with *Cd79a-Cre* (referred to as B-Tfam), which is active from the early pro-B cell stage (Fig. 4.7A)[196].

Initial analysis of B-Tfam mice revealed they were viable, fertile, and appeared healthy without clinical signs of systemic autoimmunity. Spleen sizes in B-Tfam mice were surprisingly smaller compared to B-WT controls (Fig. 4.7B).

I confirmed the deletion of *Tfam* in mature splenic B cells via flow cytometry and immunofluorescence (Fig. 4.7C-D). Interestingly, Mitotracker CMX ROS labelling revealed a highly distinct signal distribution indicative of an altered mitochondrial network in B-Tfam B cells (Fig. 4.7D).

These findings indicate that *Tfam* deletion in B cells might regulate immune cell composition and homeostasis by altering their mitochondrial dynamics.

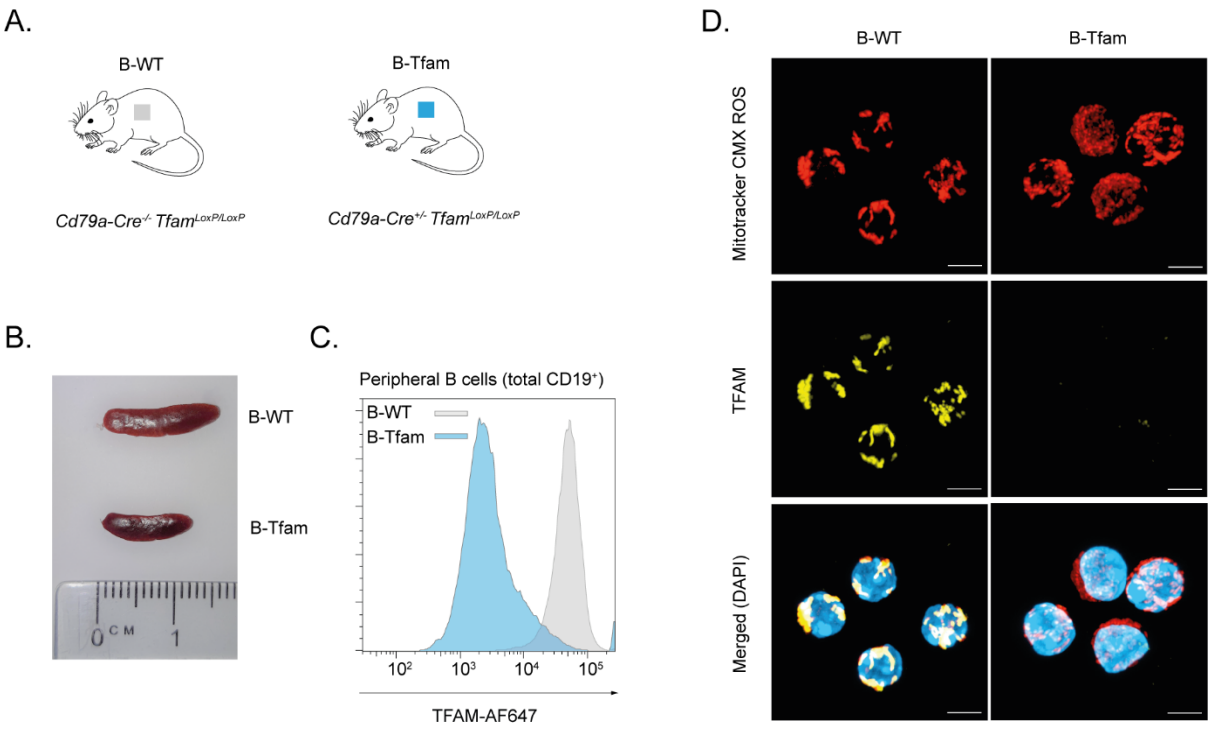


Figure 4.7. B cell-specific deletion of *Tfam* in B cells: B-Tfam mice.

(A) Schematics illustrating B cell-specific *Tfam* deletion in B-Tfam mice along with controls (B-WT). (B) Representative images of spleens from B-WT and B-Tfam mice. (C) Representative histogram of TFAM staining by intracellular flow cytometry in splenic CD19+ B cells from unimmunised B-WT and B-Tfam mice. Representative of three independent experiments. Scale bar = 3μm. (D) Airyscan ICC of B cells from unimmunised B-WT and B-Tfam mice, stained for TFAM and with Mitotracker CMX ROS. Scale bar = 3μm. Representative of three independent experiments.

4.2.8. Loss of *Tfam* leads to defective B cell numbers in the periphery

Splenic size differences in B-Tfam mice point to possible immune cell abnormalities. To investigate this further, I profiled the splenic immune cell composition in unimmunised B-Tfam and B-WT mice by flow cytometry (Fig. 4.8A). The analysis surprisingly showed a significant fall in the total number and proportion of peripheral B220^{+} B cells (Fig. 4.8B-C). The spleen is a key site for the final stages of B cell maturation, where transitional B cells differentiate into either FoB or MZB (as depicted in Fig 1.1 and illustrated in flow cytometry plots in Fig. 4.8D). Further immunophenotyping showed a severe reduction in the numbers

of both FoB and MZB cells, although their relative proportions within the B cell pool did not significantly change (Fig. 4.8E-F).

These findings suggest that loss of *Tfam* has detrimental effects on the peripheral B cell compartment, and this likely occurs due to an earlier developmental defect.

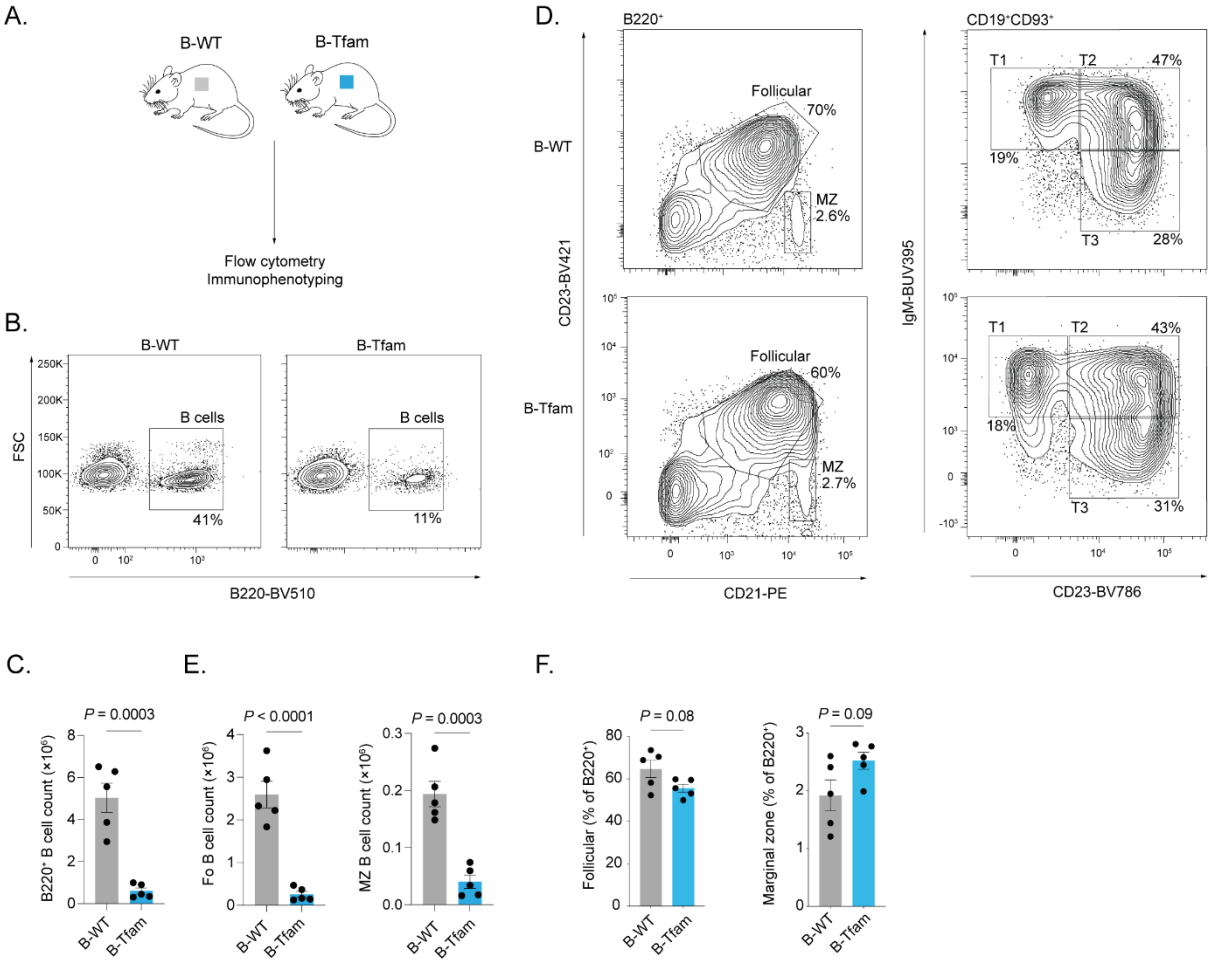


Figure 4.8. Loss of *Tfam* leads to defective B cell numbers in the periphery.

(A) Schematic illustrating experimental design of spleen immunophenotyping. (B) Representative flow cytometry plots of B220$^+$ B cells from the spleens of 6-week-old B-Tfam and B-WT mice. (C) Quantification of total splenic B cell counts. (D) Representative flow cytometry plots of splenic B cell subsets. (E) Absolute counts of follicular (CD23$^+$CD21^{int}) and MZB (CD21$^+$CD23$^-$) B cell subsets (n=5 mice). Representative of two independent experiments. (F) Frequencies of **E**. Representative of two independent experiments. Statistical significance was calculated by unpaired two-tailed t-test.

4.2.9. *Tfam* is essential during B cell development

Next, I investigated B cell precursors in the bone marrow of B-Tfam and B-WT mice (Fig. 4.9A). B cells mature in the bone marrow by undergoing several important developmental stages that involve rapid proliferation and differentiation[1] (as depicted in Fig. 4.9A). Analysis of B cell development in the bone marrow revealed an impairment in the progression from the pro-B to the pre-B cell stage, a critical checkpoint in B cell maturation that corresponds to the transition from fraction C to C' according to the Hardy classification[1] (Fig. 4.9B-C). Only a few cells were able to reach a more mature phenotype, marked by surface immunoglobulin expression (Fig. 4.9D-E). This developmental block was further reflected in the elevated numbers of precursor cells at the pro-B stage (Fr B and C) indicating a pre-block accumulation (Fig. 4.9F).

These findings therefore suggest that TFAM is required for B cells during key developmental stages in the bone marrow.

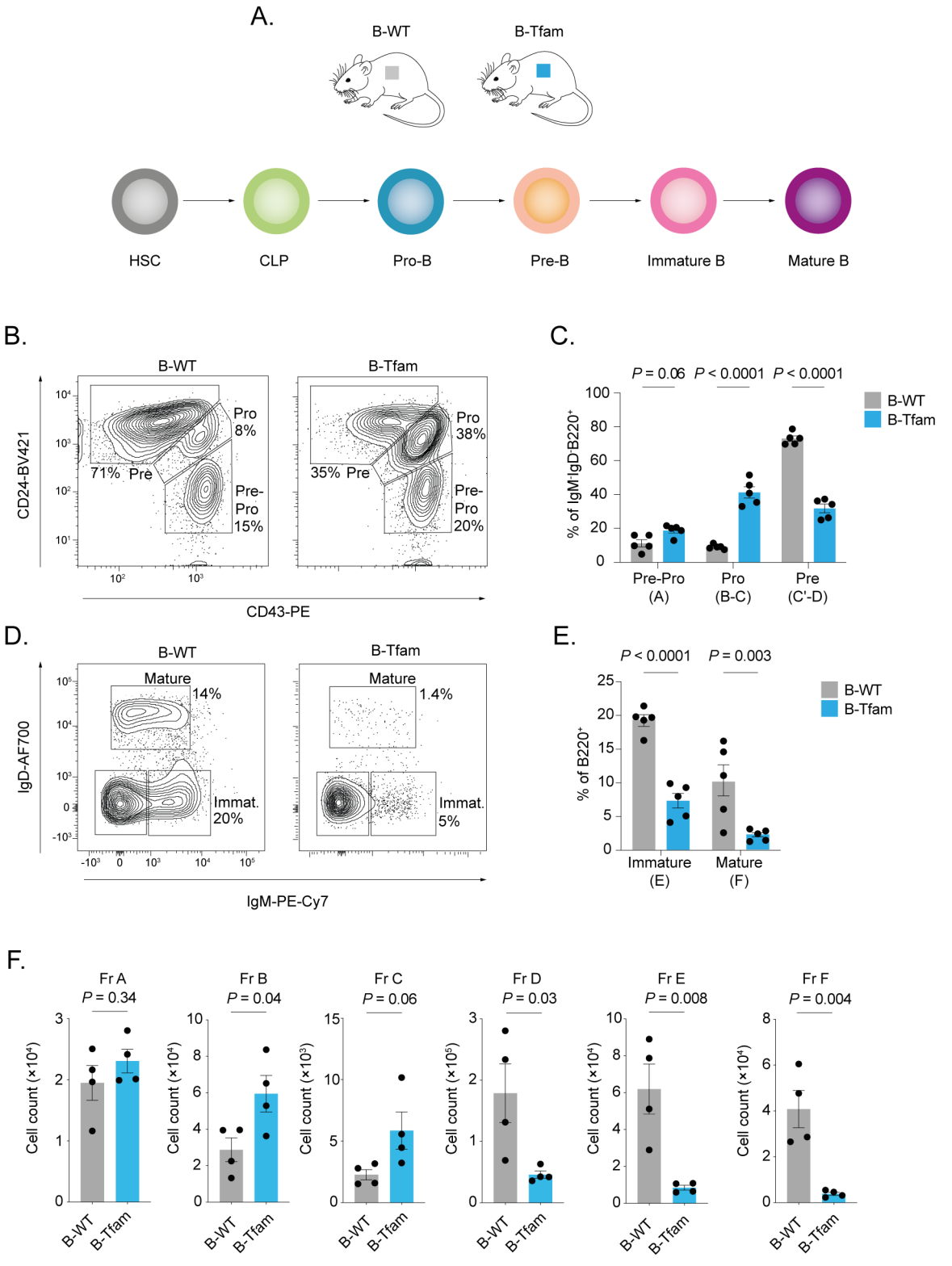


Figure 4.9. *Tfam* is essential during B cell development.
(A) Schematic illustrating B-WT and B-Tfam mice along with developmental stages of B cell precursors in the bone marrow. (B) Representative flow cytometry plots of bone marrow IgM$^-$IgD$^-$B220$^+$ pre-pro, pro and pre-B cells isolated from B-Tfam and B-WT mice. (C) Quantification of **B** (n=5 mice). Results representative of two independent experiments. Equivalent Hardy stages in parentheses. (D) Representative flow cytometry plots of bone

marrow-resident B220^{+} IgM^{+}IgD^{-} immature and B220^{+}IgD^{+} mature B cell subsets from B-WT and B-Tfam. (E) Quantification of **D** (n=5 mice). Results representative of two independent experiments. Equivalent Hardy stages in parentheses. (F) Absolute count quantification of **C** and **E** according to Hardy stages. Statistical significance was calculated by unpaired two-tailed t-test (F) or two-way ANOVA with Šidák's correction (C,E)

4.2.10. Mitochondrial homeostasis in B cells requires TFAM

To study the expression of ETC proteins during B cell development and assess the impact of *Tfam* deletion on mitochondrial processes I analysed a group of ETC proteins in bone marrow and splenic B cells from B-WT and B-Tfam mice (Fig. 4.10A). I designed and employed an extended version of the Mitoflow panel described in Chapter 3 (now detailed in Fig. 4.10B).

In B-WT bone marrow, I observed a gradual increase in the expression of most ETC proteins starting from the pre-pro B stage (Hardy Fr A), subsequently peaking at the earliest pre-B subset (fraction C′) followed by an abrupt decline in later stages (Fr D-F) (Fig. 4.10C). Notably, TFAM expression peaked early (at Fr A) suggesting it may initiate a mitochondrial transcription program that drives ETC protein upregulation. The maximum ETC protein expression coincided with the developmental block observed in B-Tfam mice at the pro- to pre-B cell transition. In B-Tfam mice, TFAM deletion was apparent from Fr A onwards in the bone marrow and carried over into peripheral subsets (Fig. 4.10C-D). As a result, mitochondrially-encoded COX I was downregulated, whilst nuclear-encoded ETC components like COX IV, Cyt c, ATP5A1, and SDHA remained unchanged or were upregulated to some extent (Fig. 4.10C).

In the periphery, ETC protein expression was comparable across transitional and FoB cells but increased in MZB cells (Fig. 4.10D). TFAM deletion led to a broad upregulation of nuclear-encoded ETC proteins, which was highly robust in MZB cells. This revealed an imbalance between nuclear- and mitochondrially-encoded proteins within the same ETC complex, reflected in the mismatch between COX I and COX IV levels in complex IV. Moreover, I observed a rise in UPR^{mt}-associated proteins, including heat shock protein 60 (HSP60) and mitochondrial 70kDa heat shock protein (mtHSP70) (Fig. 4.10D).

Seahorse extracellular flux analysis of unstimulated peripheral B cells surprisingly showed no difference in OCR, but there were signs of upregulated glycolysis reflected by increased ECAR in B-Tfam mice (Fig. 4.10E-G). This suggests under conditions of low energy demand, B cells can still achieve respiratory compensation despite a substantial reduction in mitochondrial protein translation.

Taken together, these results emphasise the dynamic balance of ETC components during B cell development and highlight the crucial role of TFAM in the expression of mitochondrially-encoded proteins.

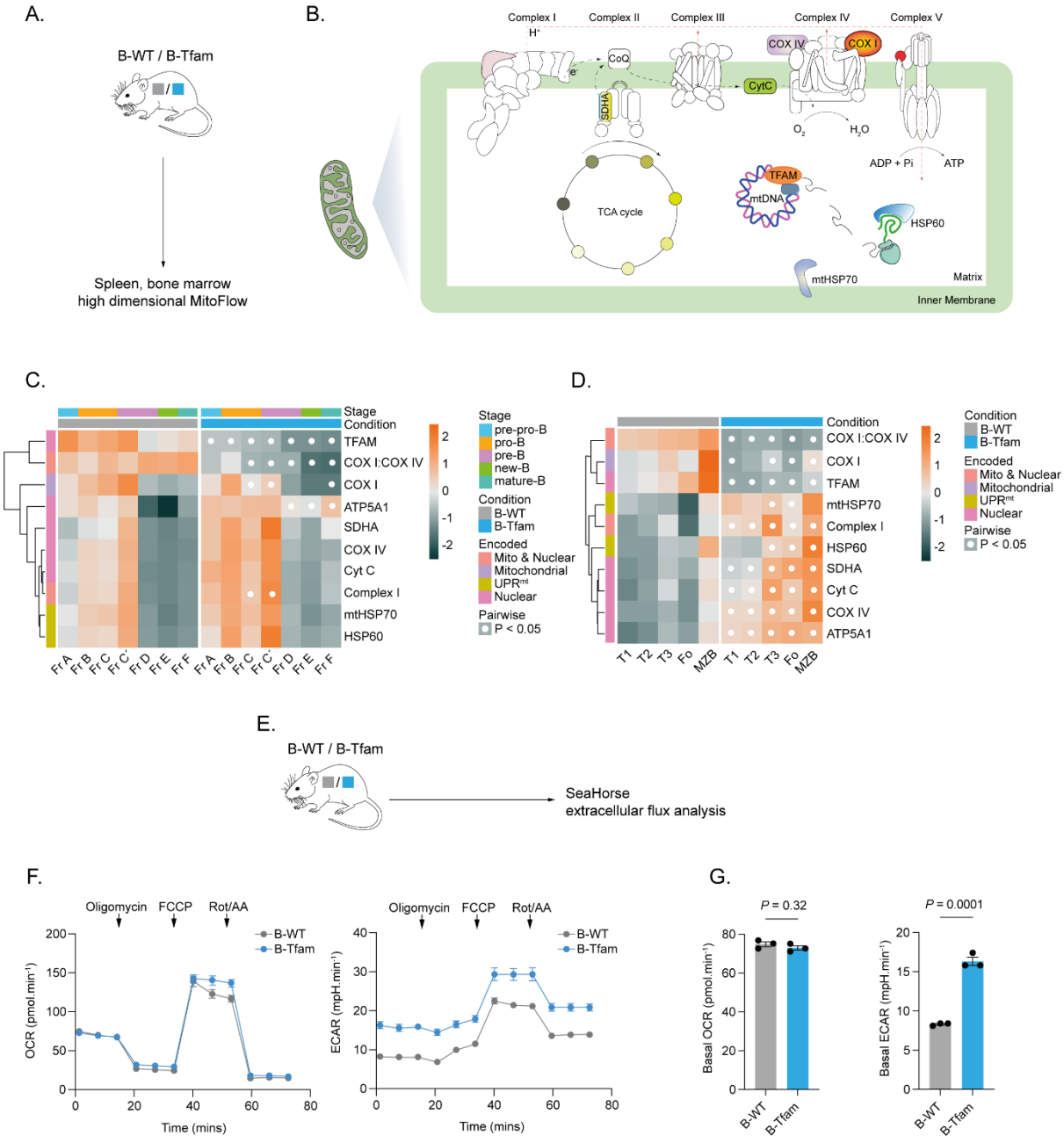


Figure 4.10. Mitochondrial homeostasis in B cells requires TFAM.
(A**)** Schematic of experimental design for Mitoflow analysis on spleen and bone marrow from unimmunised B-WT and B-Asns mice. (B) Illustration depicting key mitochondrial proteins included in the Mitoflow panels. (C) Heatmap of row Z-scores for gMFI of indicated mitochondrial proteins, measured by flow cytometry in bone marrow B cell subsets (Hardy stages) of B-WT and B-Tfam mice (mean of two biological replicates). Results representative of two independent experiments with n=4 mice per group in total. (D) Heatmap of row Z-scores for gMFI of indicated mitochondrial proteins, measured by flow cytometry in splenic B cell subsets of unimmunised B-WT and B-Tfam mice (mean of two biological replicates). Results representative of two independent experiments with n=3 mice per group in total. (E) Schematic of experimental design for SeaHorse analysis on unstimulated B cells isolated from unimmunised from B-WT and B-Asns mice. (F) OCR and ECAR measurements of unstimulated naïve B cells from B-Tfam and B-WT mice, representative of two independent experiments. (G) Quantification of **F** (n=3 mice). Statistical significance was calculated by unpaired two-tailed t-test (G) or two-way ANOVA with Tukey's correction (C-D).

4.2.11. TFAM is critical for the GC reaction

I then assessed the capacity of B-Tfam mice to generate GCs. After immunising them with SRBCs, I evaluated GC formation via immunofluorescence and flow cytometry on day 12 (Fig. 4.11A). Examination of B-Tfam spleens revealed smaller and fewer B cell follicles and a near-total absence of GL-7$^+$ GCs compared to B-WT mice (Fig. 4.11B), a finding also confirmed by flow cytometry (Fig. 4.11C).

Having identified the deleterious effects of TFAM ablation on the peripheral B cell compartment, I considered this a potential confounding factor for analysing GC responses. Therefore, to specifically study the role of TFAM in the GC B cell compartment, targeted deletion of *Tfam* after B cell maturation was achieved by generating Aicda-Cre × Tfam flox × Rosa26-stop-tdTomato × Prdm1-mVenus mice (referred to as Aicda-Tfam). This model allowed me to simultaneously identify cells that have expressed *Aicda* (activated, GC, memory B, and plasma cells) and/or currently express Blimp-1 (plasmablasts), detected by the fluorescent reporter proteins tdTomato and mVenus, respectively (Fig. 4.11D).

I then immunised Aicda-Tfam mice and appropriate controls (Aicda-WT) with SRBC and analysed them on day 12. Flow cytometry revealed a substantial reduction in the generation of CD19$^+$IgD$^-$CD38$^-$tdTomato$^+$ GC B cells in Aicda-Tfam mice, whilst naïve B cell numbers were unaffected (Fig. 4.11E-F).

Immunofluorescence staining of Aicda-Tfam spleen sections showed small GCs which were also less numerous. However, B cell follicles stained with anti-CD21/35 appeared intact, in keeping with *Tfam* deletion post-maturation (Fig. 4.11G-H).

Overall, TFAM is essential for the GC reaction independent of its roles in B cell development.

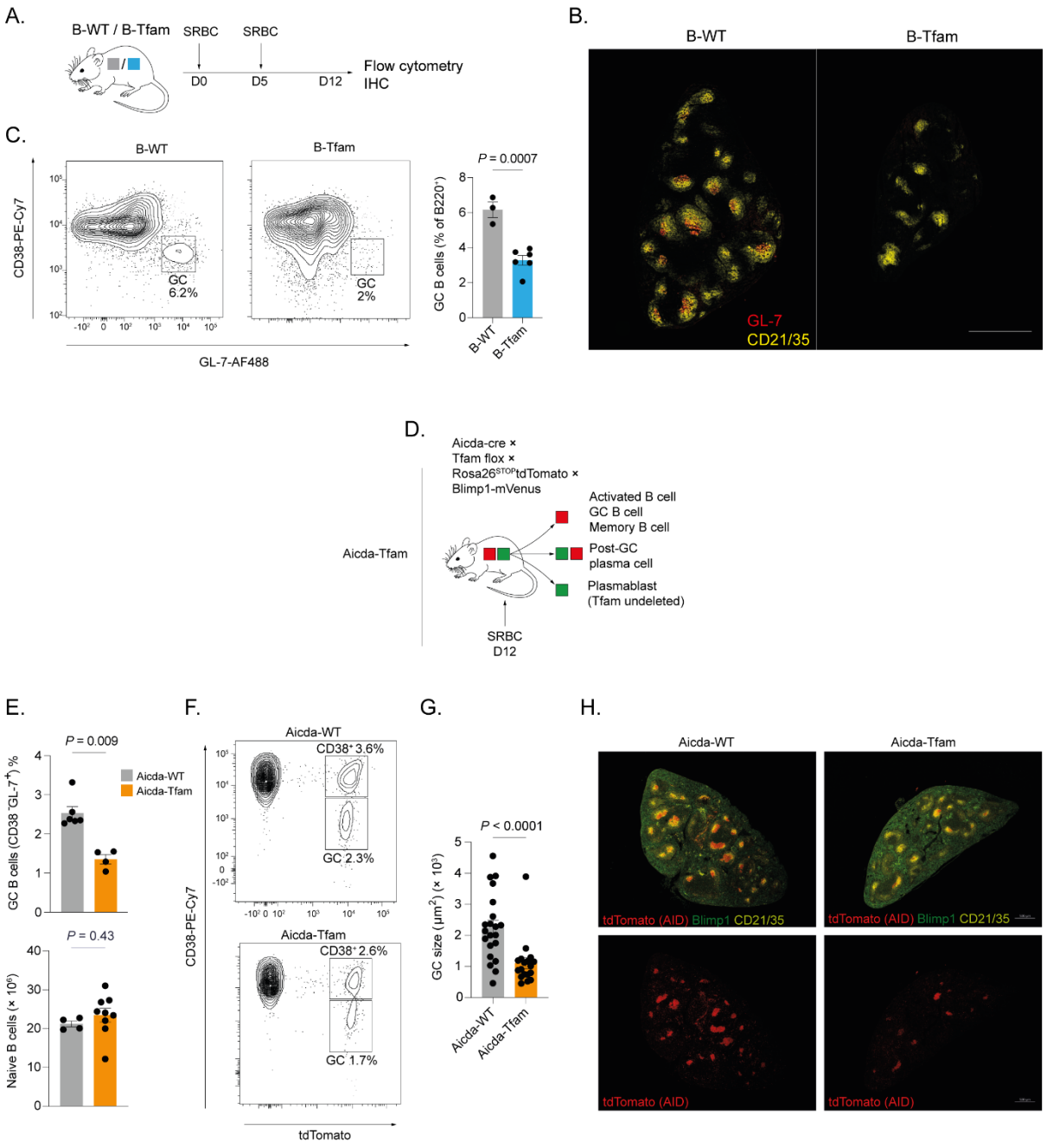


Figure 4.11. TFAM is critical for the GC reaction.
(A) Schematic illustrating immunisation strategy in B-WT and B-Tfam mice with SRBC (at days 0 and 5, enhanced protocol) with the readout on day 12. (B) Representative tile-scan images of spleen sections from B-Tfam and B-WT mice depicting GL-7$^+$ GCs and CD21/35$^+$ B cell follicles. Scale bar 500μm. Results representative of two independent experiments. (C) Flow cytometry gating strategy and quantification of CD38$^-$GL-7$^+$ GC B cells in spleens of immunised B-Tfam (n=6) and B-WT mice (n=3). Results representative of two independent experiments. (D) Schematic of Aicda-Tfam mouse (Aicda-cre × Tfam flox × Rosa26^{STOP}tdTomato × Blimp1-mVenus). Aicda-WT and Aicda-Tfam mice were immunised with SRBCs intraperitoneally, and on day 12 spleens were analysed by flow cytometry and/or immunohistochemistry (IHC). (E) Quantification of GC B cell frequencies in Aicda-WT (n=5 mice) and Aicda-Tfam (n=4 mice). Results representative of three independent experiments. (F) Representative flow cytometry plots for the identification of GC B cells as

$CD38^{-}tdTomato^{+}$. (G) Quantification of GC area (μm^2) based on tdTomato signal in Aicda-WT and Aicda-Tfam mice. Each dot represents an individual GC pooled from n=3 mice. Data pooled from two independent experiments. (H) Representative IHC images of spleen sections from Aicda-Tfam and Aicda-WT mice. Scale bar 500μm. Representative of three independent experiments. Statistical significance was calculated by unpaired two-tailed t-test.

4.2.12. Antigen-specific humoral responses are mediated by TFAM

Next, I investigated antigen-specific GC formation by immunising mice with NP-CGG, a model antigen system introduced in Chapter 3 (Fig. 4.12A). After 14 days, Aicda-Tfam mice exhibited a significant reduction in the proportion and absolute numbers of NP-binding GC B cells (Fig. 4.12B-C). The levels of IgG1 antibodies specific to NP_{20} were also significantly lower. An even greater reduction was found in NP_2-binding antibody fractions (Fig. 4.12D-F). This indicated impaired affinity maturation as reflected by decreased binding of IgG1 antibodies to NP_{1-4} relative to $NP_{>20}$ (Fig. 4.12G). However, there was no difference in IgM anti-NP antibodies, in keeping with the extrafollicular origin of this response produced by plasmablasts (Fig. 4.12H). These findings therefore highlight the requirement of TFAM for effective antigen-specific GC and antibody responses.

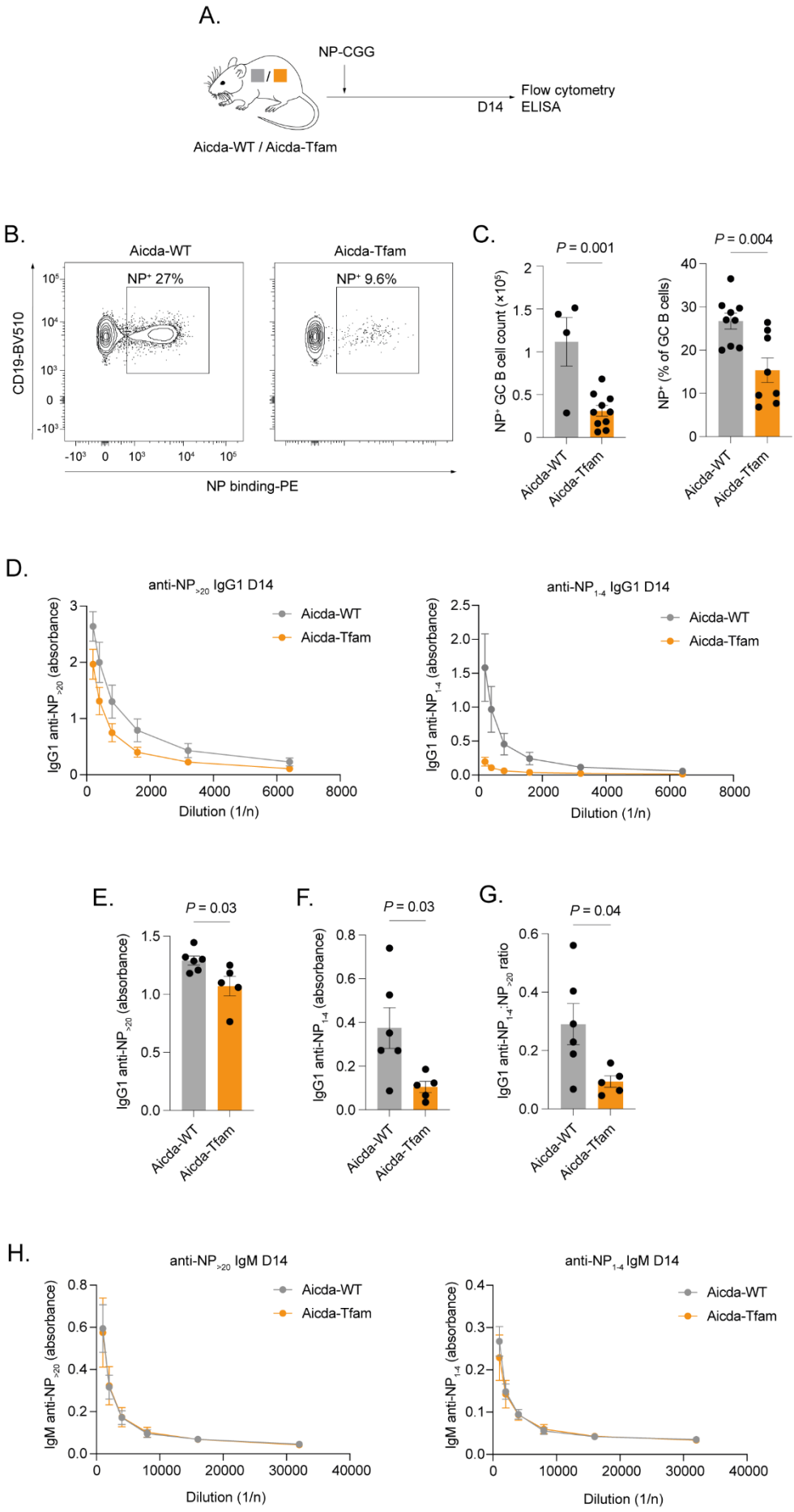

A.
NP-CGG
Flow cytometry
D14
ELISA
Aicda-WT / Aicda-Tfam
B.
Aicda-WT
Aicda-Tfam
NP+ 27%
NP+ 9.6%
CD19-BV510
NP binding-PE
C.
P = 0.001
P = 0.004
NP+ GC B cell count (×10⁵)
NP+ (% of GC B cells)
Aicda-WT
Aicda-Tfam
D.
anti-NP>20 IgG1 D14
anti-NP1-4 IgG1 D14
IgG1 anti-NP>20 (absorbance)
IgG1 anti-NP1-4 (absorbance)
Dilution (1/n)
Aicda-WT
Aicda-Tfam
E.
P = 0.03
IgG1 anti-NP>20 (absorbance)
F.
P = 0.03
IgG1 anti-NP1-4 (absorbance)
G.
P = 0.04
IgG1 anti-NP1-4:NP>20 ratio
H.
anti-NP>20 IgM D14
anti-NP1-4 IgM D14
IgM anti-NP>20 (absorbance)
IgM anti-NP1-4 (absorbance)
Dilution (1/n)

Figure 4.12. Antigen-specific humoral responses are mediated by TFAM.
(A) Aicda-WT and Aicda-Tfam mice were immunised with 50μg NP-CGG with Alum (at 1:1 ratio) intraperitoneally, and on day 14 spleens were harvested for flow cytometry and IHC analyses. (B) Representative flow cytometry plots depicting $CD19^{+}CD38^{-}GL\text{-}7^{+}$ GC B cells binding NP-PE from Aicda-Tfam (n=8) or Aicda-WT (n=9). (C) Quantification of NP-specific GC B cell counts and frequencies. Data pooled from three independent experiments. (D) ELISA dilution curve of IgG1 anti-NP antibodies detected by binding to $NP_{1\text{-}4}$-BSA and $NP_{>20}$-BSA respectively in sera from Aicda-Tfam (n=4) and Aicda-WT mice (n=3) at day 14 following NP-CGG immunisation. Data representative of two independent experiments. (E) ELISA quantification of IgG1 anti-NP antibodies detected by binding to $NP_{>20}$-BSA. Data pooled from two independent experiments. (F) Quantification of IgG1 anti-NP antibodies detected by binding $NP_{1\text{-}4}$. Data pooled from two independent experiments. (G) ELISA quantification and comparison of the ratio of IgG1 NP-specific high-affinity antibodies to low-affinity antibodies detected by binding to $NP_{1\text{-}4}$ and $NP_{>20}$ antigens respectively from Aicda-WT (n=6) and Aicda-Tfam (n=5). Data pooled from two independent experiments. (H) ELISA dilution curve of IgM anti-NP antibodies detected by binding to $NP_{1\text{-}4}$-BSA and $NP_{>20}$-BSA respectively in sera from Aicda-Tfam (n=4) and Aicda-WT mice (n=3) at day 14 following NP-CGG immunisation. Data representative of two independent experiments. Statistical significance was calculated by unpaired two-tailed t-test.

4.2.13. Plasma cell development requires *Tfam*

The plasma cell compartment is responsible for antibody production. Whilst antigen-specific IgG1 antibodies arise from GC-derived plasma cells, the IgM response is largely maintained by extrafollicular plasmablasts. Differentiating between these two types of plasma cells can be challenging with conventional immunophenotyping methods; however, permanent tdTomato labelling of GC B cells in the *Aicda* reporter system allows for lineage tracing and distinguishes between the two types. By taking advantage of this, I observed that clusters of plasma cells in the splenic cords were significantly smaller in Aicda-Tfam mice, and Blimp1-mVenus^{+}tdTomato^{+} cells were poorly represented, consistent with a lower contribution from GCs. Flow cytometry analysis pointed to a similar outcome (Fig. 4.13A-C). The proportion of $CD138^{+}$ tdTomato^{+} long-lived plasma cells in the bone marrow was also correspondingly declined (Fig. 4.13D). Consistent with the unchanged IgM levels, tdTomato-negative plasmablasts, which never expressed AID, thus are not of GC origin, were not significantly affected in Aicda-Tfam mice, unlike GC-derived tdTomato^{+} plasma cells (Fig. 4.13E-F). Additionally, the ratio of PCs to GC B cells was decreased, suggesting further disruption of GC output (Fig. 4.13G). Overall, these results illustrate that plasma cell output from GCs is TFAM-dependent.

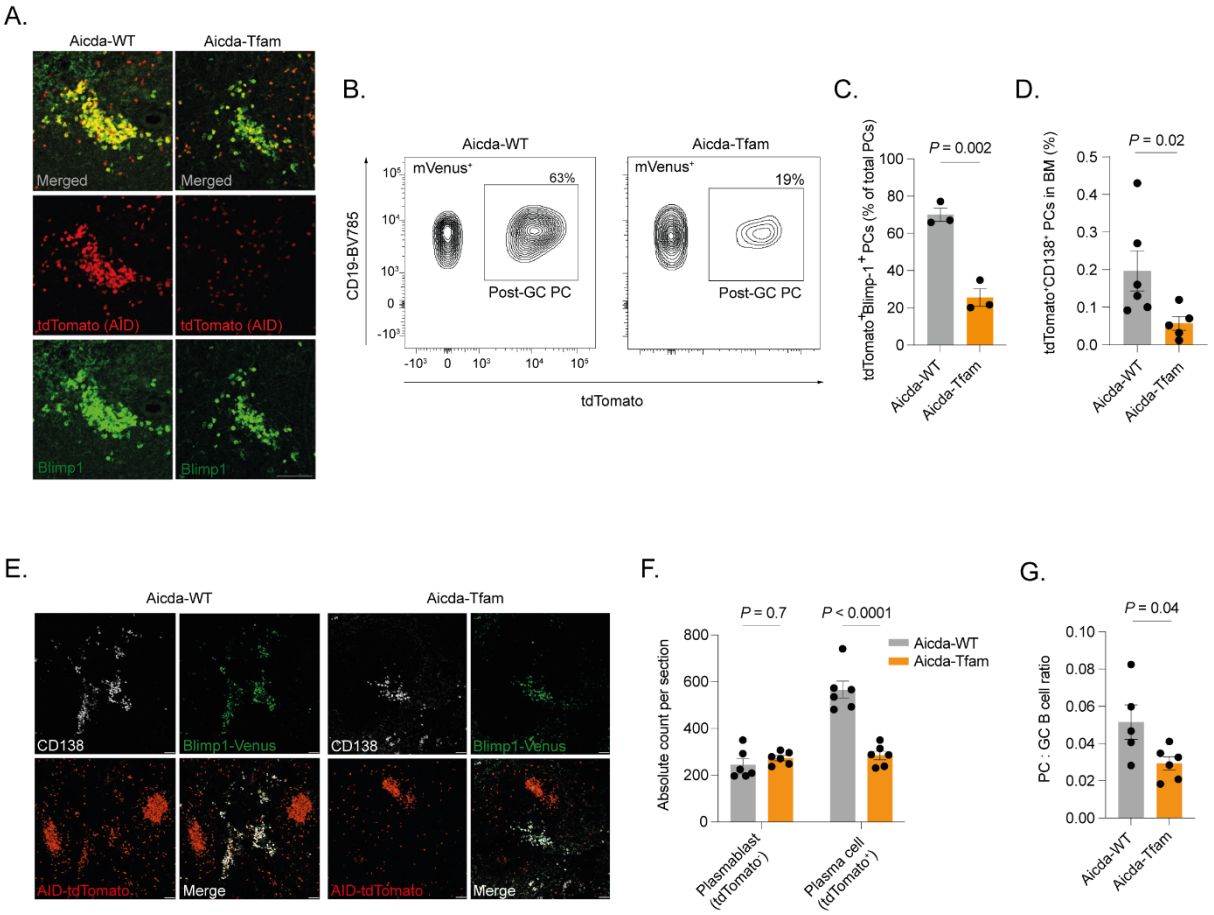


Figure 4.13. Plasma cell development requires *Tfam*.
(A) Airyscan images of plasma cell clusters in red pulp of spleen sections. tdTomato$^+$Blimp1-mVenus$^+$ double positive cells indicate post-GC plasma cells. Scale bar 75µm. (B) Representative flow cytometry plots depicting tdTomato$^+$ Blimp1-mVenus$^+$ post-GC plasma cells within the Dump$^-$mVenus-Blimp1$^+$ cell compartment. (C) Comparison of tdTomato$^+$ proportion within Dump$^-$mVenus-Blimp1$^+$ PC compartment (n=3). Data cumulative of four independent experiments. (D) Quantification of tdTomato+CD138+ plasma cells in bone marrow, expressed as a percentage of IgD$^-$Dump$^-$, in Aicda-WT and Aicda-Tfam mice immunised with SRBC and analysed at day 12. Data representative of two independent experiments. (E) Airyscan images of plasma cell clusters in red pulp of spleen sections following NP-CGG immunisation (day 14). (F) Absolute count quantification of tdTomato+Blimp1-mVenus$^+$CD138$^+$ post-GC plasma cells and tdTomato-Blimp1-mVenus$^+$CD138$^+$ plasmablasts. Each point indicates count per non-serial splenic section, pooled from n=3 mice. Data cumulative of two independent experiments. (G) Flow cytometric quantification of the ratio of GC B cells to post-GC plasma cells (IRF4$^+$tdTomato$^+$) in Aicda-Tfam (n=6 mice) and Aicda-WT (n=4 mice). Statistical significance was calculated by unpaired two-tailed t-test (C,D,G) or two-way ANOVA with Šidák's multiple comparison test (F).

4.2.14. TFAM is essential for the emergence of memory B cell responses

After establishing that the GC reaction was perturbed in B-Tfam mice, I asked whether the loss of *Tfam* affected B cell memory and immunised Aicda-Tfam and Aicda-WT mice with NP-CGG in alum, followed by a booster dose in PBS at day 30 (Fig. 4.14A). By day 49, I observed a decrease in IgG1 anti-NP antibodies reactive to NP_{1-4} and $NP_{>20}$, which indicated defective affinity maturation and largely reproduced the measurements from day 14 (Fig. 4.14B). Similarly, by day 70, there were fewer NP-binding $CD38^{+}IgG1^{+}$ memory B cells, especially those that were $tdTomato^{+}$ and, therefore, of GC origin (Fig. 4.14C-E). Additionally, the number of plasma cells in the bone marrow was significantly reduced at day 70, suggesting defective long-lived humoral immunity (Fig. 4.14F).

Overall, these results demonstrate the critical role of TFAM in maintaining both humoral and cellular arms of B cell memory.

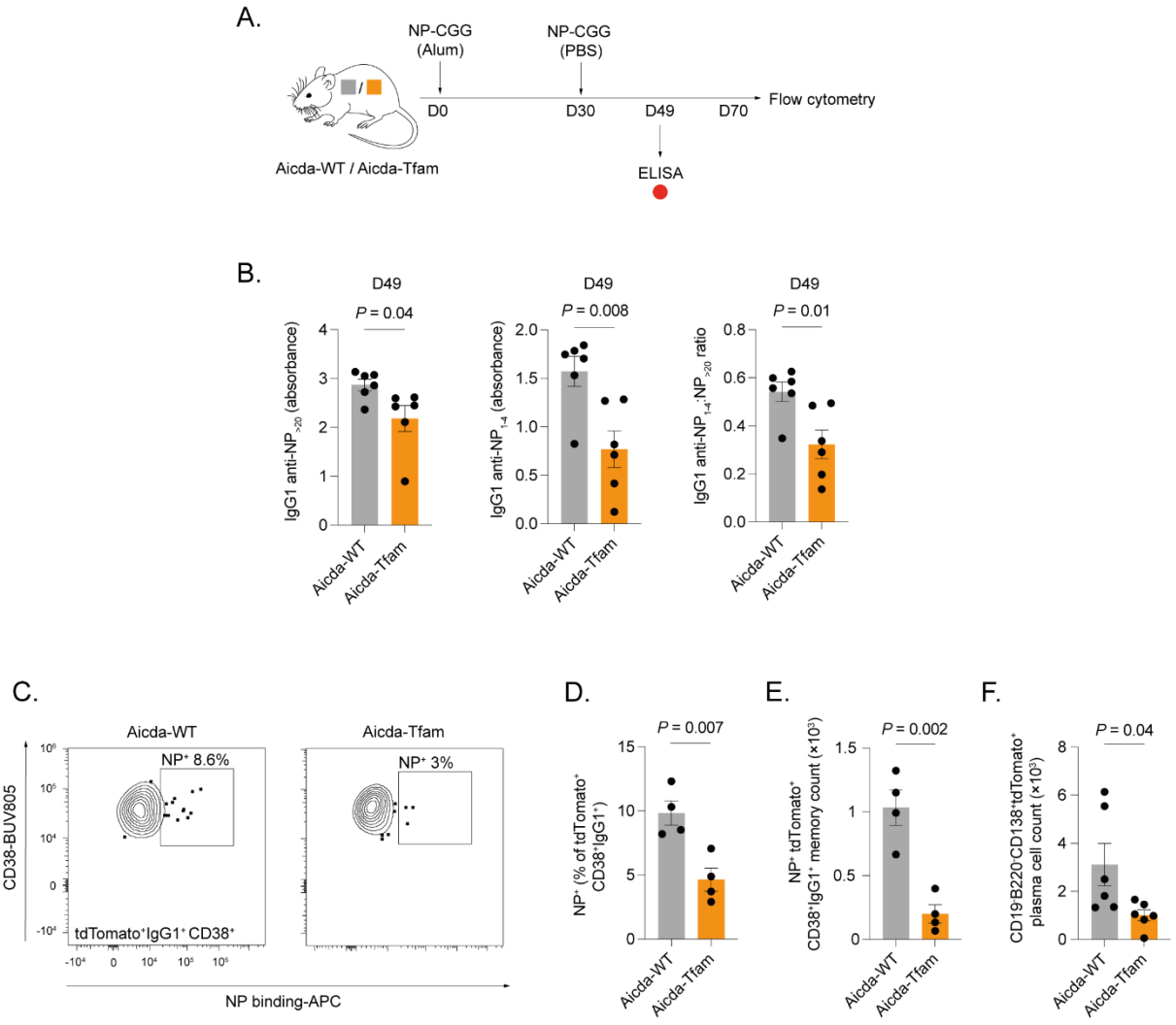


Figure 4.14. TFAM is essential for the emergence of memory B cell responses.

(A) Aicda-WT and Aicda-Tfam mice were immunised with 50µg NP-CGG with Alum (at 1:1 ratio) intraperitoneally, and on day 30 boosted with 50µg NP-CGG in PBS. Spleens and bone marrow were harvested for flow cytometry at day 70. (B) ELISA quantification of IgG1 anti-NP antibodies detected by binding to $NP_{1\text{-}4}$-BSA and $NP_{>20}$-BSA respectively in sera from Aicda-Tfam and Aicda-WT mice (n=6) and their ratio at day 49 following NP-CGG immunisation. Data pooled from two independent experiments. (C) Representative flow cytometry plots depicting tdTomato$^+$ IgG1$^+$ CD38$^+$ memory B cells binding NP-APC from Aicda-WT and Aicda-Tfam mice. (D) Proportional comparison of NP-binding within CD38$^+$ IgG1$^+$ tdTomato$^+$ memory B cells from Aicda-WT and Aicda-Tfam mice (n=4). Cumulative of two independent experiments. (E) Absolute count quantification of D. (F) Absolute plasma cell counts in bone marrow of Aicda-WT and Aicda-Tfam (n=6) at day 70. Representative of two independent experiments. Statistical significance was calculated by unpaired two-tailed t-test.

4.2.15. Rates of apoptosis and cell division remain unaffected in TFAM deficiency

GCs are sites of active cell death and mitochondria are critical regulators of apoptosis, yet surprisingly, the apoptosis rate in Aicda-Tfam GC B cells was similar to that of Aicda-WT controls when assessed by activated caspase 3 labelling (Fig. 4.15A). *In situ* terminal deoxynucleotidyl transferase dUTP nick end labelling (TUNEL) staining also showed comparable apoptosis (Fig. 4.15B). I further assessed the cell cycle dynamics of Aicda-Tfam GC B cells and examined G2 and M phases by measuring cyclin B1 and phospho-H3 expression, which were not significantly different between Aicda-Tfam and Aicda-WT mice (Fig. 4.15C-D). Additionally, EdU incorporation, an indicator of S phase, remained unaffected (Fig. 4.15E-F).

These findings indicate that whilst loss of *Tfam* severely impairs GC B cell differentiation and output, these defects were not primarily linked to proliferation or survival of cells already at the GC stage.

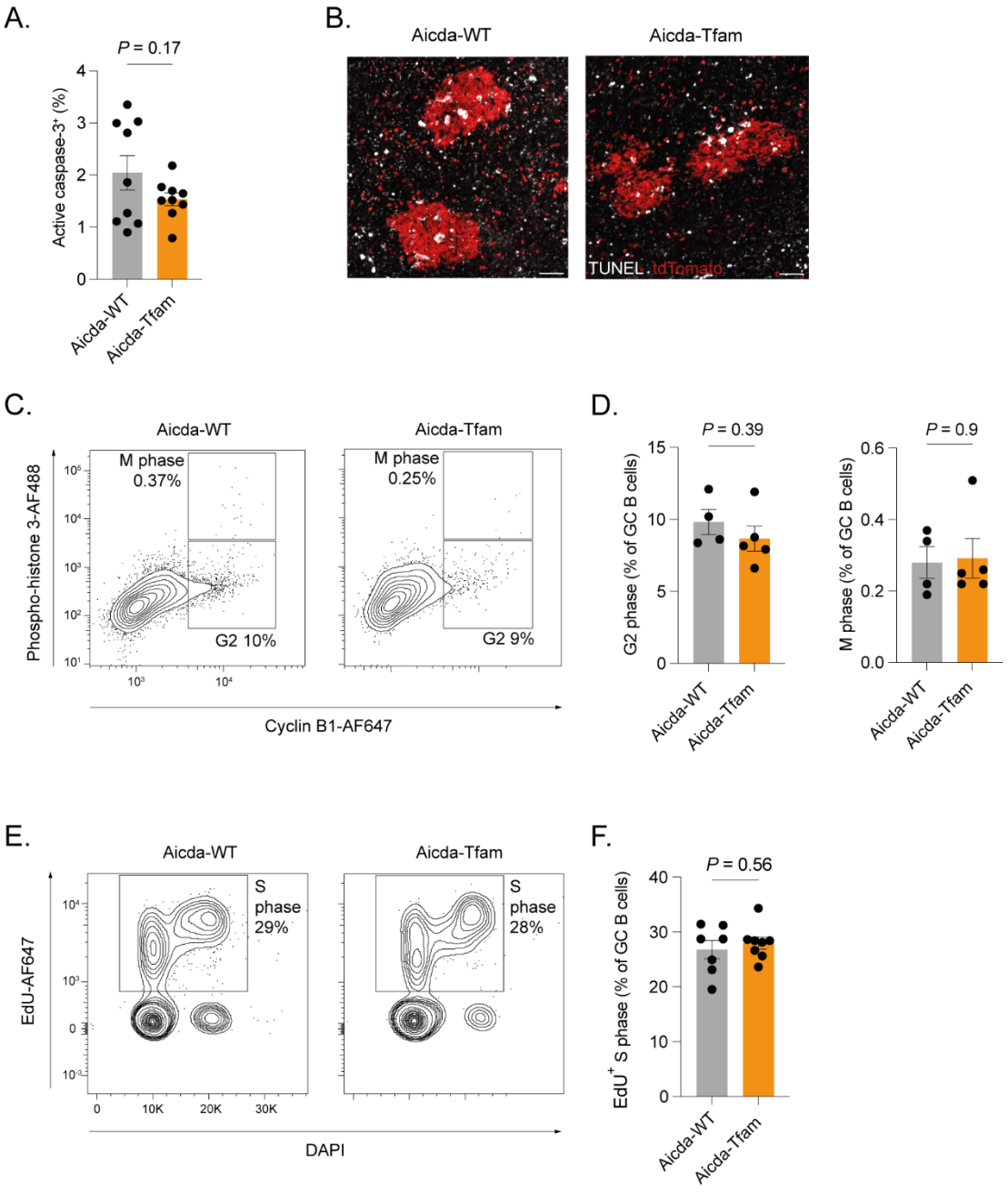


Figure 4.15. Rates of apoptosis and cell division remain unaffected in TFAM deficiency.
(A) Quantification of active (cleaved) caspase 3^+ apoptotic GC B cells as a percentage of total GC B cells in Aicda-Tfam and Aicda-WT mice (n=9). Data pooled from two independent experiments. (B) IHC images of in situ TUNEL assay on Aicda-WT and Aicda-Tfam spleens following immunisation. Scale bar 50μm. Representative of two independent experimental. (C) Representative flow cytometry plots depicting identification of M and G2 cell cycle stages in GC B cells based on phospho-histone 3 and cyclin B1 expression from Aicda-WT and Aicda-Tfam mice (n=4). (D) Quantification of **C**. Data representative of two independent experiments. (E) Representative flow cytometry plots depicting identification of S phase cell cycle stage in GC B cells from Aicda-WT and Aicda-Tfam mice, based on EdU and DAPI uptake (n=7). Data representative of two independent experiments. (F) Quantification of **E**. Statistical significance was calculated by unpaired two-tailed t-test (C,D,G) or two-way ANOVA with Šidák's multiple comparison test (F).

4.2.16. TFAM regulates the GC transcriptional program

To investigate the impact of *Tfam* deletion on the transcriptional program of GC B cells, I conducted a combined single-cell gene expression profiling and V(D)J sequencing experiment. I immunised Aicda-Tfam and Aicda-WT mice with NP-CGG, then sorted tdTomato^{+} cells at day 14 (Fig. 4.16A). This population includes B cells that have expressed *Aicda* such as pre-GC, GC, memory, and plasma cells. A total of 9,948 cells from Aicda-Tfam and 9,667 cells from Aicda-WT mice were sequenced. After the integration of the two experimental groups, a total of 9 shared clusters were identified, broadly belonging to GC B cell, CD38+ non-GC cell, and plasma cell subsets (Fig. 4.16B-C). Interestingly, Cluster 0 (C0), which exhibited markers suggesting an activated precursor (AP) state (such as *Ighd, Ccr6, Gpr183, Cd38*, Sell, and low levels of *Bcl6*), was substantially expanded in Aicda-Tfam mice compared to Aicda-WT mice (Fig. 4.16D).

Differential gene expression analysis in C0 revealed extensive dysregulation of mitochondrial gene signatures in Aicda-Tfam mice, consistent with the role of TFAM as a regulator of mitochondrial transcription (Fig. 4.16E). Pathway analysis using Single cell pathway analysis (SCPA) demonstrated significant downregulation of translation initiation and elongation gene sets (Fig. 4.16F). Gene components of the AP-1 signalling pathway, including *Jun*, *Junb*, and *Fos*, were all significantly upregulated. The AP-1 pathway is known to be upregulated by cellular stress, ROS, and other environmental cues (Fig. 4.16G).

Analysis of the main GC cluster (C1) showed similar dysregulation of mitochondrial and ribosomal gene transcription, with upregulation of *Jun, Fos, and Junb* (Fig. 4.16H-I). Importantly, *Rgs1* (regulator of G-protein signalling-1), a GTPase activating protein crucial for restraining cell movement in response to chemokines (e.g., CXCL12), was upregulated in Aicda-Tfam cells (Fig. 4.16J). Conversely, regulatory genes of actin cytoskeleton *Coro1a* (coronin-1) and *Arpc3* (actin-related protein 2/3 complex subunit 3), were downregulated. I also observed reduced *Mef2b*, an activator of GC enhancer genes, and *Bcl6* during GC B cell commitment (Fig. 4.16H).

In other clusters, similar dysregulation of mitochondrial and ribosomal genes was noted in Aicda-Tfam cells. However, no compensatory upregulation of glycolysis or other metabolic pathway genes were found.

Therefore, transcriptional programs during GC entry and beyond are regulated by TFAM.

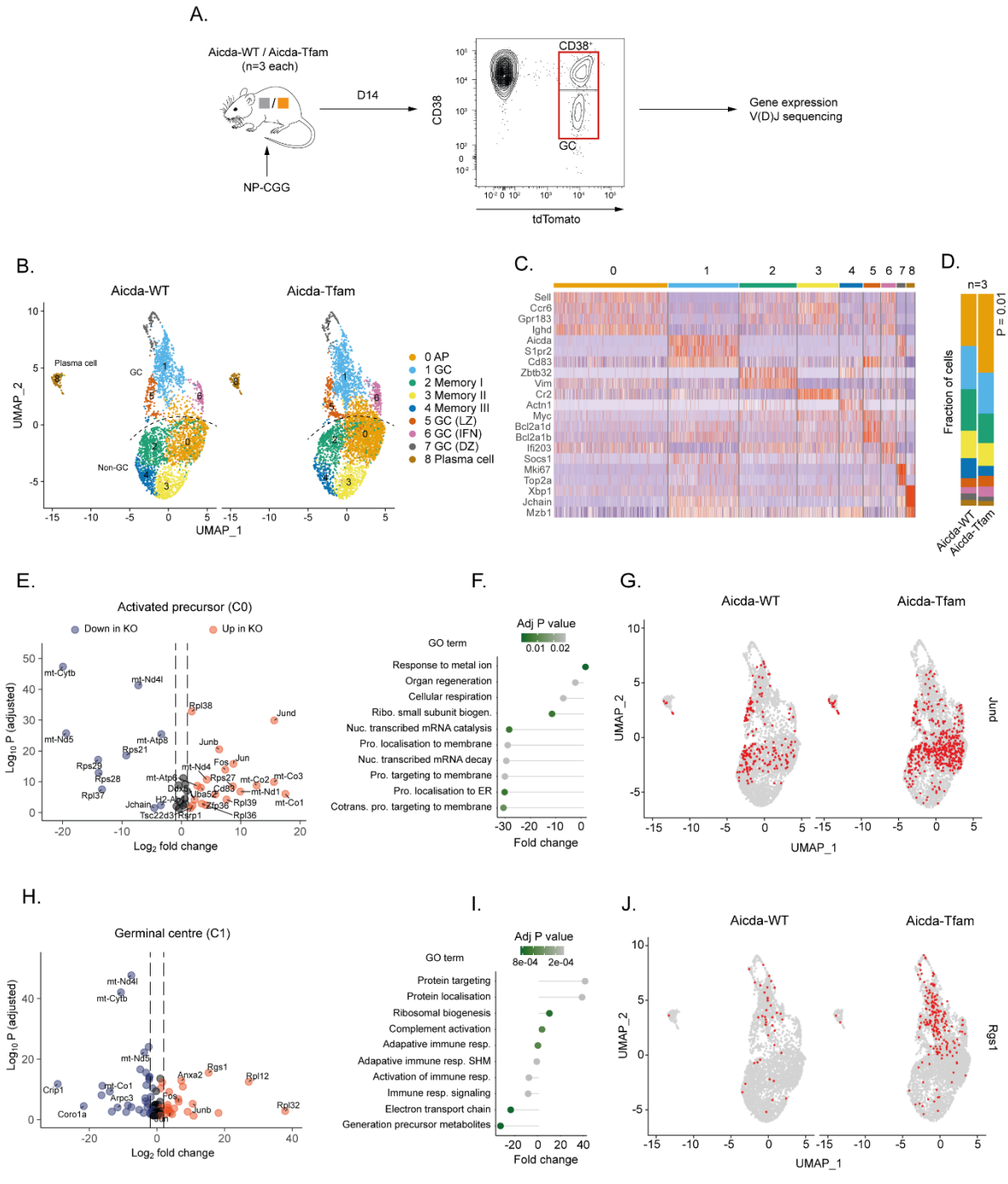


Figure 4.16. TFAM regulates the GC transcriptional program.
(A) Schematic of experimental design. Aicda-WT and Aicda-Tfam mice (n=3 per group) were immunised with 50μg NP-CGG with Alum (at 1:1 ratio) intraperitoneally and Dump$^-$ CD19$^+$tdTomato$^+$ cells were flow sorted before bead capture and 10x library preparation and sequencing. (B) UMAP projections and clustering of integrated Aicda-WT and Aicda-Tfam datasets. (C) Heatmap of selected differentially expressed marker genes by cluster for all samples. (D) Cluster proportions between groups. (E) Volcano plot of differentially expressed genes in cluster 0 (activated precursors). (F) SCPA of Gene Ontogeny Biologicals Processes (GO BP) in AP cluster. (G) *Jund* gene expression projected onto clustered data. (H) Volcano plot of differentially expressed genes in cluster 1 (germinal centre). (I) SCPA of GO BP in germinal centre cluster (cluster 1). (J) *Rgs1* gene expression projected onto clustered data. Statistical significance was calculated by t-test with correction for multiple comparison by the Bonferroni method (E, H). (I designed and conducted the scRNAseq experiment, the analysis was performed by Dr. Alexander Clarke)

4.2.17. GC B cell somatic hypermutation and clonal evolution depend on TFAM

B cell clonality was next assessed by analysing V(D)J sequences. Given that all tdTomato$^+$ B cells were sequenced (not just those binding to NP), there was high clonal diversity across all samples (Fig. 4.17A). However, heavy chain *V_H1-72* gene usage was frequent as anticipated during the anti-NP immune response[88] (Fig. 4.17B).

In Aicda-Tfam mice, greater clonal diversity with fewer dominant clones was determined. This indicates a reduced capacity for the evolution of dominant clones in the GCs lacking TFAM. A significant reduction in somatic hypermutation was observed in Aicda-Tfam B cells, including within the *Ighv1-72* gene in GC B cells (Fig. 4.17C-E). The W33L substitution in CDR1 and K59 substitutions in the V_H1-72 heavy chain, which enhance affinity for NP[197,198], were substantially lower in Aicda-Tfam GC B cells. This is in keeping with the previously observed decline in high-affinity NP binding (Fig. 4.17E-F). No W33L substitutions and negligible K59 mutations were present in the AP cluster (C0) of both Aicda-WT and Aicda-Tfam mice, in keeping with their pre-GC state (Fig. 4.17G).

These results collectively suggest that clonal selection and SHM rates in GC B cells are promoted by TFAM.

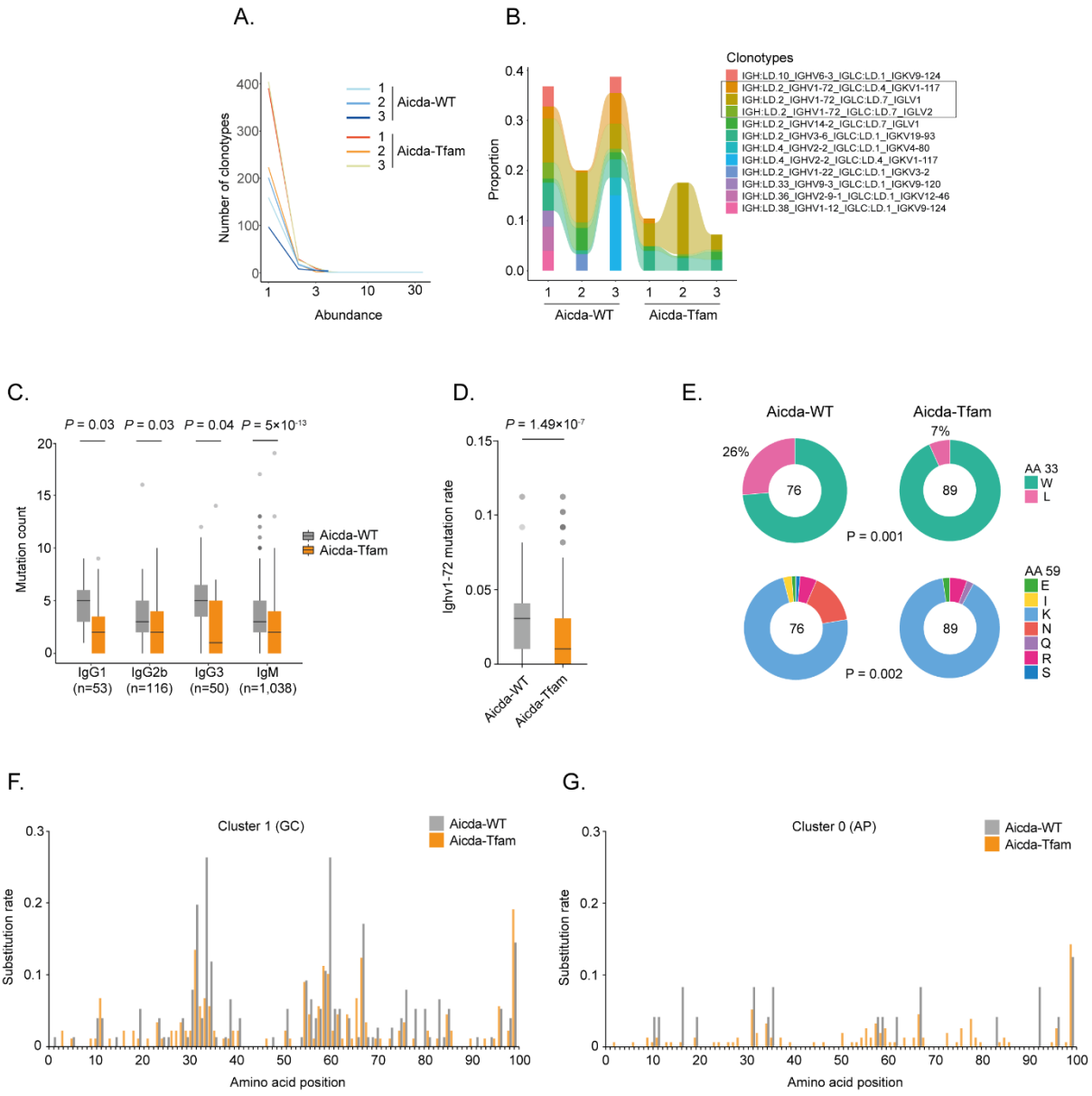


Figure 4.17. GC B cell somatic hypermutation and clonal evolution depend on TFAM. **(A)** Plot of clonotype abundance distribution for each sample. (B) Plot of proportions of top clonotypes for each sample. Clonotypes with *Ighv1-72* usage are highlighted. (C) Quantification of somatic hypermutation by Igh mutation count for indicated immunoglobulin isotype across all sequenced B cells. (D) Quantification of overall mutation rate for Ighv1-72 gene segment. (E) Quantification of substitution at *Ighv1-72* amino acid coding positions 33 and 59 for GC B cell and AP clusters. (F) Amino acid substitution rate across Ighv1-72 in GC B cell cluster for Aicda-WT and Aicda-Tfam mice (n=76 cells in Aicda-WT, n=89 in Aicda-Tfam). (G) Amino acid substitution rate across Ighv1-72 in AP B cell cluster for Aicda-WT and Aicda-Tfam mice (n=24 cells in Aicda-WT, n=154 in Aicda-Tfam). Statistical

significance was calculated by Chi-square test (E), t-test with correction for multiple comparison by the Benjamini-Hochberg method(C), or unpaired t-test (D). (I designed and conducted the scRNAseq experiment, the analysis in this figure was performed by Dr. Alexander Clarke and Iwan Raza)

4.2.18. TFAM is essential for GC B cell commitment

Given the accumulation of activated precursor B cells (AP) with high expression of *Sell* (L-selectin), *Ccr6*, and a GC transcriptional profile in Aicda-Tfam tdTomato$^+$ B cells suggestive of changes in cell trafficking and cytoskeleton dynamics, I hypothesised that *Tfam* is required for activated B cells to enter the GC and remain properly positioned.

I first confirmed the proportional expansion of AP in Aicda-Tfam mice after NP-CGG immunisation, which was identified as tdTomato$^+$CD38$^+$IgD$^+$ (Fig. 4.18A-C). Despite a significant numerical fall in GC B cells, the AP population was maintained (Fig. 4.18D).

In Aicda-WT mice, a lower proportion of APs bound NP compared to GC B cells, and they exhibited lower affinity by showing reduced binding to the low-conjugation NP probe. I found this highly consistent with their lack of W33L mutation and overall low SHM rates (Fig. 4.18E).

Immunofluorescence analysis of splenic sections from immunised Aicda-Tfam mice revealed highly disorganised GC architecture as well as numerous poorly compartmentalised GC B cells. Within the follicle marked by IgD, there were relatively more tdTomato$^+$ IgD$^+$ B cells in Aicda-Tfam mice (Fig. 4.18F). Additionally, Aicda-Tfam GC B cells showed lower BCL6 protein levels, the key transcriptional regulator for GC entry and commitment, which was in keeping with reduced *Mef2b* in the single-cell transcriptional dataset (Fig. 4.18G).

These findings collectively suggest that *Tfam* deficiency disrupts the ability of activated B cells to commit to the GC B cell fate.

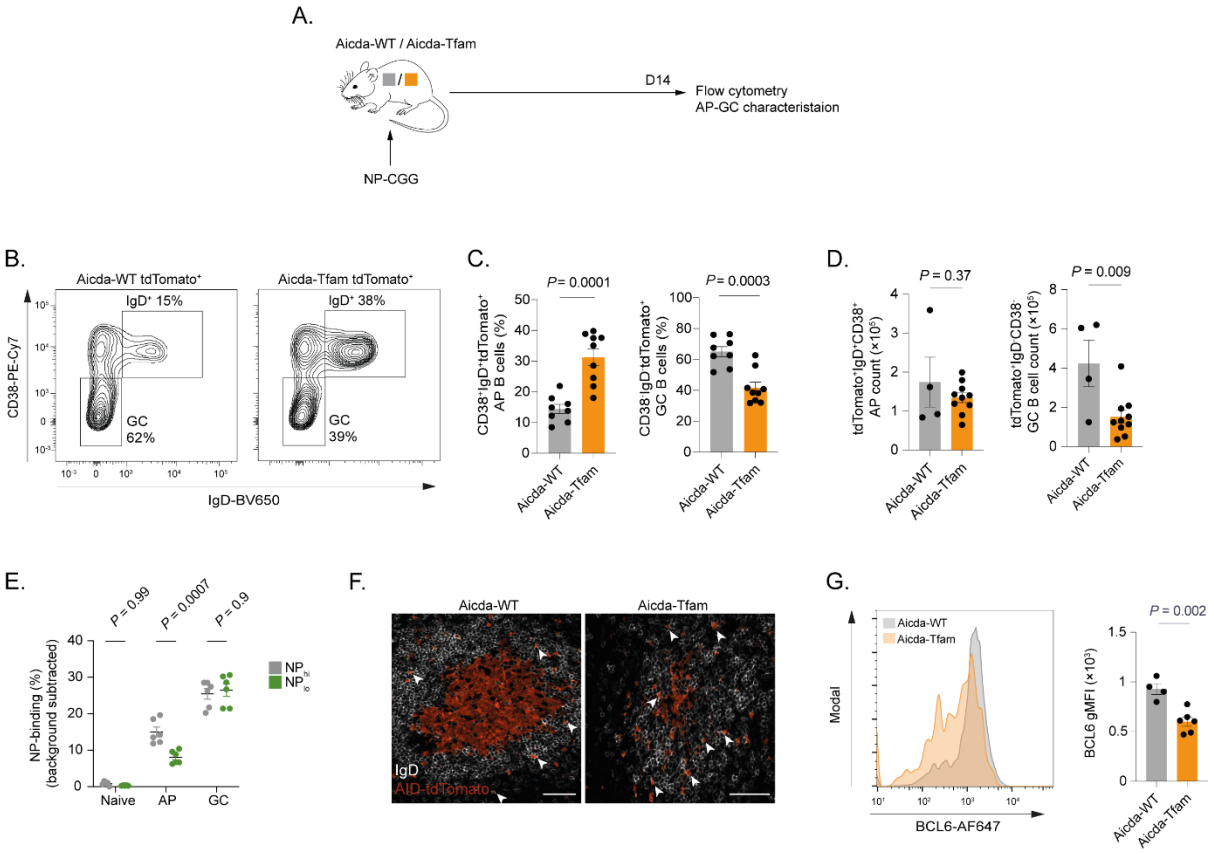


Figure 4.18. TFAM is essential for GC B cell commitment.

(A) Schematic of experimental design. Aicda-WT and Aicda-Tfam mice were immunised with NP-CGG and spleens were profiled by flow cytometry on day 14. (B) Representative flow cytometry plots depicting gating of $CD38^{+}IgD^{+}$ activated precursors (AP) and $CD38^{-}IgD^{-}$ GC B cells within the $CD19^{+}tdTomato^{+}$ population. (C) Quantification of AP and GC B cell percentages from NP-CGG immunised Aicda-WT (n=8) and Aicda-Tfam mice (n=9). Data pooled from two independent experiments. (D) Absolute count quantification of C. Data pooled from two independent experiments. (E) Quantification of NP-binding rates of naïve B cells, APs, and GC B cells isolated from Aicda-WT to high (NP^{hi}) and low NP (NP^{lo})-APC conjugates corresponding to low and high affinity to NP respectively. Non-specific background was subtracted based on labelling in unimmunised mice. Data pooled from two independent experiments. (F) Representative IHC images of GCs from Aicda-WT and Aicda-Tfam mice. Arrows identify $tdTomato^{+}IgD^{+}$ APs. 20× magnification, scale bar 20μm. Representative of two independent experiments. (G) Representative histogram flow plot and quantification of BCL6 expression (gMFI) in GC B cells from Aicda-WT and Aicda-Tfam mice. Data representative of two independent experiments. Statistical significance was calculated by two-way ANOVA with Šidák's multiple comparison test (E) or unpaired two-tailed t test (C-D,G)

4.2.19. Deletion of *Tfam* disrupts GC entry

I then investigated whether the failure of AP B cells to enter the GC could be overcome by adoptively transferring pre-activated *Tfam*$^{-/-}$ AP-like B cells into immunised CD45.1 mice.

To do this, I took advantage of the iGB B cell culture system and TAT-Cre to delete *Tfam* in Tfam flox × Rosa26-stop-tdTomato B cells (Fig. 4.19A). By day 4 of culture, TAT-Cre-treated iGB cells carrying $Tfam^{flox}$ had effectively deleted TFAM, which was reflected in reduced expression of mitochondrially-encoded ETC proteins and reciprocal upregulation of nuclear-encoded proteins (Fig. 4.19B). This was surprisingly very similar to what was observed during B cell maturation in B-Tfam mice (Fig 4.10). Despite the loss of *Tfam*, I found that cell expansion over the four-day culture period was unaffected (Fig. 4.19C).

By employing congenically marked Rosa26-stop-tdTomato × CD45.1/2 wild type B cells, I performed mixed adoptive transfer of $Tfam^{-/-}$ and wild type iGB cells. A fraction of transferred wild type iGBs showed specific characteristics of GC B cells and active GC participation *in vivo*. However, $Tfam^{-/-}$ iGB cells were at a marked competitive disadvantage in GC entry (Fig. 4.19D-G), which was confirmed by immunofluorescence imaging following a non-competitive transfer setup (Fig. 4.19H). These findings highlight the critical requirement for TFAM during GC entry and subsequent participation in the GC reaction.

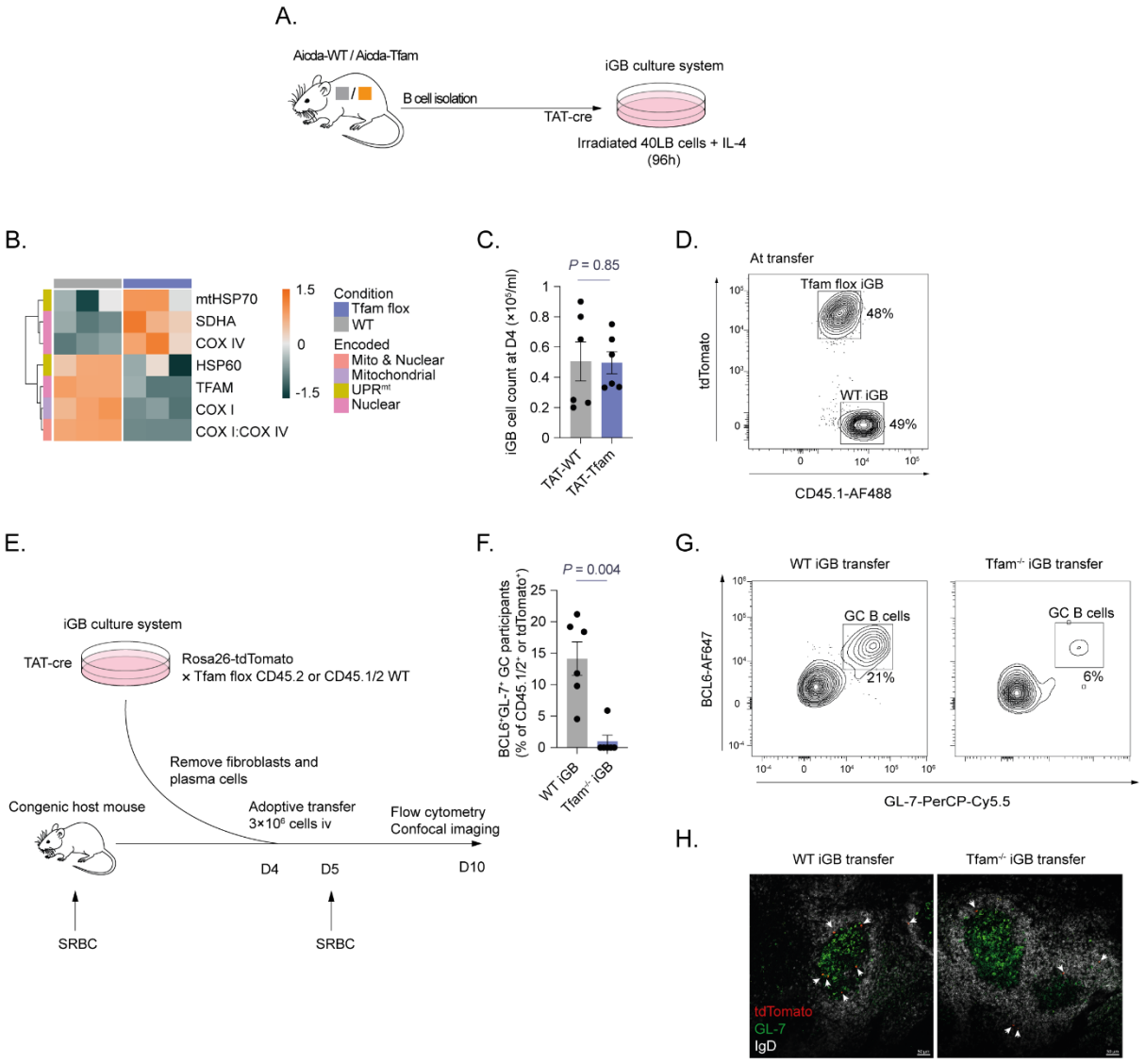


Figure 4.19. Deletion of *Tfam* disrupts GC entry. (A) Illustration depicting iGB culture system. (B) Heatmap of row Z-scores for gMFI of indicated mitochondrial proteins, measured by flow cytometry in TAT-Cre treated *Tfam*$^{-/-}$ or WT iGB cells (n=3). Results representative of three independent experiments. (C) Live cell counts of WT and *Tfam*$^{-/-}$ iGB cells at day 4. Results pooled from two independent experiments. (D) Flow cytometry confirmation of pre-transfer tdTomato^{+}*Tfam*$^{-/-}$ and CD45.1/2^{+} WT iGB cell ratio in competitive iGB transfer experiment. (E) Schematic of experimental design for iGB culture and adoptive transfer to assess in vivo GC entry/recruitment. (F) Quantification of GC Entry of iGB cells. (G) Flow cytometric characterisation of GC entry of adoptively transferred WT and *Tfam*$^{-/-}$ iGB cells in SRBC-immunised CD45.1 congenic hosts. GC B cells defined as (BCL6^{+} GL-7^{+}). Representative of two independent experiments. (H) Confocal images of splenic sections depicting tdTomato^{+} WT and *Tfam*$^{-/-}$ iGB cells adoptively transferred as in C. Arrows indicate transferred iGB cells. Representative of two independent experiments. Statistical significance was calculated by unpaired two-tailed t test (C,F).

4.2.20. Requirement for TFAM in GC B cells is cell intrinsic

Activated B cells require assistance from cognate T_{FH} cells to enter the GC, whilst T_{FH} cells depend on interaction with activated B cells for their maintenance. I hypothesised that the defects observed following *Tfam* deletion might be due to a diminished T_{FH} pool or abnormal T_{FH}-B cell co-operation. Following immunisation, I found no numerical defect in the GC-resident T_{FH} compartment (Fig. 4.20A-B). However, when I co-cultured *ex vivo* isolated T_{FH} cells with TAT-Cre-treated Rosa26-stop-tdTomato × Tfam flox or wild type control B cells, I observed a reduction in tdTomato^{+}GL-7^{+}IgG1^{+} induced GC B cells (iGC) lacking *Tfam* (Fig. 4.20C-E). To confirm, then, whether the defect in Aicda-Tfam mice was intrinsic to B cells, I generated mixed competitive bone marrow chimeras with CD45.1 congenic wild type donors, ensuring that T_{FH} generation would be unaffected. Aicda-Tfam GC B cells were significantly outcompeted by CD45.1 wild type cells in both spleens and Peyer's patches (Fig. 4.20F-H), pointing to a primarily cell-intrinsic defect.

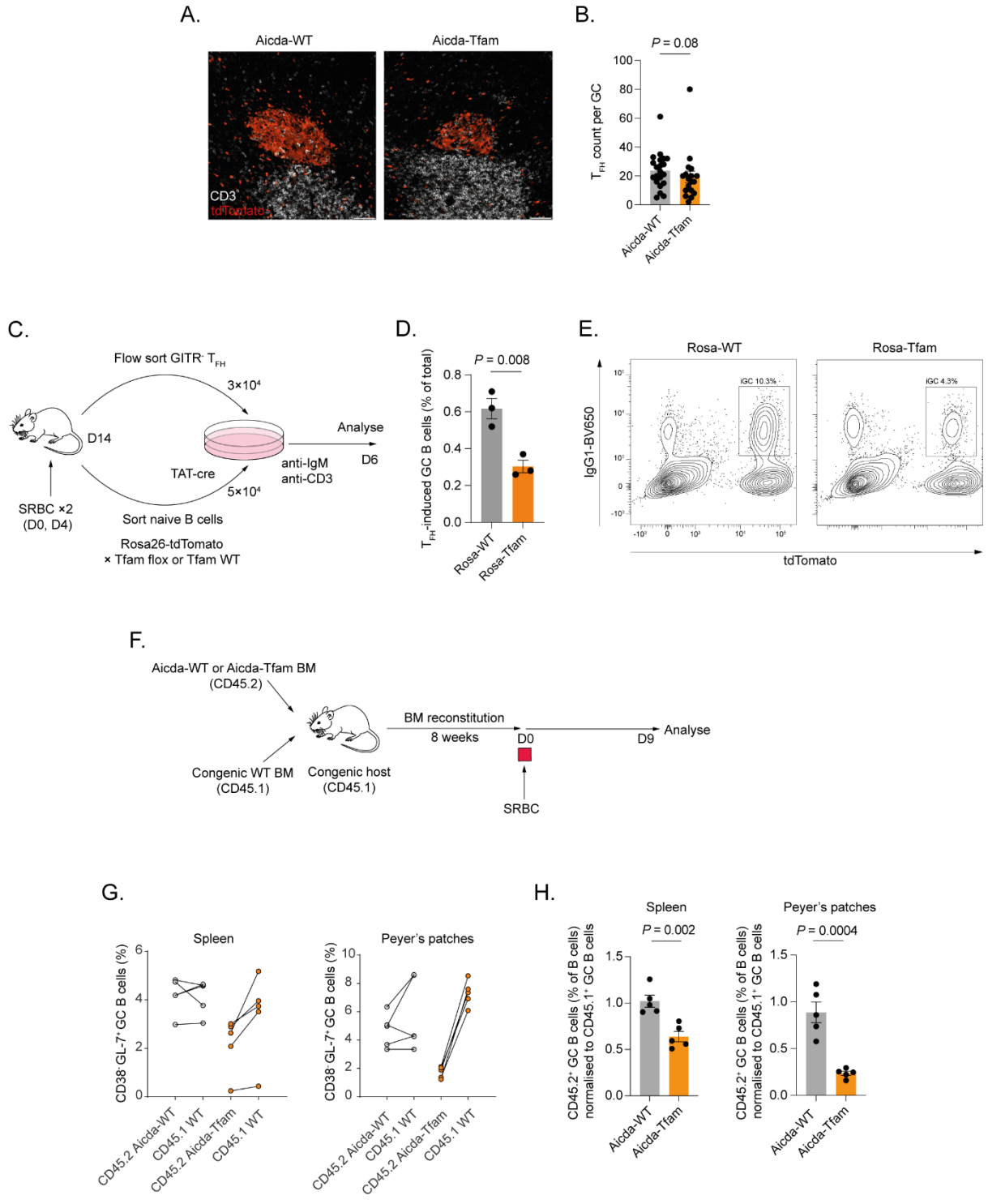


Figure 4.20. Requirement of TFAM in GC B cells is cell intrinsic.
(A) Representative confocal images of T_{FH} cell compartment in Aicda-WT and Aicda-Tfam mice. Representative of three independent experiments. (B) T_{FH} cell counts per GC from immunised Aicda-WT and Aicda-Tfam (data pooled from n=4 mice). Representative of three independent experiments. (C) Schematic of experimental design of T_{FH}-B cell co-culture. (D) Percentages of *in vitro* T_{FH}-induced Aicda-WT or Aicda-Tfam GC B cells (GL-7$^+$ tdTomato$^+$ IgG1$^+$) (of total viable cells). Technical replicates of n=2 pooled biological replicates shown. Data pooled from two independent experiments with n=3 biological replicates in total. (E) Representative flow cytometry plots of in vitro generated GC B cells

(iGCs). (F) Schematic illustrating BM chimera setup. (G) GC B cell frequencies in CD45.2 Aicda-WT or Aicda-Tfam and CD45.1 WT B cell populations from spleens and Peyer's patches of 50:50 competitive bone marrow chimeras at day 7 following SRBC immunisation. (H) Quantification of **F** normalised to CD45.1 WT GC B cell proportions. Data pooled from two independent experiments. Statistical significance was calculated by unpaired two-tailed t test.

4.2.21. TFAM regulates mitochondrial translation in activated B cells

To directly examine and compare mitochondrial translation activity, I measured the incorporation of the amino acid analogue OPP in *ex vivo* isolated mitochondria from Aicda-WT and Aicda-Tfam B cells using flow cytometry (Fig. 4.21A). First, I treated total splenic B cells from immunised mice with OPP and harringtonine, which inhibits ribosomal protein synthesis in the cytoplasm but not in mitochondria. Since tdTomato is widely distributed in cytoplasm and enters mitochondria, it served as a marker for *Aicda* expression of its host cells, therefore indicating AP or GC B cell origin post-homogenisation. I detected OPP via Click chemistry and immunostained for COX IV and tdTomato (using anti-RFP). Mitochondria were identified by their size, COX IV expression, and side scatter properties in flow cytometry after subcellular fractionation (Fig. 4.21B). A distinct RFP^+ mitochondrial population was easily detectable and appeared in reduced proportion in Aicda-Tfam mice, mirroring the overall reduction in the GC B cell pool (Fig. 4.21B). OPP uptake was significantly higher in RFP^+ mitochondria compared to RFP^- ones (non-AP or GC origin) (Fig. 4.21C-D). Importantly, translation activity was reduced in RFP^+ mitochondria from Aicda-Tfam B cells compared with Aicda-WT counterparts (Fig. 4.21E), and treating *Tfam*$^{-/-}$ iGB cells with the mitochondrial translation inhibitor chloramphenicol[184] reduced translation in WT mitochondria, an effect not seen in those from *Tfam*$^{-/-}$ cells, further confirming the selective impairment of mitochondrial protein synthesis (Fig. 4.21F).

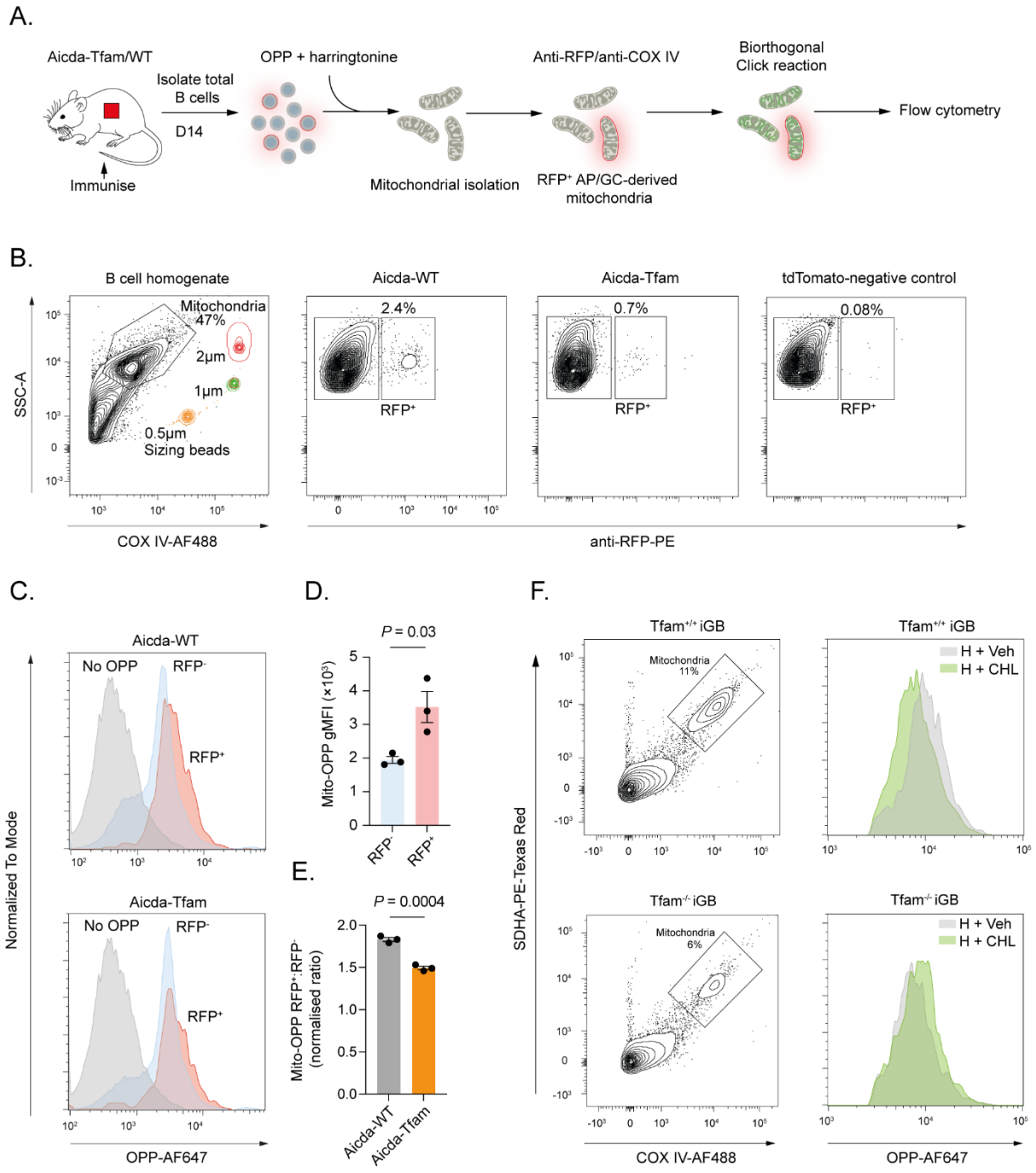


Figure 4.21. TFAM regulates mitochondrial translation in activated B cells.
(A) Schematic of single mitochondrion translation assay. (B) Gating strategy for isolated mitochondria based on SSC-A and COX IV-AF488 expression, and for RFP⁺ AP-GC-derived mitochondria. (C) FACS histogram plots depicting OPP-AF647 signal in AP-GC derived RFP⁺ and naïve B cell-derived RFP⁻ mitochondria. (D) Quantification of OPP gMFI in RFP⁺ vs RFP⁻ mitochondria from immunised Aicda-WT (n=3). Data pooled from three independent experiments. (E) Normalised OPP in RFP⁺ AP-GC-derived mitochondria from Aicda-Tfam and Aicda-WT mice. The experiment was performed in three batches and Aicda-Tfam values were normalised to Aicda-WT in each batch. Representative of 3 independent experiments. (F) Mitochondrial OPP incorporation assay performed on WT and Tfam$^{-/-}$ iGB cells at day 6. Flow cytometry gating strategy of mitochondria as COX IV⁺ SDHA⁺

particles. Shifts in OPP-AF647 signal in response to harringtonine (H, 1μg/ml) and/or chloramphenicol (CHL, 300μg/ml) treatments depicted in flow cytometry histogram plots. Representative of two independent experiments. Statistical significance was calculated by unpaired two-tailed t test with batch correction (E).

4.2.22. Mitochondrial translation is dynamically regulated across B cell subsets

I next analysed the expression of TFAM and other mitochondrial ETC components following immunisation. TFAM expression was dynamic in Aicda-WT mice, peaking at the AP stage before declining after GC entry, while COX I expression progressively increased, reaching its highest level in GC B cells (Fig. 4.22A-B). In Aicda-Tfam mice, immunofluorescence staining showed clear loss of TFAM along with visible organisational defects. As expected, the nuclear-encoded subunit SDHB remained abundant (Fig. 4.22C). Switching to B-Tfam mice, there was a more extensive relative expansion of $IgD^{+}GL\text{-}7^{int}$ APs, along with a more severe GC B cell deficiency (Fig. 4.22D). ETC proteins, encoded by both nuclear and mitochondrial DNA, were highly expressed in GC B cells in immunised B-WT mice consistent with my previous findings (Fig. 4.22E). Deletion of TFAM caused drastic changes in mitochondrial ETC protein expression in both AP and GC B cells (Fig. 4.22E), and these were similar to alterations observed during B cell development. The ratio of mitochondrial DNA-encoded subunits to nuclear DNA-encoded subunits within the same ETC complex may be reflect mitochondrial translation efficiency[199]. Thus, I measured two adjacent subunits of complex IV (COX I from mtDNA and COX IV from nuclear DNA) across B cell subsets. Under normal conditions, the COX I to COX IV ratio followed a dynamic pattern across all B cell subsets tested in bone marrow and spleen, not surprisingly peaking at the GC stage. In B-Tfam mice, however, a significant imbalance in this ratio was observed, consistent with their decreased mitochondrial OPP incorporation (Fig. 4.22F).

Overall, TFAM controls ETC homeostasis through dynamically regulating mitochondrial translation across B cell subsets.

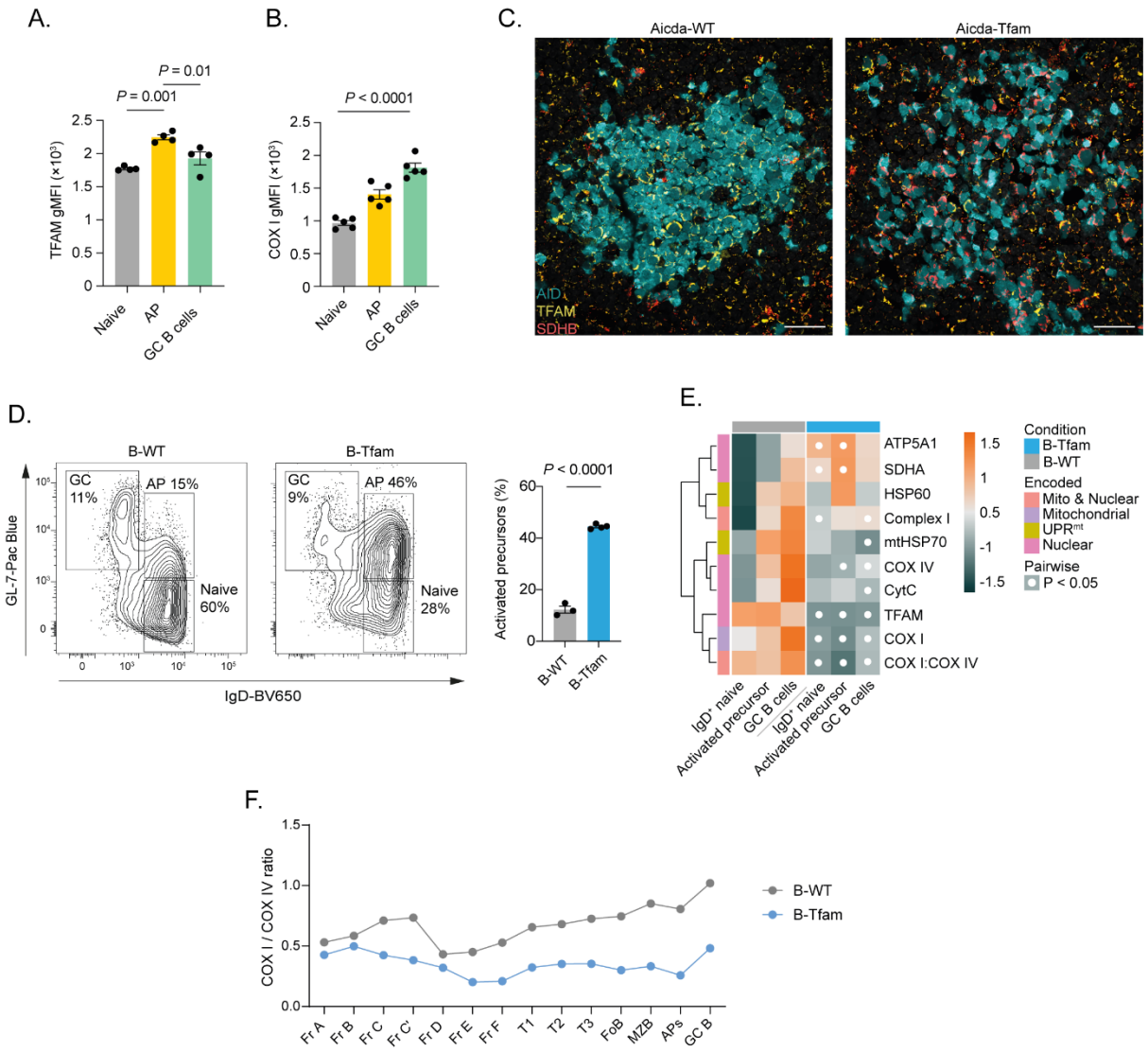


Figure 4.22. Mitochondrial translation is dynamically regulated across B cells subsets.

(A) Quantification of TFAM gMFI in tdTomato$^+$CD38$^-$ GC B cells, tdTomato$^+$IgD$^+$ AP, and tdTomato$^-$IgD$^+$ naïve B cell compartments from SRBC immunised Aicda-WT and Aicda-Tfam mice (n=5). Data representative of three independent experiments. (B) Quantification of COX I gMFI in tdTomato$^+$CD38$^-$ GC B cells, tdTomato$^+$IgD$^+$ AP, and tdTomato$^-$IgD$^+$ naïve B cell compartments from SRBC immunised Aicda-WT and Aicda-Tfam mice (n=5). Data representative of three independent experiments. (C) Airyscan confocal images of splenic GCs from Aicda-WT and Aicda-Tfam immunised with NP-CGG (D14) depicting TFAM, SDHB and tdTomato (AID). Representative of two independent experiments. (D) Representative flow cytometry plots depicting IgD+GL-7int AP and IgD-GL-7+ GC B cell subsets in B-WT and B-Tfam mice immunised with SRBC (enhanced protocol). Quantification and comparison of IgD+GL-7+ AP proportions in B-WT (n=3) and B-Tfam mice (n=4). Data representative of three independent experiments. (E) Heatmap of row Z-scores for gMFI of indicated mitochondrial proteins, measured by flow cytometry in splenic B cell subsets of NP-CGG immunised (D14) B-WT and B-Tfam mice (mean of 3 biological replicates). Results representative of two independent experiments with n=4 mice per group in total. (F) COX I:COX IV ratio plotted across B cell subsets derived from E and Fig 4.10.

Statistical significance was calculated by one-way ANOVA with Tukey's multiple comparison test (A-B), unpaired two tailed t-test (D), or two-way ANOVA with Tukey's comparison test (E).

4.2.23. TFAM is essential for metabolic reprogramming of activated B cells

I next investigated the metabolic consequences of *Tfam* deficiency in AP and GC B cells by measuring protein translation rates, using OPP incorporation as an indicator of metabolic activity. This was from a method known as SCENITH that has recently been reported [163]. By adding inhibitors of glycolysis (2-deoxyglucose) or ATP synthase (oligomycin), which disrupt the electron transport chain, I could estimate the relative contributions of these pathways (Fig. 4.23A). GC B cells had significantly higher OPP incorporation than AP B cells, reflecting their increased metabolic activity (Fig. 4.23A). In the absence of *Tfam*, AP B cells showed heightened glucose dependence and glycolytic capacity with a marked decline in mitochondrial pathways such as fatty acid oxidation (Fig. 4.23B-C). Again, similar but less severe effects were observed in GC B cells (Fig. 4.23B-C). In Seahorse analysis performed on stimulated B cells, *Tfam* deletion led to a significant reduction in OCR and SRC, in keeping with the metabolic maladaptation revealed by SCENITH (Fig. 4.23D-F). Although glycolysis was slightly elevated in activated B-Tfam B cells at baseline, it could not be upregulated to the same extent as in wild type cells following ATP synthase inhibition by oligomycin (Fig. 4.23G-H). These metabolic alterations were also largely reproduced during SeaHorse measurements on $Tfam^{-/-}$ iGB cells (Fig. 4.23I-K). Overall, TFAM is required for metabolic homeostasis in activated B cells, and respiratory compensation in its absence is not possible in activated cells.

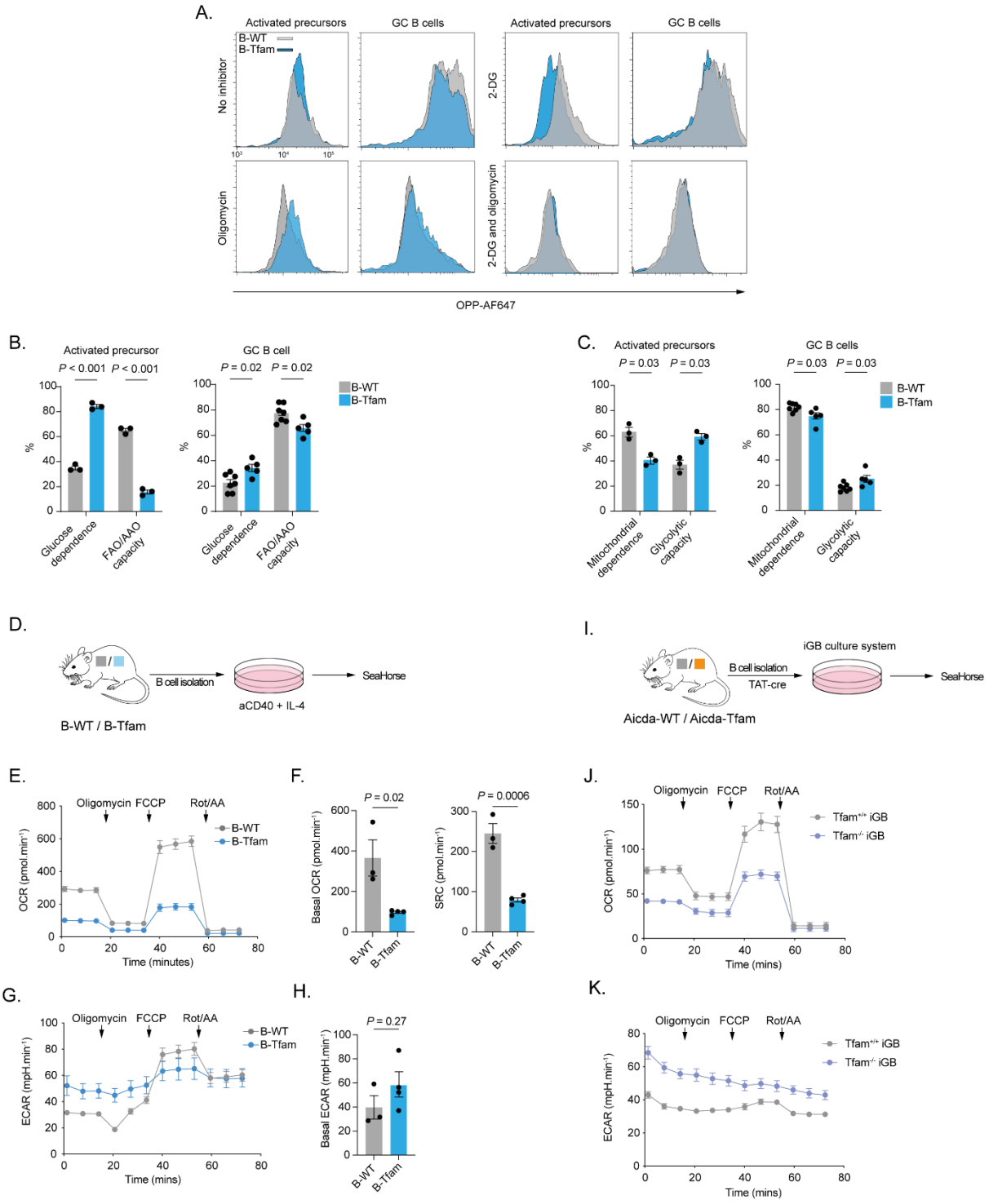


Figure 4.23. TFAM is essential for metabolic reprogramming of activated B cells. (A) Flow cytometry histogram plots depicting OPP incorporation in splenic IgD^{+}GL-7^{int} AP and IgD^{-}CD38^{-}GL-7^{+} GC B cells from B-WT and B-Tfam mice in response to metabolic inhibitors (oligomycin and/or 2-DG), shifts in OPP-AF647 signal indicate metabolic properties. Representative of three independent experiments. (B) Quantification of glucose dependence and FAO or AAO capacity of cells based on OPP incorporation into splenic IgD^{+}GL-7^{int} APs ($n = 3$ mice per group) and CD38^{-}IgD^{-}GL-7^{+} GC B cells from B-WT ($n = 7$) and B-Tfam mice ($n = 5$) treated *ex vivo* with metabolic inhibitors (oligomycin or 2-deoxy-d-glucose). Data were pooled from two independent experiments. (C) Quantification of

mitochondrial dependence and glycolytic capacity of cells based on OPP incorporation in splenic $IgD^{+}GL\text{-}7^{int}$ AP (n = 3 mice per group) and $IgD^{-}GL\text{-}7^{+}CD38^{-}$ GC B cells from B-WT (n = 7 mice) and B-Tfam mice (n = 5), treated *ex vivo* with metabolic inhibitors (oligomycin and/or 2-DG). Data pooled from two independent experiments. (D) Schematics of SeaHorse experiment on B cells from B-WT and B-Tfam stimulated with IL-4 and anti-CD40 overnight. (E) Real-time OCR measurements (from the Mito Stress test) of stimulated 3×10^5 B cells from B-Tfam ($n = 4$) and B-WT ($n = 3$) mice. (F) Quantification of basal OCR and spare respiratory capacity from E. (G) ECAR measurements (MitoStress test) of B-Tfam (n = 4) and B-WT (n = 3 mice) B cells stimulated as in **D**. Data pooled from two independent experiments. (H) Quantification of **G**. (I) Schematics of SeaHorse experiment on iGB cells from Aicda-WT and Aicda-Tfam following TAT-Cre treatment and 5 days cultures. (J) OCR measurements (MitoStress test) of 2×10^5 iGB cells (day 5, after overnight rest in IL-4) from TAT-Cre treated WT (*Tfam*$^{+/+}$) and Tfam^{loxp} (*Tfam*$^{-/-}$) B cells. (K) Corresponding ECAR measurements of J. Statistical significance was calculated by two-way ANOVA with Šidák's multiple comparison test (**B-C**) or unpaired two-tailed t-test (**F,H**).

4.2.24. *Tfam* deletion disrupts chemokine-directed GC B cell migration

GCs are organised into distinct zones. In Aicda-Tfam mice, I found defective compartmentalisation of GCs and smaller dark zones by IHC (Fig. 4.24A-B). Consequently, there was a skewed dark-to-light zone (DZ/LZ) ratio revealed by flow cytometry (Fig. 4.24C).

B cell positioning within the GC is regulated by chemokines CXCL12 and CXCL13, which guide migration to the dark and light zones, respectively[200]. Given that earlier data suggested TFAM is necessary for AP B cells to enter the GC, and that the transcriptional profile of Aicda-Tfam GC B cells indicated cytoskeletal and mobility defects, I hypothesised that TFAM is essential for correct cellular positioning within the GC.

To this end, I examined the actin cytoskeleton of *Tfam*-deficient GC B cells and found a significant increase in filamentous actin (F-actin) in Aicda-Tfam B cells by immunofluorescence and flow cytometry (Fig. 4.24D-F). This could be seen also in B cells from B-Tfam mice (Fig. 4.24G). Since actin remodelling is critical for B cell migration[201], I assessed whether *Tfam* deletion impaired GC B cell motility. In a transwell migration assay, Aicda-Tfam GC B cells displayed impaired migration in response to CXCL12 and CXCL13 (Fig. 4.24H).

Overall, these findings emphasise that loss of TFAM alters F-actin dynamics and GC B cell movement.

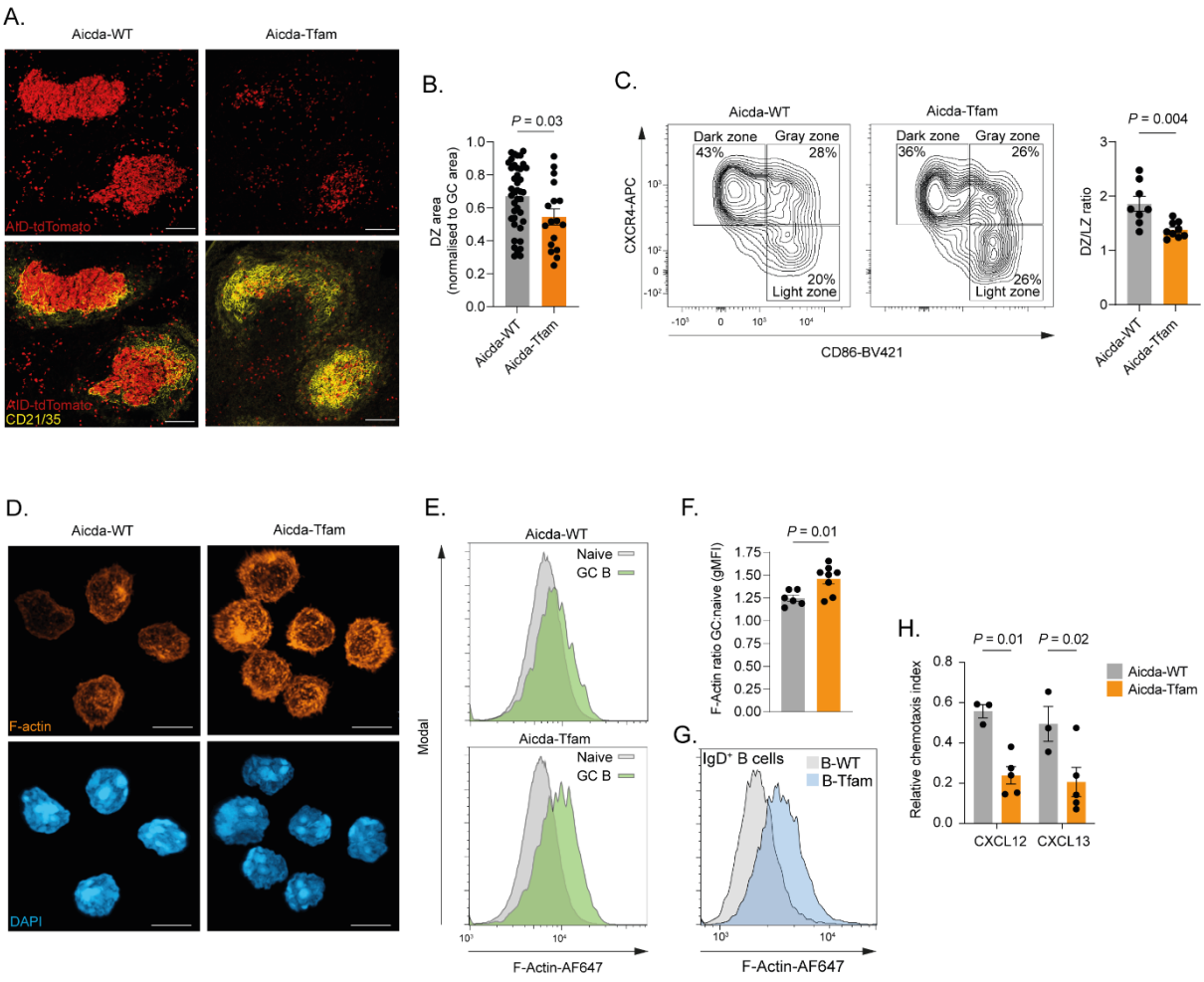


Figure 4.24. *Tfam* deletion disrupts chemokine-directed GC B cell migration (A) Representative Airyscan IHC images of spleen sections from SRBC-immunised Aicda-WT and Aicda-Tfam mice. (B) Quantification of DZ area normalised to GC area. Each symbol represents an individual GC. Image analyses were performed including all GCs identified on two sections from 2 mice of each genotype. Scale bar 100µm. Representative of 3 independent experiments. (C) Representative flow cytometry plots of DZ, GZ, and LZ subpopulations of tdTomato^{+}CD38^{-}GL-7^{+} GC B cells, based on CXCR4 and CD86 expression. Quantification of the DZ to LZ ratio from NP-CGG immunised Aicda-WT (n=8) and Aicda-Tfam mice (n=9). Representative of four independent experiments. (D) 3D Airyscan confocal image of magnetic bead-sorted and F-actin phalloidin and DAPI-stained GC B cells from Aicda-WT and Aicda-Tfam mice. All cells imaged expressed tdTomato. Scale bar 6µm. (E) Representative flow cytometry histogram of F-actin phalloidin fluorescence of tdTomato^{+}GL-7^{+} GC B cells and tdTomato^{-}IgD^{+} naïve B cells from immunised Aicda-WT (n=6) and Aicda-Tfam mice (n=8). (F) Quantification of F-actin phalloidin gMFI in tdTomato^{+}IgD^{-}GL-7^{+} GC B cells from immunised Aicda-WT and Aicda Tfam mice normalised to tdTomato^{-}IgD^{+} naïve B cells. Data pooled from three independent experiments. (G) Representative flow cytometry histogram of F-actin phalloidin fluorescence of IgD+ B cells from unimmunised B-WT and B-Tfam mice. Representative of two independent experiments. (H) Quantification of chemotaxis to CXCL12 and CXCL13 in GC B cells from Aicda-WT and Aicda-Tfam mice (n=4). Data pooled from four independent

experiments. Statistical significance was calculated by two-way ANOVA with Šidák's multiple comparison test (**H**) or unpaired two-tailed t-test (**B,C,F**).

4.2.25. Restoring mitochondrial ROS balance rescues defective mobility

Given that chemokine-driven cytoplasmic calcium mobilisation regulates F-actin organisation in B cells[202], and mitochondria are a key reservoir of intracellular calcium, I investigated whether *Tfam* deletion led to dysregulated intracellular calcium homeostasis. Interestingly, I observed a significant increase in mitochondrial calcium uniporter (MCU) levels in B-Tfam B cells, suggesting enhanced calcium uptake capacity. MCU expression in $CD3^+$ T cells remained unchanged, however (Fig. 4.25A-B).

I found that B cells from B-Tfam mice were unable to maintain peak cytoplasmic calcium levels following CXCL12 stimulation (Fig. 4.25C). This also similarly occurred after BCR stimulation with anti-IgM antibodies (Fig. 4.25D). I also noted a substantial increase in mitochondrial ROS in both naive and activated B-Tfam cells (Fig. 4.25E-F).

I asked whether suppressing mitochondrial ROS with the scavenger mitoTEMPO or inhibiting MCU function with the ruthenium compound Ru265 would improve cell motility in B-Tfam B cells in response to CXCL12. Whilst MCU inhibition did not restore migration in the transwell system, mitoTEMPO notably rescued the motility defect in B-Tfam cells (Fig. 4.25G-H).

These results collectively suggest that TFAM is essential for proper cellular motility, and that this requirement is mechanistically linked to mitochondrial ROS generation.

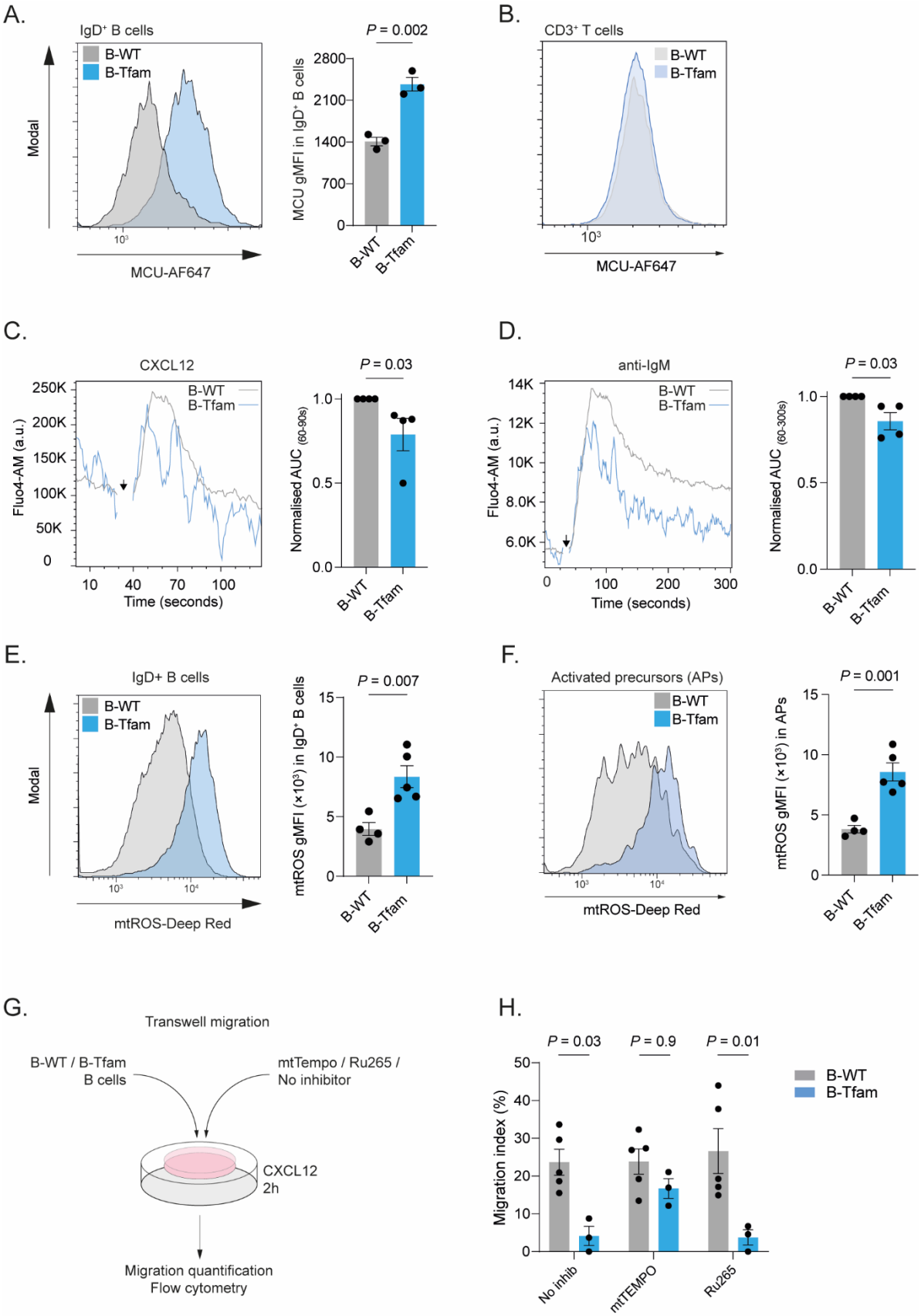

A.
IgD⁺ B cells
B-WT
B-Tfam
Modal
MCU-AF647
P = 0.002
MCU gMFI in IgD⁺ B cells
2800
2100
1400
700
0
B-WT
B-Tfam
B.
CD3⁺ T cells
B-WT
B-Tfam
MCU-AF647
C.
CXCL12
Fluo4-AM (a.u.)
250K
200K
150K
100K
50K
0
10
40
70
100
Time (seconds)
P = 0.03
Normalised AUC (60-90s)
1.0
0.5
0.0
D.
anti-IgM
Fluo4-AM (a.u.)
14K
12K
10K
8.0K
6.0K
0
100
200
300
Time (seconds)
P = 0.03
Normalised AUC (60-300s)
E.
IgD+ B cells
Modal
mtROS-Deep Red
P = 0.007
mtROS gMFI (×10³) in IgD⁺ B cells
15
10
5
0
F.
Activated precursors (APs)
mtROS-Deep Red
P = 0.001
mtROS gMFI (×10³) in APs
G.
Transwell migration
B-WT / B-Tfam
B cells
mtTempo / Ru265 /
No inhibitor
CXCL12
2h
Migration quantification
Flow cytometry
H.
P = 0.03
P = 0.9
P = 0.01
Migration index (%)
50
40
30
20
10
0
No inhib
mtTEMPO
Ru265

Figure 4.25. Restoring mitochondrial ROS balance rescues defective mobility.

(A) Representative flow cytometry histogram of MCU fluorescence in $B220^+$ IgD^+ B cells from unimmunised B-Tfam and B-WT mice. Quantification of MCU gMFI in IgD^+ B cells from B-Tfam and B-WT mice (n=3). Data representative of 3 independent experiments. (B) Representative flow cytometry histogram of MCU fluorescence in $CD3^+$ T cells. (C) Representative Fluo4-AM geometric mean signal intensity kinetics (moving average) of B-WT and B-Tfam $B220^+$ B cells stimulated with CXCL12 (200ng/ml) for 120s. Quantification of fold change in geometric MFI between 30-90s (corresponding to peak response) normalised to baseline (F_0, 0-30s pre-stimulation). Experiment was run as technical duplicates in four independent replicate experiments consisting of one B-Tfam and one wild-type mouse. Data points from B-Tfam were normalised to wild type data run in the same batch. (D) Representative Fluo4-AM gMFI signal kinetics (moving average) of B-WT and B-Tfam $B220^+$ B cells stimulated with anti-IgM (10µg/ml) for 300s. Quantification of fold change in geometric MFI between 270-300s (corresponding to 5 min response) normalised to baseline (F_0, 0-30s). Experiment was run as technical duplicates in four independent replicate experiments consisting of one B-Tfam and one wild-type mouse in each. Data points from B-Tfam were normalised to wild-type data run in the same batch. (E) Representative flow cytometry histograms and quantification of mtROS Deep Red fluorescence in IgD^+ B cells from immunised B-WT (n=4) and B-Tfam mice (n=5). Data representative of two independent experiments. (F) Representative flow cytometry histogram and quantification of mtROS Deep Red fluorescence in $IgD^+GL\text{-}7^{int}$ B cells from immunised B-WT (n=4) and B-Tfam mice (n=5). Data representative of two independent experiments. (G) Illustration depicting the design of transwell migration experiment to test the rescue effect. (H) Quantification of chemotaxis to CXCL12 (100ng/ml) in naive B cells from B-Tfam (n=3) and B-WT mice (n=5) in the presence of mtSOX scavenger mitoTEMPO (100µM) or MCU inhibitor Ru265 (30µM). Data representative of two independent experiments and pooled after batch correction. Statistical significance was calculated by unpaired two-tailed t-test (A,E-F), two-tailed Mann-Whitney U test, or two-way ANOVA with Šidák's multiple comparison test with batch as a covariate (H).

4.2.26. B cell lymphoma is critically dependent on TFAM

After establishing the important role of TFAM in B cell development and GC entry, I investigated whether TFAM is necessary for lymphoma development. *MYC* translocations are commonly found in DLBCLs. Since *c-Myc* encodes an important transcription factor that regulates cell cycle progression, growth, cellular metabolism, and mitochondrial biogenesis[203], I hypothesised that deleting *Tfam* might counteract the oncogenic effects of *c-Myc* overexpression.

I employed the Eμ-Myc transgenic mouse model of lymphoma, where transgenic *Myc* is driven by the *Igh* enhancer, thus conferring B cell specificity[204]. Eμ-Myc mice develop lymphoma with high penetrance, typically at around 11 weeks of age. To assess the impact

of *Myc* overexpression on mitochondrial translation, I transferred lymphoma cells from Eμ-Myc mice (CD45.2) into wild type CD45.1 congenic hosts. This allowed comparison of B cells in the same tissue environment (Fig. 4.26A). I observed significantly higher COX I expression and increased TFAM levels in CD45.2 lymphoma cells compared to wild type B cells (Fig. 4.26B-C).

Next, I generated *Cd79a-Cre* × *Tfam* flox × Eμ-Myc mice (B-Tfam-Myc) to delete *Tfam* on the Eμ-Myc genetic background. B-Tfam-Myc mice were fully protected from lymphoma development over a 30-week observation period, whilst *Tfam* flox × Eμ-Myc controls had a median survival of 14 weeks, and *Cd79a*-Cre × *Tfam* het × Eμ-Myc heterozygous mice showed basically the same trend (Fig. 4.26D).

Finally, I deleted *Tfam* in established lymphoma cells from Eμ-Myc-Tfam flox or wild type mice (Cre negative) using TAT-Cre *ex vivo* and then adoptively transferred them into wild type CD45.1 recipients (Fig. 4.26E). Mice that received Tfam-deficient lymphoma cells exhibited reduced lymphadenopathy after 3 weeks suggesting impaired lymphoma progression in the absence of *Tfam* (Fig. 4.26F-G).

These findings highlight elevated rates of mitochondrial translation enabled by *Tfam* as an essential requirement for the development and progression of B cell lymphoma.

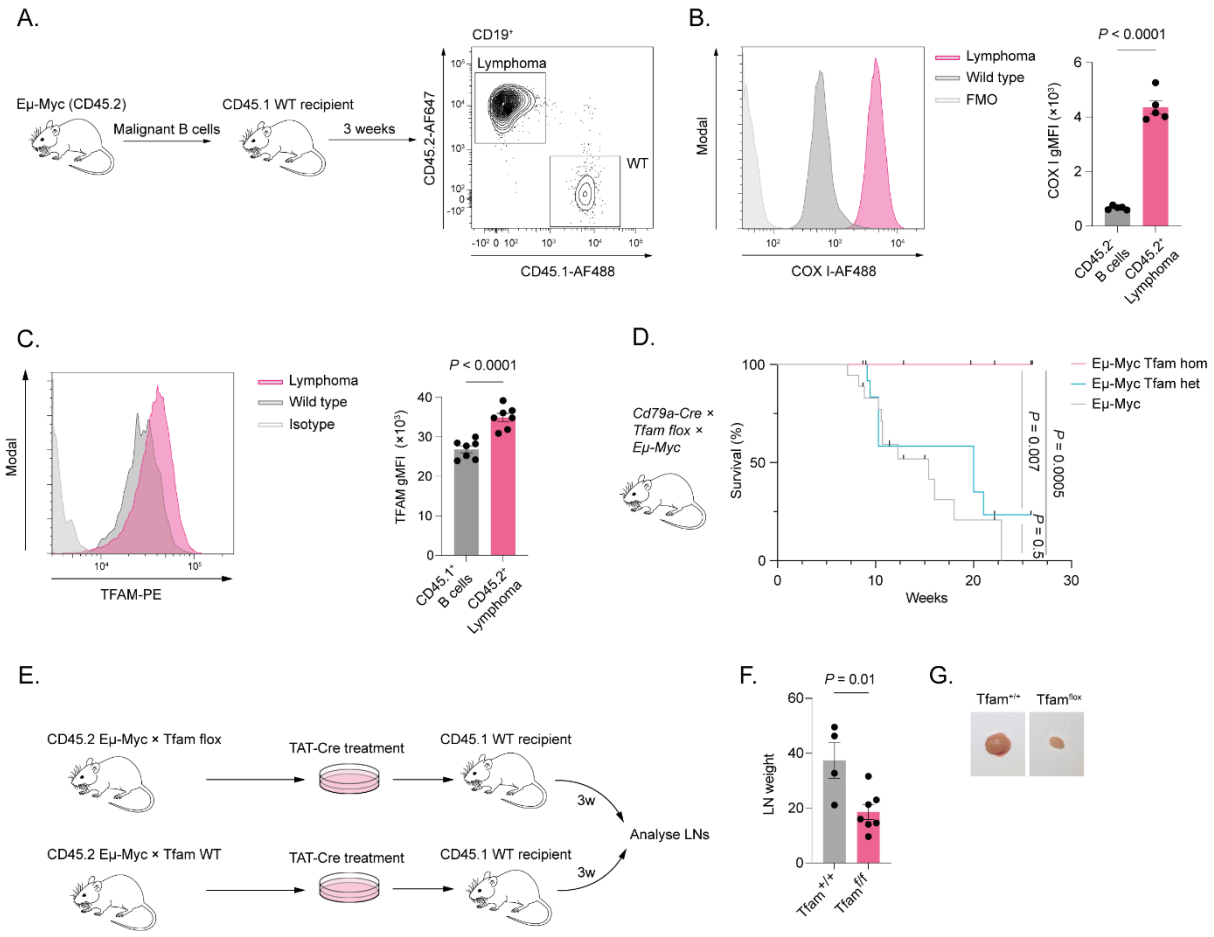


Figure 4.26. B cell lymphoma is critically dependent on TFAM.
(A) Schematic depicting adoptive transfer strategy of lymphoma cells from Eμ-Myc mice. Following development of lymphoma, cells were transferred into wild type congenic (CD45.1$^+$) recipients. Representative flow cytometry plots showing identification of CD19$^+$CD45.2$^+$ donor lymphoma cells and CD19$^+$CD45.1$^+$ wild type B cells from the inguinal lymph nodes of recipient mice after 3 weeks. (B) Flow cytometry histogram depicting COX I expression in CD45.2$^+$ lymphoma cells and CD45.1$^+$ wild type B cells as described in A. Quantification of COX I gMFI. Data representative of two independent experiments. (C) Flow cytometry histogram depicting TFAM expression in CD45.2$^+$ lymphoma cells and CD45.1$^+$ WT B cells as described in A. Quantification of TFAM gMFI. Data representative of two independent experiments. (D) Kaplan-Meier graph depicting survival curve of Eμ-Myc × Tfam Hom (Cd79a$^{cre/+}$ Tfam$^{fl/fl}$ × Eμ-Myc, n=9), Eμ-Myc Tfam Het (Cd79a$^{cre/+}$ Tfam$^{fl/+}$ × Eμ-Myc, n=13) and Eμ-Myc (Cd79a$^{+/+}$ Tfam$^{fl/fl}$ × Eμ-Myc or Cd79a$^{+/+}$ Tfam$^{fl/+}$ × Eμ-Myc, n=18) mice followed for up to 6 months of age. (E) Schematic of post-transformation *Tfam* deletion and adoptive transfer into congenic hosts for three weeks. (F) Quantification of inguinal lymph node weight from lymphoma recipients after three weeks. (G) Representative images of inguinal lymph nodes from lymphoma recipients for size comparison. Statistical significance was calculated by unpaired two-tailed t-test (B-C,F), or Mantel-Cox log-rank test (D).

4.3. Discussion

Here, I showed that as B cells enter the GC, their mitochondria undergo dramatic remodelling, increasing in mass and substantially altering their structure. Mitochondrial translation becomes highly active during this process. I also found that a nuclear-encoded regulator of mitochondrial transcription and translation TFAM is not only dynamically regulated in B cells, but is also essential for their development, spatial anchoring, and entry into the GC reaction. Moreover, I demonstrated that TFAM is essential during lymphoma development and progression.

Studying mitochondrial biology in primary tissues and cells is challenging. Labelling mitochondria and conducting metabolic assays often require *ex vivo* handling, which largely deviates from tissue microenvironments *in vivo* in terms of nutrient and oxygen availability. To address these limitations, I employed the mitochondrial reporter system Mito-QC[191]. Surprisingly, GC B cells showed no signs of active mitophagy, in keeping with their inactive autophagic program[46].

Further characterisation of GC B cell mitochondria revealed markedly increased mitochondrial mass and a fused elongated architecture. Mitochondrial morphology is intimately linked to bioenergetic status[205]. Fusion is often associated with enhanced OxPhos, while fragmentation is necessary for both mitochondrial degradation and cell division[65]. These morphological changes have been reported to be important during T lymphocyte differentiation and fate commitment[206,207]. However, the extent to which such processes occur in GC B cells remains unclear. Another unresolved question is how GC B cells sustain such high mitochondrial mass while undergoing rapid cycles of cell division. This may be attributed to increased mtDNA transcription promoting mitochondrial biogenesis.

TFAM packages mtDNA into nucleoids and maintains mtDNA copy numbers[186]. Studies have shown that after *in vitro* stimulation, B cells reduce mtDNA copy number, along with the number of nucleoids per mitochondrion. However, the size of the remaining nucleoids

increases[208]. Using super-resolution imaging I noted an elevated number of TFAM-packaged nucleoids in GC B cells, which were significantly larger and ellipsoid in shape compared to those in naïve B cells.

Interestingly, GC B cells display relatively unchanged total TFAM expression compared to naive counterparts, in spite of having increased mitochondrial mass and nucleoid numbers. This is suggestive of a relatively lower TFAM abundance in individual nucleoids. The ratio of TFAM to mtDNA in nucleoids controls mitochondrial gene expression through the degree of genomic compaction[195,209]. Therefore, the relative downregulation of TFAM may be associated with a looser compaction state, resulting in larger nucleoids and heightened transcriptional activity in GC B cells. The single-cell transcriptional data indicated that mitochondrial transcription is globally reduced in GC B cells lacking TFAM, further underscoring its important regulatory role in mitochondrial transcription. Additionally, TFAM is known to undergo post-translational modifications such as phosphorylation and acetylation, which affect its binding strength to mtDNA[210,211]. Whether these modifications also occur during GC transition is yet to be determined.

I have comprehensively quantified expression of ETC proteins using high dimensional spectral flow cytometry across 15 different B cell subsets. This revealed a robust upregulation in mitochondrially encoded ETC proteins in GC B cells, pointing to increased translational capacity in their mitochondria at the GC entry. This was then confirmed functionally at single mitochondrial level by a novel assay I developed, which includes detection of cell-of-origin via fluorescent protein tagging and subsequent measurement of amino acid analogue OPP incorporation. Mitochondrial translation is crucial for maintaining mitochondrial homeostasis, and TFAM is critical for this process[20]. Deletion of TFAM disrupts the balance of ETC protein expression. This imbalance leads to metabolic disturbances, including impaired OxPhos and an increased reliance on glycolysis following activation.

I was surprised to find that TFAM was essential for entry into the GC, a phenotype also reproduced in a recent study[88]. This defective entry was B cell intrinsic and fully recapitulated by iGB cells followed by adoptive transfer into immunised hosts. Although the contribution of iGB cells to the memory cell pool has been previously documented *in vivo*[212], their active participation in ongoing GC reactions along with the requirement for TFAM in this process represent novel findings.

It is possible that TFAM is required for an initial burst of mitochondrial biogenesis to facilitate GC entry. Interestingly, a similar trend was also observed in the bone marrow during B cell development, where high TFAM expression in Fr A preceded upregulation of mitochondrial subunits during later developmental stages. This upregulation together with the associated developmental progression was severely blocked in B cells upon *Tfam* deletion. However, it remains to be elucidated whether the underlying molecular perturbations are shared between the defects in the GC and those in the bone marrow.

Loss of TFAM resulted in mitochondrial ROS generation, even in unstimulated cells. Since ROS activate the AP-1 signalling pathway, this observation is in keeping with its transcriptional activation in TFAM-deficient B cell subsets. Additionally, TFAM loss led to an aberrant F-actin network. Dynamic modifications to the actin cytoskeleton are key to normal cell movement, and its disruption probably contributes to the abnormal positioning and motility defects I observed. This adds weight to idea that mitochondria are closely linked to cytoskeletal function. Furthermore, mitochondria concentrating at the rear of the cell during lymphocyte migration were demonstrated recently further suggesting that mitochondrial network organisation is critical for cellular movement and may be affected in TFAM deficiency[213].

TFAM deletion also led to significant defects in calcium regulation characterised by upregulation of the MCU. Whilst MCU inhibition did not restore B cell migration, dysregulated calcium balance may still remain disruptive to B cell function. B cells are particularly sensitive to MCU deletion, highlighting their dependence on mitochondrial

homeostasis[214]. Additionally, B cell-specific deletion of *Slc8b1*, which encodes the mitochondrial Na^+/Ca^{2+} exchanger (NCLX), causes impaired GC B cell responses to foreign antigens and pathogen-driven immune challenges. Surprisingly, this phenotype was attributed to altered bioenergetic activity and ROS generation rather than calcium export from mitochondria.

I did not detect an increase in GC B cell apoptosis following *Tfam* deletion. However, it should be noted that the highly effective efferocytosis by tingible body macrophages in the GC might mask potential differences[215,216]. Also unchanged was the proliferative capacity of GC B cells. This is particularly interesting given that GC B cells lacking *Cox10* have been reported to proliferate less effectively. It is possible that divergent mechanisms between these two perturbation models exist.

Loss of TFAM disrupts mitochondrial DNA integrity and induces immune aging in T cells, but whether this happens in B cells was previously unknown. A recent study has identified skewed B cell differentiation towards an age-associated phenotype in the absence of TFAM[88]. The exact underlying mechanisms warrant further investigation, however, they were shown to be associated with defective lysosomal function, a phenomenon also observed in T cells[189].

I demonstrate that deletion of TFAM sufficiently prevents the development of *Myc*-driven lymphoma. Although early-stage loss of TFAM results in B cell lymphopenia, reducing the pool of potentially malignant B cells, the high penetrance of the model, coupled with complete protection against lymphoma, suggests that this alone does not fully account for the observed phenotype. Indeed, TFAM deletion after lymphoma development led to significantly milder lymphadenopathy, therefore, suggesting lymphoma progression remains sensitive to loss of *Tfam*. The mechanisms by which TFAM supports lymphomagenesis require further investigation, but its role in promoting mitochondrial translation may be a key contributing factor. This should be prioritised as a therapeutic

target given the current availability of safe and specific inhibitors of mitochondrial transcription and translation.

Chapter 5: General Discussion

Although I have uncovered several previously unknown aspects of B cell metabolism, many critical questions remain unanswered. For example, it is not yet known why GCs are hypoxic. Some studies have suggested that this is due to limited access to nearby blood vessels[217]. However, GC hypoxia might simply be associated with high oxygen consumption by GC B cells. I have presented multiple layers of evidence showing that GC B cells have increased mitochondrial content. Irrespective of the underlying mechanism of hypoxia, the mechanism by which OxPhos is maintained under low oxygen availability remains unknown and warrants further research. It has been previously shown that fumarate can serve as a terminal electron acceptor, permitting ETC activity at low oxygen[218]; however, whether this pathway is active in GC B cells remains to be tested.

The factors driving the metabolic shift towards OxPhos are not completely understood in GC B cells. It has been shown that BCL6 suppresses glycolysis in T cells[219]. Mechanistically, this might be responsible for the low glycolytic capacity observed in GC B cells. This also suggests a potentially conserved OxPhos signature in T_{FH} cells, as they also express high levels of BCL6. Interestingly, I found that the increase in mitochondrial mass during T_{FH} commitment resembles the changes that occur during GC B cell differentiation, although the requirement for exogenous asparagine was not shared between these two subsets.

Outside GCs, effector T and B cells have distinct mitochondrial activities and programs[65]. Whether this extends to GC-resident counterparts, and specifically whether T_{FH} cells are similarly reliant on OxPhos, remains to be investigated.

Beyond oxygen, the availability of other critical supplies in lymphoid tissues, particularly in GCs, remains largely unknown. I measured asparagine and glutamine levels in the interstitial fluids eluted from the lymph nodes. Although these findings are novel, it is unclear whether they apply to GCs given the extreme heterogeneity of the metabolic landscape in lymphoid tissues. Nutrient levels are likely to vary across different cellular zones, especially in confined niches, such as GCs, where altered metabolite diffusion and distinct patterns of cellular demand and consumption may play a role. Recent advances, such as *in vivo* isotope tracing[166], spatial transcriptomics[220], imaging mass spectrometry[221], and *in vivo* metabolic biosensor imaging[222], represent promising tools for mapping the metabolic landscape of GCs and uncovering the pathways involved.

Recent *ex vivo* and *in vitro* studies have improved our ability to recapitulate GC biology and its complex cellular interactions using 3D organoid and tissue slicing techniques[223,224]. I demonstrated that a lymph node slicing system is highly effective *ex vivo* for testing the impact of nutrient availability, such as Asn, on GCs. However, a significant knowledge gap remains regarding how the media used in these culture systems should be supplemented to approximate *in vivo* tissue conditions. The development of cell culture media based on human plasma is a major step forward[225], but as demonstrated in this thesis, tissue metabolite abundance may deviate considerably from systemic levels. Therefore, future studies establishing local tissue metabolite concentrations and translating them into reproducible culture medium formulations are important. This also pertains to oxygen availability, as GC hypoxia has only been documented qualitatively using hypoxia probes[38,44]. Determining absolute tissue oxygen levels within GCs is another important challenge in the field.

Investigating GC formation has recently received attention, and several groups are actively investigating the metabolic changes that occur during this process. However, it remains unclear how this initial metabolic reprogramming is maintained throughout the GC reaction. Two previous studies have shown that GC B cells use more OxPhos[49] and are reliant on

fatty acids[21], largely abandoning glycolysis over time. They speculated that this shift may have evolved to utilise lipid-rich fragments derived from dying GC B cell clones. Apoptosis occurs at a very high rate in GCs[226]. Some studies have estimated that 10% of GC B cells undergo apoptosis every hour, indicating that half of the GC B cell pool is replenished every six hours by newly generated cells[215].

This raises several interesting questions: are GCs active sites for nutrient recycling? If so, which cell subsets are responsible for liberating metabolites from dying cells and redistributing them within GCs?

Another important topic in the B cell field is the GC exit process. When B cells differentiate into plasma cells, they switch to a metabolic program characterised by elevated glucose consumption and glycolysis[22,49]. This suggests that the metabolic and mitochondrial states of B cells may be tuned during their exit from the GC reaction. Although some studies have identified metabolic remodelling in subsets completing and exiting the GC reaction, it remains unclear whether these changes in metabolism directly instruct GC exit and subsequent B cell fate[227]. Addressing these questions is challenging due to the difficulty of experimentally targeting clones leaving the GC without affecting the other clones participating in the ongoing GC reaction.

Further investigation into how metabolism controls B cell fate decisions, along with improvements in *in vivo* experimental techniques, would improve our understanding and may pave the way for future therapies. This is particularly important for vaccine strategies and autoimmune diseases that involve humoral components.

The termination of GCs also known as ‘GC shutdown’ remains an understudied area. Unlike GC formation, which occurs within a well-established timeline, their termination follows an unpredictable time course, primarily because GCs can persist for months[154]. It is important to explore whether nutrient availability or changes in cell-intrinsic metabolic pathways contribute to this enigmatic process.

Determining the specific metabolic needs of B cells at different stages of their development is crucial for understanding their functions and identifying potential therapeutic targets[65].

Bibliography

1. Hardy, R. R. & Hayakawa, K. B Cell Development Pathways. *Annu. Rev. Immunol.* **19**, 595–621 (2001).
2. Fu, Y., Wang, L., Yu, B., Xu, D. & Chu, Y. Immunometabolism shapes B cell fate and functions. *Immunology* **166**, 444–457 (2022).
3. Boothby, M. R., Brookens, S. K., Raybuck, A. L. & Cho, S. H. Supplying the trip to antibody production—nutrients, signaling, and the programming of cellular metabolism in the mature B lineage. *Cell. Mol. Immunol.* **19**, 352–369 (2022).
4. Egawa, T. & Bhattacharya, D. Regulation of metabolic supply and demand during B cell activation and subsequent differentiation. *Curr. Opin. Immunol.* **57**, 8–14 (2019).
5. LeBien, T. W. & Tedder, T. F. B lymphocytes: how they develop and function. *Blood* **112**, 1570–1580 (2008).
6. Elsner, R. A. & Shlomchik, M. J. Germinal Center and Extrafollicular B Cell Responses in Vaccination, Immunity, and Autoimmunity. *Immunity* **53**, 1136–1150 (2020).
7. Victora, G. D. & Nussenzweig, M. C. Germinal Centers. *Annu. Rev. Immunol.* **40**, 413–442 (2022).
8. Gitlin, A. D., Shulman, Z. & Nussenzweig, M. C. Clonal selection in the germinal centre by regulated proliferation and hypermutation. *Nature* **509**, 637–640 (2014).
9. Nakagawa, R. & Calado, D. P. Positive Selection in the Light Zone of Germinal Centers. *Front. Immunol.* **12**, (2021).
10. Long, Z., Phillips, B., Radtke, D., Meyer-Hermann, M. & Bannard, O. Competition for refuelling rather than cyclic re-entry initiation evident in germinal centers. *Sci. Immunol.* **7**, eabm0775 (2022).
11. Inoue, T. & Kurosaki, T. Memory B cells. *Nat. Rev. Immunol.* **24**, 5–17 (2024).
12. Mayer, C. T. *et al.* The microanatomic segregation of selection by apoptosis in the germinal center. *Science* **358**, eaao2602 (2017).

13. Stewart, I., Radtke, D., Phillips, B., McGowan, S. J. & Bannard, O. Germinal Center B Cells Replace Their Antigen Receptors in Dark Zones and Fail Light Zone Entry when Immunoglobulin Gene Mutations are Damaging. *Immunity* **49**, 477-489.e7 (2018).
14. Robbiani, D. F. *et al.* AID Is Required for the Chromosomal Breaks in c-myc that Lead to c-myc/IgH Translocations. *Cell* **135**, 1028–1038 (2008).
15. Xu, S. *et al.* von Hippel-Lindau Protein Maintains Metabolic Balance to Regulate the Survival of Naive B Lymphocytes. *iScience* **17**, 379–392 (2019).
16. Burrows, N. *et al.* Dynamic regulation of hypoxia-inducible factor-1α activity is essential for normal B cell development. *Nat. Immunol.* **21**, 1408–1420 (2020).
17. Waters, L. R., Ahsan, F. M., Wolf, D. M., Shirihai, O. & Teitell, M. A. Initial B Cell Activation Induces Metabolic Reprogramming and Mitochondrial Remodeling. *iScience* **5**, 99–109 (2018).
18. Xiao, G. *et al.* B-Cell-Specific Diversion of Glucose Carbon Utilization Reveals a Unique Vulnerability in B Cell Malignancies. *Cell* **173**, 470-484.e18 (2018).
19. Sharma, R. *et al.* Distinct metabolic requirements regulate B cell activation and germinal center responses. *Nat. Immunol. 24, 1358–1369 (2023)*
20. Yazicioglu, Y. F. *et al.* Dynamic mitochondrial transcription and translation in B cells control germinal center entry and lymphomagenesis. *Nat. Immunol.* **24**, 991–1006 (2023).
21. Weisel, F. J. *et al.* Germinal center B cells selectively oxidize fatty acids for energy while conducting minimal glycolysis. *Nat. Immunol.* **21**, 331–342 (2020).
22. Brookens, S. K. *et al.* Plasma Cell Differentiation, Antibody Quality, and Initial Germinal Center B Cell Population Depend on Glucose Influx Rate. *J. Immunol.* **212**, 43–56 (2023).
23. Bierling, T. E. H. *et al.* GLUT1-mediated glucose import in B cells is critical for anaplerotic balance and humoral immunity. *Cell Rep.* **43**, (2024).
24. Bertolotti, M., Sitia, R. & Rubartelli, A. On the Redox Control of B Lymphocyte Differentiation and Function. *Antioxid. Amp Redox Signal.* **16**, 1139–1149 (2012).

25. Muri, J. & Kopf, M. Redox regulation of immunometabolism. *Nat. Rev. Immunol.* **21**, 363–381 (2021).
26. Franchina, D. G. *et al.* Glutathione-dependent redox balance characterizes the distinct metabolic properties of follicular and marginal zone B cells. *Nat. Commun.* **13**, 1789 (2022).
27. Vijay, R. *et al.* Infection-induced plasmablasts are a nutrient sink that impairs humoral immunity to malaria. *Nat. Immunol.* **21**, 790–801 (2020).
28. Crawford, J. & Cohen, H. J. The essential role of L-glutamine in lymphocyte differentiation in vitro. *J. Cell. Physiol.* **124**, 275–282 (1985).
29. Yang, L. *et al.* Amino acid metabolism in immune cells: essential regulators of the effector functions, and promising opportunities to enhance cancer immunotherapy. *J. Hematol. Oncol.J Hematol Oncol* **16**, 59 (2023).
30. Torigoe, M. *et al.* l-Leucine influx through Slc7a5 regulates inflammatory responses of human B cells via mammalian target of rapamycin complex 1 signaling. *Mod. Rheumatol.* **29**, 885–891 (2019).
31. Cantor, J. *et al.* CD98hc facilitates B cell proliferation and adaptive humoral immunity. *Nat. Immunol.* **10**, 412–419 (2009).
32. Wang, Z. *et al.* Leucine-tRNA-synthetase-2-expressing B cells contribute to colorectal cancer immunoevasion. *Immunity* **55**, 1067-1081.e8 (2022).
33. D'Avola, A. *et al.* PHGDH is required for germinal center formation and is a therapeutic target in *MYC*-driven lymphoma. *J. Clin. Invest.* **132**, (2022).
34. van Beek, A. A. *et al.* Frontline Science: Tryptophan restriction arrests B cell development and enhances microbial diversity in WT and prematurely aging Ercc1-/Δ7 mice. *J. Leukoc. Biol.* **101**, 811–821 (2017).
35. Luo, W. *et al.* SREBP signaling is essential for effective B cell responses. *Nat. Immunol.* **24**, 337–348 (2023).
36. Zhou, X. *et al.* Stearoyl-CoA Desaturase-Mediated Monounsaturated Fatty Acid Availability Supports Humoral Immunity. *Cell Rep.* **34**, 108601 (2021).

37. Sanchez, H. N. *et al.* B cell-intrinsic epigenetic modulation of antibody responses by dietary fiber-derived short-chain fatty acids. *Nat. Commun.* **11**, 60 (2020).
38. Cho, S. H. *et al.* Germinal centre hypoxia and regulation of antibody qualities by a hypoxia response system. *Nature* **537**, 234–238 (2016).
39. Warburg, O. The Metabolism of Carcinoma Cells1. *J. Cancer Res.* **9**, 148–163 (1925).
40. Jellusova, J. Cross-talk between signal transduction and metabolism in B cells. *Immunol. Lett.* **201**, 1–13 (2018).
41. D'Souza, A. D., Parikh, N., Kaech, S. M. & Shadel, G. S. Convergence of multiple signaling pathways is required to coordinately up-regulate mtDNA and mitochondrial biogenesis during T cell activation. *Mitochondrion* **7**, 374–385 (2007).
42. Waickman, A. T. & Powell, J. D. mTOR, metabolism, and the regulation of T-cell differentiation and function. *Immunol. Rev.* **249**, 43–58 (2012).
43. Caro-Maldonado, A. *et al.* Metabolic Reprogramming is Required for Antibody Production That is Suppressed in Anergic but Exaggerated in Chronically BAFF-Exposed B cells. *J. Immunol. Baltim. Md 1950* **192**, 3626–3636 (2014).
44. Jellusova, J. *et al.* Gsk3 is a metabolic checkpoint regulator in B cells. *Nat. Immunol.* **18**, 303–312 (2017).
45. Wang, R. *et al.* The Transcription Factor Myc Controls Metabolic Reprogramming upon T Lymphocyte Activation. *Immunity* **35**, 871–882 (2011).
46. Raza, I. G. A. & Clarke, A. J. B Cell Metabolism and Autophagy in Autoimmunity. *Front. Immunol.* **12**, (2021).
47. Boothby, M. & Rickert, R. C. Metabolic Regulation of the Immune Humoral Response. *Immunity* **46**, 743–755 (2017).
48. Chen, D. *et al.* Coupled analysis of transcriptome and BCR mutations reveals role of OXPHOS in affinity maturation. *Nat. Immunol.* **22**, 904–913 (2021).
49. Haniuda, K., Fukao, S. & Kitamura, D. Metabolic Reprogramming Induces Germinal Center B Cell Differentiation through Bcl6 Locus Remodeling. *Cell Rep.* **33**, 108333 (2020).

50. Biram, A. *et al.* Bacterial infection disrupts established germinal center reactions through monocyte recruitment and impaired metabolic adaptation. *Immunity* **55**, 442-458.e8 (2022).
51. Chandel, N. S. Evolution of Mitochondria as Signaling Organelles. *Cell Metab.* **22**, 204–206 (2015).
52. Spinelli, J. B. & Haigis, M. C. The multifaceted contributions of mitochondria to cellular metabolism. *Nat. Cell Biol.* **20**, 745–754 (2018).
53. Martínez-Reyes, I. & Chandel, N. S. Mitochondrial TCA cycle metabolites control physiology and disease. *Nat. Commun.* **11**, 102 (2020).
54. Desdín-Micó, G., Soto-Heredero, G. & Mittelbrunn, M. Mitochondrial activity in T cells. *Mitochondrion* **41**, 51–57 (2018).
55. Jang, K.-J. *et al.* Mitochondrial function provides instructive signals for activation-induced B-cell fates. *Nat. Commun.* **6**, (2015).
56. Fischer, M. *et al.* Early effector maturation of naïve human CD8+ T cells requires mitochondrial biogenesis. *Eur. J. Immunol.* **48**, 1632–1643 (2018).
57. Bailis, W. *et al.* Distinct modes of mitochondrial metabolism uncouple T cell differentiation and function. *Nature* **571**, 403–407 (2019).
58. Rausser, S. *et al.* Mitochondrial phenotypes in purified human immune cell subtypes and cell mixtures. *eLife* **10**, e70899 (2021).
59. Franklin, I. G. *et al.* T cell differentiation drives the negative selection of pathogenic mitochondrial DNA variants. *Life Sci. Alliance* **6**, (2023).
60. Lareau, C. A. *et al.* Single-cell multi-omics of mitochondrial DNA disorders reveals dynamics of purifying selection across human immune cells. *Nat. Genet.* **55**, 1198–1209 (2023).
61. Walker, M. A. *et al.* Purifying Selection against Pathogenic Mitochondrial DNA in Human T Cells. *N. Engl. J. Med.* **383**, 1556–1563 (2020).
62. Gordon-Lipkin, E. M. *et al.* Primary oxidative phosphorylation defects lead to perturbations in the human B cell repertoire. *Front. Immunol.* **14**, (2023).

63. Bantug, G. R., Galluzzi, L., Kroemer, G. & Hess, C. The spectrum of T cell metabolism in health and disease. *Nat. Rev. Immunol.* **18**, 19–34 (2018).
64. Psarras, A. & Clarke, A. A cellular overview of immunometabolism in systemic lupus erythematosus. *Oxf. Open Immunol.* **4**, iqad005 (2023).
65. Yazicioglu, Y. F., Mitchell, R. J. & Clarke, A. J. Mitochondrial control of lymphocyte homeostasis. *Semin. Cell Dev. Biol.* **161–162**, 42–53 (2024).
66. Stewart, J. B. & Chinnery, P. F. Extreme heterogeneity of human mitochondrial DNA from organelles to populations. *Nat. Rev. Genet.* **22**, 106–118 (2021).
67. Stewart, J. B. & Chinnery, P. F. The dynamics of mitochondrial DNA heteroplasmy: implications for human health and disease. *Nat. Rev. Genet.* **16**, 530–542 (2015).
68. Kramer, P. A., Ravi, S., Chacko, B., Johnson, M. S. & Darley-Usmar, V. M. A review of the mitochondrial and glycolytic metabolism in human platelets and leukocytes: Implications for their use as bioenergetic biomarkers. *Redox Biol.* **2**, 206–210 (2014).
69. van der Windt, G. J. W. *et al.* Mitochondrial Respiratory Capacity Is a Critical Regulator of CD8+ T Cell Memory Development. *Immunity* **36**, 68–78 (2012).
70. Akkaya, B. *et al.* Increased Mitochondrial Biogenesis and Reactive Oxygen Species Production Accompany Prolonged CD4+ T Cell Activation. *J. Immunol.* **201**, 3294–3306 (2018).
71. Ron-Harel, N. *et al.* Mitochondrial Biogenesis and Proteome Remodeling Promote One-Carbon Metabolism for T Cell Activation. *Cell Metab.* **24**, 104–117 (2016).
72. Zhang, R., Wang, Y., Ye, K., Picard, M. & Gu, Z. Independent impacts of aging on mitochondrial DNA quantity and quality in humans. *BMC Genomics* **18**, 890 (2017).
73. Kukat, C. *et al.* Cross-strand binding of TFAM to a single mtDNA molecule forms the mitochondrial nucleoid. *Proc. Natl. Acad. Sci. U. S. A.* **112**, 11288–11293 (2015).
74. Ngo, H. B., Kaiser, J. T. & Chan, D. C. The mitochondrial transcription and packaging factor Tfam imposes a U-turn on mitochondrial DNA. *Nat. Struct. Mol. Biol.* **18**, 1290–1296 (2011).

75. Kukat, C. *et al.* Super-resolution microscopy reveals that mammalian mitochondrial nucleoids have a uniform size and frequently contain a single copy of mtDNA. *Proc. Natl. Acad. Sci.* **108**, 13534–13539 (2011).
76. Brüser, C., Keller-Findeisen, J. & Jakobs, S. The TFAM-to-mtDNA ratio defines inner-cellular nucleoid populations with distinct activity levels. *Cell Rep.* **37**, 110000 (2021).
77. Urbanczyk, S. *et al.* Mitochondrial respiration in B lymphocytes is essential for humoral immunity by controlling the flux of the TCA cycle. *Cell Rep.* **39**, 110912 (2022).
78. Tang, Z. *et al.* A Genetic Bottleneck of Mitochondrial DNA During Human Lymphocyte Development. *Mol. Biol. Evol.* **39**, (2022).
79. Mimitou, E. P. *et al.* Scalable, multimodal profiling of chromatin accessibility, gene expression and protein levels in single cells. *Nat. Biotechnol.* **39**, 1246–1258 (2021).
80. Larsson, N.-G. *et al.* Mitochondrial transcription factor A is necessary for mtDNA maintance and embryogenesis in mice. *Nat. Genet.* **18**, 231–236 (1998).
81. Gao, X. *et al.* TFAM-Dependent Mitochondrial Metabolism Is Required for Alveolar Macrophage Maintenance and Homeostasis. *J. Immunol.* **208**, 1456–1466 (2022).
82. Wculek, S. K. *et al.* Oxidative phosphorylation selectively orchestrates tissue macrophage homeostasis. *Immunity* **56**, 516-530.e9 (2023).
83. Lu, T. *et al.* TFAM deficiency in dendritic cells leads to mitochondrial dysfunction and enhanced antitumor immunity through cGAS-STING pathway. *J. Immunother. Cancer* **11**, e005430 (2023).
84. Baixauli, F. *et al.* Mitochondrial Respiration Controls Lysosomal Function during Inflammatory T Cell Responses. *Cell Metab.* **22**, 485–498 (2015).
85. Desdín-Micó, G. *et al.* T cells with dysfunctional mitochondria induce multimorbidity and premature senescence. *Science* **368**, 1371–1376 (2020).
86. Fu, Z. *et al.* Requirement of Mitochondrial Transcription Factor A in Tissue-Resident Regulatory T Cell Maintenance and Function. *Cell Rep.* **28**, 159-171.e4 (2019).

87. Chapman, N. M. *et al.* mTOR coordinates transcriptional programs and mitochondrial metabolism of activated Treg subsets to protect tissue homeostasis. *Nat. Commun.* **9**, 2095 (2018).
88. Iborra-Pernichi, M. *et al.* Defective mitochondria remodelling in B cells leads to an aged immune response. *Nat. Commun.* **15**, 2569 (2024).
89. O'Sullivan, D. *et al.* Fever supports CD8 $^{+}$ effector T cell responses by promoting mitochondrial translation. *Proc. Natl. Acad. Sci.* **118**, e2023752118 (2021).
90. Almeida, L. *et al.* Ribosome-Targeting Antibiotics Impair T Cell Effector Function and Ameliorate Autoimmunity by Blocking Mitochondrial Protein Synthesis. *Immunity* **54**, 68-83.e6 (2021).
91. Lisci, M. *et al.* Mitochondrial translation is required for sustained killing by cytotoxic T cells. *Science* **374**, eabe9977 (2021).
92. Dominguez-Sola, D. *et al.* The proto-oncogene MYC is required for selection in the germinal center and cyclic reentry. *Nat. Immunol.* **13**, 1083 EP-.
93. Cato, M. H., Yau, I. W. & Rickert, R. C. Magnetic-based purification of untouched mouse germinal center B cells for ex vivo manipulation and biochemical analysis. *Nat. Protoc.* **6**, 953–960 (2011).
94. Yazicioglu, Y. F., Aksoylar, H. I., Pal, R., Patsoukis, N. & Boussiotis, V. A. Unraveling Key Players of Humoral Immunity: Advanced and Optimized Lymphocyte Isolation Protocol from Murine Peyer's Patches. *J. Vis. Exp.* e58490 (2018) doi:10.3791/58490.
95. McAllister, E. J., Apgar, J. R., Leung, C. R., Rickert, R. C. & Jellusova, J. New Methods To Analyze B Cell Immune Responses to Thymus-Dependent Antigen Sheep Red Blood Cells. *J. Immunol.* **199**, 2998–3003 (2017).
96. Delaunay, S. *et al.* Mitochondrial RNA modifications shape metabolic plasticity in metastasis. *Nature* **607**, 593–603 (2022).
97. Pelgrom, L. R. *et al.* QUAS-R: An SLC1A5-mediated glutamine uptake assay with single-cell resolution reveals metabolic heterogeneity with immune populations. *Cell Rep.* **42**, 112828 (2023).

98. Ollion, J., Cochennec, J., Loll, F., Escudé, C. & Boudier, T. TANGO: a generic tool for high-throughput 3D image analysis for studying nuclear organization. *Bioinformatics* **29**, 1840–1841 (2013).

99. Chaudhry, A., Shi, R. & Luciani, D. S. A pipeline for multidimensional confocal analysis of mitochondrial morphology, function, and dynamics in pancreatic β-cells. *Am. J. Physiol.-Endocrinol. Metab.* **318**, E87–E101 (2020).

100. Nojima, T. *et al.* In-vitro derived germinal centre B cells differentially generate memory B or plasma cells in vivo. *Nat. Commun.* **2**, 465–11 (2011).

101. Neely, H. R. & Flajnik, M. F. CXCL13 responsiveness but not CXCR5 expression by late transitional B cells initiates splenic white pulp formation. *J. Immunol. Baltim. Md 1950* **194**, 2616–2623 (2015).

102. Chatterjee, D. *et al.* Avid binding by B cells to the Plasmodium circumsporozoite protein repeat suppresses responses to protective subdominant epitopes. *Cell Rep.* **35**, 108996 (2021).

103. Sage, P. T. *et al.* Suppression by TFR cells leads to durable and selective inhibition of B cell effector function. *Nat. Immunol.* **17**, 1436–1446 (2016).

104. Argüello, R. J. *et al.* SCENITH: A Flow Cytometry-Based Method to Functionally Profile Energy Metabolism with Single-Cell Resolution. *Cell Metab.* **32**, 1063-1075.e7 (2020).

105. Xia, J., Sinelnikov, I. V., Han, B. & Wishart, D. S. MetaboAnalyst 3.0—making metabolomics more meaningful. *Nucleic Acids Res.* **43**, W251–W257 (2015).

106. Fugger, K. *et al.* Targeting the nucleotide salvage factor DNPH1 sensitizes BRCA-deficient cells to PARP inhibitors. *Science* **372**, 156–165 (2021).

107. Clarke, A. J., Riffelmacher, T., Braas, D., Cornall, R. J. & Simon, A. K. B1a B cells require autophagy for metabolic homeostasis and self-renewal. *J. Exp. Med.* **215**, 399–413 (2018).

108. Geiger, R. *et al.* L-Arginine Modulates T Cell Metabolism and Enhances Survival and Anti-tumor Activity. *Cell* **167**, 829-842.e13 (2016).

109. Ron-Harel, N. *et al.* Mitochondrial Biogenesis and Proteome Remodeling Promote One-Carbon Metabolism for T Cell Activation. *Cell Metab.* **24**, 104–117 (2016).

110. Sinclair, L. V. *et al.* Control of amino-acid transport by antigen receptors coordinates the metabolic reprogramming essential for T cell differentiation. *Nat. Immunol.* **14**, 500–508 (2013).

111. Fernández-García, J. *et al.* CD8+ T cell metabolic rewiring defined by scRNA-seq identifies a critical role of ASNS expression dynamics in T cell differentiation. *Cell Rep.* **41**, (2022).

112. Wu, J. *et al.* Asparagine enhances LCK signalling to potentiate CD8 + T-cell activation and anti-tumour responses. *Nat. Cell Biol.* **23**, 75–86 (2021).

113. Hope, H. C. *et al.* Coordination of asparagine uptake and asparagine synthetase expression modulates $CD8^+$ T cell activation. *JCI Insight* **6**, (2021).

114. Gnanaprakasam, J. N. R. *et al.* Asparagine restriction enhances CD8+ T cell metabolic fitness and antitumoral functionality through an NRF2-dependent stress response. *Nat. Metab.* 1–17 (2023) doi:10.1038/s42255-023-00856-1.

115. Ma, E. H. *et al.* Serine Is an Essential Metabolite for Effector T Cell Expansion. *Cell Metab.* **25**, 345–357 (2017).

116. Kelly, B. & Pearce, E. L. Amino Assets: How Amino Acids Support Immunity. *Cell Metab.* S1550413120303119 (2020) doi:10.1016/j.cmet.2020.06.010.

117. Eraslan, Z., Papatzikas, G., Cazier, J.-B., Khanim, F. L. & Günther, U. L. Targeting Asparagine and Serine Metabolism in Germinal Centre-Derived B Cells Non-Hodgkin Lymphomas (B-NHL). *Cells* **10**, 2589 (2021).

118. Parsa, S. *et al.* The serine hydroxymethyltransferase-2 (SHMT2) initiates lymphoma development through epigenetic tumor suppressor silencing. *Nat. Cancer* **1**, 653–664 (2020).

119. D'Avola, A. *et al.* PHGDH is required for germinal center formation and is a therapeutic target in MYC-driven lymphoma. *J. Clin. Invest.* **132**, e153436 (2022).

120. Grima-Reyes, M. *et al.* Tumoral microenvironment prevents de novo asparagine biosynthesis in B cell lymphoma, regardless of ASNS expression. *Sci. Adv.* **8**, eabn6491 (2022).

121. Clarke, A. J., Riffelmacher, T., Braas, D., Cornall, R. J. & Simon, A. K. B1a B cells require autophagy for metabolic homeostasis and self-renewal. *J. Exp. Med.* **215**, 399–413 (2018).

122. Painter, M. W. *et al.* Transcriptomes of the B and T Lineages Compared by Multiplatform Microarray Profiling. *J. Immunol.* **186**, 3047–3057 (2011).

123. Pavlova, N. N. *et al.* As Extracellular Glutamine Levels Decline, Asparagine Becomes an Essential Amino Acid. *Cell Metab.* **27**, 428-438.e5 (2018).

124. Krall, A. S., Xu, S., Graeber, T. G., Braas, D. & Christofk, H. R. Asparagine promotes cancer cell proliferation through use as an amino acid exchange factor. *Nat. Commun.* **7**, 11457 (2016).

125. Krall, A. S. *et al.* Asparagine couples mitochondrial respiration to ATF4 activity and tumor growth. *Cell Metab.* **33**, 1013-1026.e6 (2021).

126. Lomelino, C. L., Andring, J. T., McKenna, R. & Kilberg, M. S. Asparagine synthetase: Function, structure, and role in disease. *J. Biol. Chem.* **292**, 19952–19958 (2017).

127. Yazicioglu, Y. F. *et al.* Asparagine availability controls B cell homeostasis. 2023.04.03.535433 Preprint at https://doi.org/10.1101/2023.04.03.535433 (2024).

128. Dieterich, D. C., Link, A. J., Graumann, J., Tirrell, D. A. & Schuman, E. M. Selective identification of newly synthesized proteins in mammalian cells using bioorthogonal noncanonical amino acid tagging (BONCAT). *Proc. Natl. Acad. Sci.* **103**, 9482–9487 (2006).

129. Enam, S. U. *et al.* Puromycin reactivity does not accurately localize translation at the subcellular level. *eLife* **9**, e60303 (2020).

130. Pelgrom, L. R. *et al.* QUAS-R: An SLC1A5-mediated glutamine uptake assay with single-cell resolution reveals metabolic heterogeneity with immune populations. *Cell Rep.* **42**, (2023).

131. Müller-Winkler, J. *et al.* Critical requirement for BCR, BAFF, and BAFFR in memory B cell survival. *J. Exp. Med.* **218**, e20191393 (2020).

132. Ren, W. *et al.* Amino-acid transporters in T-cell activation and differentiation. *Cell Death Dis.* **8**, e2655–e2655 (2017).

133. Korsunsky, I. *et al.* Cross-tissue, single-cell stromal atlas identifies shared pathological fibroblast phenotypes in four chronic inflammatory diseases. *Med* **3**, 481-518.e14 (2022).

134. Akiyama, T., Kobayashi, K., Higashikage, A., Sato, J. & Yoshinaga, H. CSF/plasma ratios of amino acids: Reference data and transports in children. *Brain Dev.* **36**, 3–9 (2014).

135. Sullivan, L. B. *et al.* Aspartate is an endogenous metabolic limitation for tumour growth. *Nat. Cell Biol.* 1–12 (2018) doi:10.1038/s41556-018-0125-0.

136. Sakaguchi, N., Kashiwamura, S., Kimoto, M., Thalmann, P. & Melchers, F. B lymphocyte lineage-restricted expression of mb-1, a gene with CD3-like structural properties. *EMBO J.* **7**, 3457–3464 (1988).

137. Pelanda, R. *et al.* Cre recombinase-controlled expression of the mb-1 allele. *genesis* **32**, 154–157 (2002).

138. Nutt, S. L., Hodgkin, P. D., Tarlinton, D. M. & Corcoran, L. M. The generation of antibody-secreting plasma cells. *Nat. Rev. Immunol.* **15**, 160–171 (2015).

139. Yabas, M., Yazicioglu, Y. F., Hoyne, G. F., Goodnow, C. C. & Enders, A. Loss of hnRNPLL-dependent splicing of Ptprc has no impact on B-cell development, activation and terminal differentiation into antibody-secreting cells. *Immunol. Cell Biol.* **99**, 532–541 (2021).

140. Scharer, C. D., Barwick, B. G., Guo, M., Bally, A. P. R. & Boss, J. M. Plasma cell differentiation is controlled by multiple cell division-coupled epigenetic programs. *Nat. Commun.* **9**, 1698 (2018).

141. Belanger, M. C. *et al.* Acute Lymph Node Slices Are a Functional Model System to Study Immunity Ex Vivo. *ACS Pharmacol. Transl. Sci.* **4**, 128–142 (2021).

142. Crotty, S. T Follicular Helper Cell Differentiation, Function, and Roles in Disease. *Immunity* **41**, 529–542 (2014).

143. Qi, H. T follicular helper cells in space-time. *Nat. Rev. Immunol.* **16**, 612–625 (2016).

144. Choi, S.-C. *et al.* Inhibition of glucose metabolism selectively targets autoreactive follicular helper T cells. *Nat. Commun.* **9**, 4369 (2018).

145. Mesin, L., Ersching, J. & Victora, G. D. Germinal Center B Cell Dynamics. *Immunity* **45**, 471–482 (2016).

146. Kennedy, D. E. *et al.* Novel specialized cell state and spatial compartments within the germinal center. *Nat. Immunol.* **21**, 660–670 (2020).

147. Crosio, C. *et al.* Mitotic Phosphorylation of Histone H3: Spatio-Temporal Regulation by Mammalian Aurora Kinases. *Mol. Cell. Biol.* **22**, 874–885 (2002).

148. Heise, N. & Klein, U. Somatic Hypermutation and Affinity Maturation Analysis Using the 4-Hydroxy-3-Nitrophenyl-Acetyl (NP) System. in *Germinal Centers: Methods and Protocols* (ed. Calado, D. P.) 191–208 (Springer, New York, NY, 2017). doi:10.1007/978-1-4939-7095-7_16.

149. Knott, S. R. V. *et al.* Asparagine bioavailability governs metastasis in a model of breast cancer. *Nature* **554**, 378–381 (2018).

150. McAllister, E. J., Apgar, J. R., Leung, C. R., Rickert, R. C. & Jellusova, J. New Methods To Analyze B Cell Immune Responses to Thymus-Dependent Antigen Sheep Red Blood Cells. *J. Immunol.* **199**, 2998–3003 (2017).

151. García de Vinuesa, C., O'Leary, P., Sze, D. M.-Y., Toellner, K.-M. & MacLennan, I. C. M. T-independent type 2 antigens induce B cell proliferation in multiple splenic

sites, but exponential growth is confined to extrafollicular foci. *Eur. J. Immunol.* **29**, 1314–1323 (1999).

152. de Vinuesa, C. G. *et al.* Germinal Centers without T Cells. *J. Exp. Med.* **191**, 485–494 (2000).

153. Nakagawa, R. *et al.* Permissive selection followed by affinity-based proliferation of GC light zone B cells dictates cell fate and ensures clonal breadth. *Proc. Natl. Acad. Sci.* **118**, e2016425118 (2021).

154. Matz, H. C., McIntire, K. M. & Ellebedy, A. H. 'Persistent germinal center responses: slow-growing trees bear the best fruits'. *Curr. Opin. Immunol.* **83**, 102332 (2023).

155. Liu, X., Liu, B. & Qi, H. Germinal center reaction and output: recent advances. *Curr. Opin. Immunol.* **82**, 102308 (2023).

156. Xu, Y. *et al.* Asparagine reinforces mTORC1 signaling to boost thermogenesis and glycolysis in adipose tissues. *EMBO J.* **40**, e108069 (2021).

157. León, B., Ballesteros-Tato, A., Randall, T. D. & Lund, F. E. Prolonged antigen presentation by immune complex–binding dendritic cells programs the proliferative capacity of memory CD8 T cells. *J. Exp. Med.* **211**, 1637–1655 (2014).

158. Keating, R. *et al.* Broadly Reactive Influenza Antibodies Are Not Limited by Germinal Center Competition with High-Affinity Antibodies. *mBio* **11**, 10.1128/mbio.01859-20 (2020).

159. Wang, M., Huang, Y., Gu, W. & Wang, H. Evaluation of T Follicular Helper Cells and Germinal Center Response During Influenza A Virus Infection in Mice. *JoVE J. Vis. Exp.* e60523 (2020) doi:10.3791/60523.

160. Urbanczyk, S. *et al.* Mitochondrial respiration in B lymphocytes is essential for humoral immunity by controlling the flux of the TCA cycle. *Cell Rep.* **39**, 110912 (2022).

161. Sharma, R. *et al.* Distinct metabolic requirements regulate B cell activation and germinal center responses. *Nat. Immunol.* 1–12 (2023) doi:10.1038/s41590-023-01540-y.

162. Luo, W. *et al.* SREBP signaling is essential for effective B cell responses. *Nat. Immunol.* 1–12 (2022) doi:10.1038/s41590-022-01376-y.

163. Argüello, R. J. *et al.* SCENITH: A flow cytometry based method to functionally profile energy metabolism with single cell resolution. *Cell Metab.* **32**, 1063-1075.e7 (2020).

164. Landgraf, P., Antileo, E. R., Schuman, E. M. & Dieterich, D. C. BONCAT: Metabolic Labeling, Click Chemistry, and Affinity Purification of Newly Synthesized Proteomes. in *Site-Specific Protein Labeling: Methods and Protocols* (eds. Gautier, A. & Hinner, M. J.) 199–215 (Springer, New York, NY, 2015). doi:10.1007/978-1-4939-2272-7_14.

165. Masle-Farquhar, E., Bröer, A., Yabas, M., Enders, A. & Bröer, S. ASCT2 (SLC1A5)-Deficient Mice Have Normal B-Cell Development, Proliferation, and Antibody Production. *Front. Immunol.* **8**, 549 (2017).

166. Sheldon, R. D., Ma, E. H., DeCamp, L. M., Williams, K. S. & Jones, R. G. Interrogating in vivo T-cell metabolism in mice using stable isotope labeling metabolomics and rapid cell sorting. *Nat. Protoc.* **16**, 4494–4521 (2021).

167. Jones, M. A. *et al.* Discovering New Lipidomic Features Using Cell Type Specific Fluorophore Expression to Provide Spatial and Biological Specificity in a Multimodal Workflow with MALDI Imaging Mass Spectrometry. *Anal. Chem.* **92**, 7079–7086 (2020).

168. Rossi, M. *et al.* PHGDH heterogeneity potentiates cancer cell dissemination and metastasis. *Nature* **605**, 747–753 (2022).

169. Noree, C., Monfort, E. & Shotelersuk, V. Human asparagine synthetase associates with the mitotic spindle. *Biol. Open* **7**, bio038307 (2018).

170. Price, M. J., Patterson, D. G., Scharer, C. D. & Boss, J. M. Progressive Upregulation of Oxidative Metabolism Facilitates Plasmablast Differentiation to a T-Independent Antigen. *Cell Rep.* **23**, 3152–3159 (2018).

171. Cecconello, D. K. *et al.* Asparaginase: an old drug with new questions. *Hematol. Transfus. Cell Ther.* **42**, 275–282 (2020).

172. Semba, R. D. The Rise and Fall of Protein Malnutrition in Global Health. *Ann. Nutr. Metab.* **69**, 79–88 (2016).

173. Tripathy, S. K., Das, S. & Malik, A. Vaccine and malnutrition: A narrative review. *J. Fam. Med. Prim. Care* **12**, 1808–1813 (2023).

174. Hoang, T., Agger, E. M., Cassidy, J. P., Christensen, J. P. & Andersen, P. Protein Energy Malnutrition during Vaccination Has Limited Influence on Vaccine Efficacy but Abolishes Immunity if Administered during Mycobacterium tuberculosis Infection. *Infect. Immun.* **83**, 2118–2126 (2015).

175. Ott, G., Rosenwald, A. & Campo, E. Understanding MYC-driven aggressive B-cell lymphomas: pathogenesis and classification. **122**, 8 (2013).

176. Caro, P. *et al.* Metabolic Signatures Uncover Distinct Targets in Molecular Subsets of Diffuse Large B Cell Lymphoma. *Cancer Cell* **22**, 547–560 (2012).

177. Akkaya, M. *et al.* Second signals rescue B cells from activation-induced mitochondrial dysfunction and death. *Nat. Immunol.* **19**, 871–884 (2018).

178. Emrich, S. M. *et al.* The mitochondrial sodium/calcium exchanger NCLX (Slc8b1) in B lymphocytes. *Cell Calcium* **108**, 102667 (2022).

179. Tsui, C. *et al.* Protein Kinase C-β Dictates B Cell Fate by Regulating Mitochondrial Remodeling, Metabolic Reprogramming, and Heme Biosynthesis. *Immunity* **48**, 1144-1159.e5 (2018).

180. Akkaya, M. *et al.* Second signals rescue B cells from activation-induced mitochondrial dysfunction and death. *Nat. Immunol.* **19**, 871–884 (2018).

181. Jang, K.-J. *et al.* Mitochondrial function provides instructive signals for activation-induced B-cell fates. *Nat. Commun.* **6**, 6750 (2015).

182. Shpilka, T. & Haynes, C. M. The mitochondrial UPR: mechanisms, physiological functions and implications in ageing. *Nat. Rev. Mol. Cell Biol.* **19**, 109–120 (2018).

183. Lisci, M. *et al.* Mitochondrial translation is required for sustained killing by cytotoxic T cells. *Science* **374**, eabe9977 (2021).

184. Almeida, L. *et al. Ribosome-Targeting Antibiotics Impair T Cell Effector Function and Ameliorate Autoimmunity by Blocking Mitochondrial Protein Synthesis*. http://biorxiv.org/lookup/doi/10.1101/832956 (2019) doi:10.1101/832956.

185. O'Sullivan, D. *et al.* Fever supports CD8+ effector T cell responses by promoting mitochondrial translation. *Proc. Natl. Acad. Sci.* **118**, e2023752118 (2021).

186. Kaufman, B. A. *et al.* The Mitochondrial Transcription Factor TFAM Coordinates the Assembly of Multiple DNA Molecules into Nucleoid-like Structures□D. *Mol. Biol. Cell* **18**, 12 (2007).

187. Hillen, H. S., Temiakov, D. & Cramer, P. Structural basis of mitochondrial transcription. *Nat. Struct. Mol. Biol.* **25**, 754–765 (2018).

188. Stiles, A. R. *et al.* Mutations in TFAM, encoding mitochondrial transcription factor A, cause neonatal liver failure associated with mtDNA depletion. *Mol. Genet. Metab.* **119**, 91–99 (2016).

189. Desdín-Micó, G. *et al.* T cells with dysfunctional mitochondria induce multimorbidity and premature senescence. *Science* **368**, 1371–1376 (2020).

190. West, A. P. *et al.* Mitochondrial DNA stress primes the antiviral innate immune response. *Nature* **520**, 553–557 (2015).

191. McWilliams, T. G. *et al.* mito-QC illuminates mitophagy and mitochondrial architecture in vivo. *J. Cell Biol.* **214**, 333–345 (2016).

192. Chen, P.-M. *et al.* CD38 reduces mitochondrial fitness and cytotoxic T cell response against viral infection in lupus patients by suppressing mitophagy. *Sci. Adv.* **8**, eabo4271 (2022).

193. Martinez-Martin, N. *et al.* A switch from canonical to noncanonical autophagy shapes B cell responses. *Sci. N. Y. NY* **355**, 641–647 (2017).

194. Kennedy, D. E. *et al.* Novel specialized cell state and spatial compartments within the germinal center. *Nat. Immunol.* **21**, 660–670 (2020).

195. Brüser, C., Keller-Findeisen, J. & Jakobs, S. The TFAM-to-mtDNA ratio defines inner-cellular nucleoid populations with distinct activity levels. *Cell Rep.* **37**, 110000 (2021).

196. Hobeika, E. *et al.* Testing gene function early in the B cell lineage in mb1-cre mice. *Proc. Natl. Acad. Sci.* **103**, 13789–13794 (2006).

197. Allen, D., Simon, T., Sablitzky, F., Rajewsky, K. & Cumano, A. Antibody engineering for the analysis of affinity maturation of an anti-hapten response. *EMBO J.* **7**, 1995–2001 (1988).

198. Weiser, A. A. *et al.* Affinity maturation of B cells involves not only a few but a whole spectrum of relevant mutations. *Int. Immunol.* **23**, 345–356 (2011).

199. Morén, C. *et al.* Study of oxidative, enzymatic mitochondrial respiratory chain function and apoptosis in perinatally HIV-infected pediatric patients. *Drug Chem. Toxicol.* **36**, 496–500 (2013).

200. Allen, C. D. C. *et al.* Germinal center dark and light zone organization is mediated by CXCR4 and CXCR5. *Nat. Immunol.* **5**, 943–952 (2004).

201. Keppler, S. J. *et al.* The Lack of WIP Binding to Actin Results in Impaired B Cell Migration and Altered Humoral Immune Responses. *Cell Rep.* **24**, 619–629 (2018).

202. Maus, M. *et al.* B cell receptor-induced Ca^{2+} mobilization mediates F-actin rearrangements and is indispensable for adhesion and spreading of B lymphocytes. *J. Leukoc. Biol.* **93**, 537–547 (2013).

203. Li, F. *et al.* Myc Stimulates Nuclearly Encoded Mitochondrial Genes and Mitochondrial Biogenesis. *Mol. Cell. Biol.* **25**, 6225–6234 (2005).

204. Harris, A. W. *et al.* The E mu-myc transgenic mouse. A model for high-incidence spontaneous lymphoma and leukemia of early B cells. *J. Exp. Med.* **167**, 353–371 (1988).

205. Yao, C.-H. *et al.* Mitochondrial fusion supports increased oxidative phosphorylation during cell proliferation. *eLife* **8**, e41351 (2019).

206. Buck, M. D. *et al.* Mitochondrial Dynamics Controls T Cell Fate through Metabolic Programming. *Cell* **166**, 63–76 (2016).

207. Stevens, M. G., Mason, F. M. & Bullock, T. N. J. The mitochondrial fission protein DRP1 influences memory CD8+ T cell formation and function. *J. Leukoc. Biol.* **115**, 679–694 (2024).

208. Waters, L. R., Ahsan, F. M., Wolf, D. M., Shirihai, O. & Teitell, M. A. Initial B Cell Activation Induces Metabolic Reprogramming and Mitochondrial Remodeling. *ISCIENCE* **5**, 99–109 (2018).

209. Bonekamp, N. A. *et al.* High levels of TFAM repress mammalian mitochondrial DNA transcription in vivo. *Life Sci. Alliance* **4**, (2021).

210. King, G. A. *et al.* Acetylation and phosphorylation of human TFAM regulate TFAM–DNA interactions via contrasting mechanisms. *Nucleic Acids Res.* **46**, 3633–3642 (2018).

211. Zhang, M. *et al.* Reduced acetylation of TFAM promotes bioenergetic dysfunction in the failing heart. *iScience* **26**, 106942 (2023).

212. Nojima, T. *et al.* In-vitro derived germinal centre B cells differentially generate memory B or plasma cells in vivo. *Nat. Commun.* **2**, 465 (2011).

213. Campello, S. *et al.* Orchestration of lymphocyte chemotaxis by mitochondrial dynamics. *J. Exp. Med.* **203**, 2879–2886 (2006).

214. Liu, J. C. *et al.* MICU1 Serves as a Molecular Gatekeeper to Prevent In Vivo Mitochondrial Calcium Overload. *Cell Rep.* **16**, 1561–1573 (2016).

215. Gurwicz, N. *et al.* Tingible body macrophages arise from lymph node–resident precursors and uptake B cells by dendrites. *J. Exp. Med.* **220**, e20222173 (2023).

216. Grootveld, A. K. *et al.* Apoptotic cell fragments locally activate tingible body macrophages in the germinal center. *Cell* **186**, 1144-1161.e18 (2023).

217. Abbott, R. K. *et al.* Germinal center hypoxia potentiates immunoglobulin class switch recombination. *J. Immunol. Baltim. Md 1950* **197**, 4014–4020 (2016).

218. Spinelli, J. B. *et al.* Fumarate is a terminal electron acceptor in the mammalian electron transport chain. *Science* **374**, 1227–1237 (2021).

219. Oestreich, K. J. *et al.* Bcl-6 directly represses the gene program of the glycolysis pathway. *Nat. Immunol.* **15**, 957–964 (2014).

220. Khaliq, A. M. *et al.* Spatial transcriptomic analysis of primary and metastatic pancreatic cancers highlights tumor microenvironmental heterogeneity. *Nat. Genet.* 1–11 (2024) doi:10.1038/s41588-024-01914-4.

221. Zhang, H., Delafield, D. G. & Li, L. Mass spectrometry imaging: the rise of spatially resolved single-cell omics. *Nat. Methods* **20**, 327–330 (2023).

222. Ulbricht, C. *et al.* Intravital quantification reveals dynamic calcium concentration changes across B cell differentiation stages. *eLife* **10**, e56020 (2021).

223. Wagar, L. E. *et al.* Modeling human adaptive immune responses with tonsil organoids. *Nat. Med.* **27**, 125–135 (2021).

224. Purwada, A. & Singh, A. Immuno-engineered organoids for regulating the kinetics of B-cell development and antibody production. *Nat. Protoc.* **12**, 168–182 (2017).

225. Cantor, J. R. *et al.* Physiologic medium rewires cellular metabolism and reveals uric acid as an endogenous inhibitor of UMP synthase. *Cell* **169**, 258-272.e17 (2017).

226. Grootveld, A. K. *et al.* Apoptotic cell fragments locally activate tingible body macrophages in the germinal center. *Cell* **186**, 1144-1161.e18 (2023).

227. Inoue, T. *et al.* Exit from germinal center to become quiescent memory B cells depends on metabolic reprograming and provision of a survival signal. *J. Exp. Med.* **218**, e20200866 (2020).

Appendix

Appendix 1. Antibody list for Chapter 3

CellDIVE

Antibody (CellDIVE)	**Catalogue number**	**Manufacturer**
IgD	324502	Biolegend
ASNS	14681-1-AP	Proteintech
CD21	ab202692	Abcam
CD3	ab307335	Abcam
MZB1	NBP2-90320AF647	Novus
SLC1A5/ASCT2	HPA035240-25UL	Atlas

Flow cytometry

Antibody (Catalogue number)	**Clone**	**Manufacturer**
Anti-GL-7 (144612)	GL-7	Biolegend
Anti-CD138(142504)	281-2	Biolegend
Anti-CD19 (115538)	6D5	Biolegend
Anti-IgD (405721)	11-26c-2a	Biolegend
Anti-CD38 (102718)	90	Biolegend
Anti-CXCR4 (146513)	L276F12	Biolegend
Anti-CD98 (128211)	RL388	Biolegend
Anti-IgG1 (406617)	RMG1-1	Biolegend
Anti-MHCII (107605)	M5/114.15.2	Biolegend
Anti-CD23 (101608)	B3B4	Biolegend
Anti-CD43 (12-0431-82)	eBioR2/60	ThermoFisher
Anti-CD86 (105031)	GL-1	Biolegend
Anti-B220 (103247)	RA3-6B2	Biolegend
Anti-IgM (406513)	RMM-1	Biolegend
Anti-CD21/35 (123409)	7E9	Biolegend

Anti-TACI (133403)	8F10	Biolegend
Anti-CD16/32 (Fc Block)	2.4G2	ThermoFisher
Anti-CXCR4 (741783)	2B11	BD Bioscience
Anti-CD38 (741955)	90	BD Bioscience
Anti-CD4 (100547)	RM4-5	Biolegend
Anti-PD-1 (135213)	29F.1A12	Biolegend
Anti-CXCR5 (145511)	L138D7	Biolegend
Anti-CD45.1 (110717)	A20	Biolegend
Anti-CD45.2 (109817)	104	Biolegend
Anti-CD3 (100215)	17A2	Biolegend
Anti-IRF4 (12-9858-82)	3E4	ThermoFisher
Anti-BCL6 (561525)	K112-91	BD Bioscience
Anti-CHOP (NB600-1335AF700)	9C8	Novus Bio
Anti-Foxp3 (25-5773-82)	FJK-16	ThermoFisher
Anti-phospho-Rb (Ser807/811) (8516T)	D20B12	Cell Signalling Technologies
Anti-phospho-S6 (Cat #17-9007-42)	cupk43k	ThermoFisher
Anti-phospho-EIF2α (EIF2S1) (CL488-68023)	1A4A11	Proteintech
Anti-phospho-4EBP1 (12-9107-42)	V3NTY24	ThermoFisher
Anti-COXIV (ab197491)	mAbcam33985	Abcam
Anti-COXIV (CL488-60251)	3C7D2	Proteintech
Anti-COX I (MTCO1) (ab198600 & ab154477)	1D6E1A8	Abcam
Anti-Cytochrome C (NB100-56503AF700)	7H8.2C12	Novus
Anti-SDHA (ab170172)	2E3GC12FB2AE2	Abcam
Anti-Cyclin B1 (647903)	V152	Biolegend
Anti-phospho-H3 (3465S)	D2C8	Cell Signalling Technologies

Appendix 2. Antibody list for Chapter 4

Flow cytometry antibodies					
Antibody &	**Fluorochrome**	**Clone**	**Dilution (1/n)**	**Manufacturer**	**Cat no:**
Anti-CD45.2	BV605	104	75	BioLegend	109841
Anti-CD45.2	BV785	104	100	BioLegend	109839
Anti-CD45.1	AF488	A20	100	BioLegend	110718
Anti-CD45.1	AF700	A20	100	BioLegend	110724
Anti-CXCR4	APC	REA107	40	Miltenyi Biotec	130-123-274
Anti-CD19	BV510	6D5	200	Biolegend	115545
Anti-B220	BV510	RA3-6B2	200	Biolegend	103247
Anti-CD38	PE-Cy7	90	200	Biolegend	102717
Anti-CD138	BV421	281-2	100	Biolegend	142507
Anti-CD138	AF647	281-2	100	Biolegend	142525
Anti-CD86	BV421	GL-1	100	Biolegend	105031
Anti-CD86	BV785	GL-1	75	Biolegend	105043
Anti-CXCR4	eFluor 450	2B11	50	Thermofisher	48-9991-82
Anti-IgD	BV510	11-26c.2a	200	Biolegend	405723
Anti-IgD	BV650	11-26c.2a	400	Biolegend	405721
Anti-IgM	PE-Cy7	RMM-1	200	Biolegend	406513
Anti-CD21/35	PE	7E9	200	Biolegend	123409
Anti-BP-1	APC	6C3	40	Miltenyi Biotec	130-102-181
Anti-CD23	BV421	B3B4	200	Biolegend	101621
Anti-CD43	PE	S11	200	Biolegend	143205
Anti-CD24	PacBlue	M1/69	200	Biolegend	101819
Anti-GL-7	AF647	GL7	75	Biolegend	144605
Anti-GL-7	AF488	GL7	75	Biolegend	144611
Anti-GL-7	PacBlue	GL7	75	Biolegend	144613
Anti-Gr1	APC-Cy7	RB6-8C5	100	Biolegend	108423
Anti-CD3	APC-Cy7	17A2	100	Biolegend	100221
Anti-CD4	BV510	RM4-5	100	Biolegend	100553
Anti-CD19	BV421	6D5	150	Biolegend	115537
Anti-CXCR5	PE	L138D7	40	Biolegend	145503
Anti-IgG1	BV650	RMG1-1	100	Biolegend	406629
Anti-ICOS	BV650	C398.4A	100	Biolegend	313549
Anti-GITR	APC	DTA-1	50	Biolegend	126311
Anti-cyclin B1	AF647	V152	20	Biolegend	647905
Anti-cleaved caspase 3 (Asp175)	unconjugated	9661	750	Cell signaling	9661T
Anti-phospho histone 3 (Ser10)	AF488	D2C8	50	Cell signaling	3465S
Anti-SDHB	AF647	21A11AE7	100	Abcam	ab197722
Anti-COX I	AF488	1D6E1A8	100	Abcam	ab154477
Anti-TOMM20	unconjugated	EPR15581-54	250	Abcam	ab186735
Anti-TFAM	unconjugated	EPR23548-120	600	Abcam	ab252432
Anti-LAMP1	AF647	EPR21026	500	Abcam	ab237307
Anti-MCU	unconjugated	D2Z3B	250	Cell Signaling	14997S
Fixable viability dye	eFluor780		1000	eBioscience™	65-0865-14
Fixable viability dye	Aqua		1000	Invitrogen™	L34957
Anti-CD16/32 (BD mouse Fc Block)		2.4G2	200	BD	553142
NP-PE	PE		200	Biosearch	N-5070-1
NP-APC	APC		100	in-house	in-house
Goat Anti-Rabbit IgG (H&L) SuperClonal antibody	AF488		500	Thermo Fisher	A27034
Goat Anti-Rabbit IgG (H&L) SuperClonal antibody	AF647		500	Thermo Fisher	A55055
Donkey anti-rabbit IgG	PE		200	BioLegend	406421
Spectral flow cytometry antibody panel					
Antibody	**Fluorochrome**	**Clone**	**Dilution (1/n)**	**Manufacturer**	**Cat no:**
Anti-CD19	BV510	6D5	150	BioLegend	115545
Anti-CD21/35	BV711	7E9	200	Biolegend	123435
Anti-CD93	BUV805	AA4.1	100	BD Bioscience	741989
Anti-IgD	BV650	11-26c.2a	400	Biolegend	405721
Anti-CD4	BV605	RM4-5	150	Biolegend	100547
Anti-IgM	BUV395	II/41	150	BD Bioscience	743329

Anti-CD23	BV786	B3B4	150	BD Bioscience	563988
Anti-B220	BV510	RA3-6B2	200	Biolegend	103247
Anti-CD19	BV785	6D5	100	Biolegend	115543
Anti-CD24	BV711	M1/69	200	BD Bioscience	563450
Anti-BP-1 (CD249)	BUV737	6C3	100	BD Bioscience	741743
Anti-CD43	BV605	S7	200	BD Bioscience	747726
Anti-CXCR4	BUV737	2B11	50	BD Bioscience	741783
Anti-CD86	BV785	GL-1	75	Biolegend	105043
Anti-CD38	BUV805	90/CD38 (Ab90)	400	BD Bioscience	741955
Anti-CD138	BV711	281-2	200	Biolegend	142519
Anti-GL-7	PerCP-Cy5.5	GL7	75	Biolegend	144609
Anti-TFAM	unconjugated	EPR23548-120	600	Abcam	ab252432
Complex I Monoclonal Antibody	PE-Cy7 in house co	18G12BC2	250	Invitrogen	43-8800
Anti-Cytochrome C	AF700	7H8.2C12	400	Novus Bio	NB100-56503AF
Anti-COX I (MTCO1)	AF647	1D6E1A8	200	Abcam	ab198600
Anti-COX IV	CoraLite 488 (CL48	3C7D2	150	Proteintech	CL488-60251
Anti-SDHA	AF594	2E3GC12FB2AE2	500	Abcam	ab170172
Anti-ATP5A1	CoraLite 555	1B10H3	200	Proteintech	CL555-66037
Anti-HSP60	CoreLite 594 (CL59	2F10E7	100	Proteintech	CL594-66041
Anti-Grp75/mtHSP70	AF532	OTI9F8	40	Novus Bio	NBP2-70963AF5
Zombie fixable viability dye	NIR		1000	Biolegend	423105
Anti-CD16/32 (FcBlock)		2.4G2	200	BD	553142
Goat anti-Rabbit IgG (H+L) Highly Cross-Adsorbed Secondary Antibody	Alexa Fluor™ Plus 405		1500	ThermoFisher	A48254

IHC & ICC					
Antibody	**Fluorochrome**	**Clone**	**Dilution (1/n)**	**Manufacturer**	**Cat no:**
Anti-CD38	AF647	90	50	Biolegend	102716
Anti-CD21/35	AF647	7E9	75	Biolegend	123423
Anti-CD21/35	FITC	7E9	75	Biolegend	123407
Anti-CD138	AF647	281-2	50	Biolegend	142525
Anti-IgD	AF647	11-26c.2a	50	Biolegend	405707
Anti-GL-7	AF647	GL-7	50	Biolegend	144605
Anti-GL-7	AF488	GL-7	50	Biolegend	144611
Anti-GL-7	PacBlue	GL-7	50	Biolegend	144613
CD3e Monoclonal Antibody	unconjugated	500A2	100	eBioscience	14-0033-82
Anti-SDHB	AF647	21A11AE7	75	Abcam	ab197722
Anti-COX I	AF488	1D6E1A8	1:100 (IHC) / 1:500 (ICC)	Abcam	ab198600
Anti-TOMM20	unconjugated	EPR15581-54	500	Abcam	ab186735
Anti-Lonp1	unconjugated	Polyclonal	300	Atlas	HPA002192
Anti-TFAM	unconjugated	EPR23548-120	500	Abcam	ab252432
Goat Anti-Hamster IgG (H+L)-0.5 mL	AF647		1000	Thermofisher	A-21451
Goat Anti-Rabbit IgG (H&L) SuperClonal antibody	AF488		500	ThermoFisher	A27034
Goat Anti-Rabbit IgG (H&L) SuperClonal antibody	AF647		500	ThermoFisher	A55055